UNIVERSITY OF SOUTHAMPTON

FACULTY OF ENGINEERING AND PHYSICAL SCIENCES
Optoelectronics Research Centre

# Novel ultra-fast pulsed laser sources for bio-imaging applications

by

**Duanyang Xu**

A thesis for the degree of Doctor of Philosophy

Supervisors: Dr Lin Xu
Prof Sumeet Mahajan
Prof David Richardson

September 14, 2023

UNIVERSITY OF SOUTHAMPTON

## ABSTRACT

FACULTY OF ENGINEERING AND PHYSICAL SCIENCES
Optoelectronics Research Centre

Doctor of Philosophy

### NOVEL ULTRA-FAST PULSED LASER SOURCES FOR BIO-IMAGING APPLICATIONS

by Duanyang Xu

This thesis presents new techniques for the development of compact and reliable laser sources using advanced fibre laser technology, aiming to enhance the multiphoton microscopy (MPM) for biomedical imaging applications.

Our work explores second-order multiphoton-based imaging systems, including second harmonic generation (SHG), two-photon exited fluorescence (TPEF), and coherent anti-Stokes Raman scattering (CARS) microscopy. These systems require picosecond (ps) pulsed lasers with specific spectral and tunability characteristics. I demonstrate a compact, continuous wave (CW) seeded, synchronization-free optical parametric amplifier (OPA), bypassing the complex cavity design of optical parametric oscillators (OPOs). The OPA with 175 mW power level, 8 $\mathrm{cm}^{-1}$ spectral resolution, and 2 ps pulse duration is optimized for CARS microscopy, with rapid and precise tuning achieved through the periodically-poled lithium niobate (PPLN) OPA crystal. We also delve into third-order multiphoton imaging and three-photon microscopy (3PM) systems, which offer improved resolution and penetration depth. These systems require ultrafast laser excitation in the short-wave infrared (SWIR) region, hence necessitating efficient fibre lasers. We develop and optimize mode-locked thulium-doped fibre lasers for these applications. An all-fiberized 1840-nm thulium-doped laser, with a chirped-pulse-amplification system, generates pulses of 7 ps and 1nJ energy. After compression, the pulses deliver 120 kW peak power, enabling successful label-free third-harmonic generation (THG) microscopy imaging. Furthermore, we address environmental sensitivity of non-polarization maintaining (PM) fibre lasers and propose the use of all-PM fibre lasers for better stability and robustness. We develop an all-PM thulium-doped dissipative soliton mode-locked fibre laser, employing nonlinear optical loop mirror (NOLM) mechanism, delivering pulses with 4nJ energy and 350fs width.

By enabling several multi-photon techniques using compact laser sources, our work paves the way for the translation of label-free multi-photon microscopy imaging from scientific research to an imaging-based diagnostic tool for use in the healthcare arena.

# Acknowledgements

I would like to express my deepest gratitude to Jonathan Price, who was not only my supervisor, but also a mentor and friend. Jonathan Price passed away during my PhD studies, but his guidance and support were invaluable to me. Jonathan Price always believed in me and encouraged me to pursue my research with passion and dedication. I feel privileged to have had the opportunity to work with Jonathan Price and will always remember his generosity, kindness, and unwavering support. This thesis is dedicated to Jonathan Price, in loving memory of all he taught me and all the ways in which he touched my life.

I would like to express my sincere gratitude to my supervisors, David Richardson, Sumeet Mahajan and Lin Xu, for their guidance, support, and encouragement throughout my PhD journey. David Richardson, as my primary supervisor, provided invaluable guidance on my research topic and always had time to discuss my progress, no matter how busy he was. David Richardson's vast knowledge of lasers and his ability to think critically and creatively have been a constant source of inspiration to guide me. Sumeet Mahajan, as my co-supervisor, provided invaluable feedback on my work and helped me to refine my research approach and methodology. Sumeet Mahajan's expertise in life science and bioimaging was instrumental in helping me bridge the gap between different areas of my research. I express my heartfelt gratitude to my direct supervisor, Lin Xu, for his invaluable guidance and support. Lin Xu has been a most important part of my research, and his expertise in lasers has been instrumental in the success of my experiments. Lin Xu has provided me with invaluable technical assistance and troubleshooting, and has always been available to answer my questions and provide guidance. Lin Xu's wealth of knowledge and experience in the field has been an invaluable asset to my research. I am extremely proud to have spent all this time working with them.

I am very grateful to my group mates Qiang Fu, Sijing Liang, Di Lin, Yujun Feng, Krzysztof Herdzik, Neda Baktash, Xin Huang, Kunhao Ji, Panuwat Srisamran, Matthew Gerard, and Ibrahim Abughazaleh in Optoelectronics Research Centre and Konstantinos N. Bourdakos, Peter Johnson, James Read, Anna Crisford, Niall Hanrahan and Hiroki Cook in Institute for Life Sciences. Working with them was a true pleasure, they provided valuable insights and feedback on my research and was always available to discuss ideas and troubleshoot problems. They were great collaborators, they helped me to explore new research directions and provided valuable input on my work. They were always willing to lend a helping hand, whether it was with experiments, data collection, analysis, or manuscript preparation. I feel fortunate to have had such a supportive and collaborative group of friends during my PhD studies. Their camaraderie, encouragement, and willingness to share their expertise have been invaluable to me. I would like to express my deepest gratitude to all of them for making this journey so much more enjoyable.

Finally, I extend my deep gratefulness to my family and friends, especially my wife Yiyuan Zhang. She has been my partner, my confidant, and my best friend, and I could not have completed this thesis without her support. I am really thankful to my parents. Their support has been instrumental in making my PhD studies possible, and they have always been there for me when I needed them.

# Contents

# List of Figures

# Declaration of Authorship

I, Duanyang Xu , declare that the thesis entitled *Novel ultra-fast pulsed laser sources for bio-imaging applications* and the work presented in the thesis are both my own, and have been generated by me as the result of my own original research. I confirm that:

- this work was done wholly or mainly while in candidature for a research degree at this University;
- where any part of this thesis has previously been submitted for a degree or any other qualification at this University or any other institution, this has been clearly stated;
- where I have consulted the published work of others, this is always clearly attributed;
- where I have quoted from the work of others, the source is always given. With the exception of such quotations, this thesis is entirely my own work;
- I have acknowledged all main sources of help;
- where the thesis is based on work done by myself jointly with others, I have made clear exactly what was done by others and what I have contributed myself;
- parts of this work have been published as the journal and conference publications listed in Chapter 6.

Signed:........................................................................................................................

Date:...........................................................................................................................

# Chapter 1

# Introduction

## 1.1 Motivation

This study was motivated by the need for a quick, non-invasive detection tool for biological applications. Medical diagnostic techniques have recently been created to satisfy very precise measurements. One illustration of these techniques is X-ray imaging. Most X-rays have a wavelength ranging from 10 picometers to 10 nanometers, corresponding to frequencies in the range 30 petahertz to 30 exahertz ($3\times10^{16}$ Hz to $3\times10^{19}$ Hz) [29]. The efficiency of an organ to absorb radiation is used to assess its properties and structure, including the fat, muscle, and bone in the human body. The different absorption efficiency of each organ provides a variation in a grey-scale intensity at the detection grid. This information is resolved to provide a topological image of the body. However, X-ray images are unable to show organs with equal absorption efficiencies in high contrast. Computer tomography (CT) scans, which are used to increase the detection effectiveness, can help X-ray imaging provide for three-dimensional examination. Another method for topologically detecting organs is magnetic resonance imaging (MRI). The information is provided by how each organ's atoms react to the (external) strong magnetic field differently [94]. However, long examination times and huge instruments are needed for MRI and CT scans. In addition, no metallic or magnetic material should be placed in the MRI or CT scanning region since this could cause magnetic attenuation and cause the scans to fail. Patients with metallic artificial implants will have problems when taking these examinations. Another method for inspecting inside organs is an ultrasound scan [85]. Sound waves are transmitted into the body by an ultrasound probe. It reflects off of organs, producing "echoes" that can be resolved to produce an image of the scanning area in real time. This method performs relatively well for quick tomography analysis, but the sample specification and precision fail to meet patient needs.

Optical imaging employs light and the unique characteristics of photons to acquire comprehensive images of tissues, organs, cells, and molecules. This approach provides small or even non-invasive techniques for examining the interior of the body, which can considerably diminish patient exposure to harmful radiation such as X-ray and can be employed for ongoing procedures to track the evolution of disease or the outcomes of treatment. Multiphoton microscopy (MPM) has progressively cemented its position as one of the top non-invasive methods for fluorescence microscopy in tissue samples and living animals or human-beings in the realm of biological imaging.

MPM represents a laser-scanning microscopy method that relies on localized 'nonlinear' excitation to induce fluorescence exclusively within a narrow raster-scanned plane, leaving other areas unaffected. Since W. Denk's initial demonstration in 1990 [48], MPM has been utilized for various imaging purposes, and it has emerged as the preferred technique for fluorescence microscopy in dense tissue and living organisms [221]. Neuroscientists have employed it to examine detailed calcium dynamics in brain slices [213, 116, 163, 184, 44, 118, 62, 145, 105, 166] and in living creatures [181, 78, 178], to investigate neuronal plasticity [182], and to track the progression of neurodegenerative disease models by monitoring brain sections [102] and live mice [9, 41, 10, 45]. MPM has been extremely useful for various fields of research. Cancer researchers have utilized it to investigate angiogenesis [20, 125] and metastasis [194, 204]. Immunologists have used MPM to study lymphocyte trafficking [23, 133, 196, 132, 2]. Additionally, embryologists have employed MPM to capture the development of a hamster embryo over the course of a day [174]. MPM has found its most crucial niche in applications that involve high-resolution imaging of morphology, physiology, and intercellular interactions in tissues and living animals [221].

MPM exhibits several notable features compared to one-photon microscopy, such as widefield fluorescence and confocal microscopy. The first characteristic is the smaller point spread functions, which inherently eliminate most out-of-plane fluorescence and provide extremely thin optical sectioning. This occurs because only the focal point of the objective lens has a sufficiently high photon density to ensure the concurrent presentation of two photons to the fluorophore. Essentially, it can be stated that multiphoton microscopy eliminates out of focus emission light such that all light observed at the emission wavelength must originate from that single location. Furthermore, this technique uses longer wavelengths of light to excite molecules, thereby reducing scattering in tissue types such as the brain. As a result, 2PEF allows imaging of deeper regions of living tissues, with a range of up to roughly 1.6 mm [99], which is significantly greater than the approximately 200 $\mu$m that can be imaged with single photon confocal microscopy. Consequently, multiphoton microscopy offers enhanced optical access into tissue compared to single-photon fluorescence microscopy and also permits 3D visualization of structures [124].

The utilization of two photon process in multi-photon microscopy (MPM) encompasses a range of techniques, including two-photon excited fluorescence (TPEF), second harmonic generation (SHG), and coherent anti-Stokes Raman scattering (CARS) microscopy. In contrast to TPEF and SHG microscopy, CARS microscopy obtains contrast straight from Raman-active vibrational modes in molecules and necessitates a pair of synchronized pulsed lasers operating at distinct wavelengths. As a label-free technique, CARS presents considerable benefits such as chemical specificity and z-sectioning capability in comparison to widely-used fluorescence-based one-photon imaging approaches. It also provides considerably quicker signal acquisition times than Raman spectroscopy [38, 56]. In biological imaging, CARS is almost an ideal technique for investigating lipids and their metabolism[223], and it can differentiate lipids from proteins through its contrast mechanism[114]. Furthermore, CARS can be integrated with other nonlinear imaging techniques like TPEF [49] and SHG [28] within a single microscope system employing a multi-channel output scheme[190, 32, 149]. This fusion of imaging methods is achieved through a method termed multimodal-CARS, which has demonstrated its usefulness in various applications necessitating structure- and chemical-specific imaging contrast, as each mode can isolate different sample details [111, 212, 112, 139] and facilitate the imaging of live cells and tissues [138]. Utilizing multimodal-CARS offers a comprehensive and versatile approach for obtaining structural, molecular, and functional information about biological samples, enhancing our understanding of complex cellular processes and biological systems. By capitalizing on the unique advantages of each nonlinear imaging modality, multimodal-CARS paves the way for more accurate and efficient research across various fields, including cell biology, biophysics, and biomedical research.

For efficient vibrational coherence and fast image acquisition in CARS, it is crucial to overlap the incident pulses of pump and Stokes in time and space when focused into the sample tightly. Pulses with a duration of a few picoseconds are generally optimum for CARS bio-imaging, as their bandwidths align well with the Raman resonance peak in common cellular structures, while also delivering the high peak powers necessary for efficient excitation of this nonlinear process. However, the technical intricacy, elevated costs, and substantial footprint of bulk laser-based synchronously pumped optical parametric oscillator (OPO) sources typically mandate a dedicated optics laboratory for CARS microscopy, thus limiting its broader adoption. The development of a streamlined laser system that offers the high performance required for CARS, while maintaining a compact, robust form and affordability, is an urgent need.

One of the main objectives of this thesis work is to design and develop a new technique to enable realization of a compact an alow cost laser system that offers few ps pulses with wide wavelength tunability for multimodal two-photon microscopy such as CARS, SHG and TPEF microscopy.

In my work, I designed an optical parametric amplifier (OPA) system that employed a low-power continuous wave (CW) tunable seed laser pumped by 2-ps pulses. The

OPA provided a very high gain, amplified the seed laser and transformed the CW beam into a train of 2-ps pulses. In contrast to OPOs, the OPA does not require temporal synchronization between the pump and the signals and therefore offers good stability, robustness and compactness. The OPA offers a wavelength tunability that covers the entire Raman lipid band in biological tissues ($\sim$ 2700 - 3200 cm$^{-1}$). Good CARS imaging of animal tissues has been successfully demonstrated using the OPA system. In addition to providing great CARS imaging capability, the OPA also enables concurrent SHG and TPEF imaging multi-modality. The powers and beam quality were both well optimized, enabling us to obtain strong signals in the backward direction compared to the signal beam (epi-detection), rather than using forward detection that requires thin samples to allow the signal to be collected. Hence the system offers good potential to be suitable for imaging clinically-relevant and simple-to-prepare thick samples.

In high-resolution second-order nonlinear optical microscopy, the ability to image deeper within scattering biological tissue is limited by the signal-to-background ratio (SBR) of the excitation. To enhance the imaging depth, a useful approach is to employ longer excitation wavelengths that experience lower attenuation by the tissue.

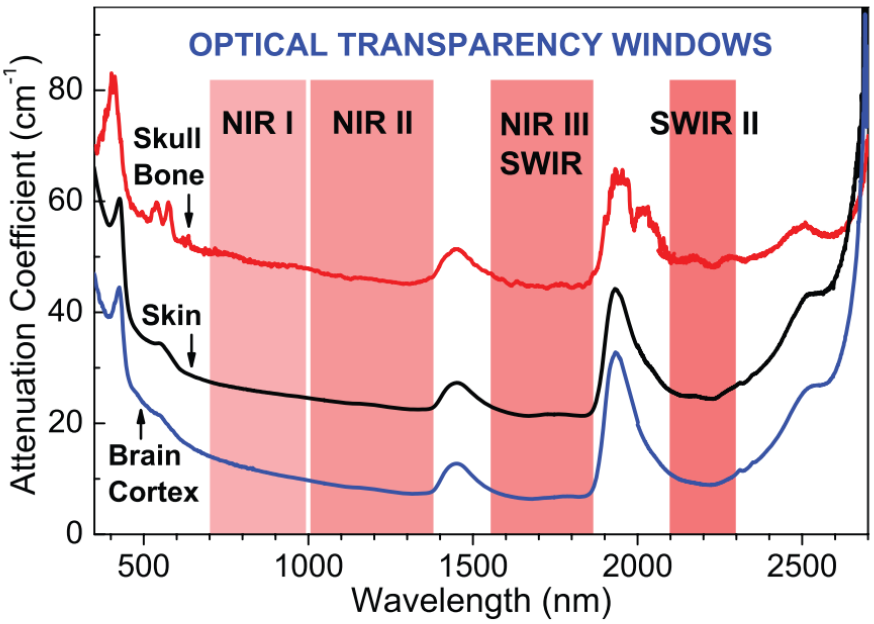

Figure 1.1: Spectra of attenuation coefficient for head tissues: brain cortex, cranial bone and skin. Four optical transparency windows are indicated: ~700 to 1000 nm (NIR-I), ~1000 to 1350 nm (NIR-II), ~1550 to 1870 nm (NIR-III or SWIR) and ~2100 to 2300 nm (SWIR-II). This figure has been reproduced from [67], permission granted. © 2018 WILEY - VCH VERLAG GMBH & CO. KGAA.

In comparison to CARS, SHG, and TPEF MPM techniques, more photon optical microscopy methods, such as third-harmonic generation (THG) microscopy and three-photon excited fluorescence (3PEF), can offer higher signal-to-background ratios (SBR) and deeper penetration when utilizing femtosecond excitation pulses in the short-wave infrared (SWIR) range of 1700 nm to 1870 nm, as noted in references [67, 81]. As illustrated in Figure 1.1, the SWIR presents the lowest attenuation spectral range for most biological samples, which leads to minimum absorption and scattering effects. This improved efficiency increases the power delivery of pump signals and enhances the nonlinear signal strength, thereby contributing to superior MPM resolution [81]. Furthermore, since biomedical samples exhibit less scattering at longer wavelengths, the comparably long wavelength of SWIR reduces scattering and further enhances the resolution. Additionally, the SWIR's higher water absorption compared to other wavelength ranges [202] limits penetration in human eyes, offering eye-safe operation with SWIR pump signals.

Solid-state laser sources based on an optical parametric oscillator or amplifier technique involving high-power NIR femtosecond Ti:sapphire lasers and nonlinear frequency converters have been used to demonstrate with good achievements in such higher-order nonlinear optical microscopies [148, 131]. Compared to such complex and bulky solid-state lasers, fibre lasers offer significant advantages of high efficiency, good compactness and robustness as well as good beam quality. Frequency conversion of 1.5-$\mu$m femtosecond erbium fibre lasers by soliton self-frequency shifting inside a nonlinear optical fibre can generate wavelengths within this SWIR region. However, this technique has a relatively low energy-conversion efficiency and the output wavelength and pulse energy are highly sensitive to the coupling efficiency into the nonlinear fibre [106, 193]. Thulium-doped fibres (TDF) exhibits a broad emission spectrum, spanning from 1600 nm to 2100 nm covering the entire SWIR region and hence represents an attractive gain medium for femtosecond fibre lasers that have potential in such imaging applications [191, 110]. Generally, silica-glass based TDF lasers operate at wavelengths beyond 1900 nm, where the emission cross sections of $Tm^{3+}$ ions in silica are large and high optical gain can be obtained. A TDF laser system generating 297 fs pulses at 1925 nm with pulse energy up to 1.27 $\mu$J has been demonstrated [158]. However, it is challenging to operate short-pulsed TDF laser at the SWIR wavelengths with high pulse energy due to the quasi-three-level nature of the thulium transition and the need for careful management of nonlinearity, dispersion and spectral filtering in such laser systems. A mode-locked (ML) TDF laser operating at 1746 nm has been reported (but with a low power efficiency), generating pulses with an energy of only 0.2 nJ, based on nonlinear polarization rotation (NPR), and which usually results in poor self-starting of the mode-locked laser [33]. Through the development of a dispersion engineered TDF, a mode-locked laser operating in the 1.7 - 1.8 $\mu$m region has been demonstrated and a pulse energy of 128 nJ obtained in a fibre amplifier system [34]. However, the system required a complicated fibre geometry design and fabrication process that could prevent wider application. Instead of using silica-glass TDFs, a 1820 nm fibre laser with pulse energy of 1.1 $\mu$J was developed by using fluoride-glass TDFs and 3PM imaging of a mouse brain by using such a laser was demonstrated [143]. However, a key challenge is the ability to splice the fluoride-glass TDFs used in that system to other silica-glass fibre components, hence, as a consequence, the system is bulky and involves significant free-space alignment. In addition, special preparation of biological samples is required, in which fluorescent protein is transfected to facilitate the 3PM imaging.

In this thesis work, I developed an all-fiberized 1840-nm femtosecond laser system based on standard silica-glass TDFs and successfully demonstrated a proof-of-principle study of its application in label-free THG microscopy of biological samples from hard and soft tissues. In addition, I also show the world-first demonstration of a compact, reliable and stable all-PM thulium-doped dissipative soliton mode-locked fibre laser by commercially available silica fiber and by nonlinear optical loop mirror (Huang et al. got all-PM dissipative soliton result at 2-micron [82] but they used silicate based fiber). The all-PM fibre laser significantly improved the mode locking stability that has proven to be critical for THG microscopy imaging experiment.

## 1.2 Thesis structure

This thesis is composed of 6 Chapters.

Chapter 1 introduces the background of this thesis. It discusses the motivation of my PhD project and describes the thesis structure.

Chapter 2 discusses the related theoretical and technological background of my PhD work. Topics including theories of thulium doped fibres, mode-locked fibre lasers, chirped pulse amplification, optical parametric processes, as well as an overview of multiphoton microscopy.

Chapter 3 focuses on the development of a tunable OPA source for multimodal bio-imaging. Firstly, a compact OPA followed by a SHG frequency converter has been developed and characterized by using a nanosecond-pulsed fibre MOPA system as a pump source in the lab at the ORC. The frequency converter was then moved to a lab at the IfLS and was integrated into the existing microscope using a picosecond-pulsed pump laser. Multimodal MPM imaging using the compact frequency converter has been successfully achieved.

Chapter 4 discusses the development of an 1840-nm femtosecond thulium fiber laser system and demonstrates label-free THG microscopy imaging applications. Experiments towards the development of a mode-locked laser and optimization of the amplifiers of a CPA system are presented. A proof-of-principle study of its application in label-free THG microscopy of biological samples from hard and soft tissues is also demonstrated.

Chapter 5 reports the study of an All-PM mode-locked thulium-doped fiber laser I developed. I demonstrate, to the best of my knowledge, the first experimental realization of an all-PM thulium-doped 1.9 $\mu$m dissipative soliton mode-locked fibre laser by using a nonlinear optical loop mirror (NOLM) SA. NOLM based mode-locked thulium fibre laser approaches such as conventional soliton mode locking and stretched pulse mode locking are also presented. In addition, a SESAM based conventional soliton mode-locked thulium fibre laser is presented as well.

Chapter 6 gives a concluding summary for the whole thesis work and provides a discussion of possible future directions.

All the images cited from other sources used in my thesis are sourced from open-access sources. This ensures that the intellectual property rights of the original creators are respected, and the principle of free dissemination of knowledge is upheld. It also means that readers of my thesis have the ability to easily access and verify the original sources of the images, promoting transparency and integrity in my research.

# Chapter 2

# Theoretical and technological background

In this Chapter, I discuss the theoretical and technological background knowledge that is related to the work presented in this thesis. I first briefly discuss the classical theories of Thulium doped fibre in Section 2.1. Energy level, absorption and, emission properties and pump solutions for the Tm-doped fibre laser are introduced. In Section 2.2, I discuss in detail mode-locked fibre lasers. Passive mode locking, saturable absorbers and mode locked pulse generation are discussed. Section 2.3 discusses the chirped pulse amplification technique including the system structure and the basic nonlinear fibre optics involved in the stretcher and compressor. The optical parametric process is introduced in Section 2.4. Optical Parametric Amplification and Second Harmonic Generation and the associated phase matching condition are discussed. Section 2.5 presents multiphoton microscopy including Two-photon excited fluorescence microscopy, Second Harmonic Generation microscopy, Coherent Anti-Stokes Raman Scattering microscopy and Third Harmonic Generation microscopy.

## 2.1 Thulium doped fibre

In this Section, I will introduce the optical properties of Thulium ions doped in silica glass fibres. Firstly, the energy diagram and spectral properties of $Tm^{3+}$ are discussed. Then, we examine the possible pumping schemes for Tm-doped fibre laser sources.

### 2.1.1 Energy levels

The silica fibre doped with Thulium is commonly employed as a gain medium for signal amplification in the 2 $\mu$m waveband. The energy diagram of $Tm^{3+}$ ions, which includes four manifolds along with Stark levels for $Tm^{3+}$ doped crystals or silicate glass fibres, is depicted in Figure 2.1 (a). The $^3F_4 \rightarrow {}^3H_6$ transition, with a peak near 1850 nm, is illustrated in Figure 2.1 (b) and results in a remarkably broad, featureless emission band, offering an extensive tuning range for lasers and a wide optical bandwidth for amplifiers. Additionally, the $^3H_6 \rightarrow {}^3F_4$ absorption band in Figure 2.1 (b) (red) exhibits a broad profile due to the increased number of Stark components in the $Tm^{3+}$ manifolds and the slightly larger splitting. Thulium-doped silica fibre lasers have been reported to operate at wavelengths from 1700 nm [14] to 2056 nm [107]. It is evident that the lower laser level ($^3H_6$) is in close proximity to the ground state, resulting in a significant population in that level under thermal equilibrium. Consequently, the section of the gain medium without pumping leads to some reabsorption and introduces loss at the laser wavelength, particularly for shorter wavelengths that are nearer to the ground state compared to the longer wavelengths. This phenomenon underscores the importance of considering the impact of the lower laser level population on the overall performance of Tm-doped silica fibre lasers, especially in the context of achieving optimal output power and efficiency within the desired wavelength range.

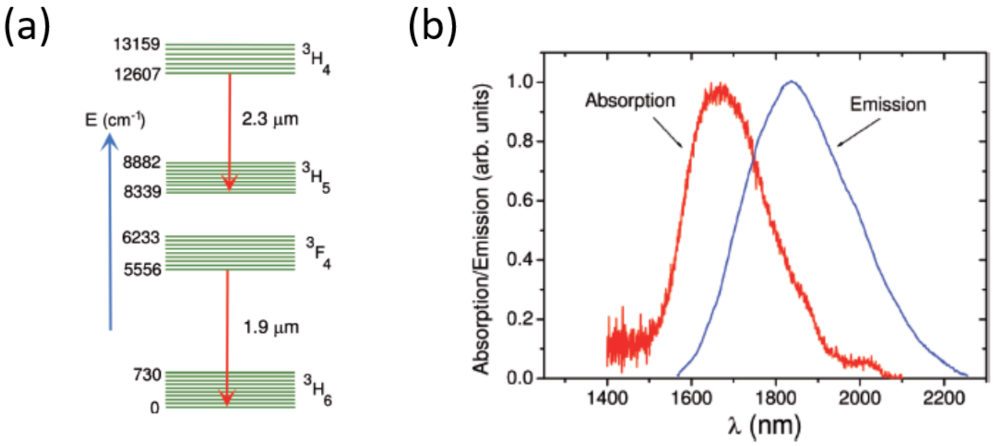

Figure 2.1: (a) Energy level schematic of Tm-Tm energy transfer. (b) Absorption and emission spectra from $^3F_4$ to $^3H_5$. This figure has been reproduced from [170], permission granted. © 2008 INSTITUTE OF ELECTRICAL AND ELECTRONICS ENGINEERS.

The transition from $^3H_4$ to $^3H_5$, corresponding to a 2.3 $\mu$m emission, has primarily been utilized in thulium doped fluorozirconate glass fibre lasers [76]. However, there have been no reports of laser transitions involving these energy levels in thulium doped silica glass fibres. This can be attributed to the exceedingly short lifetime of the $^3H_4$ energy level in silica glass and the low branching ratio from $^3H_5$ [189]. Consequently, the majority of energy transfer processes for $Tm^{3+}$ ions revolve around the $^3F_4$ to $^3H_6$ transition, resulting in stimulated emissions of approximately 1.9 $\mu$m.

### 2.1.2 Pump solution

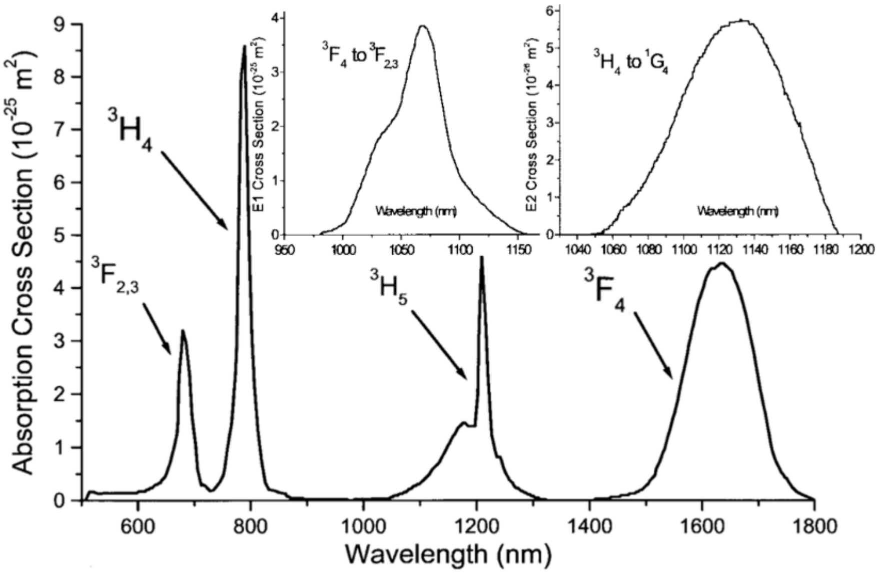

Figure 2.2: Ground state absorption cross section measured from a Tm-doped silica preform. The insets show measured excited state absorption cross-sections of the $^3F_4 \rightarrow {}^3F_{2,3}$ transition and $^3H_4 \rightarrow {}^1G_4$ transition. This figure has been reproduced from [88], permission granted. © 1999 INSTITUTE OF ELECTRICAL AND ELECTRONICS ENGINEERS.

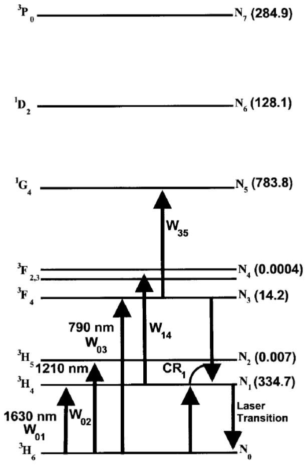

Figure 2.3: Energy diagram for $Tm^{3+}$, the numbers in parenthesis show the calculated lifetime in $\mu$s. This figure has been reproduced from [88], permission granted. © 1999 INSTITUTE OF ELECTRICAL AND ELECTRONICS ENGINEERS.

Thulium-doped fiber sources' potential pumping regimes can be identified by analyzing the $Tm^{3+}$ absorption spectrum (refer to Figure 2.2). In the absence of co-doping with sensitizers [135] like $Yb^{3+}$ [91] or $Er^{3+}/Yb^{3+}$ [65], thulium-doped fiber amplifiers exhibit four pump bands: 660-685 nm [50], 780-800 nm [160], approximately 1200 nm, and 1550-1750 nm [160]. Figure 2.3 displays the last three pump bands and associated transitions, while the 660-685 nm band aligns with the $^3H_6 \rightarrow {}^3F_{2,3}$ transition. It is crucial to note that the 660-685 nm and approximately 1200 nm pump schemes are susceptible to excited state absorption (ESA).

ESA can increase the threshold pump power and diminish the slope efficiency, as well as potentially shift the laser's operational wavelength away from the one with the highest emission cross sections. This occurs because the population of the upper laser level contributes not only to amplification via stimulated emission but also to absorption processes for the pump or laser radiation, in which laser ions are excited to a higher energy level. In order to achieve optimal efficiency for directly pumped lasers and amplifiers utilizing thulium doped fibres, it is advisable to circumvent pump bands that coincide with ESA bands.

Specifically, ESA can occur as a result of the $^3F_4 \rightarrow {}^3F_{2,3}$ transition by supplying the $^3F_4$ level with 1050 - 1120 nm pump photons [50], which may also implicate the $\sim$ 1200 nm pump band [50]. Additionally, the 660 - 685 nm band can initiate $^3F_4 \rightarrow {}^1G_4$ ESA [50].

Consequently, the alternative pumping wavelengths, $^3H_6 \rightarrow {}^3H_4$ and $^3H_6 \rightarrow {}^3F_4$, have emerged as the most prevalent choices, utilizing 793 nm and 1600 nm respectively, as depicted in Figure 2.4. The 793 nm pumping wavelength offers a substantial advantage, as the quantum efficiency can exceed 100% and, in theory, attain up to 200%. This remarkable efficiency stems from the process of cross-relaxation (CR).

As seen in Figure 2.4, upon the excitation of $Tm^{3+}$ at 793 nm, an electron in the $^3H_4$ state can convey a portion of its energy to another electron in the ground state ($^3H_6$), subsequently leading both electrons to transition to the $^3F_4$ state. In heavily Tm-doped fibers, this process may represent the primary decay mechanism from the $^3H_4$ state [90, 86, 19, 89]. This phenomenon holds significant importance for the power augmentation of Tm-doped fiber systems, as it counterbalances the otherwise substantial quantum defect between the pump and the signal (approximately 2 $\mu$m). In [72, 209], findings indicated that a quantum efficiency exceeding 150% was attained (greater than 60% efficiency) in $Tm^{3+}$-doped fiber lasers.

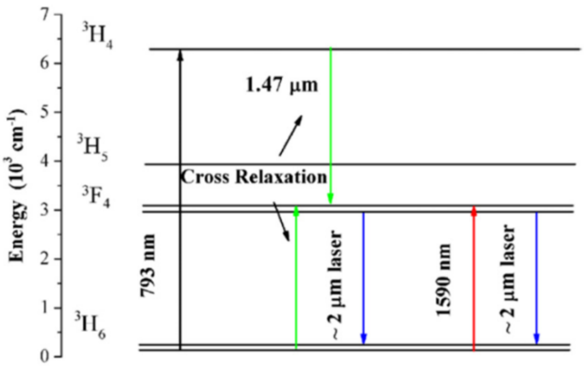

Figure 2.4: Energy level schematic of thulium ions energy transfer. This figure has been reproduced from [167], IEEE doesn't need permission for reuse in thesis. © 2015 IEEE.

The utilization of 1550-1750 nm pumping, also referred to as tandem or in-band pumping, presents a potentially more advantageous approach to attaining the highest power levels compared to 780-800 nm pumping, as suggested by [160]. This method is supported by high-power, cost-effective erbium-ytterbium co-doped fiber lasers (EYDFLs) around 1590 nm, which are capable of providing high-power and high-brightness pump beams for the thulium-doped fiber system. As a result, core pumping or cladding pumping with a substantially smaller inner cladding is made possible, paving the way for shorter devices and, consequently, short wavelength operations due to reduced reabsorption of short wavelength signals. Furthermore, this technique produces remarkably high Stokes efficiency (ranging from 75% to 87%) and minimal quantum defect, enabling highly efficient performance and diminished thermal load [168]. Reported slope efficiencies of up to 72% (relative to absorbed pump power) have been achieved [168].

In this thesis we mainly used a 1565 nm pump source for the Thulium doped fibre lasers.

## 2.2 Mode-locked fibre lasers

### 2.2.1 Passive mode-locked fibre lasers

Passive mode-locking is a technique that hinges on the manipulation of inherent nonlinear interactions between the propagating pulse and the optical fiber medium. The mode-locked operation emerges from the interplay between group velocity dispersion

(GVD) and self-phase modulation (SPM), which results in modulation instability that converts a continuous-wave (CW) signal into a pulse train [198]. This nonlinear phenomenon involves the intentional introduction of a saturable absorber into a laser cavity, which subsequently prompts a pulsed regime within the laser systems. In essence, the inclusion of the saturable absorber within the laser resonator causes reduced power losses for the intense peak of a circulating ultrashort pulse, as opposed to the higher losses experienced by low optical power light striking the absorber at other moments. This mechanism favors the pulse peak, and consequently can be perceived as forming and stabilizing a relatively short pulse.

(a) Active mode-locking

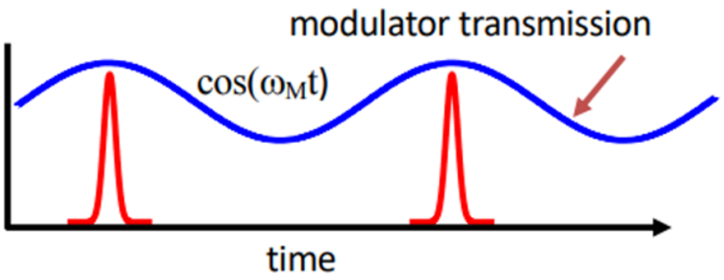

(b) Passive mode-locking

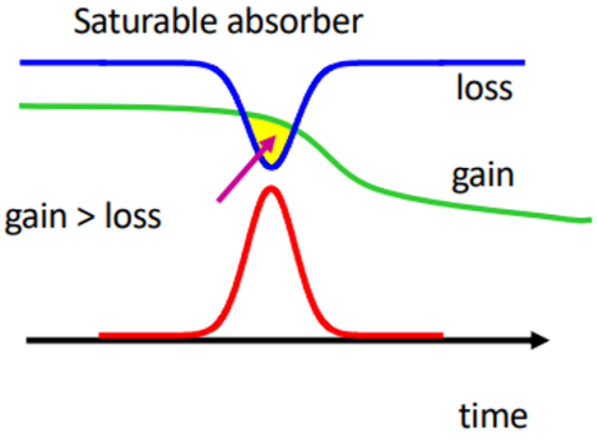

Figure 2.5: Temporal evolution of optical gain and loss in a (a) actively mode-locked laser with a modulator and (b) passively mode-locked laser with a fast saturable absorber.

Active mode-locking involves incorporating a modulator into the laser cavity that sinusoidally modulates the pulse amplitude, resulting in mode competition, coupling each mode to modulation sidebands, ultimately causing all modes to couple and phase-lock. The modulation frequency must be a harmonic of the cavity repetition rate. In contrast, passive mode-locking entails introducing components, such as saturable absorbers (SA), into the laser cavity that favor high intensities which leads to the strengthening of stronger peaks while weaker ones are compromised, ultimately concentrating all energy in a single packet (Figure 2.5). Saturable absorption represents the nonlinear intensity-dependent absorption properties of materials, which can be employed to create optical losses for low-intensity modes and bolster the self-starting process in passive mode-locking resonators. Saturable absorption will be explained further in subsequent sections. In comparison to active mode-locking, passive mode-locking has the ability to generate significantly shorter pulses. This is primarily because a saturable absorber can modulate cavity losses more rapidly than any electronic modulator: the shorter the circulating pulse becomes, the faster is the loss modulation obtained. Passive mode-locking simplifies the laser setup by automatic loss modulation synchronization, and no electronic driver or modulator is necessary.

### 2.2.2 Saturable absorber

SA is an optical component characterized by a lower absorption loss for light with stronger optical intensity. Such nonlinear absorption process can happen, for example, in a medium containing absorbing dopant ions, where a high optical intensity results in the depletion of these dopant ions' ground state. Exciting electrons from the valence band to the conduction band in semiconductors can lead to a decrease in photon absorption for energies just slightly higher than the band gap energy. [165]

The absorption of the saturable absorber decreases as the intensity of incident light increases. This relationship between absorption and intensity can be expressed as:

$$\alpha(I) = \frac{\alpha_0}{1 + \frac{I}{I_{sat}}} \tag{2.1}$$

where $\alpha(I)$ represents the transmission, while $I$ denotes the input pulse energy and $I_{sat}$ refers to the saturation energy.

Figure 2.6 illustrates an instance of absorption variation for these SAs.

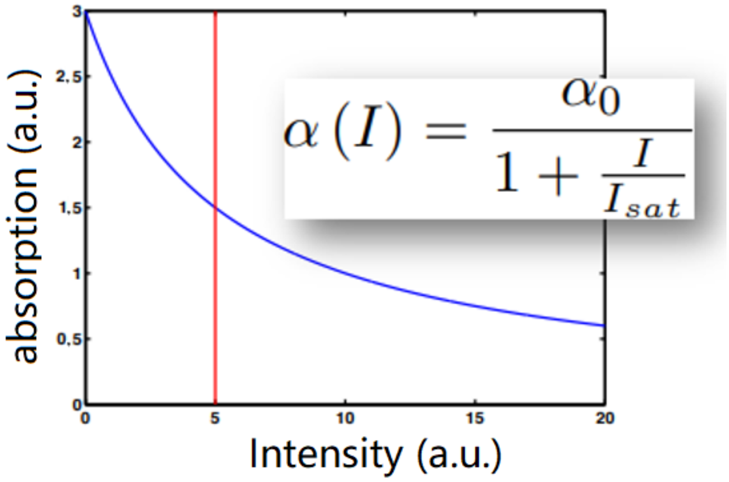

Figure 2.6: Variation of absorption with intensity.

The correlation between absorption of the SA and optical pulse intensity as a function of time through the pulse is depicted in Figure 2.7.

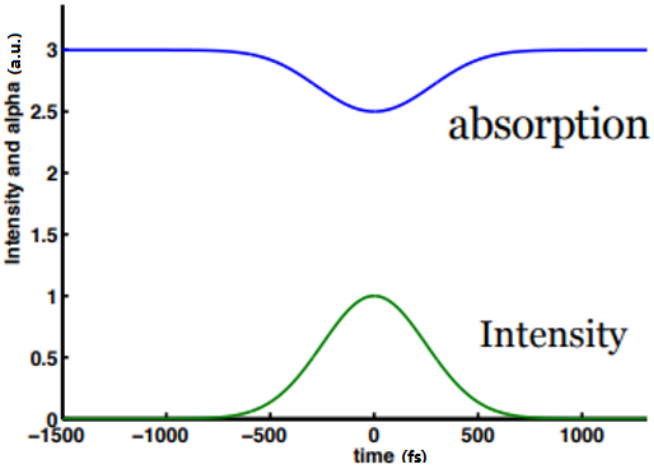

Figure 2.7: Variation of absorption with time.

#### 2.2.2.1 Nonlinear polarization rotation

Nonlinear polarization rotation (NPR) is a widely used technique for mode-locked fiber lasers. It was first introduced in 1992 by V. J. Matsas at the Optoelectronics Research Centre (ORC) at the University of Southampton [121, 122]. Nonlinear effects such as self-phase modulation and cross-phase modulation are dependent on the intensity of the pulse. These effects cause nonlinear phase shifts throughout the duration of the pulse, ultimately resulting in NPR.

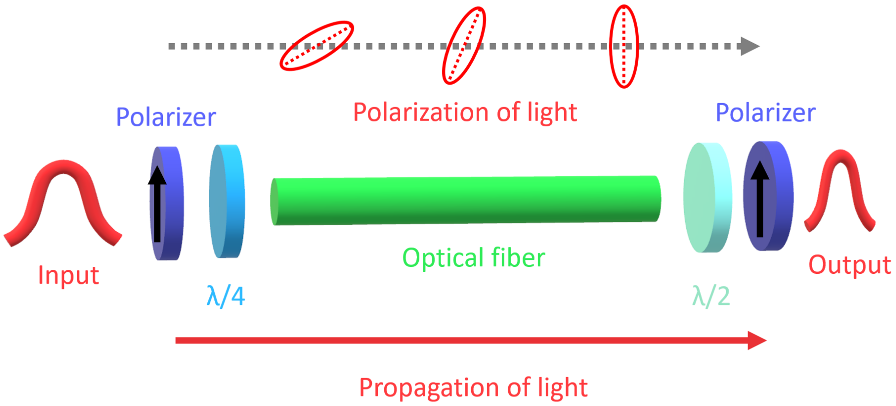

Figure 2.8: The basic structure of NPR.

Figure 2.8 presents a schematic representation to explain the NPR principle. Initially, the pulse exhibits linear polarization as it traverses the first polarizer and transitions into elliptical polarization upon going through a quarter-wave plate. Within the optical fiber, the elliptically polarized light can be separated into two orthogonally linearly polarized components, denoted as $A_x$ and $A_y$. As the $A_x$ and $A_y$ linearly polarized beams transmit through the fiber, distinct nonlinear phase shifts accumulate between the $A_x$ and $A_y$ polarization directions due to the nonlinear effects of SPM and cross-phase modulation (XPM). At the right side which is the output side of the fibre, the pulse is a combination of $A_x$ and $A_y$, exhibiting varying nonlinear phase shifts throughout the pulse width. By adjusting half-wave plates and a polarizer at the fiber's end, a small portion of the original pulse can be allowed to pass the polarizer with minimal loss. Consequently, this method enables the realization of a NPR-based rapid artificial SA suitable for application in fiber laser mode-locking.

#### 2.2.2.2 Semiconductor saturable absorber mirror

Figure 2.9 depicts the structure of a typical semiconductor saturable absorber mirror (SESAM). A semiconductor heterostructure (in this case, GaAs/AlAs) grows on a GaAs wafer (20-40 pairs), with layer thicknesses chosen to be quarter-wave at the laser's central operating wavelength. These structures function as quarter-wave Bragg mirrors. A layer of low index material (AlAs) that is half-wave thick and has a field-maximum in its center is grown on top of the Bragg mirror. At the peak of the field, a layer of either a compound semiconductor in bulk or a structure of single or multiple quantum walls is embedded, serving as a saturable absorber for the laser's operating wavelength as explained in [96].

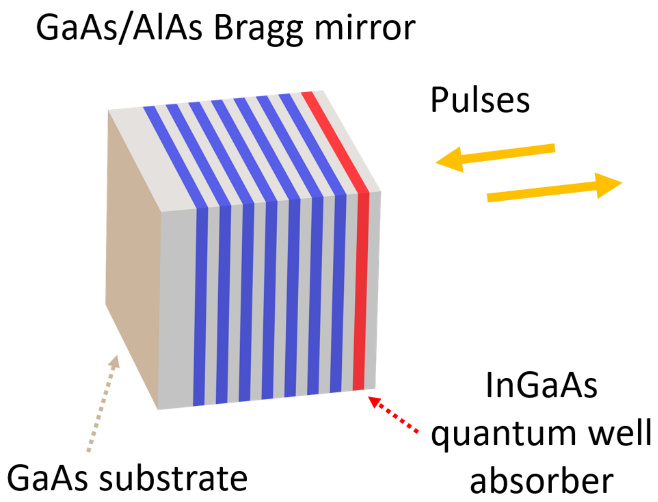

Figure 2.9: Schematic of the semiconductor saturable absorber mirror structure

SESAMs have been developed over the years and are extensively utilized in fiber laser systems including Yb, Er and Tm [68, 217, 157]. SESAMs with varying modulation depths and response times are commercially available from many companies and can also be customized. Batop is a company specializing in SESAMs, where detailed information and customer reviews can be found on their website [15]. SESAMs offer a straightforward implementation, however, they come at a relatively high cost and are susceptible to damage when used for prolonged periods or at high power levels. Furthermore, SESAMs have limited wavelength range. They are sensitive to the wavelength of the incident light, which limits their applicability to specific wavelength ranges. This means that they may not be suitable for all laser systems without modification or customization.

The wavelength dependent reflectivity at low intensity of the SESAM provided by the supplier is shown in Figure 2.10.

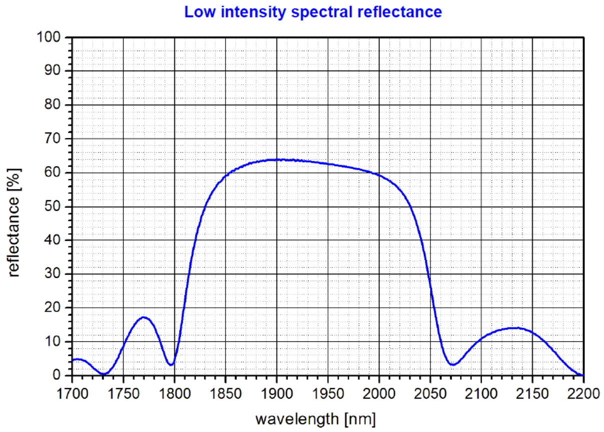

Figure 2.10: Reflective spectrum of commercial SESAM (Batop, SAM-1920-36-10ps). This figure has been reproduced from [15], in accordance with their open access policy and terms of use.

The intensity dependent reflection of a SESAM can be estimated by [16]:

$$R(F) = 1 - \frac{A_0 F_{sat}}{F}\left(1 - e^{-\frac{F}{F_{sat}}}\right) - A_{ns} \tag{2.2}$$

where $R(F)$ is the intensity dependent reflection versus the pulse fluence $F$, $A_0$ represents absorbance, $F_{\text{sat}}$ denotes saturation fluence and $A_{ns}$ stands for non-saturated loss. In Figure 2.11, the calculated intensity dependent reflectivity using Equation 2.2 is presented for the SESAM (Batop: SAM-1920-36-10ps) utilized in this thesis experiment. The figure illustrates an increase in reflectivity with higher optical intensity.

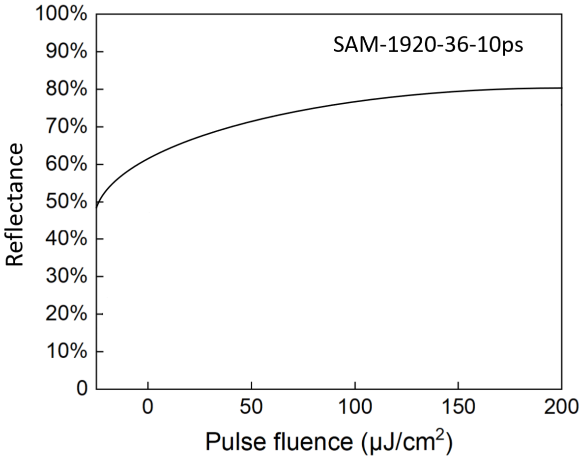

Figure 2.11: Calculated reflectance curve of the SESAM (Batop SAM-1920-36-10ps) used in this thesis.

#### 2.2.2.3 Nonlinear optical loop mirror

In 1987, N.J. Doran and D. Wood initially introduced the concept of the nonlinear optical loop mirror (NOLM) [52]. Figure 2.12 illustrates a typical structure of a NOLM, which consists of one input port, one output port, a 2 x 2 coupler, and a fiber segment forming a loop mirror.

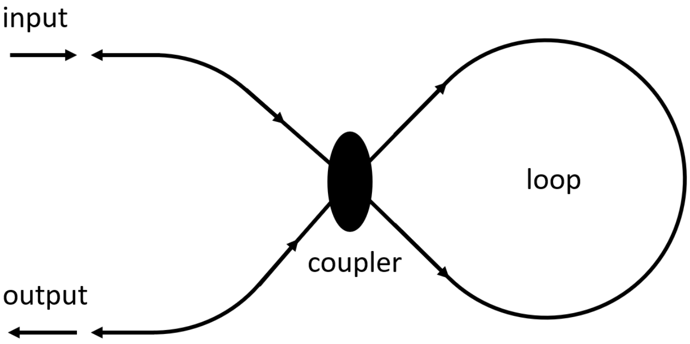

Figure 2.12: Schematic of NOLM.

The Kerr nonlinearity can significantly impact ultrashort pulses in NOLM fibres due to their high peak power. However, if the the coupling ratio is 0.5 and fibre loop is symmetrical, any nonlinear phase shifts that occur will not affect the reflectance of the fibre loop as these phase shifts are identical for light propagation in two directions, leaving the interference conditions unaltered [165].

To realize a NOLM, an asymmetric design is necessary. One method to achieve asymmetry is by introducing a rare-earth-doped fiber that can amplify light with proper pump light injection, along with a long passive fiber. This structure is known as nonlinear amplifying loop mirror (NALM). Furthermore, one side of the passive fiber exhibits significant optical attenuation or the coupler has an asymmetric coupling ratio would also result in such power dependence without amplification, resulting in a NOLM. The NOLM can be used as an artificial saturable absorber for building mode-locking laser cavities due to it is able to initiate and stabilize mode locking for example pulse formation in [54]. A well-known example is the figure-eight fiber laser, where the nonlinear fiber loop mirror constitutes one part of the "eight" and the actual laser ring forms the other [165].

Figure 2.13 presents a simulation of the saturable absorption effect for a NOLM built by a 15 meters long single-mode fiber. The two curves depict the output power to input power ratio concerning varying input power levels with 0.1 and 0.3 NOLM coupling ratio, separately.

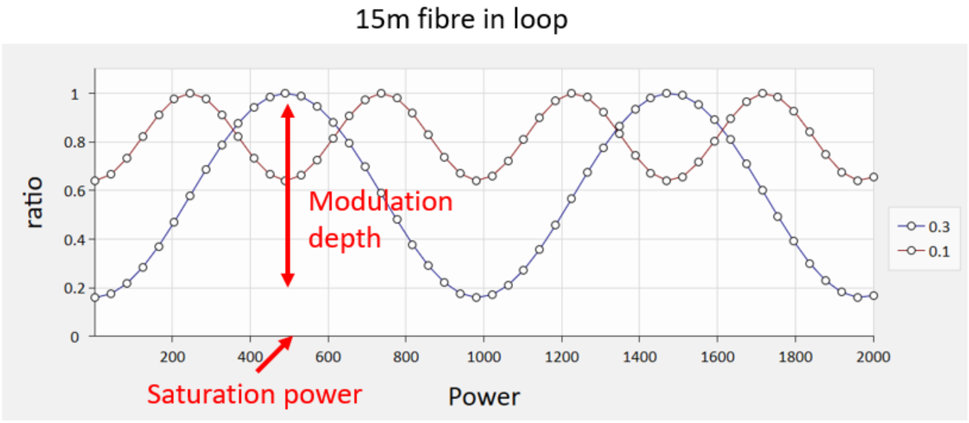

Figure 2.13: NOLM modulation depth and saturation power difference between 0.3 and 0.1 coupling ratio.

### 2.2.3 Mode locking pulses

Passively mode-locked Tm-doped fibre lasers (TDFLs) can produce various types of mode-locked pulses, including conventional solitons [136], stretched pulses [183], dissipative solitons [69], dissipative soliton resonances [53], and noise-like (NL) pulses [80] depending on distinct dynamics of mode-locking and oscillator conditions. In this section, I will focus on and provide an introduction to the conventional soliton, stretched pulse, and dissipative soliton.

#### 2.2.3.1 Conventional soliton

In 1965, the term soliton was coined to describe particles that exhibit solitary wave properties and retain their integrity even after colliding with one another [214]. In 1973, the idea of employing solitons in optical communication was first suggested in the field of optical fibers [74]. Solitons are solutions to the Nonlinear Schrödinger equation (NLSE), which models conservative systems (loss or no gain) such as the propagation of pulses in passive fibers. The first soliton laser was experimentally demonstrated by Mollenauer in 1984 using fibers with anomalous dispersion [136]. To date, soliton mode (Figure 2.14) is the most common pulse formation in mode-locked fiber lasers. Typically, ultra-short pulses undergo changes in their temporal and spectral profile due to chirps resulting from self-phase modulation and group velocity dispersion. However, there are certain circumstances where the phase shift caused by self-phase modulation and anomalous dispersion in fiber lasers can be precisely balanced, resulting in stable pulse shapes that persist over long propagation distances.

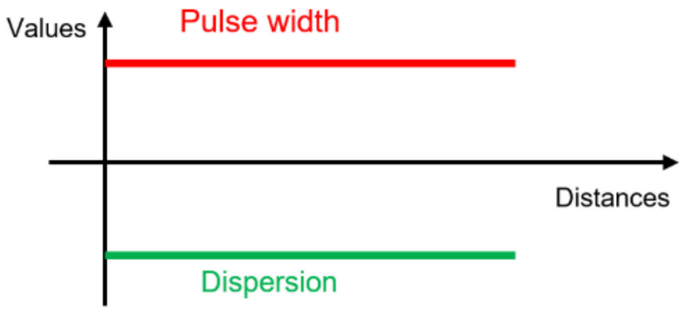

Figure 2.14: Soliton pulse evolutions with distance. This figure has been reproduced from [155], in accordance with their open access policy and terms of use.

Soliton pulses exhibit a sech$^2$ shape, stemming from a fundamental equilibrium between linear dispersion and cubic nonlinearity:

$$P\left(t\right) = P_p \; sech^2 \left(\frac{t}{\tau}\right) \tag{2.3}$$

The symbol '$P_p$' represents peak power and '$\tau$' represents soliton pulse duration. The time-bandwidth product ($\tau \triangle \nu$) for the transform limited soliton pulse is approximately 0.315.

Soliton pulses in fiber cavities have a nonlinear phase shift that is determined by their energy and width after one round-trip. This means that the maximum energy of a stable soliton pulse is limited for a fixed pulse width due to the range of nonlinear phase shifts required for stable soliton generation [142]. Another constraint in mode-locked fiber lasers is the presence of Kelly sidebands (see Figure 2.15), which are common in such lasers [171]. These sidebands arise from the coupling of soliton pulse energy into the corresponding discrete resonant waves, resulting in peaks known as Kelly sidebands. The positions of these sidebands in the optical spectrum can provide information of chromatic dispersion in the fiber. If discrete wave power reaches its lasing threshold value, it will deplete laser gain and cause mode locking to become unstable [97]. Incorporating the soliton area theorem, there is a constraint on pulse energies which results in typical laser performances around 100 pJ and 200 fs.

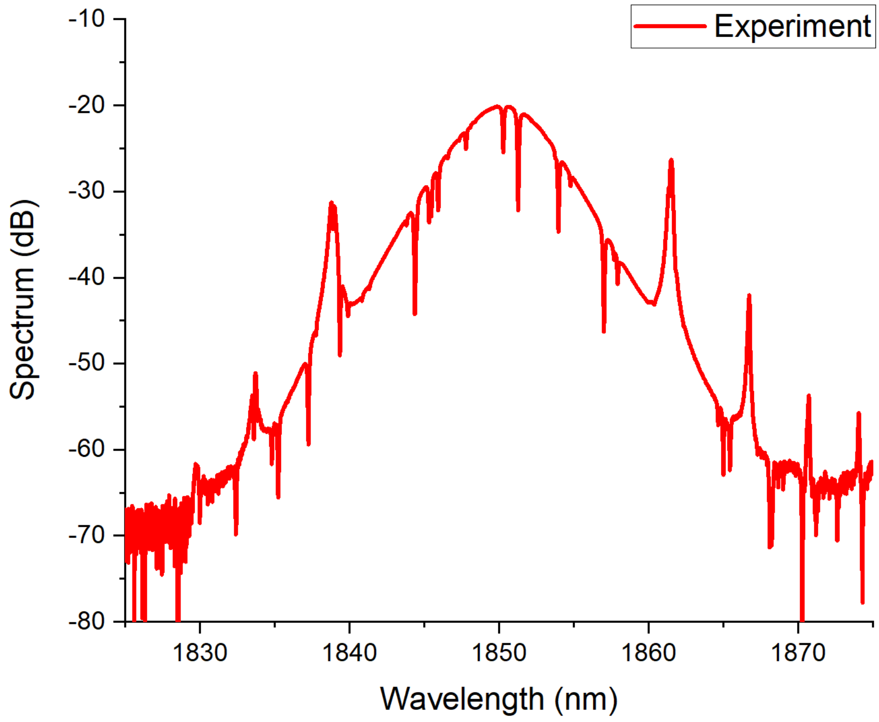

Figure 2.15: Optical spectrum of the output of a soliton fiber laser from Chapter 5, exhibiting Kelly sidebands.

#### 2.2.3.2 Stretched pulse/dispersion managed soliton

Dispersion managed solitons, also known as stretched pulses, are characteristic of stretched pulse fiber lasers where stretch and compress the pulse twice during each round-trip within the cavity. As depicted in Figure 2.16, the incorporation of both normal and anomalous dispersion via dispersion compensation fibers (DCF) and standard single-mode fibers (SMFs) enables the periodic stretching and compressing of the pulse width. Consequently, the average pulse width is significantly larger than that of soliton mode pulses in a single round trip. This feature decreases the peak power of the pulses, leading to reduced nonlinear phase shifts at higher pulse intensities. Ultimately, this allows the cavity to deliver higher pulse energies, offering approximately ten times more energy than stable soliton pulses [58, 183]. In contrast to soliton fiber lasers, the output spectrum of stretched-pulse lasers can be broader than the gain spectrum and lacks sidebands due to reduced phase-match coupling. A master equation also exists for operating a dispersion managed soliton [75] and it is worth noting that the pulse generated by the stretched pulse laser is typically closer to a Gaussian shape, as it is a solution to the master equation.

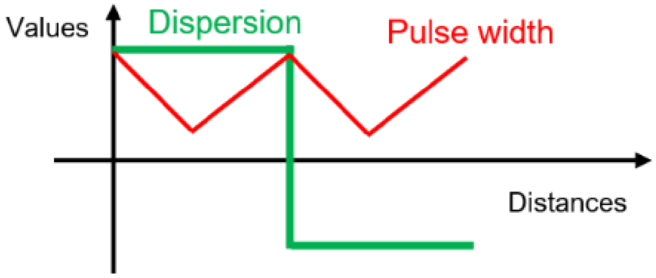

Figure 2.16: Dispersion management pulse evolutions with distance. This figure has been reproduced from [155], in accordance with their open access policy and terms of use.

Temporal breathing in stretched-pulse lasers leads to a reduction in round-trip nonlinearity compared to a static solution with the same energy. This allows the generation of higher pulse energy than in a stable soliton laser. The dispersion map in these lasers suppresses the presence of sidebands and minimizes resonant instabilities. The output pulses might be slightly up- or down-chirped, depending on the location of the output coupler in the cavity. However, these pulses can be dechirped to durations of less than 100 fs outside the cavity, with energies reaching approximately 2 nJ.

#### 2.2.3.3 Dissipative solitons

Dissipative soliton (DS) fiber lasers (Figure 2.17) offer an alternative to conventional soliton oscillators, addressing their drawbacks in terms of pulse duration and energy. DS formation in laser cavities requires balancing two additional terms compared to conventional solitons, namely gain and loss, as illustrated in Figure 2.18 [69]. The term "dissipative soliton" originates from the theory that, in contrast to conventional soliton mode locking which involves only dispersion and nonlinearity terms, gain and loss (dissipative processes) play a crucial role in mode locking process. Typically, DS fiber lasers necessitate an all-normal dispersion cavity or a net normal dispersion cavity. However, achieving normal dispersion fibers at longer wavelengths can be challenging. Consequently, most actual DS fiber lasers operate with dissipative dispersion-managed (DDM) solitons [71].

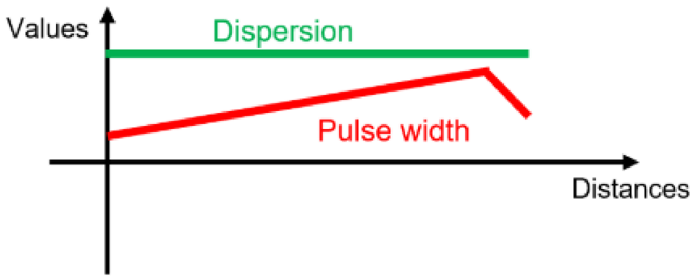

Figure 2.17: Dissipative soliton pulse evolutions with distance. This figure has been reproduced from [155], in accordance with their open access policy and terms of use.

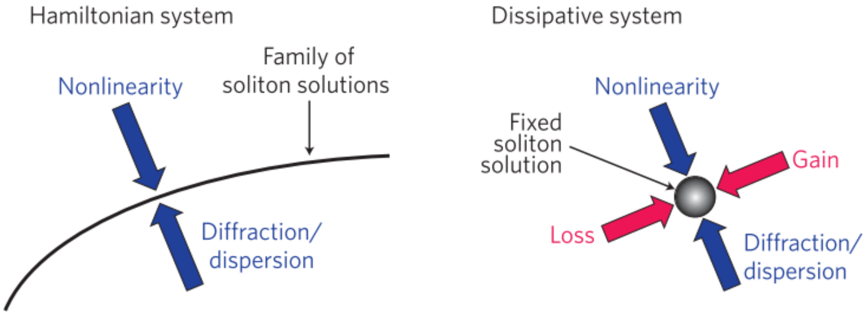

Figure 2.18: Qualitative differences between the solitons in Hamiltonian and dissipative systems. This figure has been reproduced from [69], permission granted. © 2012 Nature Research.

The evolution of optical pulses of dissipative solitons, in the presence of electronic Kerr nonlinearity, group velocity dispersion, and dissipative processes, can be represented by the complex Ginzburg-Landau equation incorporating cubic and quintic saturable absorber terms [159, 30]:

$$U_z = gU + \left(\frac{1}{\Omega} - \mathrm{i}\frac{D}{2}\right) U_{tt} + (\alpha + \mathrm{i}y)|U|^2 U + \gamma |U|^4 U \tag{2.4}$$

In this equation, 'U' represents the electric field envelope, 'z' is the propagation coordinate, 't' denotes the retarded time, 'D' refers to the group velocity dispersion, 'g' signifies the net gain and loss, 'Ω' is associated with the filter bandwidth, '$\alpha$' is a term for the cubic saturable absorber, and '$\gamma$' corresponds to the cubic refractive nonlinearity of the medium.

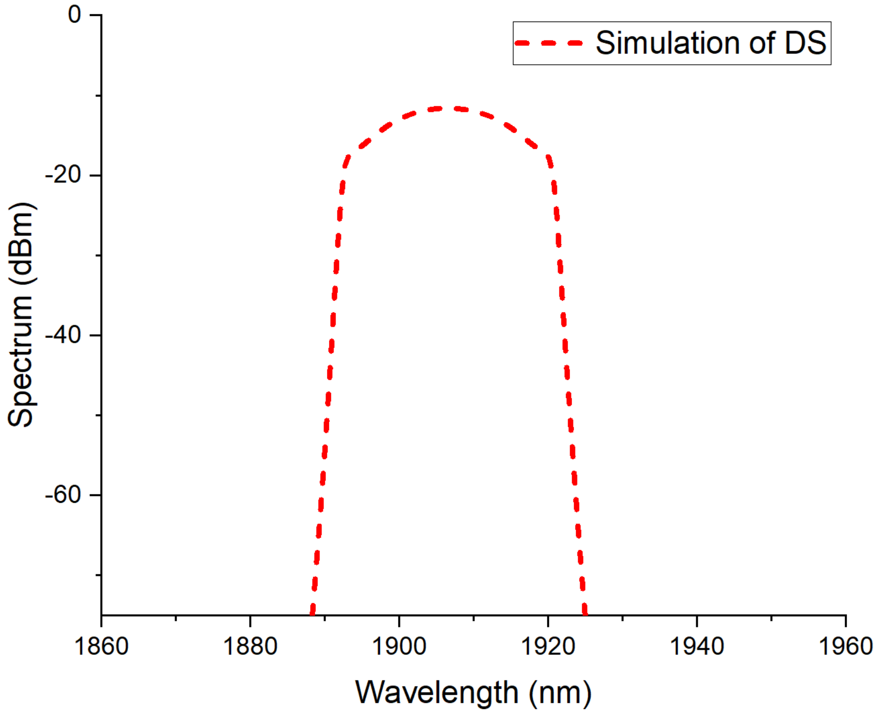

Figure 2.19: The typical spectrum of a dissipative soliton mode locking from simulation.

While pulse shaping occurs in normal-dispersion fiber lasers, the output spectrum exhibits characteristics such as steep spectral edges and a flat-top profile due to the spectral filtering effect of pulses with high chirp [159, 53]. A typical spectrum for dissipative soliton mode locking from simulation is displayed in Figure 2.19. Provided that there is an maximum energy limit for the dissipative soliton with a maximum accumulated phase shift of $10\pi$, the pulse width can be expanded arbitrarily while maintaining a constant amplitude as the pump power increases [203].

Compared to conventional solitons and stretched pulses, dissipative soliton mode locking can generate significantly higher pulse energies, which can also be compressed to achieve very short pulse durations [69].

## 2.3 Chirped pulse amplification

### 2.3.1 Introduction

Chirped-pulse-amplification (CPA) is a technique that stretches a short-duration optical pulse in time prior to amplification and then re-compresses it, effectively avoiding harmful nonlinear effects. The typical schematic of a CPA setup, depicted in Figure 2.20, involves stretching an ultra-short pulse from a mode-locked laser using a dispersive medium, amplifying it, and then re-compressing it with the opposite dispersive medium. Commonly, grating-based pulse stretchers and compressors serve as the dispersive elements. The stretched pulse possesses a time-varying instantaneous frequency, primarily influenced by the pulse stretcher, hence the term chirped pulse. Nonlinear effects set a limitation on output power, so the pulse energy that can be extracted from the amplifier is directly proportional to the duration of the pulse. Consequently, the peak power attainable after re-compression also increases according to the ratio of the pulse duration's expansion.

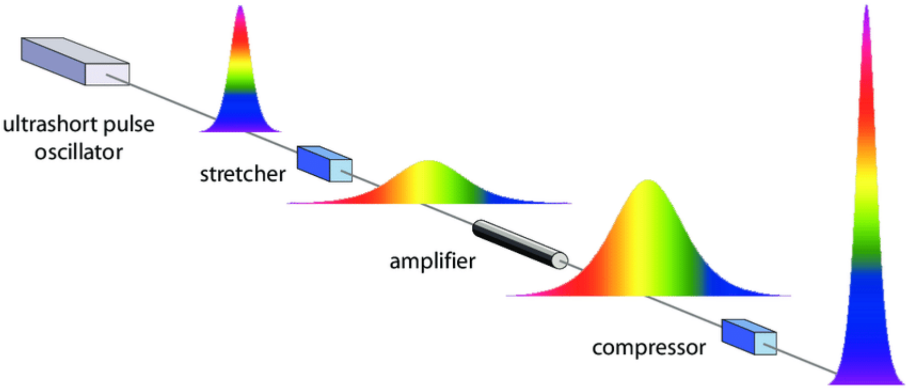

Figure 2.20: Evolution of the temporal pulse shape in a chirped-pulse amplifier.

The CPA technique has been widely implemented by academic institutions and research facilities across the globe since its initial unveiling [179]. CPA systems employing fiber amplifier have been designed to leverage the larger mode areas of active fibers. Despite being restricted by the emergence of undesirable nonlinear effects due to the confined spatial distribution of the optical signal and extended propagation distance in the material, fiber amplifiers are capable of delivering higher average power owing to their exceptional thermal management capabilities. Moreover, fiber systems boast superior beam quality and are well-suited for industrial applications, given their remarkable stability and compactness. A fiber-based CPA system exhibiting increased pulse energy and peak power has been showcased [156], generating 297-fs pulses with a 1.25 $\mu$J pulse energy and a 4.2 MW peak power. The power amlification medium incorporated in this system is a 1.5-meter-long PM double-cladding (DC) Thulium-doped fiber with a core diameter of 25 $\mu$m. The expansive mode size diminishes the intensity of the transmitted pulse, subsequently reducing the accumulation of nonlinear phase during high peak power operations. In the aforementioned fiber CPA systems, the stretcher and compressor components rely on grating-based technology. The first-ever all-fiber CPA system employed chirped-fiber-Bragg gratings for stretching and compressing pulses [64].

### 2.3.2 Fibre nonlinear optics

#### 2.3.2.1 Nonlinear pulse propagation

The fundamental nonlinear pulse propagation within a fiber is characterized by the Nonlinear Schrödinger Equation, which can be expressed through a comparatively straightforward equation [3]:

$$\frac{\partial A}{\partial z} + \frac{\alpha}{2}A + \frac{i\beta_2}{2}\frac{\delta^2 A}{\delta T^2} - \frac{\beta_3}{6}\frac{\delta^3 A}{\delta T^3} = i\gamma\left(|A|^2 A + \frac{i}{\omega_0}\frac{\partial}{\partial T}\left(|A|^2 A\right) - T_R A\frac{\partial |A|^2}{\partial T}\right) \tag{2.5}$$

In this equation, '$A$' denotes the variation of pulse envelope with respect to distance '$z$' at time '$t$'. The terms '$\beta_2$' and '$\beta_3$' represent the group velocity dispersion (GVD) and third-order dispersion, respectively. '$\alpha$' stands for the fiber's linear loss, while '$\gamma$' signifies the fiber's nonlinear parameter.

To simplify the NLSE, we can consider a relatively wide pulse width (e.g., $T \geq 5$ ps). In this situation, the last two terms '$\frac{i}{\omega_0}\frac{\partial}{\partial T}\left(|A|^2 A\right)$' and '$T_R A\frac{\partial |A|^2}{\partial T}$' in Equation 2.5 can be disregarded, as the parameters $\frac{i}{\omega_0}$ and $\frac{T_R}{T}$ are quite small ($\leq 0.0001$). Additionally, the third-order dispersion term '$\frac{\beta_3}{6}\frac{\delta^3 A}{\delta T^3}$' is also minimal, unless the operating wavelength is in close proximity to the zero-dispersion wavelength. Ultimately, we derive the most simplified NLSE, which accounts for the third-order nonlinearity and can be expressed as:

$$\frac{\partial A}{\partial z}+\frac{\alpha}{2}A+\frac{i\beta_2}{2}\frac{\delta^2 A}{\delta T^2}=i\gamma\left(|A|^2A\right) \tag{2.6}$$

In summary, there are three components in the fundamental NLSE (Equation 2.6): the loss term ($\frac{\alpha}{2}A$), the GVD term ($\frac{i\beta_2}{2}\frac{\delta^2 A}{\delta T^2}$), and the nonlinear term (Self-Phase Modulation) ($i\gamma\left(|A|^2A\right)$). To incorporate higher-order nonlinearity terms, the NLSE in Equation 2.6 must be adjusted [3].

The nonlinear parameter ($\gamma$) in Equations 2.5 and 2.6 is defined as follows:

$$\gamma=\frac{\omega n_2}{cA_{eff}} \tag{2.7}$$

and the effective mode area ($A_{eff}$) can be defined as:

$$A_{eff}=\frac{\left(\iint_{-\infty}^{\infty}|F(x,y)|^2dxdy\right)^2}{\iint_{-\infty}^{\infty}|F(x,y)|^4dxdy} \tag{2.8}$$

The parameter $n_2$ is nonlinear with units of $m^2/W$, and so is $\gamma$ when it has a unit of $W^{-1}/m$. It is helpful to introduce the following two length-related terms:

$$L_D=\frac{{T_0}^2}{|\beta_2|} \tag{2.9}$$

$$L_{NL}=\frac{1}{\gamma P_0} \tag{2.10}$$

The dispersion length ($\mathrm{L}_D$) and nonlinear length ($\mathrm{L}_{NL}$) in Equations 2.9 and 2.10 indicate the distance a pulse must travel before either or both of these effects start to dominate the propagation. Several conditions can be derived from the relationships among L (propagation length), $\mathrm{L}_D$, and $\mathrm{L}_{NL}$: when both $\mathrm{L}_D$ and $\mathrm{L}_{NL}$ are significantly smaller than L, neither GVD nor SPM have a substantial impact on pulse propagation in the fibers; when $\mathrm{L}_D$ is considerably smaller than $\mathrm{L}_{NL}$, the GVD effect becomes dominant, and the opposite is true.

The Thulium-doped fibers (OFS TmDF200) utilized in the experiments for this thesis reportedly have a measured GVD parameter of approximately -0.02 $\mathrm{ps}^2$/m at 1.9 $\mu$m [100], so the dispersion length $\mathrm{L}_D$ is estimated to be greater than 10 km for roughly 18 ps pulses (experimental data) using Equation 2.9. Consequently, the influence of dispersion on Thulium-Doped Fiber Amplifiers (TDFAs) with “meter-scale” device lengths is minimal.

#### 2.3.2.2 Group-Velocity Dispersion

In the event that Equation 2.6 allows for the exclusion of nonlinear and loss components, it may be expressed as follows:

$$i\frac{\partial A}{\partial z} = \frac{\beta_2}{2}\frac{\delta^2 A}{\delta T^2} \tag{2.11}$$

Presuming $U(z,T)$ represents the normalised optical field, the solution for Equation 2.11 within the frequency domain (achieved via Fourier transformation of $(\widetilde{U}(z,\omega))$) can be described as:

$$\widetilde{U}(z,\omega) = \widetilde{U}(0,\omega)exp(\frac{i}{2}\beta_2\omega^2 z) \tag{2.12}$$

The equation 2.12 indicates that there are no additional frequency terms introduced, except for the phase shift of the original frequency components. If we assume that the initial pulse has a Gaussian shape, its function can be expressed as:

$$U(0,T) = exp(-\frac{T^2}{2{T_0}^2}) \tag{2.13}$$

Here, $T_0$ represents the pulse width, although the full width at half maximum (FWHM) is commonly used to describe the pulse width. For a Gaussian pulse, these two terms are related by $T_{FWHM} \approx 1.665 \times T_0$. As a result, the change in pulse amplitude with propagation distance can be written as:

$$U(z,T) = \frac{T_0}{\sqrt{{T_0}^2 - i\beta_2 z}} e^{[-\frac{T^2}{2({T_0}^2 - i\beta_2 z)}]} \tag{2.14}$$

While phase of the pulse varies with propagation distance and can be expressed as:

$$\phi(z,T) = -\frac{sgn(\beta_2)\left(\frac{z}{L_D}\right))}{1+\left(\frac{z}{L_D}\right)^2}\frac{T^2}{2{T_0}^2} + \frac{1}{2}tan^{-1}\left(sgn(\beta_2)\left(\frac{z}{L_D}\right)\right) \tag{2.15}$$

The sign of the dispersion parameter $\beta_2$ is given by $sgn(\beta_2)$. For instance, for single-mode fiber at 2 $\mu$m, $\beta_2$ is negative. Furthermore, the change in central frequency (chirp) can be determined from Equation 2.15. The degree of dispersion-induced broadening for a Gaussian pulse can be observed from Figure 2.21, which displays $|U(z,T)|^2$ at $z/L_D$ = 2 and 4. The plot also depicts the frequency chirp as a function of $z/L_D$, along with the dispersion parameter $\beta_2$.

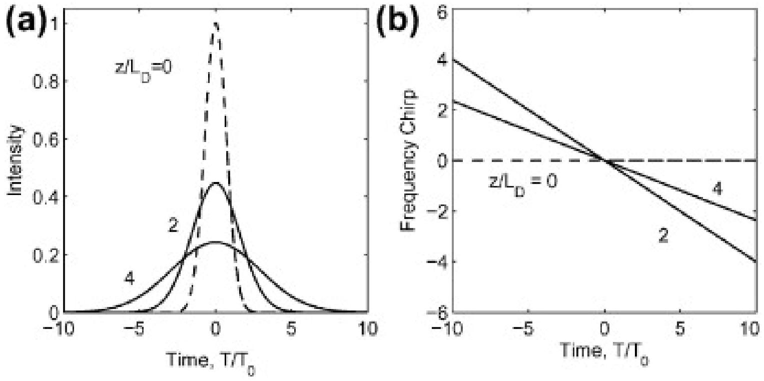

Figure 2.21: Normalized (a) intensity $|U|^2$ and (b) frequency chirp as a function of $z/L_D$ as well as the dispersion parameter $\beta_2$. This figure has been reproduced from [3], © 2012 ELSEVIER.

#### 2.3.2.3 Self-Phase Modulation

In situations where nonlinear effects such as SPM become prevalent, and the GVD term can be disregarded, the equation can be simplified as follows:

$$\frac{\partial A}{\partial z} = \frac{ie^{-\alpha z}}{L_{NL}}|A|^2 A \tag{2.16}$$

The general solution for Equation 2.16, utilizing the normalized optical field $U(z,T)$, can be expressed as:

$$U(L,T) = U(0,T)exp[i\phi_{NL}(L,T)] \tag{2.17}$$

which includes a nonlinear phase shift:

$$\phi_{NL}(L,T) = |U(0,T)|^2 \left(L_{eff}/L_{NL}\right) \tag{2.18}$$

$$L_{eff} = \frac{|1 - e^{-\alpha L}|}{\alpha} \tag{2.19}$$

Here, $L_{eff}$ represents the effective fiber length that depends on the fiber's linear losses $\alpha$, for a fiber length of $L$. In the case of a Gaussian pulse, the frequency chirp $(\delta\omega)$ can be calculated using Equation 2.20:

$$\delta\omega(T) = -\frac{\partial \phi_{NL}}{\partial T} = \frac{2}{T_0}\frac{L_{eff}}{L_{NL}}\frac{T}{T_0}\exp\left|-\left(\frac{T}{T_0}\right)^2\right| \tag{2.20}$$

In the case of a Gaussian beam with a beam radius of ‘w’ propagating through a medium of length ‘L’, the phase shift per unit optical power is proportional to the constant $\gamma_{SPM}$, which is expressed in units of ‘rad/W’. This implies that the phase shift per unit power can be represented as:

$$\gamma_{SPM} = \frac{4n_2L}{\lambda w^2} \tag{2.21}$$

Hence, the maximum nonlinear phase shifts arising from SPM at the pulse center can be characterized as:

$$\delta\varphi_{NL,max} = \gamma_{SPM} \cdot P_{peak} \tag{2.22}$$

Thus, it can be inferred from Equations 2.21 and 2.22 that the nonlinear phase shift in the amplifier decreases linearly with an increase in pulse width. Consequently, stretching the pulse width before amplification in the CPA system can lead to higher pulse energy as compared to direct amplification. Additionally, the amplifier’s nonlinear phase shift reduces with an increase in the fiber mode-field area. Therefore, the utilization of large mode area fiber in the power amplifier is preferable for achieving high-energy pulses. To reduce the nonlinear phase shift, the use of high-concentration thulium-doped fiber to shorten the amplifier length can be beneficial. This motivates the development of highly-doped rare-earth fibers to minimize nonlinearity in pulse amplification, particularly when the limitations of stretched ratio and fiber mode-field area are encountered.

### 2.3.3 Stretcher

Various methods exist for constructing compressors and stretchers, but a standard Ti:sapphire-based chirped-pulse amplifier necessitates stretching the pulses to several hundred picoseconds. This implies that there must be a 10 cm path length difference between the distinct wavelength components. The most feasible approach to accomplish this is by employing grating-based stretchers and compressors. These devices are defined by their dispersion properties. Higher frequency light (shorter wavelengths) travels faster through the device than lower frequency light (longer wavelengths) for negative dispersion, while positive dispersion is the reverse. In a CPA system, the dispersions of the stretcher and compressor must counterbalance each other. Practical constraints typically lead to the design of a compressor with negative dispersion which is high-power side, while the stretcher is designed with positive dispersion which is low-power side.

Chromatic dispersion is caused by the restricted spectral bandwidth of the pulse introduced into the fiber, as the pulse's various spectral components propagate at differing speeds within the fiber due to the frequency-dependent refractive index $\mathrm{n}(\omega)$. This velocity variation among different spectral components causes the propagating pulse to spread over time and the pulse to widen. The change in the original pulse's width, denoted as '$\Delta\tau$', is given by Equation 2.23:

$$\Delta\tau = D\Delta\omega L \tag{2.23}$$

In this equation, '$D$' represents chromatic dispersion, in units of '$ps/(nmkm)$', while '$\beta_2$' is referred to as the group velocity dispersion, which is related to '$D$' and has a basic unit of $\mathrm{s}^2/\mathrm{m} : \mathrm{D} = -\left(2\pi\mathrm{c}/\lambda^2\right)\beta_2$. The spectral width is denoted as '$\Delta\omega$'.

Most standard commercial silica-based fibers exhibit anomalous dispersion in the 2 $\mu$m wavelength range, such as a $\beta_2$ value of -0.067 $\mathrm{ps}^2/\mathrm{m}$ for SM28 fiber. UHNA4, a commercially available fiber, demonstrates normal dispersion of +0.09 $\mathrm{ps}^2/\mathrm{m}$ at approximately 1.9 $\mu$m.

In this thesis, I utilized tens of meters of dispersive fibers (Nufern UHNA4) for the stretcher, given their excellent wavelength compatibility and affordability compared to a custom CFBG. It is obvious that dispersive fibers offer more compactness and durability than traditional grating pair-based stretchers.

### 2.3.4 Compressor

Grating pairs are a prevalent method employed as compressors in standard CPA systems. Two primary categories of gratings exist: conventional reflection gratings and fused silica transmission gratings. In contrast to conventional reflection gratings, which utilize a metallic coating that restricts optical performance and power handling capabilities, fused silica transmission gratings exhibit lower absorption for high-energy pulses and improved thermal stability [84].

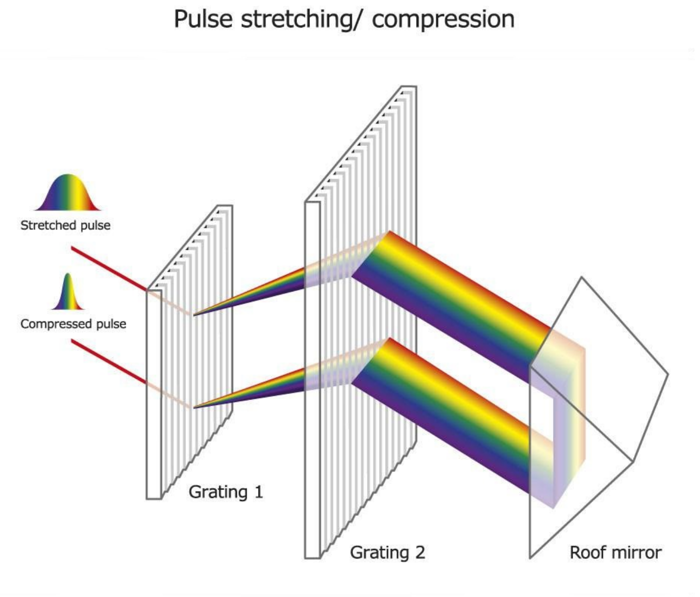

Figure 2.22: The schematic of the Treacy stretcher or compressor. This figure has been reproduced from [84], in accordance with their open access policy and terms of use.

The most basic configuration of a grating pair, depicted in Figure 2.22, is referred to as the Treacy configuration. It can generate adjustable negative dispersions as a result of the distinct optical paths experienced by different wavelengths [186]. A reflector, such as a roof mirror, is present at the output of a grating pair, retro-reflecting light back into the grating pair, and thereby doubling the negative dispersion produced.

In this thesis, a grating pair was chosen for the compressor due to its flexibility in terms of waveband and availability when compared to custom chirped volume Bragg gratings.

## 2.4 Optical parametric process

### 2.4.1 Optical parametric amplification

An optical parametric amplifier (OPA) is a light source capable of producing light at varying wavelengths through the process of optical parametric amplification, as illustrated in Figure 2.23 [5]. It operates similarly to an optical parametric oscillator (OPO) but without the optical cavity, meaning that the light beam passes through the device only once or twice rather than numerous times. Crystal materials that lack inversion symmetry can exhibit a $\chi^{(2)}$ nonlinearity which enables parametric amplification in addition to frequency doubling and sum and difference frequency generation. In this process, the signal beam travels through the crystal alongside a shorter wavelength pump beam. Pump wave photons are then converted into lower-energy signal photons and an equal number of idler photons. The idler wave's photon energy is the difference between the pump and signal waves' photon energies. As the pump energy is entirely transformed into the energy of the signal and idler beams, the crystal material does not heat up during this process. However, some parasitic absorption may occur, the extent of which depends on the crystal material, potentially disrupting phase matching and limiting gain and output power.

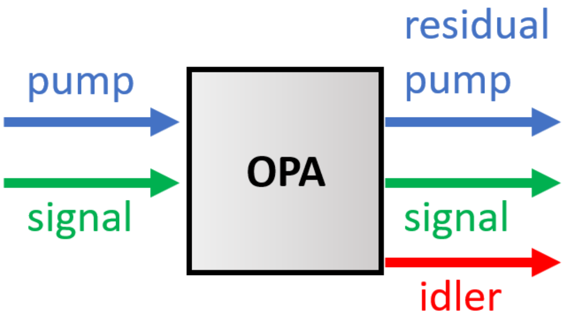

Figure 2.23: Schematic of an optical parametric amplifier.

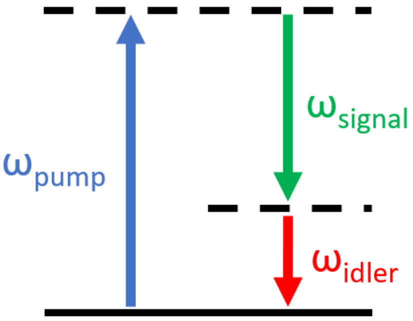

Figure 2.24: Energy level of an optical parametric amplifier.

The high parametric gain achievable with pulses, sometimes exceeding 80 dB within a few millimeters of crystal material, combined with the capability to operate at vastly different wavelengths and minimal heating (solely due to typically weak parasitic absorption), makes parametric amplifiers highly appealing for various applications.

While many OPAs are primarily based on bulk nonlinear crystals, there has been growing interest in fiber-based OPAs due to their potential advantages [73]. In 1975, Stolen demonstrated optical parametric amplification (OPA) in low-loss optical fibers [177].

For instance, fiber-based OPAs can offer increased flexibility and compactness, high efficiencies due to long interaction lengths, and the ability to handle high peak power due to the large surface-area-to-volume ratio of optical fibers [205]. However, they present challenges including difficulty in phase matching, high pump power needs, susceptibility to environmental changes, and complex design. High gain levels can lead to high noise figures in fiber and risk of damage, especially with small core diameters [120]. Despite these, we've chosen a bulk-based OPA for our system due to its robustness, mature technology, and broad phase-matching bandwidths, providing us the reliability and performance we need.

### 2.4.2 Second-harmonic generation/frequency doubling

Like an OPA, non-centrosymmetric crystal materials exhibiting the $\chi^{(2)}$ nonlinearity can enable second-harmonic generation (SHG) [59]. In this process, an input (pump) wave generates another wave with double the optical frequency (and half the vacuum wavelength) within the medium, as depicted in Figure 2.25. The energy levels of SHG process are displayed in Figure 2.26. This process is also referred to as frequency doubling. Typically, the pump wave is delivered as a laser beam, generating the frequency-doubled (second-harmonic) wave as a beam propagating in the same or a similar direction.

Lithium niobate ($LiNbO_3$), potassium titanyl phosphate (KTP = $KTiOPO_4$), and lithium triborate (LBO = $LiB_3O_5$) are common nonlinear inorganic crystal materials utilized for frequency doubling. SHG microscopy for biomedical imaging in biological samples and materials will be discussed in subsequent sections.

Lithium niobate ($LiNbO_3$), potassium titanyl phosphate (KTP = $KTiOPO_4$), and lithium triborate (LBO = $LiB_3O_5$) are common nonlinear inorganic crystal materials used for frequency doubling. Later sections will introduce SHG microscopy for biomedical imaging in biological samples and materials.

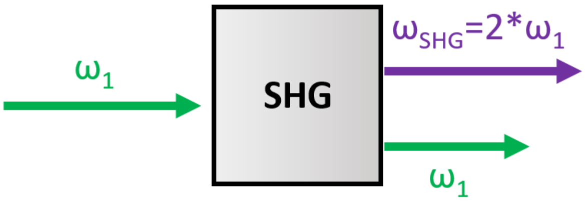

Figure 2.25: Schematic of second-harmonic generation.

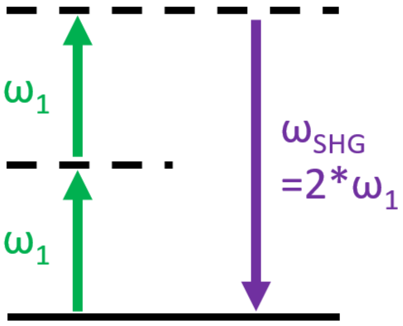

Figure 2.26: Energy level of second-harmonic generation.

Lithium niobate ($LiNbO_3$), potassium titanyl phosphate (KTP = $KTiOPO_4$), and lithium triborate (LBO = $LiB_3O_5$) are common nonlinear inorganic crystal materials utilized for second-harmonic generation. SHG microscopy for biomedical imaging in biological samples and materials will be discussed in subsequent sections.

### 2.4.3 Phase matching

In both OPA and SHG processes, photon energy conservation is maintained; however, for any of these second-order nonlinear interactions to take place, momentum conservation, or so-called phase matching, must also be achieved.

Phase matching pertains to maintaining a fixed relative phase between two or more light frequencies as they travel through a material. The refractive index is dependent on the light frequency, causing the phase relationship between photons of different frequencies to change as they propagate through the crystal. To ensure efficient nonlinear conversion of input photons, the phase relationship between input and generated photons must be preserved throughout the crystal. If this condition is not met, generated photons will oscillate in and out of phase with each other in a sinusoidal pattern, restricting the number of photons exiting the crystal, as demonstrated in the Figure 2.28 below. Traditional phase matching entails propagating light through the crystal in a direction where the crystal's natural birefringence matches the refractive index of the generated light. Although this method offers perfect phase matching, it is restricted to a narrow range of wavelengths in materials that can be phase matched.

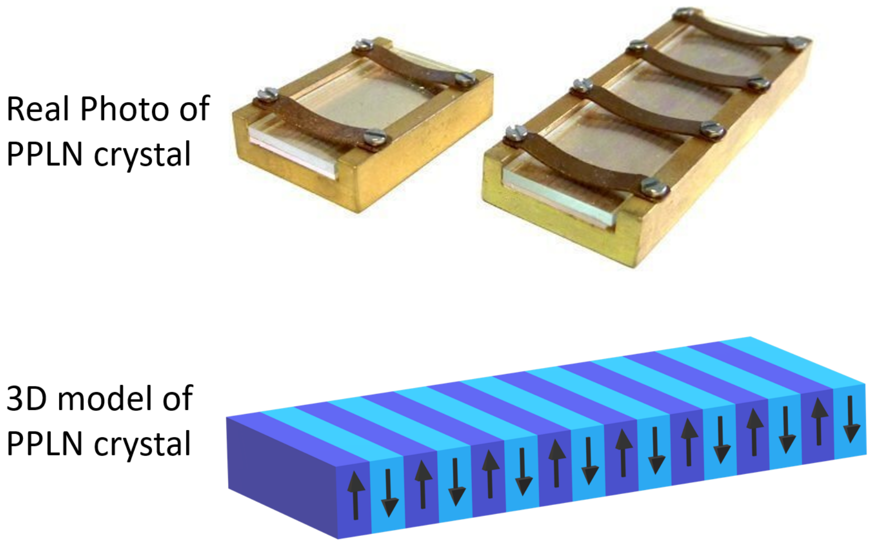

Figure 2.27: Real photo and 3D model of PPLN crystal. This figure has been reproduced from [43], in accordance with their open access policy and terms of use.

Periodically Poled Lithium Niobate (PPLN) crystal, as displayed in Figure 2.27, is a quasi-phase-matched, engineered material [43]. The term "engineered" refers to the periodic inversion (poling) of the lithium niobate crystal's orientation. By inverting the orientation of the crystal at each peak of the sinusoidal generation, the photons slipping out of phase with each other can be reset. Consequently, as the light travels through the PPLN crystal, the number of generated photons increases, resulting in a high conversion efficiency from input to generated photons. This is illustrated in Figure 2.28.

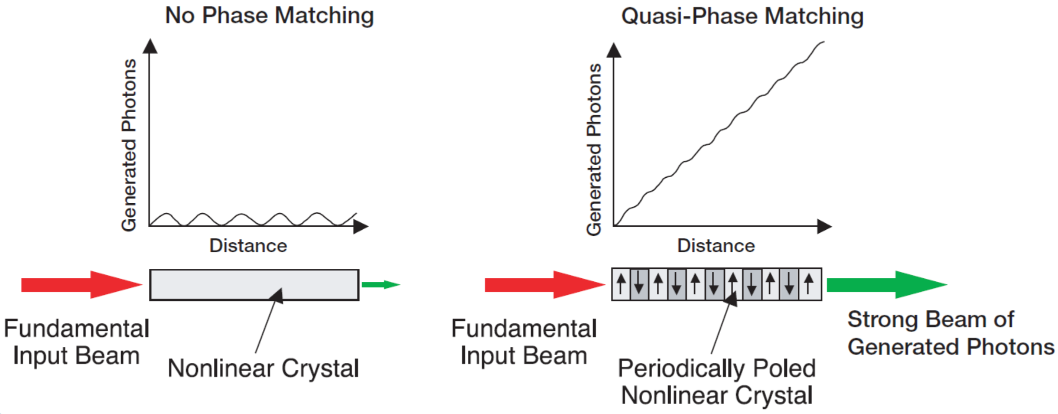

Figure 2.28: Quasi-phase matching (right) compare to no phase matching (left). This figure has been reproduced from [43], in accordance with their open access policy and terms of use.

The required poling period, or the interval at which the crystal must be inverted, depends on the interaction wavelengths and the PPLN's temperature. For instance, a PPLN crystal with a 6.6 $\mu$m poling period can efficiently generate SHG output from 1060 nm input when the crystal temperature is maintained at 100°C. By raising the crystal's temperature to 200 °C, the same PPLN crystal can efficiently generate SHG output from 1068.6 nm wavelength input. So, altering the crystal's temperature adjusts the phase matching conditions, enabling some tuning of the interacting wavelength.

In this thesis, we employed PPLNs featuring five different channels/gratings to ensure phase matching across a broad tunable wavelength range.

## 2.5 Multiphoton microscopy

### 2.5.1 Introduction

Multiphoton microscopy (MPM) has established itself as the premier noninvasive method for fluorescence microscopy in bio-imaging of tissue explants and living animals. As a type of laser-scanning microscopy, MPM employs localized 'nonlinear' excitation to stimulate fluorescence solely within a thin raster-scanned plane. Since W. Denk first demonstrated this technique in 1990 [49], MPM has been developed for applications of various imaging tasks and has emerged as the preferred method for fluorescence microscopy in thick tissue sample and live animals.

While two-photon excited fluorescence is typically the primary signal source in MPM, three-photon excited fluorescence [70, 103, 117, 201, 206, 220] and second- [220, 222, 51, 26, 27, 137, 126, 25, 61] and third-harmonic generation [11, 141, 210] can be employed for imaging as well. Indeed, SHG imaging was among the first instances of biological nonlinear microscopy, suggested [169] and demonstrated [61] long ago. Interestingly, coherent anti-Stokes Raman scattering (CARS) microscopy, one of the most intricate forms of nonlinear imaging, was developed even earlier [55]. CARS microscopy generates contrast directly from Raman-active vibrational modes in molecules and necessitates two synchronized pulsed lasers operating at distinct wavelengths, different from a single pulsed laser used in two- (or three)-photon, SHG, and THG microscopy. Similar to SHG microscopy, CARS microscopy remained inactive for years but has recently experienced significant advancements [1, 140] with the aid of tunable and pulsed lasers operating in the wavelength range of infrared (IR) [221].

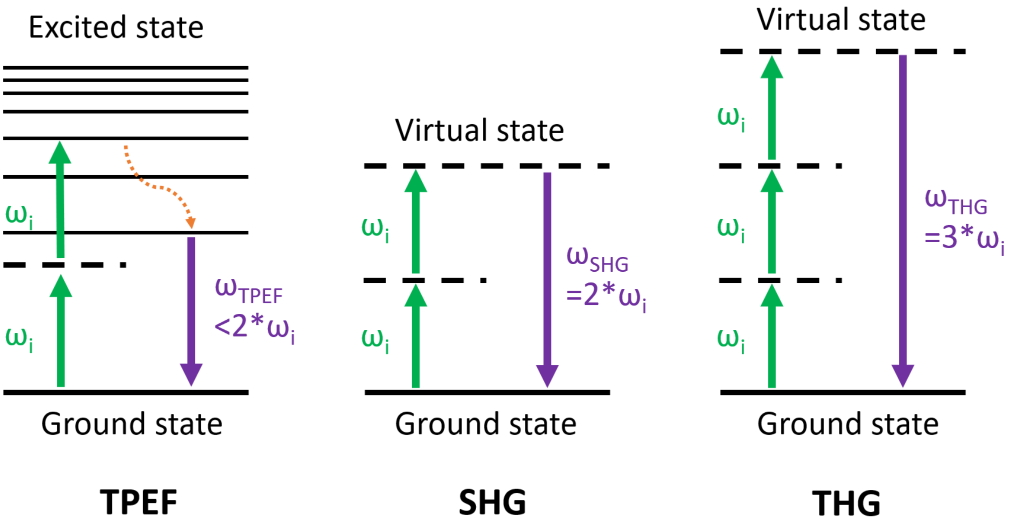

Figure 2.29: Two-photon excited fluorescence, second-harmonic generation and third-harmonic generation process in the energy-level diagram.

### 2.5.2 Two-photon excited fluorescence (TPEF) microscopy

In classic single-photon microscopy techniques, fluorescence is generated by exposing a fluorophore to light with a specific wavelength. This wavelength carries the appropriate energy to excite electrons in the fluorophore to a higher energy state. Once excited, the electrons become unstable and can only remain at this elevated state for a brief period. The electrons then return to their lower energy level, releasing energy in the form of a photon. As energy is lost during this process, the emitted light has a longer wavelength and lower energy than the excitation light. In traditional fluorescence and confocal microscopy methods, this process involves only one photon to excite the fluorophore and produce fluorescence (Figure 2.30).

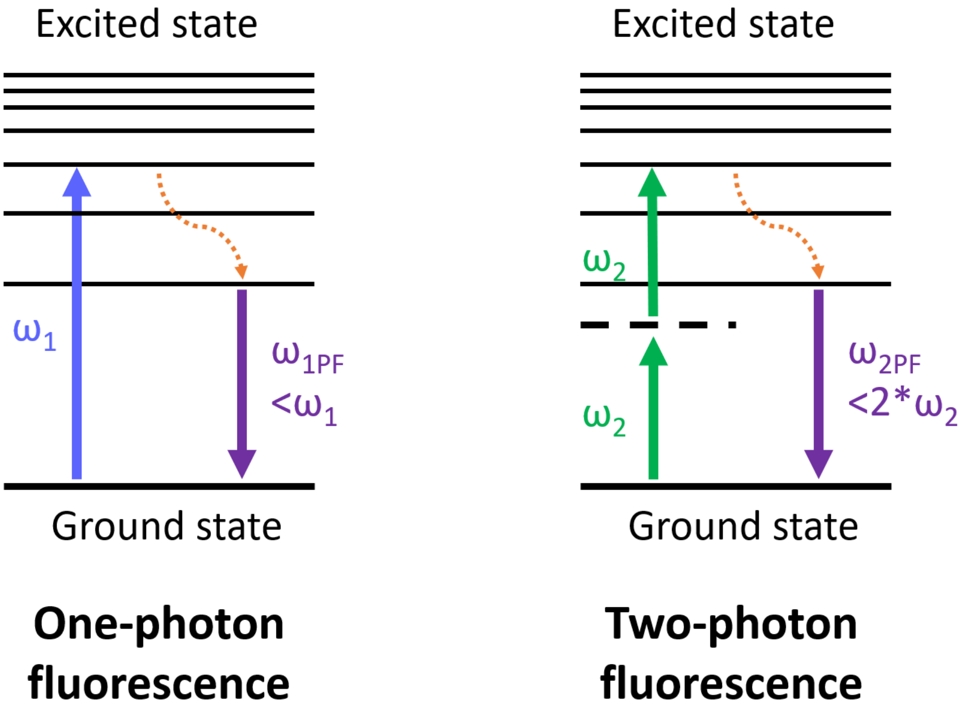

Figure 2.30: One/single-photon excited fluorescence and two-photon excited fluorescence process in the energy-level diagram.

The key distinction between one-photon and two-photon microscopes is that the former uses a single photon, while the latter employs two photons. In two-photon microscopy, two photons excite a single molecule from its ground level to a higher energy level in a single quantum event. The energy difference required for electrons to transition between energy levels is the sum of the absorbed combined energy from the two photons. Since the energy-wavelength relationship is linear, each photon has double the wavelength compared to the excitation light in single-photon methods (Figure 2.30). Although two photons are used for excitation, only one photon is emitted as the electron returns to the ground state, producing a fluorescence wavelength similar to that in single-photon methods.

Two-photon microscopy necessitates that two photons interact with the fluorescent molecule within 1 femtosecond of each other to excite it to a higher energy state. Consequently, fluorescence is generated only at the single point closest to the focal plane, leaving the planes above and below unilluminated (Figure 2.31).

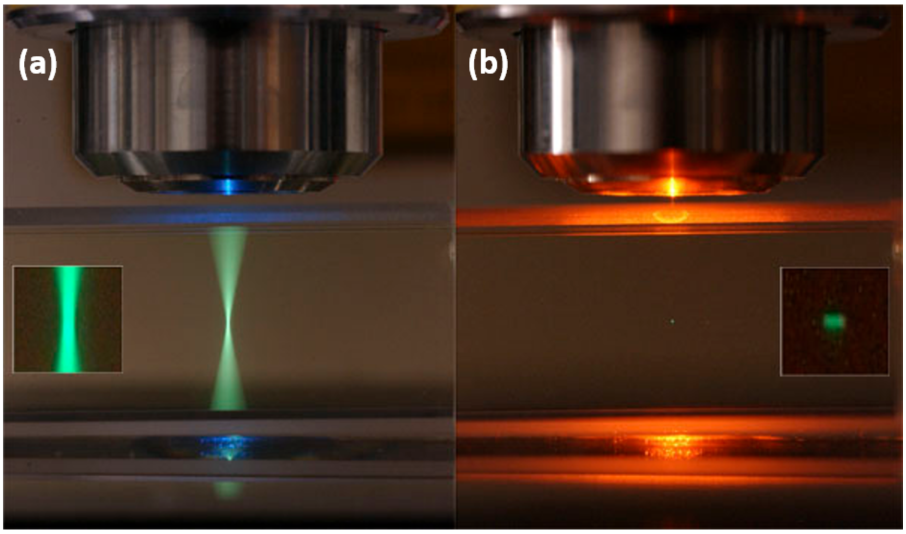

Figure 2.31: (a) One-photon microscopy (b) Two-photon microscopy. This figure has been reproduced from [146], in accordance with their open access policy and terms of use.

Utilizing the two-photon effect offers significant benefits, as the axial spread of the point spread function is considerably reduced compared to single-photon excitation. This improvement in the z-dimension allows for the creation of thinner optical sections. Moreover, in many cases, the spot's size and shape can be tailored to achieve specific objectives [95]. The longer wavelength, lower energy (usually infrared) excitation lasers used in multiphoton microscopes are particularly suitable for live cell imaging, as they cause less damage compared to the shorter-wavelength pulses commonly employed in single-photon microscopes. As a result, cells can be monitored for extended periods with minimal toxic effects.

When a fluorophore simultaneously absorbs two infrared photons, it gains enough energy to reach the excited state. The fluorophore then generates a single photon with a wavelength determined by the fluorophore type (usually in the visible spectrum). The probability of fluorescent emission from fluorophores increases quadratically with excitation intensity since two photons are absorbed during fluorophore excitation. Consequently, a significantly greater amount of two-photon fluorescence is generated at the tightly focused laser beam than at more diffuse regions. This excitation restriction to a tiny focal volume (approximately 1 femtoliter) results in high out-of-focus object rejection. This localized excitation presents an important advantage over single-photon based microscopes, which must use components such as pinholes to filter out undesirable light [200]. This significantly confines the extent of photobleaching to a considerably smaller area in comparison to confocal microscopy.

Two-photon microscopy possesses several characteristics that mitigate various effects, leading to enhanced imaging depths. Fluorescence generation in this method relies on focusing two photons of light at a single location to induce excitation and produce fluorescence, which also applies to collecting background light. For background fluorescence to occur, two excitation photons need to scatter at the exact same spot. Due to the low probability of this happening in heterogeneous biological samples at greater depths, no background signal is generated, resulting in a significantly improved image contrast. Another factor contributing to increased imaging depth is the wavelength of light used to excite the fluorophore. As mentioned earlier, two-photon microscopy employs lower energy and longer wavelengths of light compared to confocal microscopy. The use of infrared light, which scatters less compared to visible wavelengths in traditional methods, enables a larger amount of light to penetrate deeper into the sample, facilitating the visualization of areas within thick specimens [146].

### 2.5.3 Second Harmonic Generation (SHG) microscopy

SHG is a second order nonlinear optical process that occurs in materials with a non-centrosymmetric structure as introduced in previous sections. SHG microscopy has become a valuable imaging technique for visualizing cell and tissue structure and function [176]. Intense laser light needs to pass through the non-centrosymmetric material for SHG to occur [162].

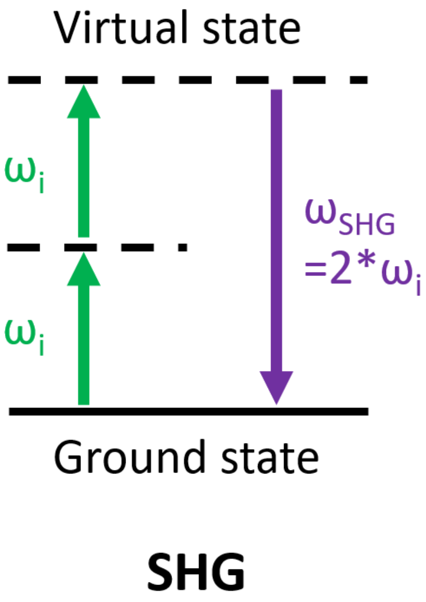

Figure 2.32: Second harmonic generation process energy-level diagram.

Second-harmonic light emitted from an SHG material has half the wavelength (doubled frequency) of the input light (Figure 2.25). Although two-photon-excited fluorescence (TPEF) is also a two-photon process, it loses some energy during the excited state relaxation, while SHG is energy-conserving and represents a nonlinear coherent scattering process. Commonly, it has been introduced in the previous sections that inorganic crystals like lithium niobate ($LiNbO_3$), potassium titanyl phosphate (KTP = $KTiOPO_4$), and lithium triborate (LBO = $LiB_3O_5$) are used to generate SHG light. Certain biological materials can form highly polarizable, ordered, and large non-centrosymmetric structures, which enables SHG. Examples include collagen, microtubules, and muscle myosin [144], even water can generate SHG signals under specific conditions, enabling label-free SHG microscopy for imaging surface potentials [162].

SHG microscopy has various benefits for imaging live cells and tissues. As it doesn't involve molecular excitation like fluorescence microscopy, phototoxicity and photobleaching are avoided. Many biological structures generate strong SHG signals, eliminating the need for exogenous probes that could change biological function. Employing near-infrared wavelengths for input light, SHG microscopy can create 3D images by imaging deeper into thick specimens [199].

SHG differs from TPEF, which involves electron excitation and de-excitation via photon emission, making it a non-coherent process both spatially (isotropic emission) and temporally (broad, sample-dependent spectrum). Furthermore, SHG is structure-specific, unlike TPEF [36].

In biological tissues, particularly collagen-based tissues, SHG signal generation is a quasi-coherent process where conversion efficiency depends on fibril alignment within the fiber [21, 101].

### 2.5.4 Coherent Anti-Stokes Raman Scattering (CARS) microscopy

Raman scattering, discovered by Indian scientist C. V. Raman in 1928, demonstrated that light energy levels are discrete and established a new research area for studying molecular chemical characteristics [153]. Raman found that scattered photons in the mid-infrared range contain molecular vibration information. By switching from infrared to visible light, the strong optical absorption of water in the infrared region is avoided, which is crucial in biomedical science. Additionally, Raman spectroscopy does not require chemical labeling to obtain chemical information, allowing for the study of biological functional characteristics without chemical interference [109].

Despite its advantages, spontaneous Raman scattering is a weak second-order radiative process with a cross-section approximately $10^{-30}$ $cm^2$ per molecule, $10^{11}$ times smaller than infrared absorption. This results in low spontaneous Raman scattering efficiency and needs very long collection time, which is acceptable for spectroscopy but not for real-time imaging [109].

The advancement of femtosecond lasers with high peak power has facilitated the exploration of numerous nonlinear processes and fostered research in coherent Raman scattering (CRS). As an emerging nonlinear optical microscopy method, coherent Raman scattering microscopy addresses the imaging speed constraints inherent in spontaneous Raman micro-imaging [123, 161, 215, 40, 57, 37].

CRS serves as an effective nonlinear microscopy approach for label-free, 3D imaging of tissues and cells by leveraging the unique vibrational response of molecules for inherent contrast [134]. CRS facilitates real-time, non-destructive chemical, label-free identification of compounds at sub-micrometer scales without the need for external markers [24], which could otherwise disrupt the molecules being examined or hinder dynamic processes like drug transport and cell differentiation. CRS microscopy has numerous applications in biomedical imaging [152, 211], and due to the robust Raman response of long-chain hydrocarbons, it is particularly suited for imaging lipids, monitoring their metabolism [223], and differentiating between lipids, DNA, and proteins inside cells [115]. Furthermore, CRS holds potential for quickly distinguishing between tumors and healthy tissue, laying the foundation for 'virtual histopathology' both ex vivo and intra-operatively [92, 93].

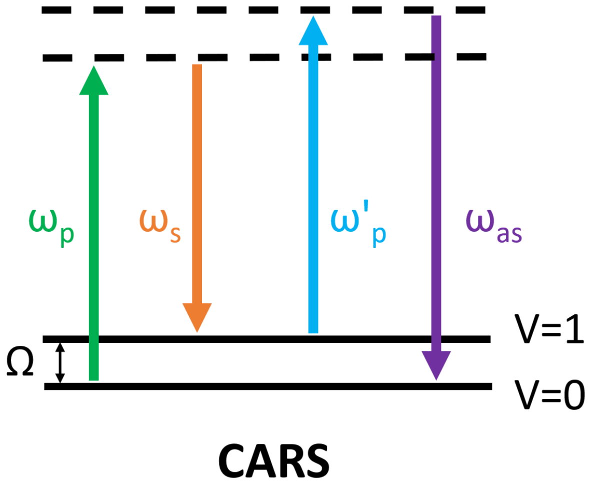

Figure 2.33: Coherent anti-Stokes scattering energy diagram.

CARS is a third-order nonlinear optical process and a four-wave mixing process used to amplify the faint Raman signal. In this process, a pump field $E_p(\omega_p)$, a Stokes field $E_s(\omega_s)$, and a probe field $E_p^{'}\left(\omega_p^{'}\right)$ (In general case the pump frequency and the probe frequency can be equal but in our case they are different.) interact with a sample and generate an anti-Stokes field $E_{as}$ at the frequency of $w_{as} = \omega_p - \omega_s + \omega_p'$. When the frequency difference between the pump and Stokes beams aligns with a vibrational mode frequency, for example the $CH_2$ symmetric stretching mode around 2800 $cm^{-1}$, molecular oscillators are excited coherently [218]. This leads to an amplified anti-Stokes (higher-frequency) Raman signal, which forms the foundation for the enhanced vibrational contrast in CARS microscopy [39]. The energy diagrams for CARS can be seen in Figure 2.33. Both stimulated Raman gain $\omega_s$ and stimulated Raman loss $\omega_p$ are utilized in another coherent Raman microscopy technique known as Stimulated Raman Scattering (SRS) Microscopy.

At room temperature, the majority of molecules reside in the lowest vibrational energy state. When exposed to intense electromagnetic radiation of a single frequency, the radiation interacts with the molecule, distorting (polarizing) the electron cloud around the nuclei to form a short-lived, high-energy state known as a 'virtual state' (dotted line in Figure 2.33). On the left side, Raman Stokes scattering occurs. During inelastic (Raman) scattering, the molecule transitions from a virtual (v=0) state to a higher energy state (v=1) than its initial state. Some of the photon energy is grabbed by the molecules to remain in the higher energy vibrational level v=1, where $E_{v=1} > E_{v=0}$ and $E_{v=0}$ represents the ground vibrational level. On the right side, as the molecule interacts with the probe light, it returns from the virtual state to the ground state v=0, causing the energy of the anti-Stokes photon to increase by $\Delta E = E_{v=1} - E_{v=0}$. This type of Raman scattering is referred to as anti-Stokes scattering and involves the transfer of energy to the scattered photon [185].

Recent advancements have emphasized label-free multimodal nonlinear microscopy, incorporating CARS, TPEF, and SHG techniques [150, 108, 127, 208]. The combination of these methods enables the exploration of various biological aspects, including lipid metabolism, cancer progression, cardiovascular disorders, and skin biology. By merging the capabilities of each nonlinear optical imaging method, the visualization of diverse structures and their interactions within intricate biological systems can be achieved simultaneously [109]. An example of multimodal CARS, SHG, and TPEF imaging from Chapter 3 is presented in Figure 2.34.

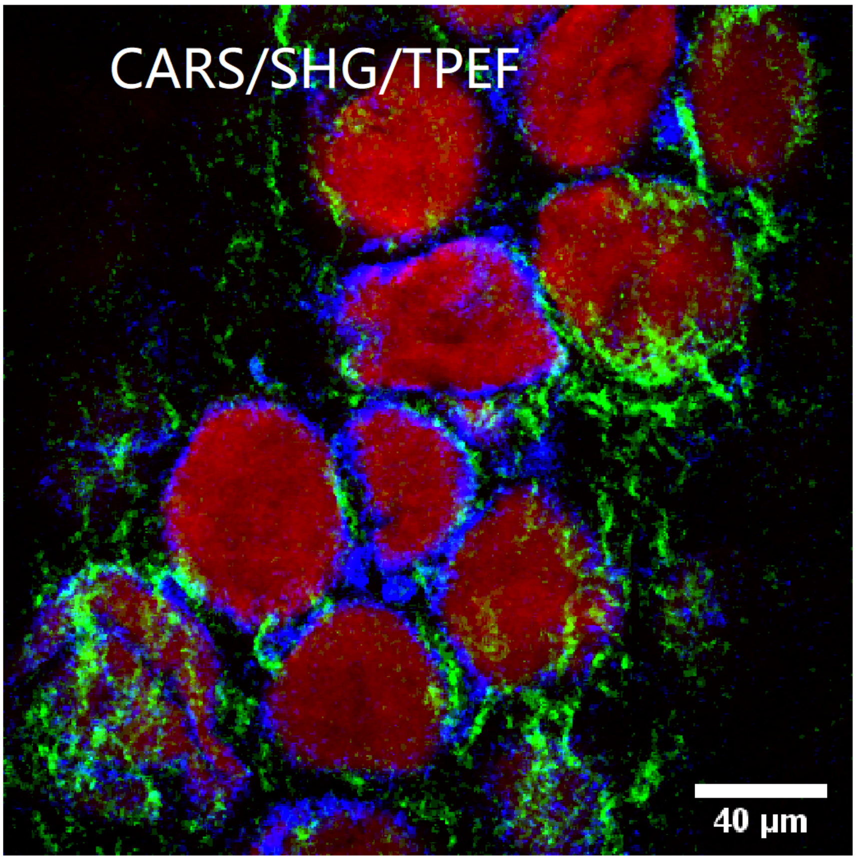

Figure 2.34: Multimodal CARS, SHG and TPEF imaging.

In this thesis, Chapter 3 demonstrated a widely-tunable synchronisation-free ps-pulsed laser source for multimodal CARS, SHG and TPEF microscopy.

### 2.5.5 Third Harmonic Generation (THG) microscopy

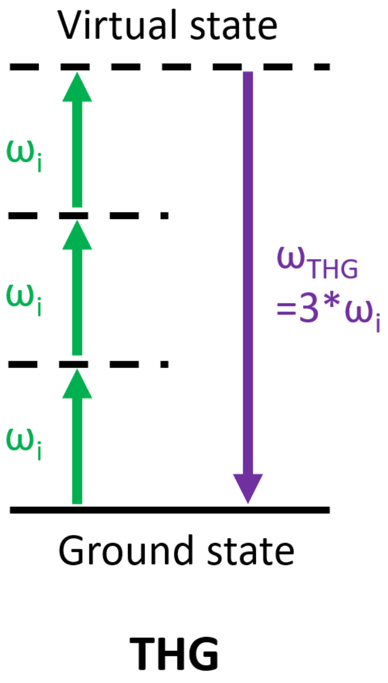

Figure 2.35: Third harmonic generation process in the energy-level diagram.

Higher harmonic generation is a nonlinear coherent scattering process that arises from the phase matching and summation of light induced by inorganic or organic structures with specific physical properties and molecular arrangements.

As discussed earlier, SHG occurs when two incoming photons are converted into one emitted photon with double the energy, resulting in light emission with half the wavelength. Third Harmonic Generation, on the other hand, involves the tripling of the excitation wavelength frequency, where the combined energy of three photons is converted into one emitted photon with one-third the excitation wavelength and triple the energy [12]. This process is depicted in Figure 2.35. THG takes place at structural interfaces, such as local transitions of the refractive index or the third-order nonlinear susceptibility $\chi^3$ [12, 141], both of which are intrinsic physical properties of materials and liquids. As a result, THG is more versatile than SHG because it does not necessitate a specific structural asymmetry for imaging. In bio-samples, THG excitation mainly occurs at interfaces formed between aqueous interstitial fluids and lipid-rich structures, such as cellular membranes [7, 154], lipid droplets [47, 188, 195], or inorganic structures like calcified bone or tooth enamel [147, 35]. Additionally, THG can also be observed at interfaces between large protein aggregates and water, for instance collagen bundles or muscle fibers [197, 154].

THG offers several unique technical and practical advantages for biological imaging applications. Unlike multiphoton and confocal fluorescence imaging, THG signal can be readily collected without tissue dyeing, providing a wide range of structural information on cell and tissue structure. Like two-photon microscopy and in contrast to one-photon confocal imaging, THG is generated only in the focused point, making the imaging process and detected signals intrinsically confocal and suitable for 3D sample scanning and volume reconstruction. Confocal imaging is restricted to superficial cell layers of tissues due to scattering, absorption, and phototoxicity drabacks. In contrast, the infrared wavelengths used for multiphoton and THG excitation enable long-term time-lapse imaging [180] and enhance penetration of deep-tissue [6]. Unlike other label-free imaging modalities such as CARS and autofluorescence, THG provides structural information rather than molecular information, similar to optical coherence tomography and ultrasound. Consequently, THG complements other imaging methods and is best utilized within multi-parameter acquisition schemes.

In this thesis, the light sources in Chapter 4 and 5 were designed to function as a powerful light source for THG microscopy.

# Chapter 3

# Widely-tunable synchronisation-free ps-pulsed laser sources for multimodal CARS, SHG and two-photon microscopy

## 3.1 Introduction

In this chapter, I demonstrate continuous wave (CW) seeded synchronization-free optical parametric amplifiers (OPAs) pumped by picosecond, 1-$\mu$m lasers and show their performance when used as simple yet powerful sources for label-free Coherent anti-Stokes Raman scattering (CARS), concurrent Second Harmonic Generation (SHG) and two-photon excited fluorescence (TPEF) microscopy employing epi-detection configurations. By utilizing a tunable-wavelength continuous wave laser for OPA seeding, we accomplished an average power output exceeding 175 mW, 8 cm$^{-1}$ spectral resolution, and a 2 ps pulse duration, rendering this source well-suited for CARS microscopy in bioscience and bio-medical imaging applications. This OPA offers a more straightforward and simpler design compared to the typically used 'gold-standard' pulsed laser and optical parametric oscillator (OPO) combination for CARS imaging or the more recent OPA systems driven by femtosecond pulses [175]. Rapid and accurate tuning between molecular resonances was realized by adjusting the poled channels and temperature of the periodically-poled lithium niobate (PPLN) OPA crystal in conjunction with the OPA seed wavelength. The Pump-Stokes frequency detuning range entirely encompassed the C-H stretching band utilized for lipid imaging.

I also present an OPA of a similar design but seeded by an inexpensive and simple CW diode laser that costs much less than a tunable laser seed and further simplifies the OPA system. This OPA represents a versatile light source module that can be tailored to the tunability and affordability requirements of the specific application. It can be used either on its own as a light source or in association with an OPO for multimodal CRS microscopy and the image performance with a variety of standard and biological samples is demonstrated.

This work facilitates the application of three multiphoton methodologies through a compact, synchronization-free laser source, laying the groundwork for transitioning label-free multi-photon microscopy imaging from the realm of biomedical research to a diagnostic tool in the healthcare field.

The entire work was undertaken and completed by me independently, under the guidance of my colleagues at ORC and IfLS. The laser related work including laser source building, characterization and optical alignment to the microscope were carried out by myself. The microscope related imaging experiments and data/bio-imaging processing were also carried out by myself. The imaging samples were prepared by Peter Johnson and James Read, who also gave me some guidance and training on operating the microscope.

This chapter of my thesis has been successfully developed into two separate research papers ‘Widely-tunable synchronisation-free picosecond laser source for multimodal CARS, SHG, and two-photon microscopy’ and ‘A synchronisation free, versatile Optical Parametric Amplifier as a low cost light source for multiphoton imaging’. Both publications stand as evidence of the substantial work and significant findings in my research.

### 3.1.1 Background and motivation

The use of laser-based spectroscopy and imaging has become increasingly widespread, turning into a nearly indispensable tool for biochemical and medical applications. Although the spectroscopically specific CARS imaging technique offers numerous appealing attributes, its adoption is limited due to the high cost, large size, and intricacy of the current ‘gold-standard’ synchronously pumped OPO systems [66]. To cater to the demand for sources delivering the few-ps pulse widths considered ideal for CARS bioimaging [38], advancements have been made with spectral-focusing CARS [77] utilizing either supercontinuum [79] or a single <20 fs laser with adequate bandwidth [104]. However, these solutions continue to grapple with technical challenges such as complex equipment, poor spectral quality, and low spectral resolution [109], hindering their widespread acceptance.

CARS is a label-free technique that presents notable advantages such as chemical specificity and z-sectioning capability in contrast to the widely used fluorescence-based one-photon imaging approaches. It also allows for considerably quicker signal acquisition times compared to Raman spectroscopy [38, 56]. Within the realm of biological imaging, CARS serves as an almost optimal method for investigating lipids and their metabolic processes [223], and is capable of differentiating lipids from proteins through its contrast mechanism [114]. Moreover, CARS can be integrated with other nonlinear imaging techniques like TPEF [49] and SHG [28] in a single microscope system by employing a multi-channel output configuration [190, 32, 149]. This integration has been accomplished through a method known as multimodal-CARS, which has demonstrated its value in various applications demanding structure- and chemical-specific imaging contrast. Each mode can isolate different sample details [111, 212, 112, 139], and can also image live cells and tissue [138].

CARS, a nonlinear optical process, necessitates pulsed lasers at a pump frequency and an offset Raman-Stokes frequency. The anti-Stokes signal is produced when the pump and Stokes frequencies are offset by the Raman resonance frequency of the target molecule. To efficiently stimulate vibrational coherence and enable rapid image acquisition, CARS requires temporally and spatially overlapped incident pulses of pump and Stokes when they are tightly focused into the sample. Generally, pulses with a few ps duration are ideal for CARS bio-imaging, as their bandwidths correspond well with Raman resonance peaks in typical cellular structures while still providing the high peak powers needed for this nonlinear process. However, the technical complexity, high cost, and sizable footprint of bulk laser-based OPO sources necessitate a dedicated optics laboratory for CARS microscopy, impeding its widespread use. A simplified, low-cost laser system that delivers high performance for CARS in a compact and robust form is in high demand.

A significant recent advancement is the introduction of a crystal-based, femtosecond laser pump and a CW-seeded PPLN-based OPA that offered high gain and remarkable stability for SRS microscopy without requiring a balanced detection system [175]. The OPA output of 1520-1640 nm was frequency-doubled using spectral compression (a lossy process) in a PPLN SHG stage, producing the ps pump beam. The system also needed a narrow spectral filter on the residual beam from the fs pump to extend its temporal width to the few ps range, increasing complexity and reducing efficiency.

In my research, I integrate various aspects of the crystal-based OPA system design [175] while further simplifying the configuration by employing a 2-ps OPA pump laser (and a 2-ns master oscillator power amplifier (MOPA) pump laser during the testing phase). This allows us to avoid power wastage and utilize commercially available crystals for both the OPA and SHG stages. The CW source is tunable across the entire Raman lipid band in biological tissues (approximately 2700 - 3200cm$^{-1}$). Tuning is primarily constrained by the poling periods of the nonlinear crystals at our disposal, but could be readily extended to cover the protein resonance band (approximately 1430 - 1550 cm$^{-1}$) by purchasing a custom crystal with the necessary poling patterns for future system improvements.

Besides delivering strong CARS imaging contrast, the OPA also facilitated simultaneous SHG and TPEF imaging. The powers and beam quality were both well optimized, enabling the acquisition of robust signals in the backward direction compared to the signal beam (epi-detection), rather than relying on forward detection, which necessitates thin samples for signal collection. Consequently, the system is suitable for imaging clinically relevant and easy-to-prepare thick specimens. The system was initially tested on chemically pure beads to confirm the chemical specificity enabled by CARS-spectroscopy. Subsequently, mouse adipose tissue imaging with epi-detection demonstrated the multimodal capabilities in bio-images, combining concurrent CARS, SHG, and TPEF signals detected in three separate output channels on our inverted microscope platform.

For specific cases, I chose to use a similar OPA but in this case seeded by a CW diode laser source which costs much less than a tunable laser source seed. I present results that show this OPA is a versatile light source module that can be tailored to the tunability and affordability requirements of specific applications. I also demonstrate that it can be used either on its own as a light source or in association with an OPO for multimodal CARS microscopy (extend to fingerprint region: 340 to 2400 cm$^{-1}$) and I show its performance by imaging a variety of standard and biological samples.

Parts of this Chapter has been reproduced from my own publication [207], © 2021 Optica Publishing Group and [18], © 2021 SPIE. Users may use, reuse, and build upon the article, or use the article for text or data mining, so long as such uses are for non-commercial purposes and appropriate attribution is maintained. All other rights are reserved.

### 3.1.2 Review of prior art

A different solution to develop an OPA system for CARS imaging was explored in my group before I started my project. In that experiment, they used a frequency-doubled 516-nm pulsed laser as a pump and a CW 795 nm diode laser as a seed to construct the OPA, as shown in Figure 3.1. The 3-ps 1032-nm pump was converted to 516 nm by using an SHG crystal. The 516-nm beam was used to pump the OPA and to generate few-ps 795-nm light that is combined with the unconverted 1032-nm pump light to perform the CARS microscopy.

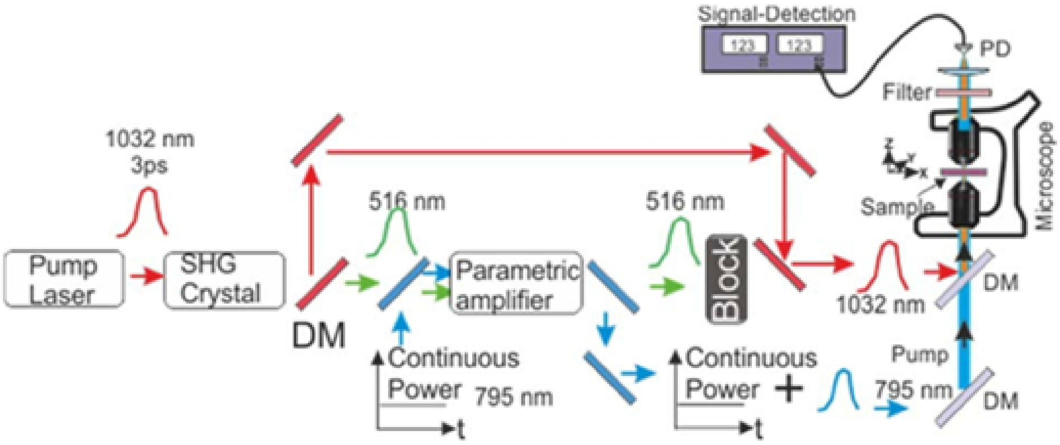

Figure 3.1: Previous OPA setup

The system was built and aligned using a low power fibre laser in our lab at ORC and was then transported into another lab at IfLS for imaging tests. Unfortunately, the parametric gain of the OPA was found to be relatively low and the system proved to be completely unsuitable for CARS microscopy. One limitation was that the damage threshold of the PPLN crystal at 516 nm was very low (less than 100 $MW/cm^2$ [43]) due to green-induced infrared absorption (GRIIRA) [63][43], which restricted the pump intensity inside the crystal and hence limited the maximum gain in the nonlinear amplification process. Apart from that, another limitation came from the large Group Velocity Mismatch (GVM) between the 516 nm pump laser and 795 nm seed. Due to this high GVM, the pump and signal pulses did not remain overlapped during the propagation in the PPLN crystal before sufficient power was generated. This problem was less notable when the laser pulses were in the ns regime, but it seriously affected the efficiency of the gain when operated with ps pulses. It was concluded that a very different approach was required to design the OPA system for CARS microscopy.

## 3.2 2-ns fibre laser pumped OPA

### 3.2.1 Introduction

In this part I aim to solve those problems mentioned above (low damage threshold and large GVM of the PPLN crystal under 0.5 $\mu$m pumping), to achieve high enough gain ($>$ 40 dB) and power ($>$ 100 mW) at the output, and finally to apply it to CARS imaging. I have designed a new system: it uses a laser with twice the previous wavelength to pump the OPA, generating signals at wavelengths around 1.5 $\mu$m, and employ a final SHG stage to convert the signals to the target wavelengths. For the PPLN crystal, the damage threshold for the 1 $\mu$m laser (1.5 $GW/cm^2$ [43]) is significantly higher due to the eliminated GRIIRA, and the GVM between 1.5 $\mu$m and 1 $\mu$m is much smaller. Furthermore, easy access to seed lasers at telecoms-compatible wavelengths allows me to test the OPA system using a single, simple diode laser as well as more complex and expensive lasers with wide tunability.

### 3.2.2 OPA and SHG development

The initial experiments used nanosecond pulses to prove the principle and necessary performance could be achieved before adapting the picosecond pulses in IfLS. For the purpose of developing a small-footprint and movable laser system that can be easily transported from the ORC into the labs in IfLS, all the components were set up on a small-size breadboard. The schematic and photo of the setup are shown in Figure 3.2 and 3.3, respectively. The pump source was a fibre laser configured as a MOPA structure providing 2 ns pulses with 250 kHz repetition rate at 1040 nm wavelength at a maximum average power of 5 W. A semiconductor-based CW tunable laser (TLS: Photonetics Osics 3610 RA00) with fiberized output generated a <10 mW average power beam in the 1500-1600 nm range which was employed as the seed and the output was spatially combined with the pump beam for the OPA. CW seeding dramatically simplifies the OPA operation, as there is no need for pump-seed synchronization in the time domain. A 20-mm-long MgO-doped periodically poled lithium niobate (PPLN) crystal with 5 different poling periods from $\Lambda$=29.52 $\mu$m to $\Lambda$=31.59 $\mu$m in 0.5 $\mu$m steps (Covesion: MOPO1-1.0-20) was used in the OPA stage, which had a temporal walkoff of 2.3 ps between the 1040 nm pump and 1560 nm signal and a pump spectral acceptance bandwidth of 1.2 nm. Both of the beams were focused down to 60 $\mu$m diameter resulting in a pump peak intensity of $\sim 300 MW/cm^2$, being in the safe operation regime of the PPLN crystal. In the SHG stage, a 10-mm-long SHG PPLN crystal with 5 grating periods from $\Lambda$=19.2 $\mu$m to $\Lambda$=20.4 $\mu$m in steps of 0.3 $\mu$m) (Covesion: MSHG1550-1.0-10) was used to generate the 780 nm pulses. Both the PPLN crystals used had 5 poling channels with different periods for phase matching and achieving different wavelengths for CARS imaging requirements. The unconverted 1040 nm beam from the OPA and the 780 nm output from the SHG can be employed as the pump and Stokes in the following CARS microscopy.

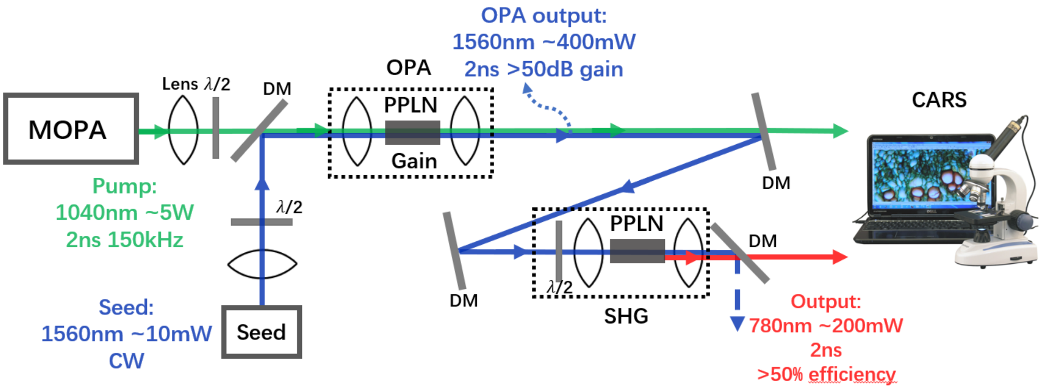

Figure 3.2: Schematic of the 2-ns fibre laser pumped OPA setup

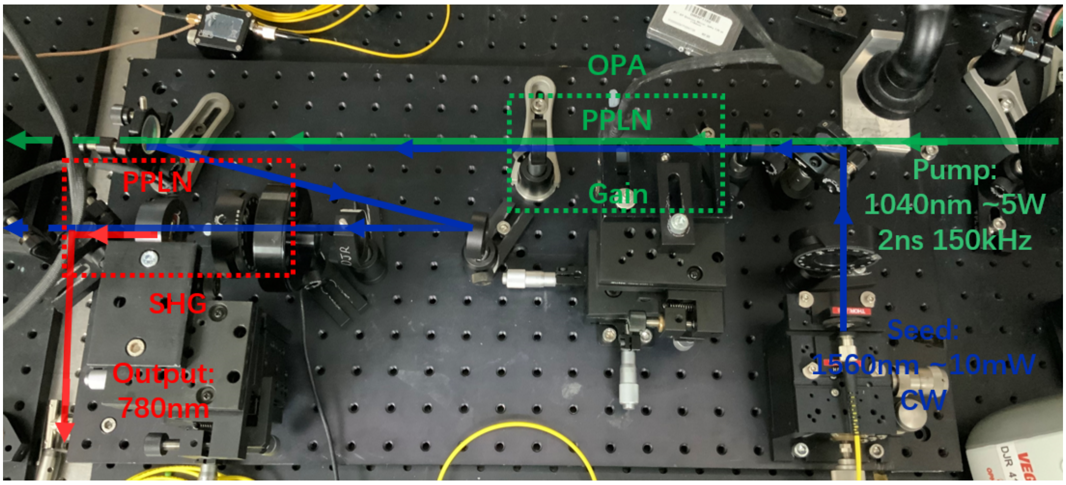

Figure 3.3: Real photo of the OPA setup constructed and ultimately installed in IfLS labs (300 mm × 600 mm).

The MOPA I used as the pump was built by Lin Xu several years ago. The pump spectrum from the MOPA output was measured, as shown in Figure 3.4, showing a 3-dB linewidth of 1.1 nm which is smaller than the OPA pump acceptance. Firstly, a CW telecom diode laser (A1905LMI) was selected as the seed source. It had an output power of 17 mW and central wavelength of 1563.6 nm. Figure 3.5 shows the spectrum of the seed laser output and the amplified seed from the OPA. The expectation of the OPA output was more than 100 mW corresponding to a gain of 40 dB and an SHG efficiency of more than 30 % corresponding to an SHG output of 30 mW. From the experiment, an average power of ∼300 mW that corresponds to a parametric gain of ∼45 dB was achieved from the OPA, and the output of the SHG reached ∼140 mW with a conversion efficiency up to ∼47%, as shown in Figure 3.6 and Figure 3.7. The SHG signal spectrum was measured and is shown in Figure 3.8.

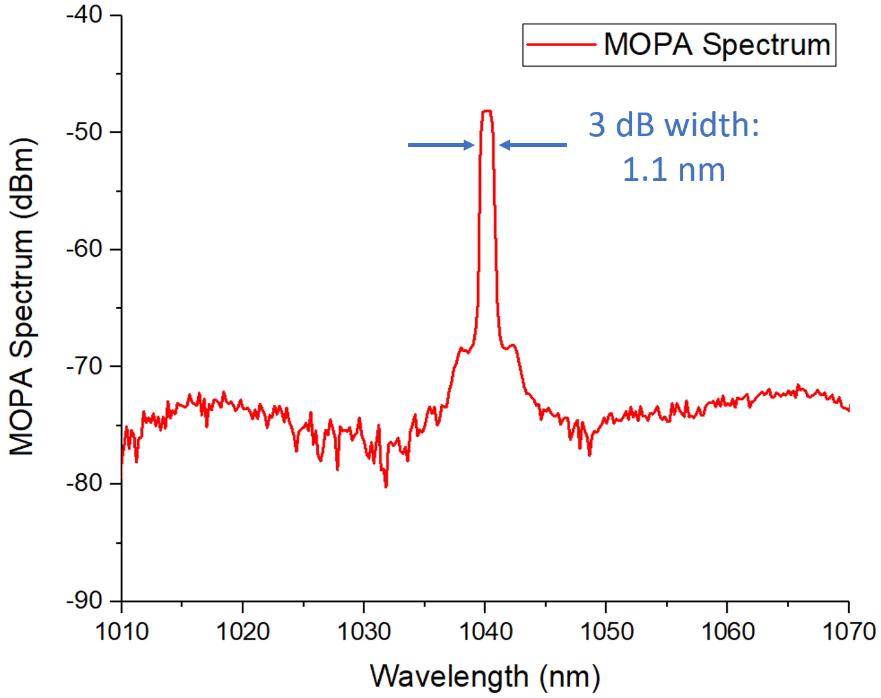

Figure 3.4: MOPA pump source spectrum (resolution 0.2 nm).

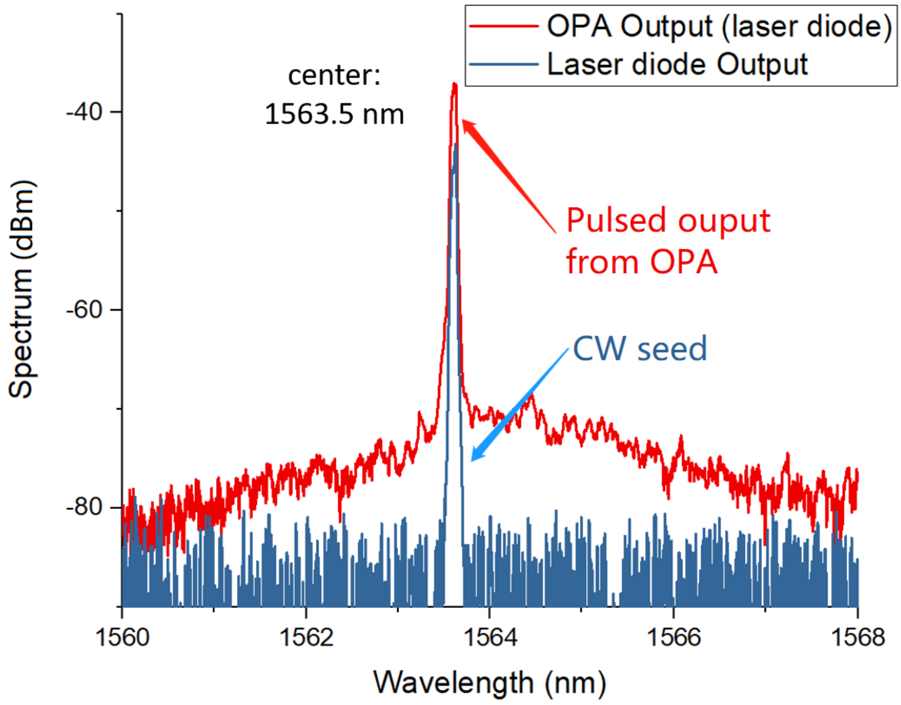

Figure 3.5: The spectrum of the laser diode source and the corresponding OPA output.

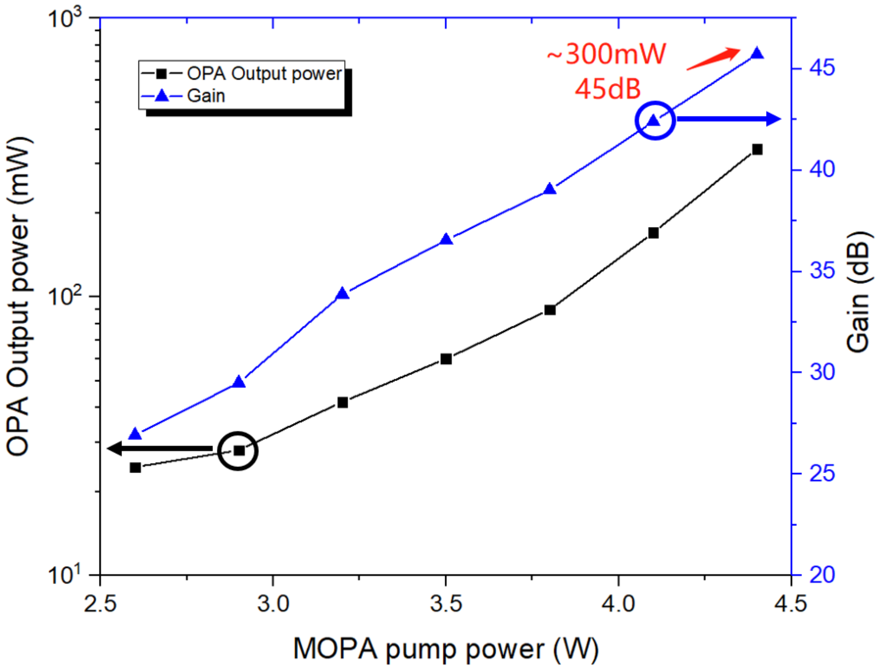

Figure 3.6: OPA output power (laser diode seeded) and OPA gain.

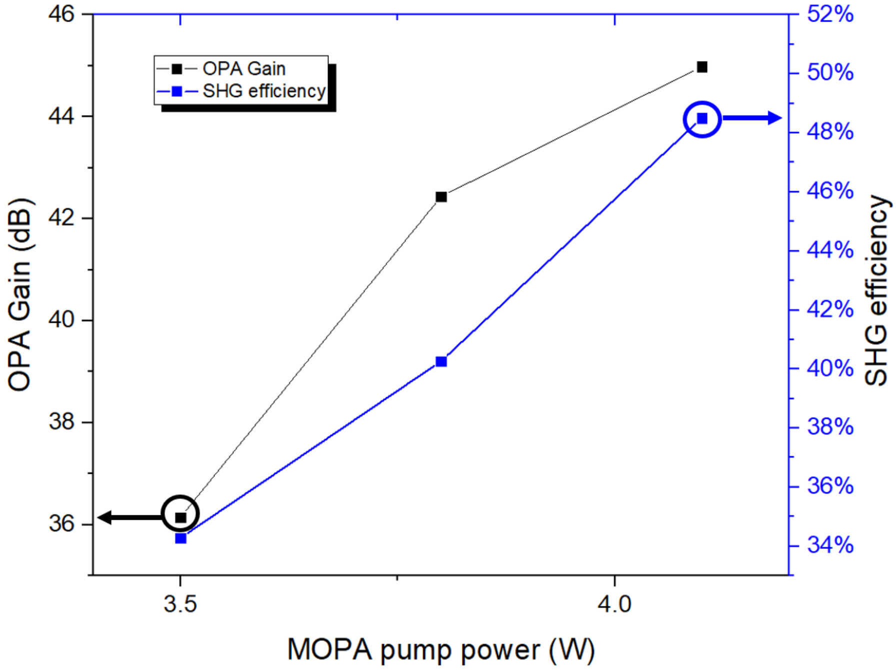

Figure 3.7: OPA gain (laser diode seeded) and SHG efficiency.

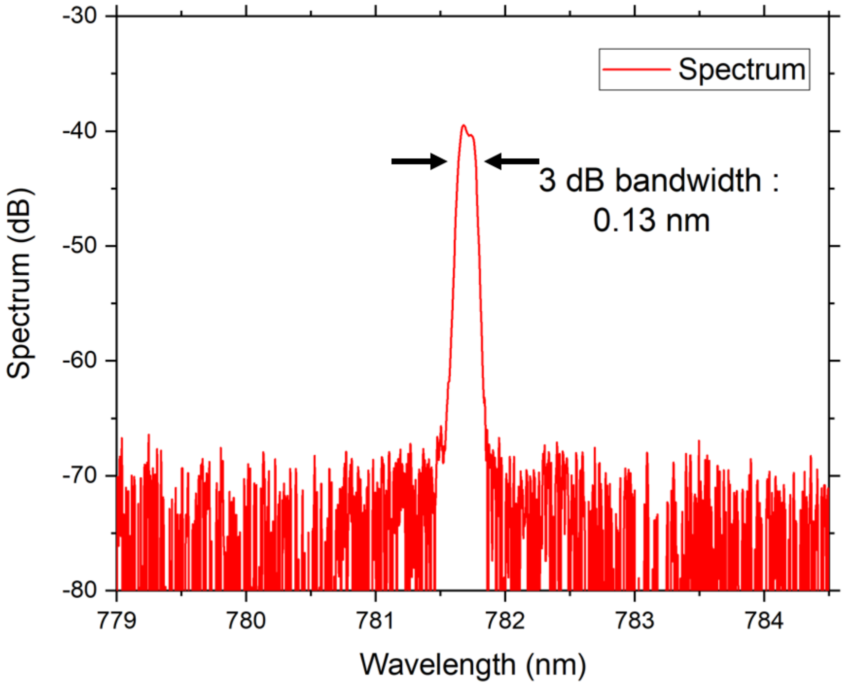

Figure 3.8: 780 nm SHG output spectrum

In order to tailor the pump-Stokes wavelengths targeting different Raman resonant frequencies of biological samples in CARS microscopy, a CW tunable laser source (TLS: Photonetics Osics 3610 RA00) was employed to seed the OPA system. The tunable laser had a wavelength tuning range from 1500 nm to 1600 nm, a maximum output power of 10 mW and a spectral linewidth of 1.8 MHz. A number of Raman resonance frequencies that are typically used for imaging lipids have been selected (listed in Table 3.1). For example, a 1593 nm seed wavelength was selected for the OPA to generate output which is then frequency-doubled to 796.5 nm in the subsequent SHG stage and combined with the 1031 nm Stokes pulses reaching a Raman resonance frequency of 2850 cm$^{-1}$ and generating 649.1 nm anti-Stokes signals in the CARS process. With further optimisation of the beam alignment and focal spot size, a maximum average power of 600 mW output at 1593 nm was achieved in the OPA, which corresponded to a parametric gain as high as 51 dB. In the SHG process, a conversion efficiency of 53% was obtained providing 320 mW of output power at 796.5 nm. For the case of seeding at 1570 nm to target the 3030 cm$^{-1}$ Raman resonance frequency, a maximum power of 500 mW at 1570 nm and 260 mW at 785.2 nm were achieved in the OPA and SHG stages, respectively, corresponding to a parametric gain of 50 dB and a conversion efficiency of 52%. The OPA and SHG system showed good and consistent performance for those different wavelengths covering the Raman resonance frequencies of interest.

| Pump (nm) | Stokes (nm) | CARS (Anti-stokes) (nm) | Raman Resonances (cm-1) |
|---|---|---|---|
| 796.5 | 1031 | 649.1 | 2850 |
| 791.5 | 1031 | 642.5 | 2930 |
| 789.0 | 1031 | 639.2 | 2970 |
| 785.2 | 1031 | 634.5 | 3030 |

Table 3.1: Raman Resonances

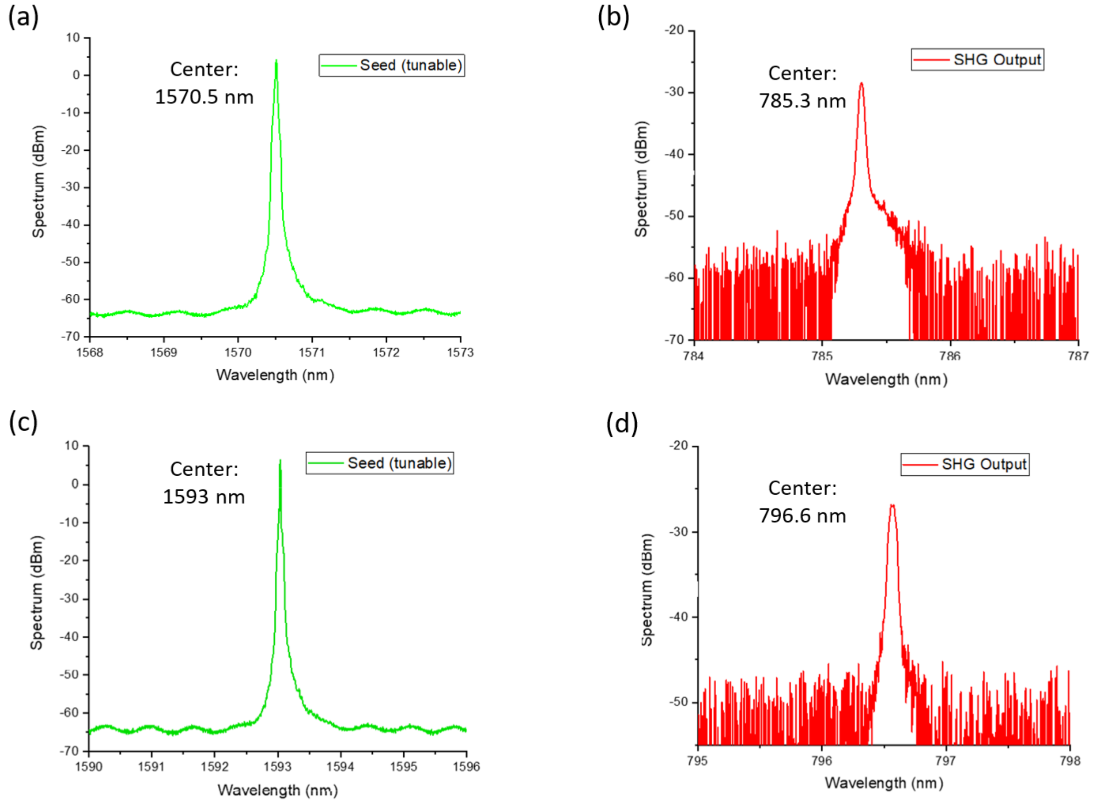

Figure 3.9: (a) 1570.5 nm seed spectrum, (b) 785.3 nm SHG output spectrum, (c) 1593 nm seed spectrum, (d) 796.6 nm SHG output spectrum.

Being satisfied with the performance of the large gain and high power of the OPA system, I transported the system to the biomedical lab in IfLS for CARS microscopy experiments. Considering the pump sources were different, a nanosecond fibre laser in my lab and a picosecond solid-state laser in the bio lab, in terms of wavelength, pulse width, peak power and etc, the final performance of the OPA system needed to be characterized and tested again in the IfLS. Table 3.2 shows the key parameters of those pump sources.

| | Rep. rate | Wavelength | Pulse duration | Pulse shape | Average power | Pulse energy | Peak power | Duty cycle |
|---|---|---|---|---|---|---|---|---|
| ORC | 250 kHz | 1040 nm | 2 ns | Square | 5 W | 20 $\mu$J | 10 kW | 1/2000 |
| IfLS | 80 MHz | 1031 nm | 2 ps | Sech$^2$ | 10 W | 125 nJ | 58 kW | 1/6250 |

Table 3.2: Difference between pump sources in ORC and IfLS

## 3.3 2-ps solid-state laser pumped OPA with a tunable laser seed

### 3.3.1 Introduction

The OPA system that I developed and tested in the ORC lab was transported into the biomedical lab in IfLS and integrated into their microscopy system using a 2-ps-pulsed solid-state laser as a pump.

A diagram illustrating the multimodal CARS laser source and microscope system can be found in Figure 3.10, while a photo depicting the OPA in operation is provided in Figure 3.11. The APE Emerald Engine laser served as the pump laser, with its output ($\sim$ 4W, 2ps, 80MHz, 1031nm, and spectrum displayed in Figure 3.14) divided into two beams: one for pumping the OPA and another for generating the Stokes beam utilized in CARS imaging platform. The same semiconductor-based CW tunable laser (TLS: Photonetics Osics 3610 RA00, spectrum displayed in Figure 3.14) mentioned in the prior section seeded the OPA. Both the OPA pump and seed were collimated and collinearly focused to a 75-$\mu$m waist within the same MgO-doped PPLN crystal (Covesion: MOPO1-1.0-20). The beam diameter was measured using an OPHIR Nanoscan beam profiler. By adjusting the TLS wavelength and selecting the appropriate poling period and PPLN crystal temperature, the OPA tuning was achieved quickly and precisely. Output power above 400 mW was obtained across the entire OPA tuning range (shown in Figure 3.16(c)). The spectral linewidth of the OPA output ranged from 17 $\mathrm{cm}^{-1}$ at 1556nm to 13 $\mathrm{cm}^{-1}$ at 1606nm, roughly in line with the pulse duration shaped by the pump. The output pulses of the OPA had a measured duration of 2.1 ps (data not displayed in Figure 3.12(a)), comparable to the pump's duration. Approximately $1.2 \times 10^5$ photons from the CW seed laser were present within the time window of each pump pulse, enough to fully suppress the noisier parametric superfluorescence generation process in the OPA [119]. The use of a low-noise solid-state laser as the pump and a CW seed ensures that the OPA exhibits minimal spectral drift over time and low temporal jitter.

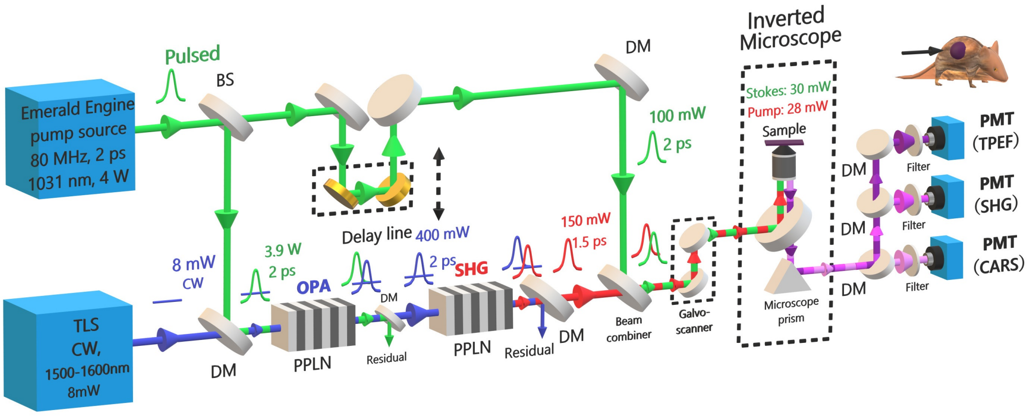

Figure 3.10: Schematic of the experimental system used for multimodal CARS. BS, beam splitter; DM, dichroic mirror; PPLN, periodically-poled lithium niobate; PMT, photomultiplier tube. This figure has been reproduced from my own publication [207].

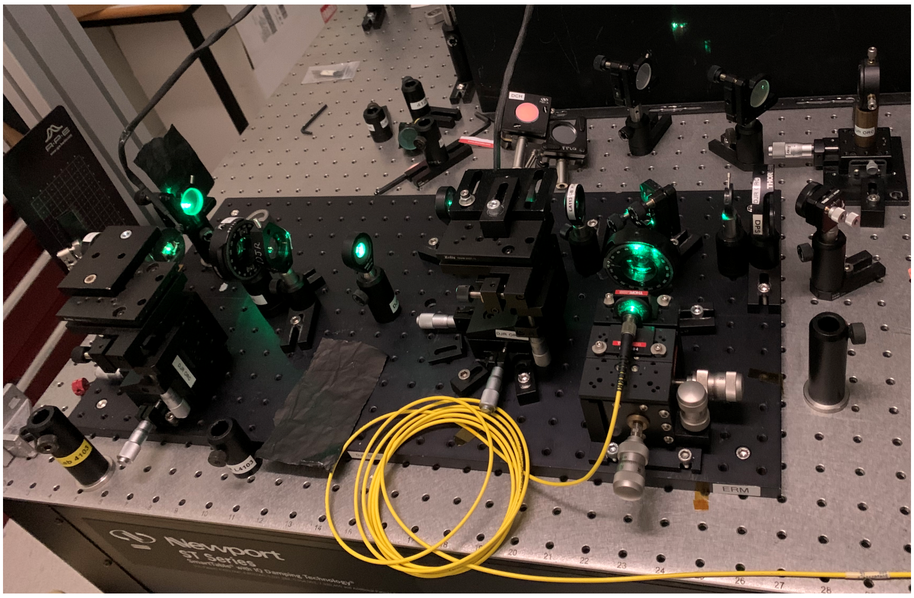

Figure 3.11: Photo of the experimental OPA setup used for multimodal CARS and installed in IfLS labs.

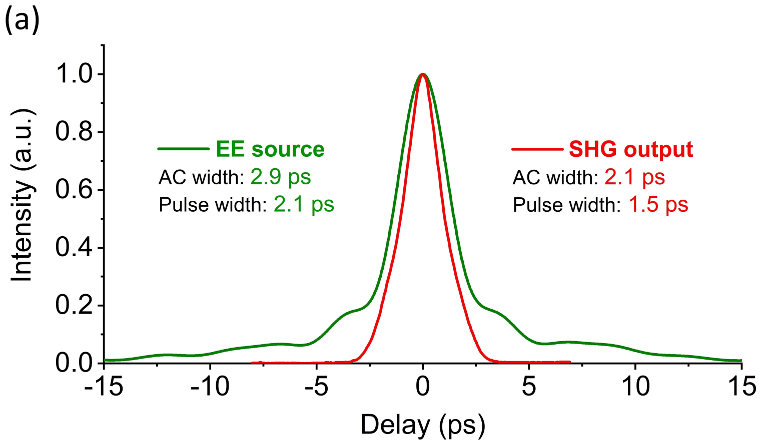

Figure 3.12: Auto-correlation measurement of the EE source (Emerald Engine pump laser) (1031 nm) (green) and OPA-SHG output (red). This figure has been reproduced from my own publication [207].

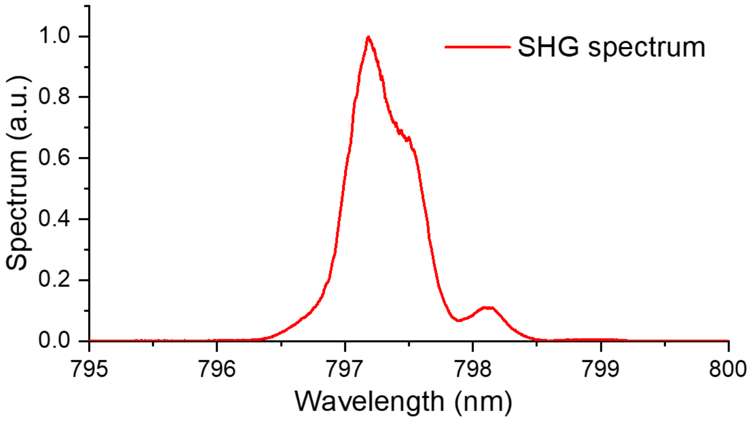

Figure 3.13: SHG output spectrum of 1594.4 nm seed input.

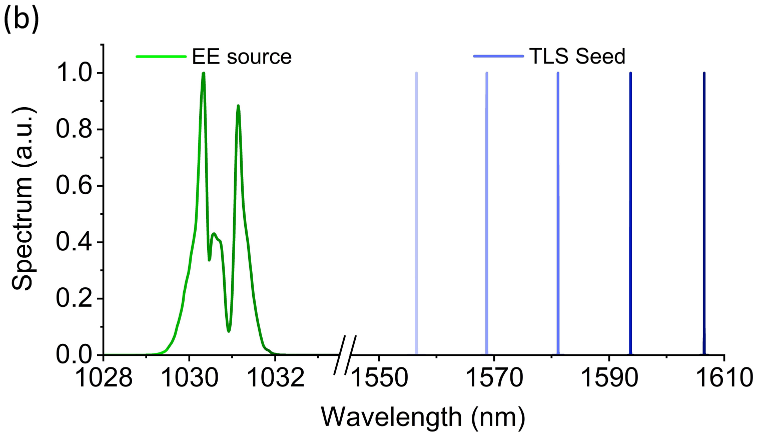

Figure 3.14: Spectrum of the Stokes beam (OPA pump source) and TLS (tunable laser) output (OPA seed). (See Figure 3.16 for the OPA spectrum.) This figure has been reproduced from my own publication [207].

The OPA output signal was separated from the residual pump and focused into a second PPLN crystal (Covesion: MSHG1550-1.0-10) for SHG, which supplied the pump beam for CARS imaging platform. The SHG output's tuning range spanned from 775 to 805 nm, constrained by the available SHG crystal; this range could be extended to encompass the entire OPA tuning range by choosing suitable poling periods in the future. The SHG pulse duration at an operating wavelength of 1594.4 nm was approximately 1.5 ps (as illustrated in Figure 3.12(a)). Additionally, the SHG process eliminated the pedestal from the pump source. The pump-Stokes frequency detuning range, from 2700 to 3200 cm$^{-1}$, fully covered the C-H stretching bands typically utilized for lipid imaging.

A delay line in the pump beam path and dichroic mirrors (DMs) were employed to combine and overlap the Pump and Stokes pulses in time and in space. Both beams were then delivered collinearly to a custom-built CARS microscope platform. Operating in reflection (epi) mode, the inverted microscope (Figure 3.15) used an air objective lens with a numerical aperture (NA) of 0.75 (Nikon 20×) to focus the Pump and Stokes on the sample. A galvo-scanner facilitated rapid spatial scanning of the beam. The epi light was gathered and detected (non-descanned) by three photo-multiplier tubes (PMTs) (filters: 400±20 nm for SHG, 520±20 nm for TPEF, and 640±20 nm for CARS).

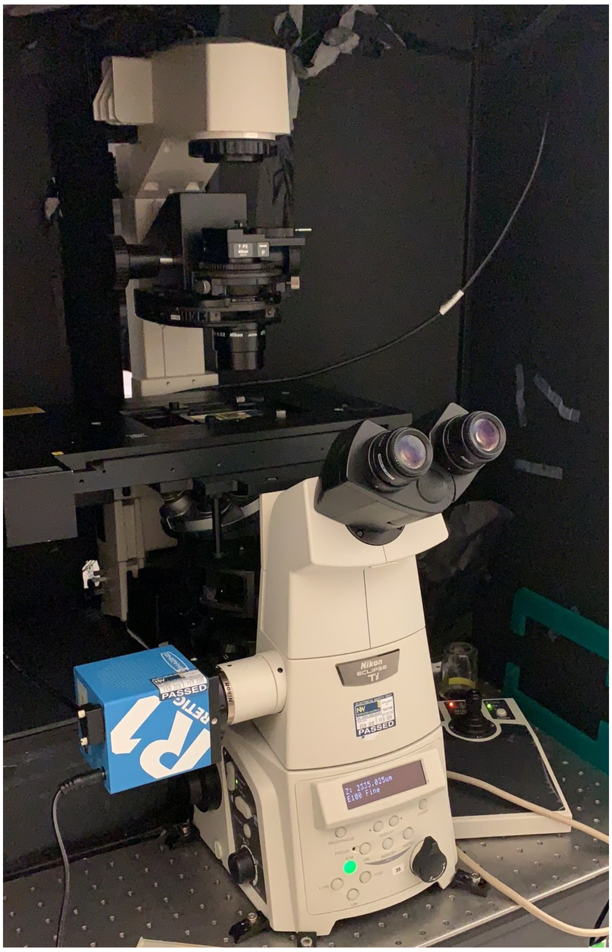

Figure 3.15: Photo of the experimental inverted microscope used for multimodal CARS.

### 3.3.2 OPA and SHG characterisation

Initially, I characterized the OPA's performance as a function of pump power and seed power. With the seed laser set at a wavelength of 1594.4 nm and an output power of 8 mW, the minimum pump required for measurable gain was 2.7 W. Beyond this point, the OPA output power increased as the pump power rose, reaching 400 mW at the maximum pump power of 3.9 W, as displayed in Figure 3.16(a). (The maximum pump power was established to remain below the PPLN crystal's 1.5 $GW/cm^2$ damage threshold [43].) The corresponding OPA gain increased with pump power up to a maximum of 55 dB. I also analyzed the gain performance concerning seed power in the OPA while maintaining the pump at 3.9 W. As seen in Figure 3.16(b), increasing the seed power resulted in an increase in output power and a decrease in gain, with saturation observed at seed powers above approximately 5 mW. Figure 3.16 also depicts the SHG output power characteristics, with a maximum SHG output power of 185 mW. The tunable output ranging from 1540 to 1620 nm is illustrated in Figure 3.16(c), with output powers nearing 450 mW achieved across the entire tuning range. The OPA spectrum had a FWHM bandwidth of 4 nm, yielding a time-bandwidth product of 0.98 (roughly 3 times the transform-limited value).

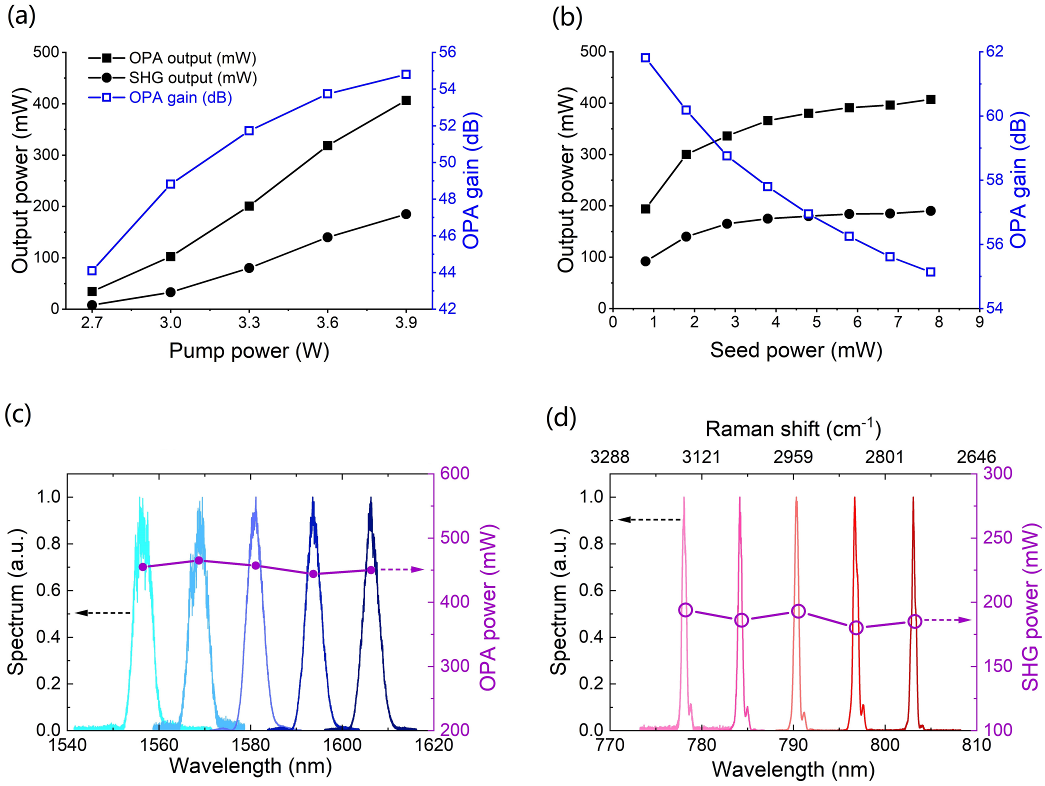

Figure 3.16: OPA output (solid square), SHG output (solid circle) and OPA gain (empty square, blue) as a function of pump power (a) or seed power (b). Spectra and power of CW seeded OPA (c) and SHG (d) later used as the tunable CARS Pump beam. This figure has been reproduced from my own publication [207].

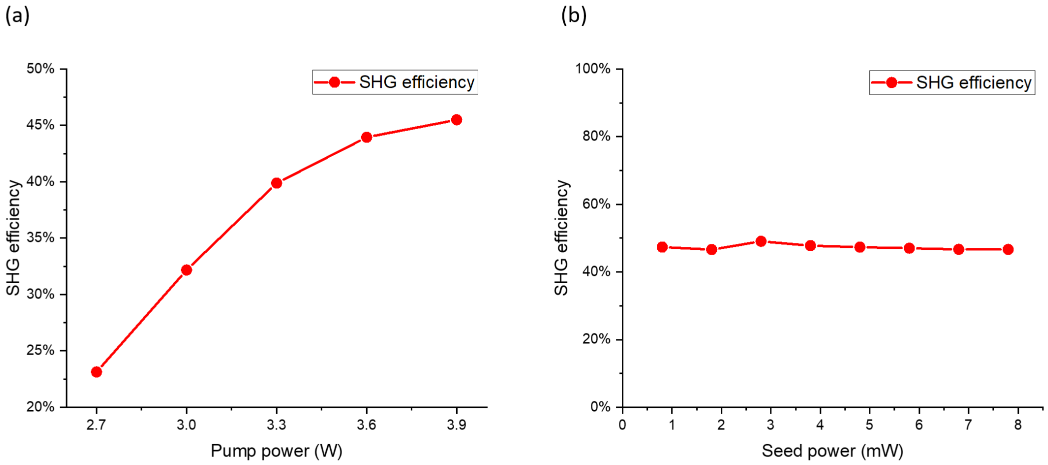

Figure 3.17: SHG efficiency as a function of pump power (a) or seed power (b).

Figure 3.16(d) presents the SHG spectrum ranging from 775 nm to 805 nm. The output power is more than adequate for CARS, SHG, and TPEF bio-imaging, taking into account the power limitations imposed by photo-toxicity. As depicted in Figure 3.16(d), the average power ranges from 175 to 200 mW across the tuning range. Figure 3.17 displays the SHG efficiency and varies with the pump power and seed power. Since the SHG crystal's 1 nm pump spectral acceptance bandwidth is smaller than the pump spectral bandwidth, the SHG process cleaned up the pump's chirp, reducing the pump spectra width and pulse width. The SH spectrum exhibited a FWHM bandwidth of 0.5 nm (8 $\text{cm}^{-1}$), and the measured SHG pulse duration was 1.5 ps (time-bandwidth product = 0.35, improving to approximately 1.11 times the transform-limited value), see Figure 3.12. The output beam was close to a Gaussian profile, with $M_x^2$ measured at 1.29 and $M_y^2$ at 1.18, as seen in Figure 3.18.

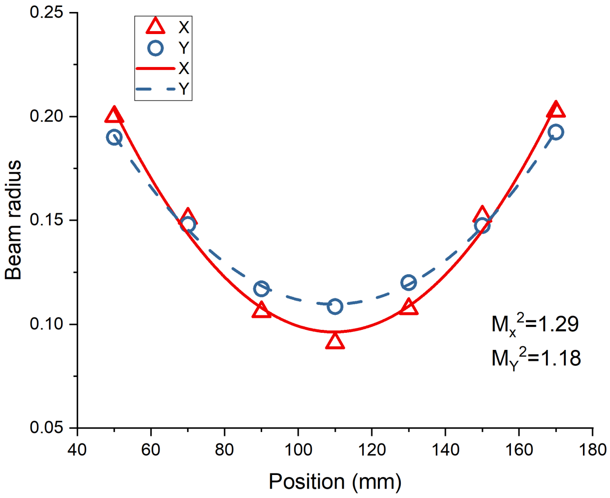

Figure 3.18: SHG output beam quality.

### 3.3.3 Chemical imaging results

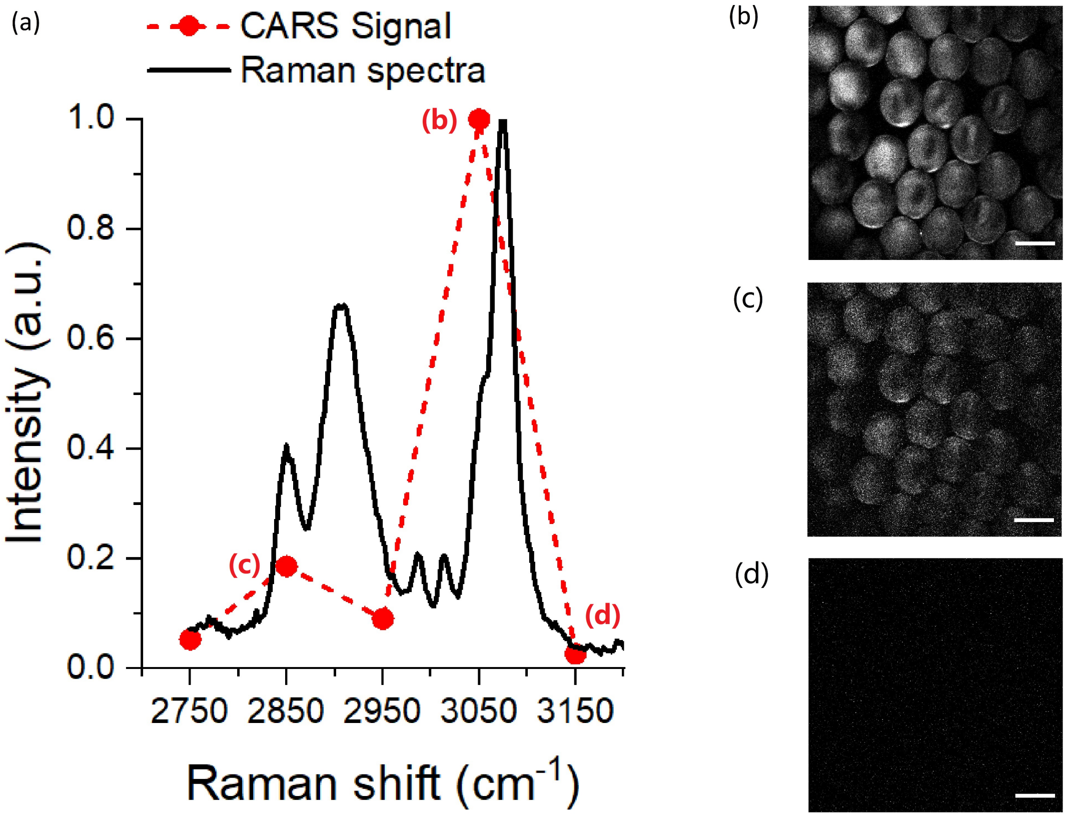

Figure 3.19: (a) Measured CARS spectra of polystyrene beads overlayed with the spontaneous Raman spectra. (b) (c) (d) show the corresponding polystyrene CARS images vs Raman excitation frequency 3050 cm$^{-1}$, 2850 cm$^{-1}$ and 3150 cm$^{-1}$ respectively (scale bar: 40 $\mu$m). This figure has been reproduced from my own publication [207].

As an initial evaluation of the system's chemical specificity and imaging capabilities, we recorded CARS spectra and microscopy images of 40-micron diameter polystyrene beads, which are standard samples for testing performance. The SHG of the OPA output was tuned from 778 to 803 nm, allowing us to probe CARS anti-Stokes signals shown in Figure 3.19 at frequencies ranging from 2750 to 3150 cm$^{-1}$. The overall profile of the CARS spectrum and the position of the two characteristic peaks at 2850 cm$^{-1}$ and 3050 cm$^{-1}$ are reasonably consistent with the spontaneous Raman spectrum. (The peaks observed in CARS are a result of convolving the signal with a dispersive non-resonant background. Therefore, it is not anticipated that these peaks will align with the spontaneous Raman peaks.) The spontaneous Raman reference spectrum for polystyrene was captured using a custom-built Raman micro-spectrometer system equipped with a Shamrock303 spectrograph, an Andor iDus 420 camera as the detector, and a 785 nm excitation laser. The spectrum was obtained with a single 10-second exposure (50-micron slit, approximately 4 $\mathrm{cm}^{-1}$ resolution) and 15 mW laser power using a 40x (0.9 NA) objective. The average power levels on the sample were 6 mW for the Pump beam and 12 mW for the Stokes beam. The pixel dwell time was 8 microseconds, meaning that a full image (512 x 512 pixels) took roughly two seconds to acquire which is remarkably fast. Good image contrast is visible at the strongest resonance frequency in Figure 3.19(b) in comparison to the weaker resonance shown in Figure 3.19(c) and the off-resonance data presented in Figure 3.19(d).

### 3.3.4 Biological imaging results

Subsequently, I demonstrated bio-imaging by presenting CARS alongside SHG and TPEF imaging in an epi-detection setup. Biological samples (Figure 3.20) were prepared by extracting tissues from culled mice. All procedures were carried out in accordance with the Animals (Scientific Procedures) Act 1986 set out by the UK Home Office. No additional ethics approval relevant to the use of biological samples in the project work is needed. Female C57BL/6 mice aged between 4-6 months were culled using $CO_2$ and cervical dislocation. Perigonadal adipose tissue was excised using scissors and forceps. The tissue was fixed in a 4% paraformaldehyde solution for 4 hours and then rinsed in phosphate-buffered saline (PBS) immediately before being placed in a glass-bottomed dish with an imaging window cover slip (#1.5; 0.17 mm thick).

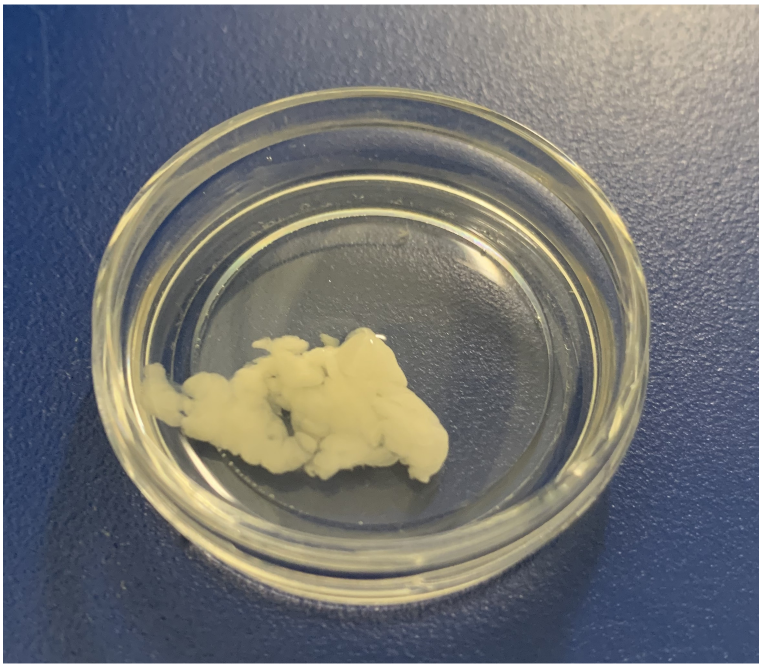

Figure 3.20: Photo of the biological sample: tissues from culled mice.

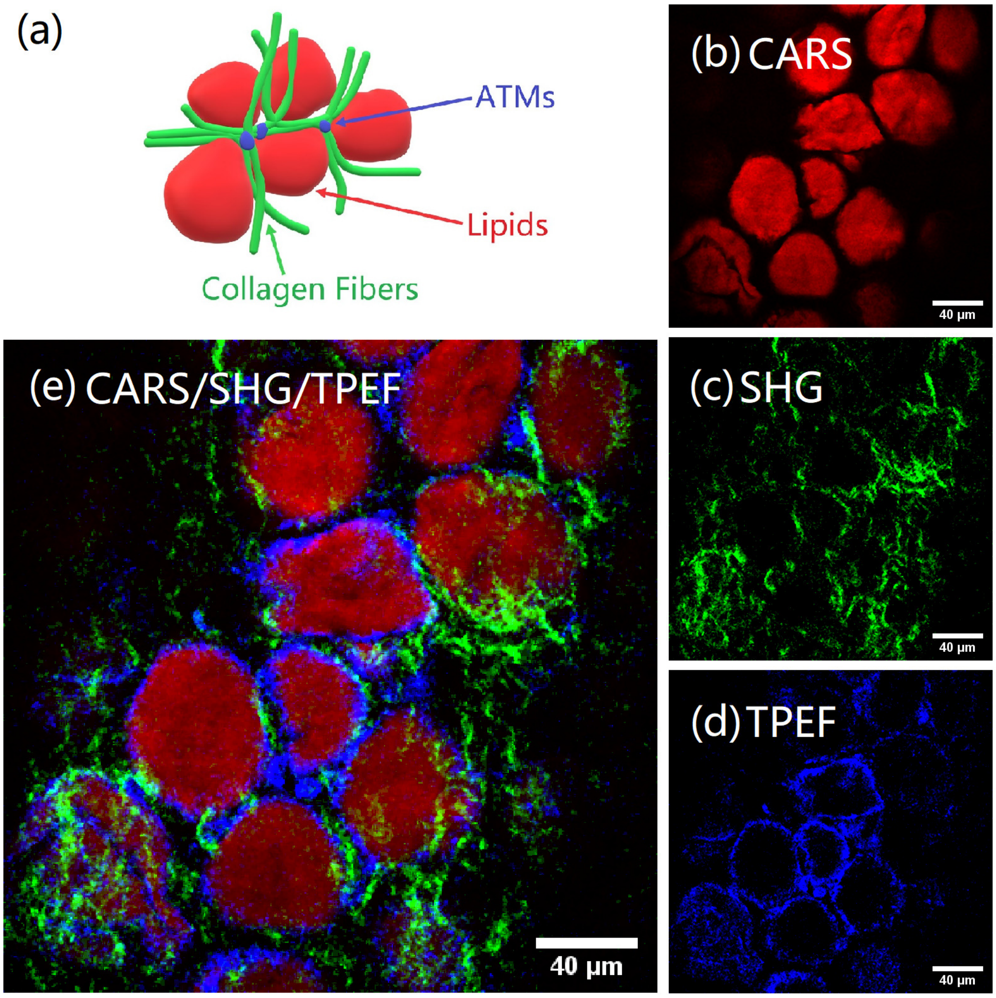

Figure 3.21: Multimodal CARS/SHF/TPEF bioimaging with our new OPA/SHG source. Images are of mouse adipose tissue acquired at the surface of the sample. (a) Schematic showing the main components of adipose tissue; (b) CARS image mapping the intensity of the 2845 $cm^{-1}$ lipid band across the tissue; (c) collagen fibers imaged with SHG; (d) TPEF images FAD autofluorescence in macrophage cells; (e) composite image with CARS, SHG and TPEF overlaid. Color intensity relates linearly to the counts on the detector, normalized to the maximum to obtain the highest contrast for each of the channels independently. The images shown are single frame CARS acquisitions with pixel dwell time of 8 $\mu$s, 28 mW pump and 30 mW of Stokes. This figure has been reproduced from my own publication [207].

Figure 3.21 displays representative images of adipose tissue from mice. The image acquisition process involved simultaneous acquisition of CARS, SHG, and TPEF images using our three-channel detection system. Each modality offers distinct chemical or structural information. It is important to note that all three signals originate from endogenous contrast mechanisms inherent to the sample, without the need for added dyes or stains to improve contrast.

Images are acquired with a Pump-Stokes frequency detuning of 2845 $cm^{-1}$ (Pump: 797.2 nm, Stokes: 1031 nm). The average power levels on the sample are 28 mW Pump and 30 mW Stokes. The pixel dwell time is 8 $\mu$s, so that the acquisition of a full image (512 $\times$ 512 pixels) takes $\sim$ two seconds. A schematic of the expected arrangement of different components in adipose tissue is shown in Figure 3.21(a). It can be seen from the CARS channel (Figure 3.21(b)) that the signal from the $CH_2$ peak at 2845 $cm^{-1}$ is diffuse and not structurally dependent, as it is from the uniform lipid distribution within the adipocyte (fat cell). Indeed, lipids are rich in C-H bonds resonant at this frequency so CARS microscopy allows selective imaging of lipid droplets in unstained live cells with very high contrast. Figure 3.21(c) shows the corresponding SHG image. SHG interrogates the $\chi^{(2)}$-related part of the hyperpolarizability (second-order electric susceptibility per unit volume) of materials. In this image the SHG was generated by the Pump as verified by turning off the Stokes beam and confirming the SHG channel signal was still there. SHG from only Stokes or SFG from Pump and Stokes would potentially be observable using a different choice of filters for the respective channel. Here, SHG selectively images collagen fibers, which are a dominant component of the adipose tissue scaffolding [98], (detection in the range of 400±20 nm) highlighting the fibrillary nature and periodicity of collagen fibers in the sample. I used TPEF to image auto fluorophores (detection in the range of 520±20 nm) in the tissue (flavin adenine dinucleotide (FAD) and flavin mononucleotide (FMN) [60]). These auto fluorophores indicate metabolic activity in cells. The TPEF images in Figure 3.21(d) show adipose tissue macrophages (ATMs) that are localized in between adipocyte cells. Blood vessels would also have good contrast with this modality and form a network around adipocytes. Elastin fibers are key components of blood vessel architecture and exhibit TPEF in the spectral range imaged here [106]. I verified that the TPEF signal was neither delay dependent nor did it reduce when the Stokes was blocked so it is not a four-wave mixing signal. The shape and distribution of the macrophages are similar to observations by others[60] and our detection window covers the expected emission spectral range[83]. Figure 3.21(e) shows the composite multimodal image of the same area of the tissue. The multimodal image thus gives the underlying chemical and structural distribution and the local adipose tissue architecture[60] through combined CARS, SHG and TPEF modalities.

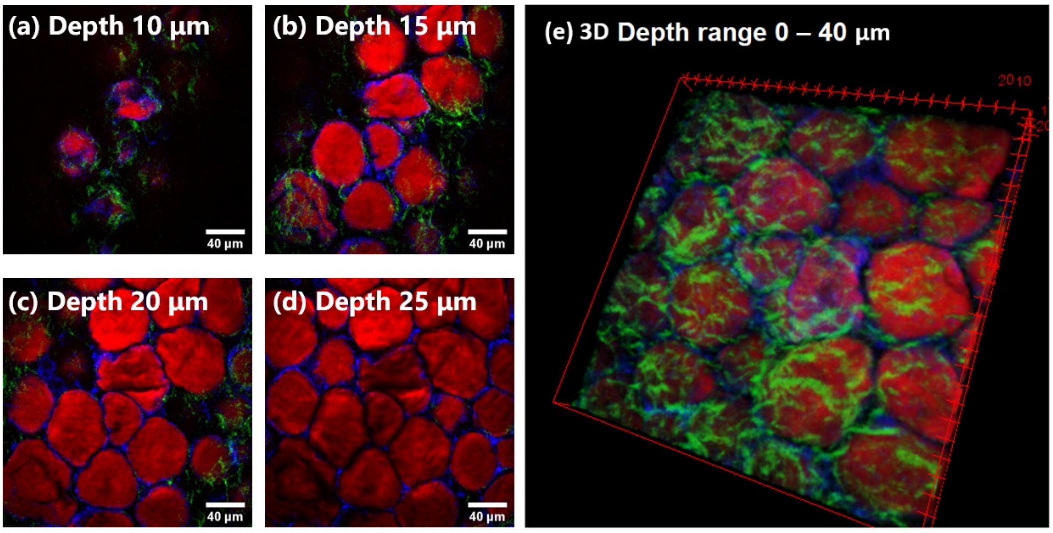

Figure 3.22: Multimodal imaging at different depths. Composite images with the combined modalities of CARS (red), SHG (green) and TPAF (blue) corresponding to the image shown in Figure 3.21 are shown at different depths (a) 10 $\mu$m, (b) 15 $\mu$m, (c) 20 $\mu$m and (d) 25 $\mu$m. (e) is the 3D construction of the image (1 $\mu$m spacing between each section for 40 slices). This figure has been reproduced from my own publication [207].

Currently tissue diagnostics makes use of colored stains on thin tissue slices (typically 5-7 $\mu$m in thickness) which are suited for the transmission images recorded so that samples require very careful preparation and sectioning. The ability to use label-free imaging on clinically relevant thick tissue samples for diagnostic applications (for example, fresh from surgery) would be greatly simplified if the epi-detection became viable. To highlight this capability, I show in Figure 3.22 that our OPA-pumped multimodal CARS imaging setup can image at depths of up to 40 $\mu$m (thick tissue samples) without compromising on contrast or localized depth sectioning capability, which is beneficial as surface-sectioning can miss crucial information.

The axial depth of focus is expected to be different for CARS (three-photon process) and SHG/TPEF (two-photon processes): However, with the 1 $\mu$m z-resolution of our microscope stage I did not observe any significant effect. Overall, the ability to concurrently generate high contrast images with multiple modalities using the new OPA based laser source should make it a valuable tool for bio-science users. The epi-detection capability with an OPA-based setup demonstrates the relevance to biological and clinical samples without the need for extensive sample preparation which would be required to create the thin sections normally used with forward detection.

## 3.4 2-ps solid-state pumped OPA with a diode laser seed

### 3.4.1 Introduction

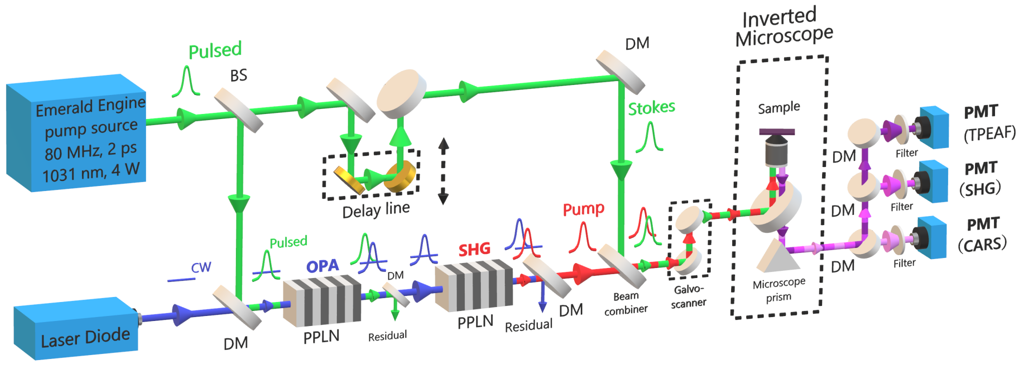

Figure 3.23: Schematic of the experimental system used for multimodal CARS. BS, beam splitter; DM, dichroic mirror; PPLN, periodically-poled lithium niobate; PMT, photomultiplier tube. This figure has been reproduced from my own publication [18].

Using the TLS as seed laser, the OPA has shown great wavelength flexibility for CARS microscopy. Despite that I also did experiments using a much less costly 1560 nm wavelength telecoms laser diode with similar power to the TLS and temperature-tuned the diode wavelength by up to 6 nm and achieved similar output power and pulse characteristics from the OPA as when using the TLS. (These telecoms diodes are readily available commercially at a very small fraction of the cost of a TLS and are much more compact.) This verified that, in principle, the costs of the system could be reduced and the tuning range maintained by using a switchable array of telecoms seed diodes with the wavelengths selected to target different molecular vibrational frequencies in the bio-samples of interest.

The experimental apparatus for performing multimodal CARS microscopy, which incorporates the OPA light source is depicted in Figure 3.23 and its basic aspects have been described in detail in the previous section. The difference in this high frequency

CARS imaging setup implementation is that I replaced the TLS with an Alcatel fibre coupled laser diode (A1905LMI: Figure 3.24) in a butterfly package with a temperature tunable wavelength in the range of 1562 to 1568 nm as a seed. With this layout a range of vibrational frequencies from 3050 to 3100 cm$^{-1}$ can be covered. The cost of this laser diode is around £ 800 versus £ 30,000 for TLS.

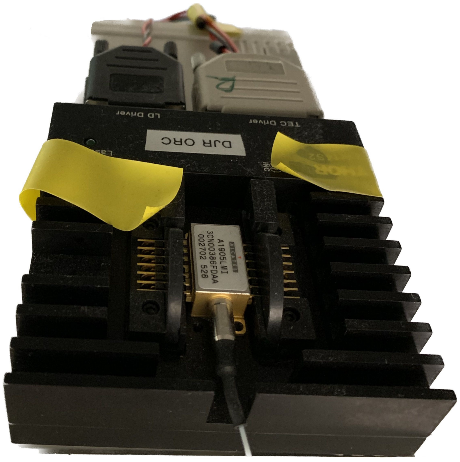

Figure 3.24: A1905LMI laser diode photo.

### 3.4.2 OPA and SHG characterisation

The OPA signal can be tuned from 1562 nm to 1568 nm (Figure 3.25(a)) by temperature tuning the laser diode seed and the PPLN OPA crystal. The bandwidth of the OPA signal pulses was 12.2 cm$^{-1}$ with an average power of 400 mW when the OPA was pumped with an average power of 4 W. The corresponding peak power of the OPA signal pulses was 2.5 kW. Similarly by adjusting the temperature of the SHG crystal the frequency doubled OPA signal could be tuned from 781 to 784 nm (Figure 3.25(b)) respectively with an average power of 170 mW. Their bandwidth was 4.88 cm$^{-1}$ and their intensity auto–correlation was fitted well with a Lorentzian curve (Figure 3.25(c)) and had a full width at half maximum (FWHM) of 2.11 ps which translates to a pulse duration of 1.055 ps. The associated peak power was calculated to be 2.1 kW. Furthermore the time–bandwidth product (TBP) was 0.15 which is very close to the transform limited value of 0.142 which means that these pulses have practically zero chirp.

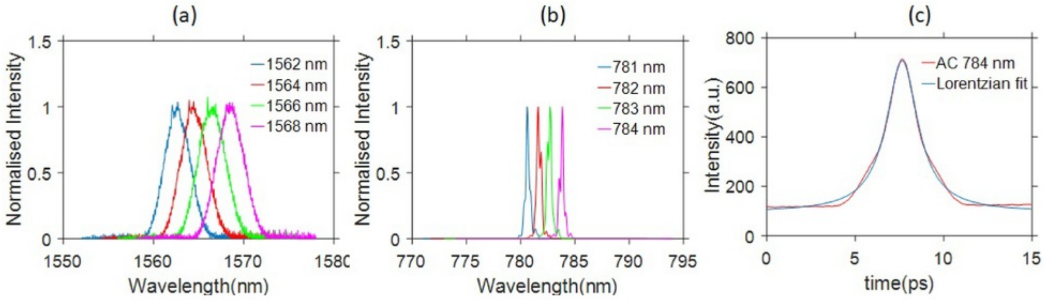

Figure 3.25: (a) Pulse spectra at the OPA output and (b) the respective pulse spectra at the SHG output. (c) Intensity auto-correlation of the SHG output for the central wavelength of 784 nm and the corresponding Lorentzian fit (FWHM of 2.11 ps which translates to a pulse duration of 1.055 ps). This figure has been reproduced from my own publication [18].

### 3.4.3 Chemical imaging results

With the configuration of Figure 3.23 a number of samples were imaged using the different imaging modalities and images acquired based on expected sample contrast. For example, a standard sample of polystyrene beads with 40 $\mu$m diameter was imaged by CARS around 3050 cm$^{-1}$ where there is a strong polystyrene Raman resonance. By temperature tuning the wavelength of the seed laser diode as well as the OPA and SHG PPLN crystals it was possible to recreate part of this resonance curve (Figure 3.26) in the range between 3056 cm$^{-1}$ to 3105 cm$^{-1}$.

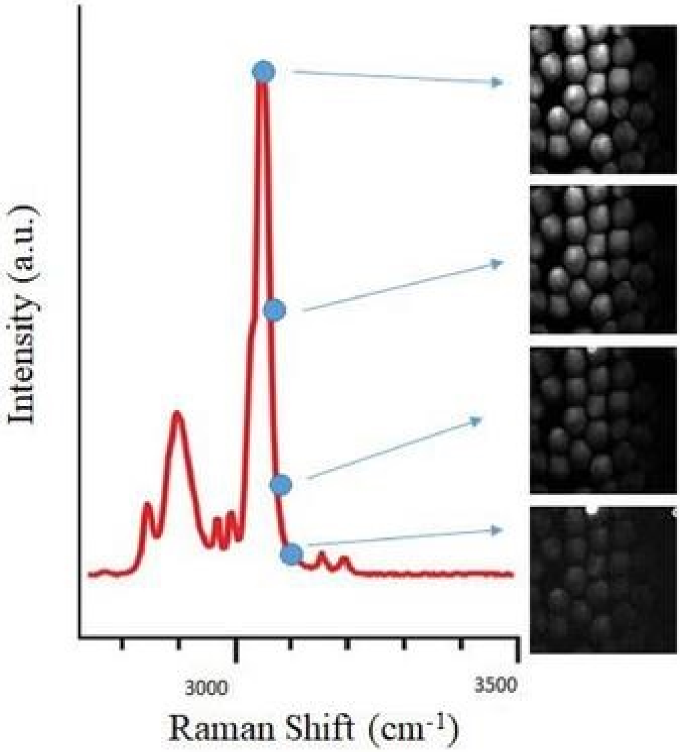

Figure 3.26: Recreated high frequency Raman resonance of polystyrene; (red curve Spontaneous Raman spectrum of polystyrene, blue dots normalised CARS signal extracted from indicated images of 40 $\mu$m polystyrene beads at frequencies 3056, 3072, 3088, 3105 cm$^{-1}$ respectively). This figure has been reproduced from my own publication [18].

### 3.4.4 Biological imaging results

Furthermore, the tail of the phospholipids Raman resonance at high frequencies ($> 3050$ cm$^{-1}$) was exploited in order to image cell membranes of adipose tissue (Figure 3.27(a)). As these frequencies are relatively distant from the 284 cm$^{-1}$ resonance of other lipids such as triglycerides and cholesterol which form globular shapes in the adipose tissue, these features appear as dark circular areas between the areas with the cell membranes.

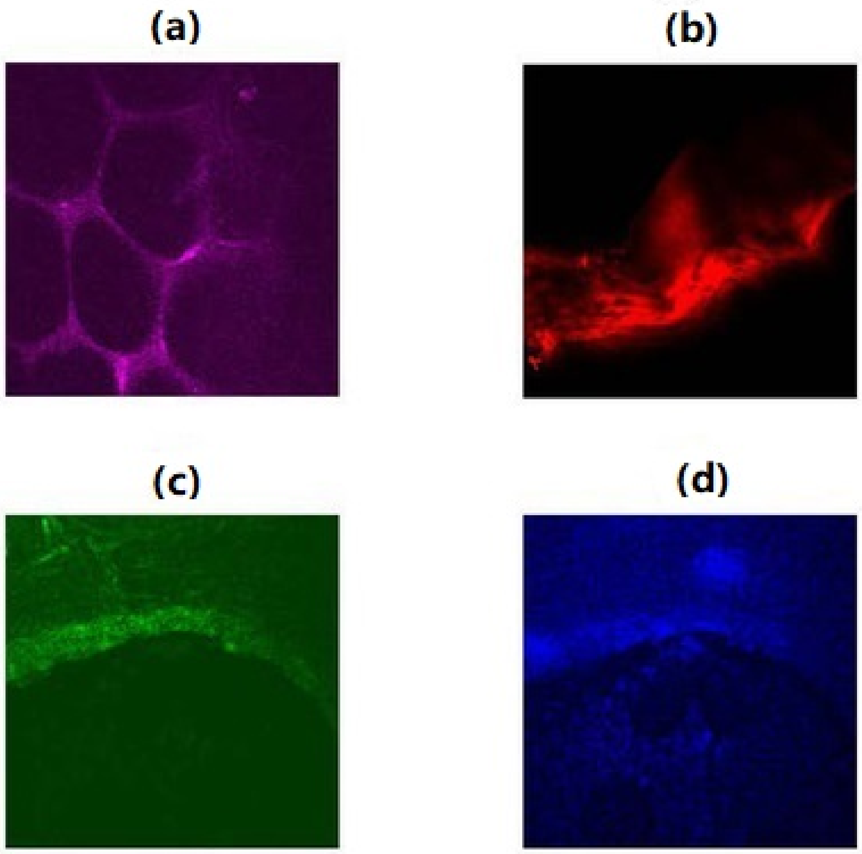

Figure 3.27: (a) CARS image at 3056 cm$^{-1}$ of areas with cell membranes in adipose tissue, the dark areas correspond to globular lipid structures of triglycerides and cholesterol. (b) SHG image of collagen fibres in rat tail tendon. (c) SHG image of bone. (d) TPEAF image of bone marrow. This figure has been reproduced from my own publication [18].

To illustrate the SHG imaging capabilities of the source a rat tail tendon sample was imaged where the fibrillar structure of collagen can be clearly distinguished (Figure 3.27(b)). Similarly a bone sample was imaged via the means of SHG imaging while the bone marrow encircled in the bone structure was imaged using the TPEAF modality (Figure 3.27(c) and (d) respectively).

## 3.5 Combined with OPO targeting finger-print region

### 3.5.1 Introduction

Due to its simplicity and low cost the OPA light source can be also used as an easy add-on to an existing OPO setup as shown in Figure 3.28, facilitating access to the fingerprint region and at the same time keeping the anti-Stokes wavelengths in the high sensitivity spectral range of the detectors.

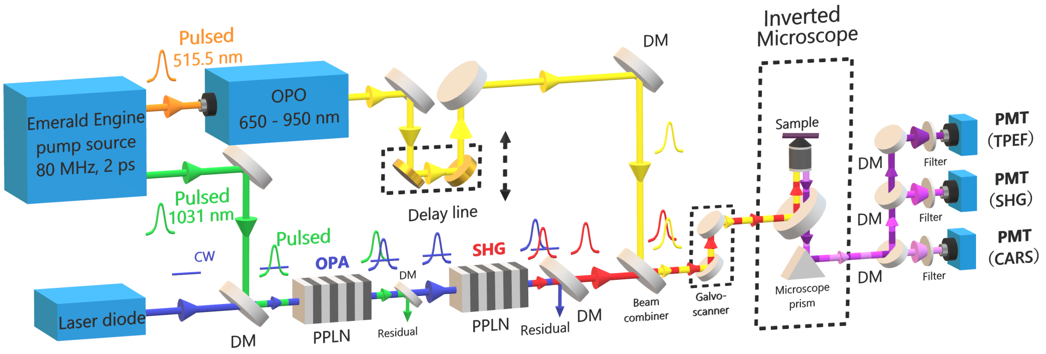

Figure 3.28: Schematic of the experimental system used for multimodal CARS. OPO, optical parametric oscillator; DM, dichroic mirror; PPLN, periodically-poled lithium niobate; PMT, photomultiplier tube. This figure has been reproduced from my own publication [18].

This layout as shown in Figure 3.28, consists of a Levante Emerald OPO (650 – 950 nm) which is synchronously pumped by the second harmonic output (515.5 nm) of the Emerald Engine solid state laser source. The signal output of the OPO is used as the Stokes for CARS imaging. Similarly as in Figure 3.23 and as shown in Figure 3.28 a fraction of the fundamental (1031 nm) of the Emerald Engine is used for pumping the OPA whose frequency doubled signal is used again as the CARS Pump. In the same way as described earlier for the high frequency setup, the CARS Pump and Stokes of this setup, are coupled into the laser scanning microscope and they overlap spatially and temporally on the sample. A wide range of vibrational frequencies from 340 to 2400 cm$^{-1}$ (most of the fingerprint region) can be covered with this layout, limited only by the availability of filters and the detector range.

### 3.5.2 Biological imaging results

In order to demonstrate the imaging capabilities of the OPA light source in the fingerprint region the configuration of Figure 3.28 was used. With this setup by tuning the OPA signal wavelength at 1564 nm and consequently its second harmonic at 782 nm (CARS pump) and the OPO signal at 845.5 nm (CARS Stokes), images of animal bone at the resonance frequency (960 $\mathrm{cm}^{-1}$) of apatite were acquired as shown in Figure 3.29(a). The corresponding anti-Stokes wavelength was 727.4 nm which is well within the detection range of our detectors (Hamamatsu H10722-20). In contrast, if instead in order to target the above mentioned apatite resonance, the OPO had been paired with the fundamental (1031 nm) of the Emerald Engine then the corresponding anti–Stokes wavelength would have been at 860.5 nm. The anode radiant sensitivity of the detector drops by almost an order of magnitude and this would result in a significant reduction of the quality of imaging at this vibrational frequency.

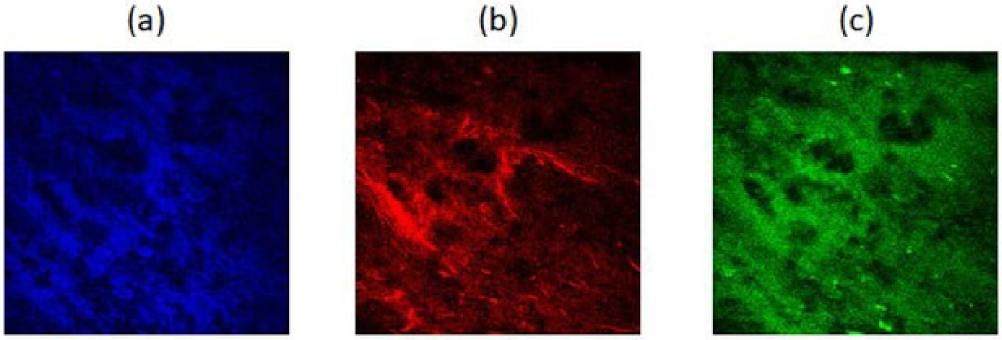

Figure 3.29: (a) CARS image of animal bone using the finger-print region OPA setup at 960 $\mathrm{cm}^{-1}$ (apatite resonce). (b) SHG/SFG and (c) TPEAF images of the same sample respectively. This figure has been reproduced from my own publication [18].

Regarding the other modalities, this setup can facilitate the acquisition of a composite Second Harmonic Generation and Sum Frequency Generation (SHG/SFG) image as depicted in Figure 3.29(b) and TPEAF image as shown in Figure 3.29(c). In more detail the SHG (which is a degenerate case of SFG) component of the image in Figure 3.29(b) appears at 392 nm (SHG of 784 nm CARS pump) while the SFG component which exhibits very strong delay dependence appears at 407 nm (non–degenerate sum frequency of CARS pump and CARS Stokes wavelengths).

## 3.6 Summary and future work

In summary, I have shown the demonstration of a compact and reliable, tunable, CW seeded synchronization-free PPLN OPA with a robust, commercial picosecond pump laser. This laser and OPA combination is shown to be well suited for label-free CARS and concurrent SHG and two-photon fluorescence microscopy in an epi detection geometry. Rapid and accurate tuning between Raman resonances was achieved by changing the channels and temperatures of OPA and SHG crystals concurrently with tuning the CW OPA seed wavelength. The corresponding pump-Stokes frequency detuning range was from 2700 to 3200 $\mathrm{cm}^{-1}$, thus fully covering the C-H stretching band that is typically used for the imaging of lipids. The epi-detection capability with an OPA-based setup demonstrates the relevance to biological and clinical samples without the need for extensive sample preparation which would be required to create the thin sections normally used with forward detection. I also presented a similar OPA but seeded by a CW laser diode source which costs much less than a tunable laser source seed. This OPA was a versatile light source module that can be tailored to the tunability and affordability requirements of the specific application. I demonstrated that it can be used either on its own as a light source or in association with an OPO for multimodal CARS microscopy corresponding to a Pump-Stokes frequency detuning range from 340 to 2400 $\mathrm{cm}^{-1}$ which covers the finger-print region.

By combining elements of multiphoton techniques in an inexpensive and compact configuration, our work paves the way for the simple implementation of multimodal CARS with concurrent SHG/TPEF imaging capability. Power level, spectral resolution and dwell times are all comparable with previous reports [175], while utilizing a much simpler setup. In principle, the costs of the system could be further reduced and the tuning range increased by switching to a switchable array of seed diodes as these are readily available in the telecoms wavelength range. This stepping stone points to a lower cost future route to translation of nonlinear laser microscopy imaging for biomedical research and imaging based diagnostics in the clinic. The next steps in the translation of the nonlinear source to clinics and hospitals will involve progressing the system into a robust prototype that can operate in a non-specialised environment. Additionally we will need to progress with clinical feasibility studies with such a microscope system based on the developed laser to demonstrate reproducible performance and visualisation ability for improved diagnosis.

The paper named ‘Widely-tunable synchronisation-free picosecond laser source for multimodal CARS, SHG and two-photon microscopy’ has been accepted and published [207].

The OPA system is continuing to be used for other imaging works in the IfLS after this project. IfLS has ordered several new laser diodes as seeds of the OPA to extend the wavelength tuning range. In the future, IfLS might take over this OPA system of mine and apply it to SRS by other researchers as this next work is primarily related to bioimaging and has little to do with light source development itself. I consider this is a strong validation of the value of the source I have developed and a significant outcome from my project.

# Chapter 4

# 1840-nm femtosecond thulium fibre laser system for label-free third-harmonic generation microscopy

## 4.1 Introduction

In this Chapter, an all-fiberized 1840-nm thulium fibre laser source comprising a dissipative soliton mode-locked seed laser and a chirped-pulse-amplification (CPA) system has been developed and applied for label-free biological imaging through multiphoton microscopy. This work is part of EPSRC funded project 'Lighting the Way to a Healthy Nation - Optical 'X-rays' for Walk Through Diagnosis & Therapy'. The laser development work was undertaken and completed by me and Lin Xu together. The microscope related imaging experiments and data/bio-imaging processing were carried out by me and Konstantinos N. Bourdakos. The imaging samples were prepared by Peter Johnson and Anna Crisford.

## 4.2 Background

Nonlinear optical microscopy using short-pulsed fibre lasers has been widely used for biological imaging research because it allows for minimal invasion, fast speed and high resolution imaging based on various well-established techniques [212, 220]. Femtosecond lasers from ytterbium and neodymium fibre systems operating in the near infrared (NIR) region at wavelengths around 1 $\mu$m have shown good performances in biological imaging based on two-photon excitation microscopy (TPM) and second-harmonic generation

(SHG) microscopy [31, 151]. In contrast to TPM and SHG microscopy, higher-order nonlinear optical microscopy, such as three-photon excitation microscopy (3PM) and third-harmonic generation (THG) microscopy, provide high signal-to-background ratios and deep penetration [67, 81] when using femtosecond excitation pulses in the short-wave infrared (SWIR) region from 1700 nm to 1870 nm. This is due to this wavelength region providing the window in which the sum of absorption and scattering is minimized from most biological tissues. Solid-state laser sources based on optical parametric oscillator or amplifier techniques involving high-power NIR femtosecond Ti:sapphire lasers and nonlinear frequency converters have been used to demonstrate such higher-order nonlinear optical microscopies with good achievements made [148, 131]. Compared to such complex and bulky solid-state lasers, fibre lasers offer significant advantages of high efficiency, good compactness and robustness as well as good beam quality. Frequency conversion of 1.5-$\mu$m femtosecond erbium fibre lasers to this wavelength region by soliton self-frequency shifting inside a nonlinear optical fibre can generate wavelengths within this SWIR region. However, this technique has a relatively low energy-conversion efficiency and the output wavelength and pulse energy are highly sensitive to the coupling efficiency into the nonlinear fibre [106, 193]. We are targeting around 1840 nm because this wavelength has the best feedback from the tissue (especially human bone) and relatively low water absorption.

Thulium-doped fibre (TDF) exhibit a broad emission spectrum, spanning from 1600 nm to 2100 nm covering the entire SWIR region and hence represents an attractive gain medium for femtosecond fibre lasers that have potential in such imaging applications [191, 110]. Generally, silica-glass based TDF lasers operate at wavelengths beyond 1900 nm, where the emission cross sections of $Tm^{3+}$ ions in silica are large and high optical gain can be obtained. A TDF laser system generating 297 fs pulses at 1925 nm with a pulse energy up to 1.27 $\mu$J has been demonstrated [158]. However, it is challenging to operate the short-pulsed TDF laser at the SWIR wavelengths with high pulse energy due to the quasi-three-level nature of the thulium laser and the need for careful management of nonlinearity, dispersion and spectral filtering in such laser system. A mode-locked (ML) TDF laser operating at 1746 nm has been reported but with a low power efficiency generating a pulse energy of only 0.2 nJ, based on nonlinear polarization rotation (NPR), and which usually results in poor self-starting of the mode-locked laser [33]. Through the development of a dispersion engineered TDF, a mode-locked laser operating in the 1.7 - 1.8 $\mu$m region has been demonstrated and a pulse energy of 128 nJ obtained in a fibre amplifier system [34]. However, the system required a complicated fibre geometry design and fabrication process that could prevent wider application. Instead of using silica-glass TDFs, a 1820-nm fibre laser with pulse energy of 1.1 $\mu$J was developed by using fluoride-glass TDFs and 3PM imaging of mouse brain by using such laser was demonstrated [143]. However, a key challenge is the ability to splice the fluoride-glass TDFs used in that system to other silica-glass fibre components, hence, as a consequence, the system is bulky and involves significant free-space alignment. In addition, special preparation of biological samples is required, in which a fluorescent protein is transfected to facilitate the 3PM imaging. Here we report the development of an all-fiberized 1840-nm femtosecond laser system based on standard silica-glass TDFs and demonstrate a proof-of-principle study of its application in label-free THG microscopy of biological samples from hard and soft tissues.

## 4.3 Fibre laser source

### 4.3.1 Introduction

In this section, I showed the laser development part in the ORC lab. It includes a 1840-nm Thulium-doped fibre dissipative-soliton mode-locked seed laser and a dual stage CPA (Figure 4.1).

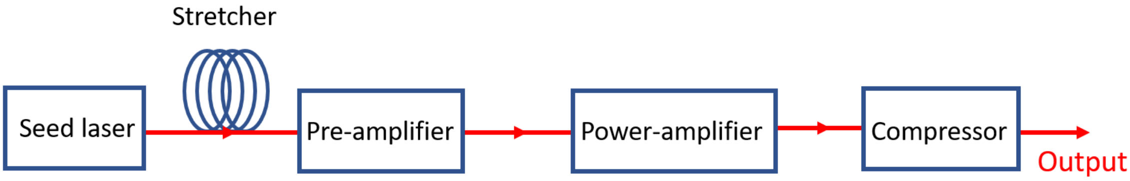

Figure 4.1: Schematic of the fibre laser source.

### 4.3.2 Mode-locked Thulium-doped fibre laser

Here I introduce the seed laser development. The target of this seed is to get dissipative soliton mode locking with a central wavelength around 1840 nm and an output power >10 mW. A schematic of the mode-locked cavity is shown in Figure 4.2. A unidirectional ring cavity consisting of a length of single-mode TDF (OFS, TmDF200) as the gain medium, pumped by a 1565 nm diode laser (Princeton Lightwave, DEI14919) through a 1560 nm / 1840 nm wavelength-division multiplexer (WDM). A semiconductor saturable absorber mirror (SESAM) with a non-saturable reflection of 60% and a modulation depth of 20% (Batop, SAM-1920-36-10ps) was attached to the fibre end of a polarization-dependent (PD) circulator, which ensured unidirectional oscillation in the cavity. To compensate for the anomalous dispersion of the single-mode fibres (SMF) in the cavity, a length of dispersion-compensating fibre (DCF) (Coherent, UHNA4) was employed to provide an overall net normal dispersion for the targeted dissipative-soliton mode locking operation. Two in-line polarization controllers (PC) were used to adjust the polarization state of the intra-cavity pulses generating Lyot filtering effects and stabilizing the mode locking in the cavity [158]. An output coupler with a 50% transmission was used to extract the laser output. The laser cavity was placed on a metal plate with a size of 30 cm (long) and 19 cm (wide), as shown in Figure 4.3. All fibres and components were carefully taped and fixed on the plate to ensure stable mode locking operation.

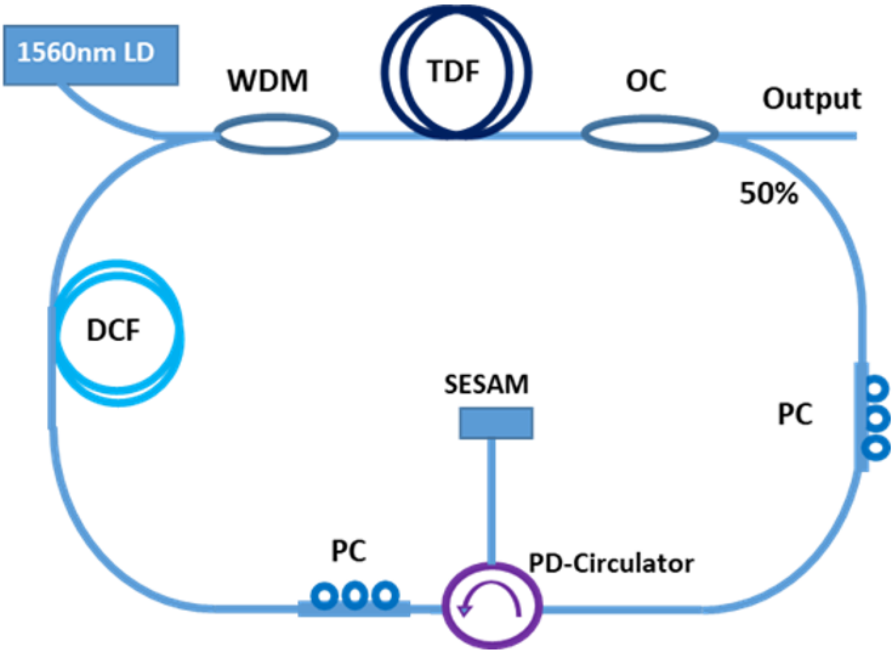

Figure 4.2: Schematic of the mode-locked thulium fibre laser cavity. WDM: wavelength-division multiplexer; TDF: thulium doped fibre; OC: output coupler; SMF: single mode fibre; PC: polarization controller; PD-Circulator: polarization dependant circulator; DCF: dispersion compensate fibre; LD: laser diode.

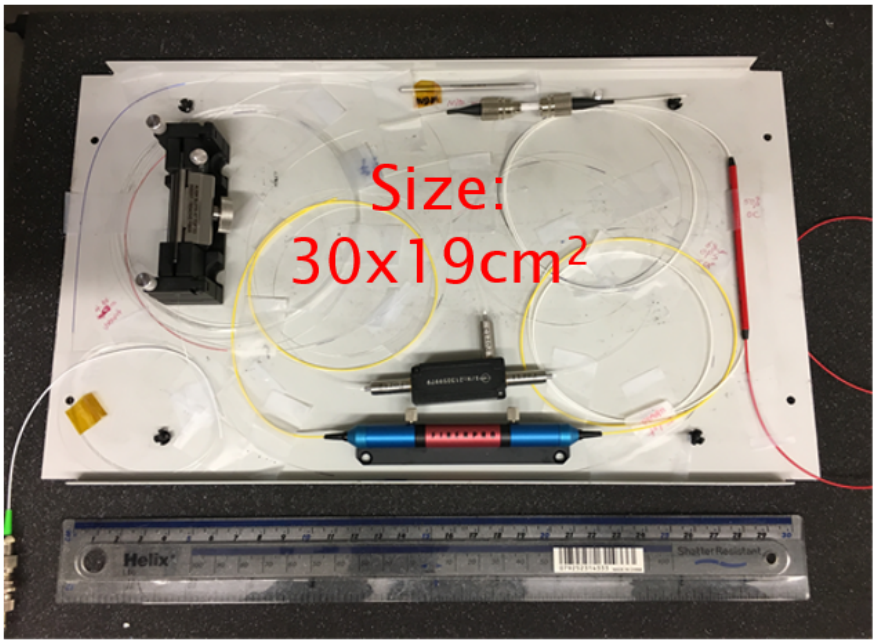

Figure 4.3: Photo of the mode-locked seed laser.

The TDF had an absorption coefficient of 20 dB/m at the pump wavelength, and a length of 1.3 m was initially chosen in order to favor laser operation at the short wavelength end of the thulium emission bandwidth. The total lengths of the SMF and DCF used in the cavity were measured to be 6.2 m and 5 m, respectively. Considering the group-velocity dispersion of the fibres used in the cavity at the laser wavelength (SMF: -0.06 ps$^2$/m, TDF: -0.02 ps$^2$/m, DCF: +0.093 ps$^2$/m), the net cavity dispersion was estimated to be 0.07 ps$^2$. With proper adjustment of the PCs in the cavity, self-starting, single-pulse, stable mode locking was observed at a pump power of 150 mW. The output pulses had a repetition rate of 16.36 MHz, which was consistent with the cavity length. The output spectrum was measured showing a central wavelength at 1900 nm. In order to characterize the influence on the operating wavelength and optimize the gain fibre length, the mode locking was tested by shortening the TDF length and the corresponding output spectra are shown in Figure 4.4. The central wavelength of the mode-locked laser could be effectively shortened by using a shorter length of TDF due to the quasi-three level system of the thulium ions [46]. The influence of the net dispersion on the output spectral bandwidth was also characterized by fixing the TDF length while changing the length of DCF. Figure 4.5 shows the results, in which a smaller net normal dispersion resulted in a broader output spectrum that would generally produce shorter pulses after de-chirping.

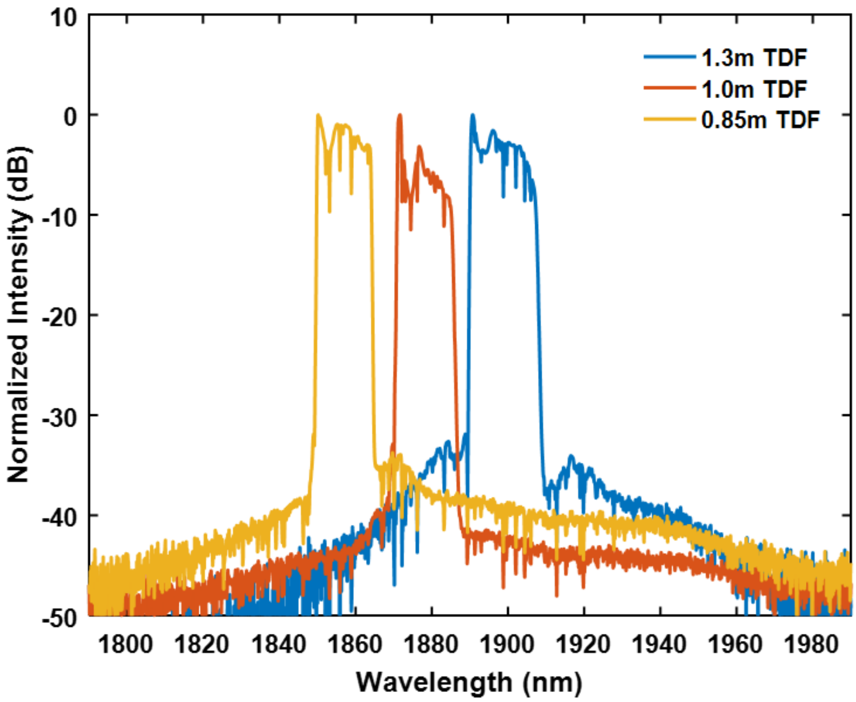

Figure 4.4: Output spectrum of the mode-locked fibre laser with varying the length of TDF.

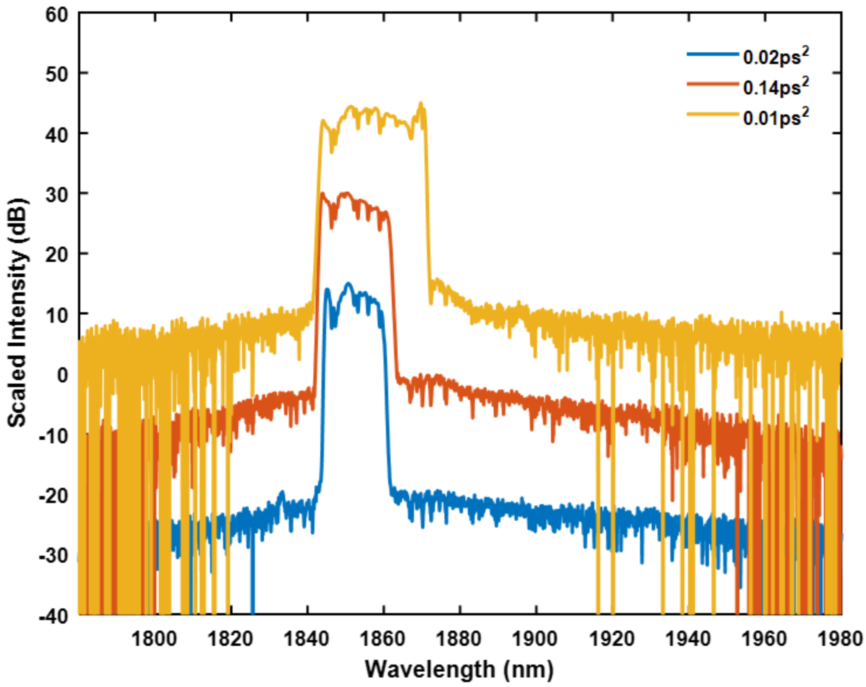

Figure 4.5: Output spectrum of the mode-locked fibre laser with changing the net cavity dispersion.

In order to achieve the target operating wavelength of 1840 nm, a TDF length of 0.7 m and net cavity dispersion of $\sim 0.01$ ps$^2$ were chosen for the mode-locked laser. The mode locking output spectrum had a central wavelength of 1840 nm and 10-dB spectral bandwidth of 22 nm. The output pulse was measured to have an auto-correlation width of 9 ps corresponding to a Gaussian pulse with a width of 7 ps, as shown in Figure 4.6. The output power of the mode-locked laser increased with the pump power at a slope efficiency of 17%, reaching a maximum of 17 mW at the maximum available pump power from the 1565-nm LD, as shown in Figure 4.7. The RF spectrum measurement of the output pulses shows a fundamental frequency of 16.6 MHz and an signal-to-noise ratio of 70 dB, as shown in Figure 4.8.

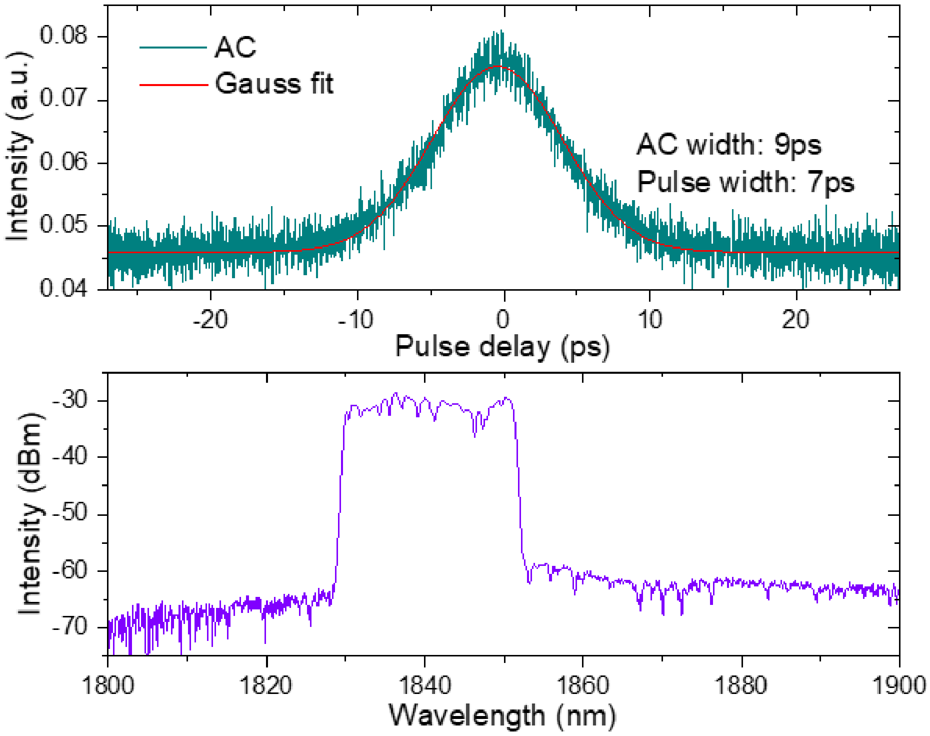

Figure 4.6: Autocorrelation trace (AC) and spectrum measurement of the 1840 nm mode-locked fibre laser.

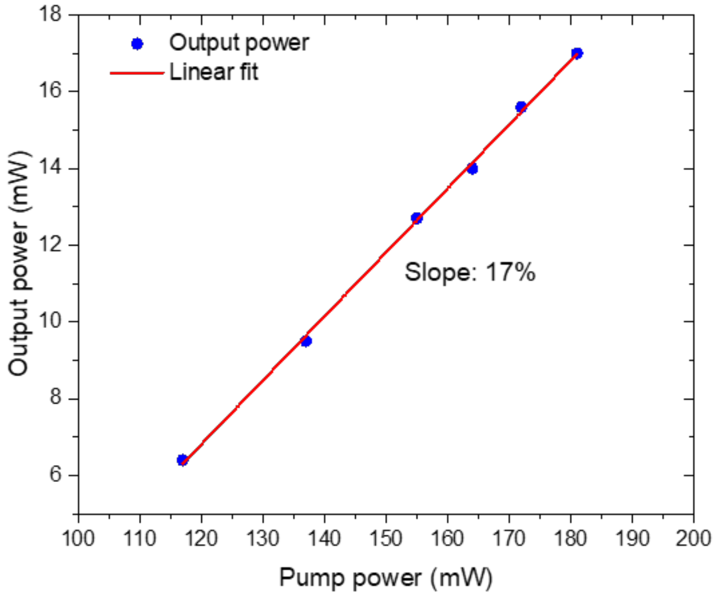

Figure 4.7: Output power vs pump power of the 1840-nm mode-locked fibre laser.

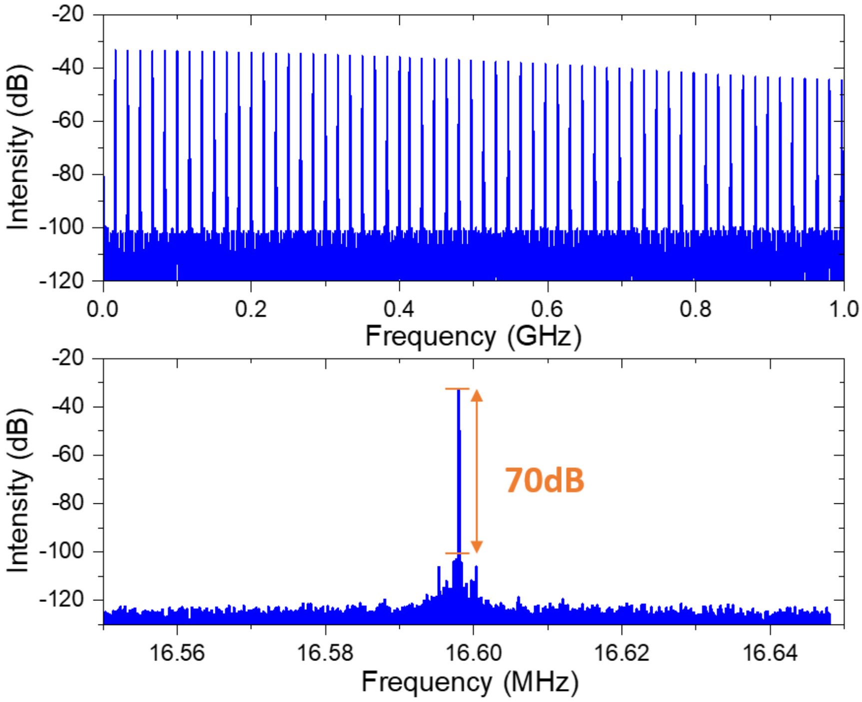

Figure 4.8: RF spectrum measurement of the 1840-nm mode-locked fibre laser.

### 4.3.3 Thulium-doped fibre amplifiers

#### 4.3.3.1 Stretcher and pre-amplifier

After the seed laser, pulses will be stretched by a stretcher and then amplified by a pre-amplifier. After the fiberized isolator, the output pulses from the mode-locked laser were attenuated to an average power of 5 mW and passed through a 23-m-length of DCF (Coherent, UHNA4) to stretch the pulse width to 18 ps shown in Figure 4.10. 23-m-length of DCF is a reasonable choice because it will stretch the pulse to $\sim$ 20 ps so the pulse can be amplified efficiently and avoid nonlinear distortion in the following fibre amplifiers. In addition it doesn't require too long distance in the compressor to compress the pulse back to femtosecond level.

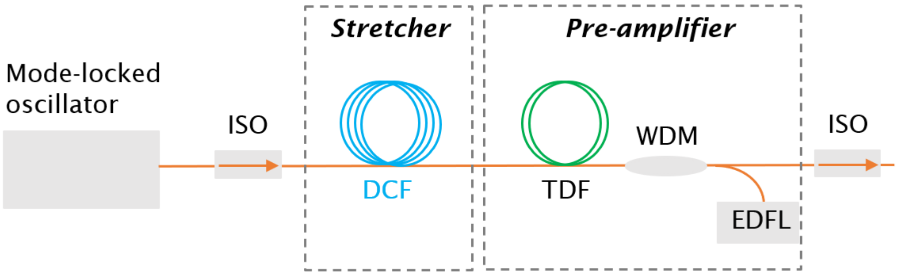

Figure 4.9: Schematic of the stretcher and pre-amplifier.

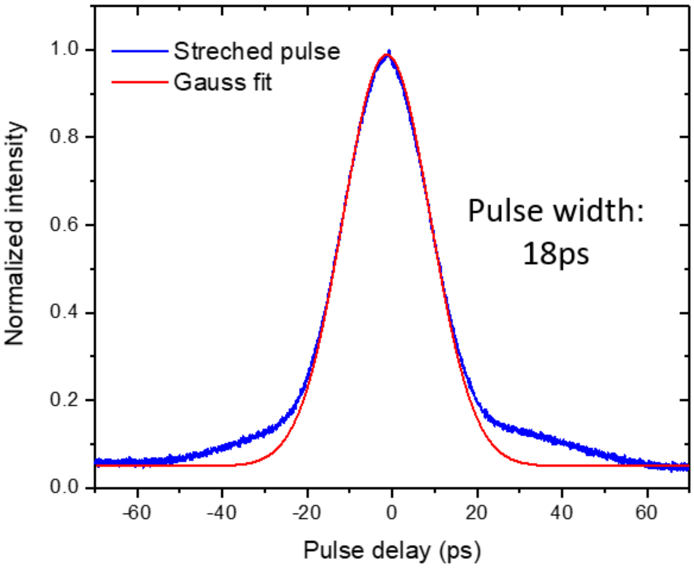

Figure 4.10: Autocorrelation trace of the stretched pulse.

To develop the TDF pre-amplifier, an 1565 nm EDFL (shown in Figure 4.11) was built as a pump source. The EDFL was pumped by a wavelength-stabilized 976 nm laser diode (BL976-PAG900, Thorlabs) with a maximum power of 900 mW. The output power verus pump current of the laser diode was characterized and shown in Figure 4.12. In-house fabricated single-mode erbium-doped fibre (EDF) was used as the gain medium. Two fibre Bragg gratings (FBGs) with reflectivities of 99.9% and 6%, respectively, were employed as cavity mirrors. In order to find the optimum gain fibre length for the EDFL, different lengths of 5 m, 6 m and 7 m were tested with the output power performance showing in Figure 4.13. It can be found that the EDFL, with using 6 m length EDF provided the best result, offered output power slope efficiency of 36% reaching a maximum power of 300 mW. It is a reasonable good efficiency. The output spectrum of the EDFL at the maximum power had a central wavelength of 1565 nm and a 3-dB linewidth of 0.1 nm, as shown in Figure 4.14.

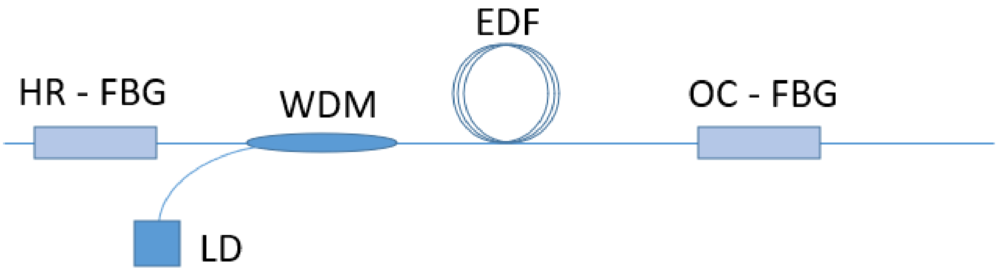

Figure 4.11: Schematic of the homemade EDFL.

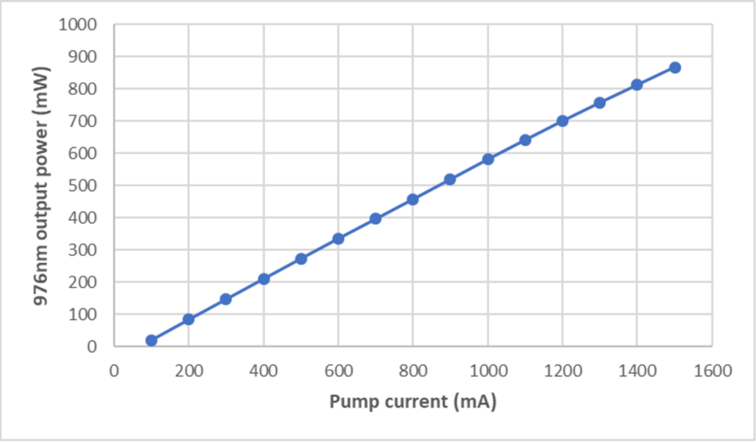

Figure 4.12: LD output vs current.

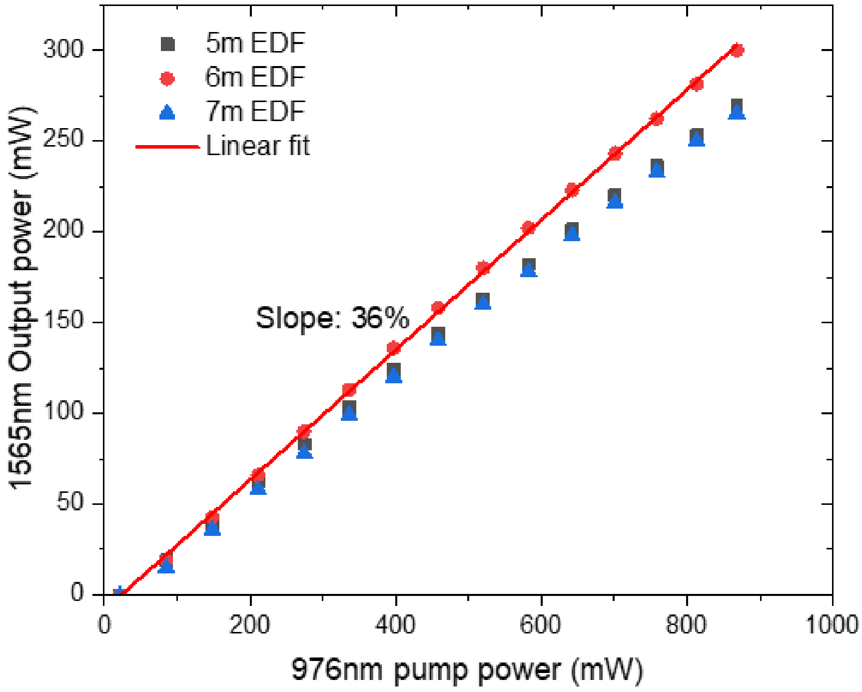

Figure 4.13: Output power vs pump power of the homemade EDFL by varying the length of EDF.

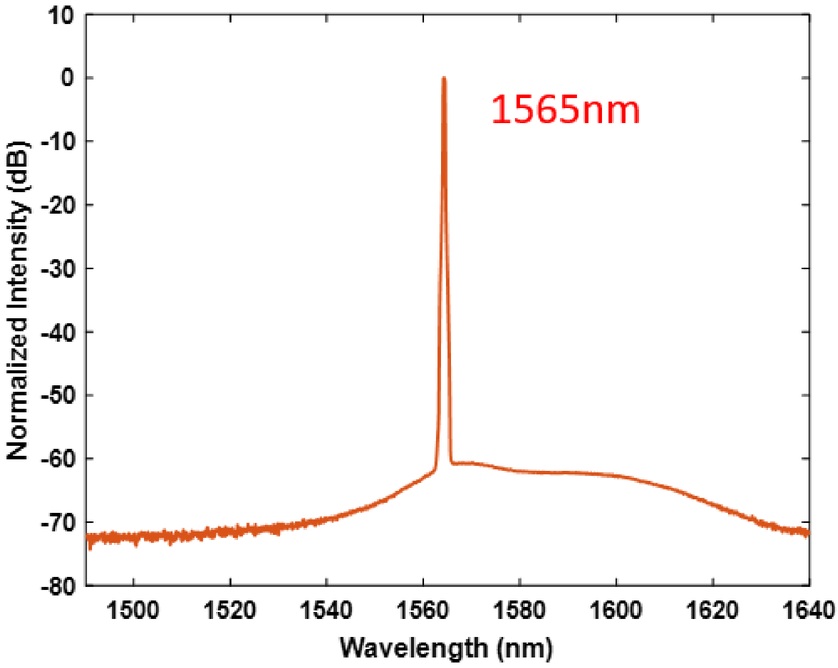

Figure 4.14: Output spectrum of the homemade EDFL

The fibre pre-amplifier shown in Figure 4.9 consisted of a 1-m-length of TDF (OFS, TmDF200) backward-pumped by a home-built 1565-nm Erbium-doped fibre laser (EDFL). Core-pumping solution was used to get compact device and low noise level. At a maximum pump power of 300 mW, the first fibre amplifier generated an average power of 50 mW at the output.

#### 4.3.3.2 Power amplifiers and compressor

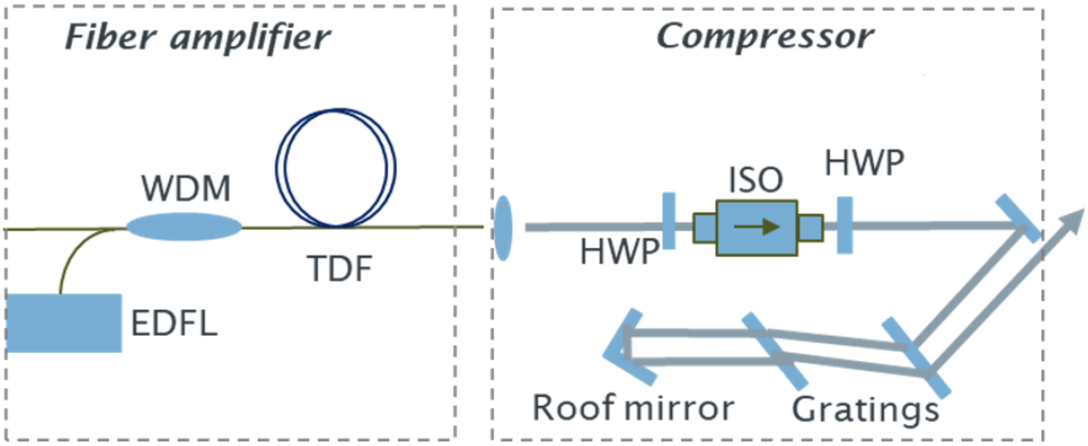

Figure 4.15: Schematic of the fibre amplifier and pulse compressor.

In the second fibre amplifier, single-mode TDFs with bigger cores were required to realize Watt-level output powers without nonlinear distortion. Firstly, a commercial TDF with a core diameter of 9 $\mu$m (Coherent, TSF-9/125) and a core absorption of 12 dB/m at 1550 nm was used and core pumped by a 1550-nm EDFL with a maximum available power of 10 W. Core-pumping leads to a shorter length of fibre and lower noise level compared to cladding pumping. To optimize the gain fibre length for the second fibre amplifier, three different lengths of the TDF (1.9 m, 2.3 m and 2.9 m) were selected and tested for their output power performance. As shown in Figure 4.16, the 2.3-m-TDF amplifier provided a power slope efficiency of 37% and a maximum output power of 2.1 W at a pump power of 6 W. However, the output spectrum showed significant nonlinear distortions with increasing power, as shown in Figure 4.17, which is probably due to modulation instability in the anomalous dispersion region.

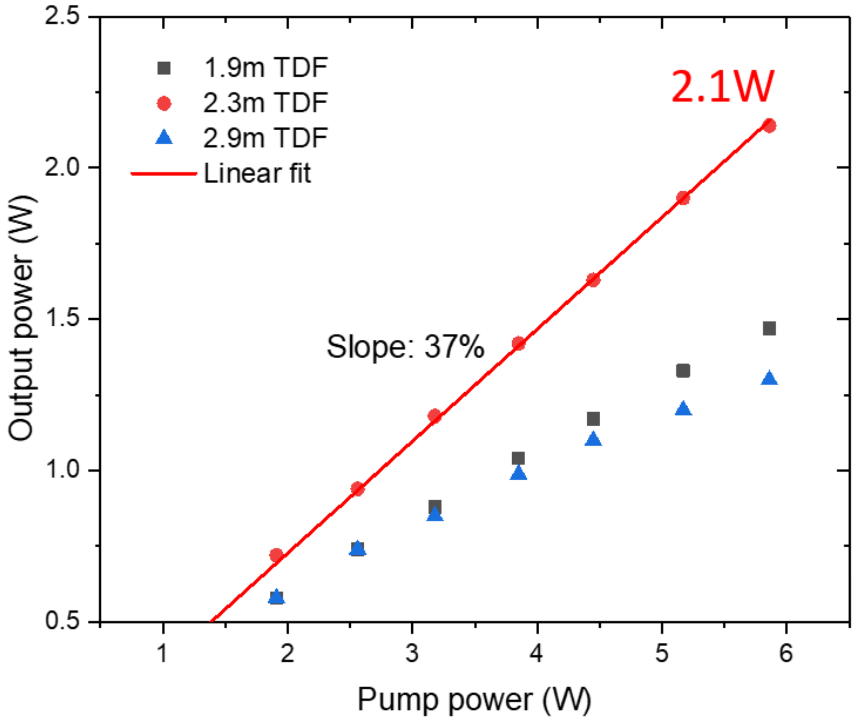

Figure 4.16: Output power measurement of the second fibre amplifier with the 9-$\mu$m core diameter TDF.

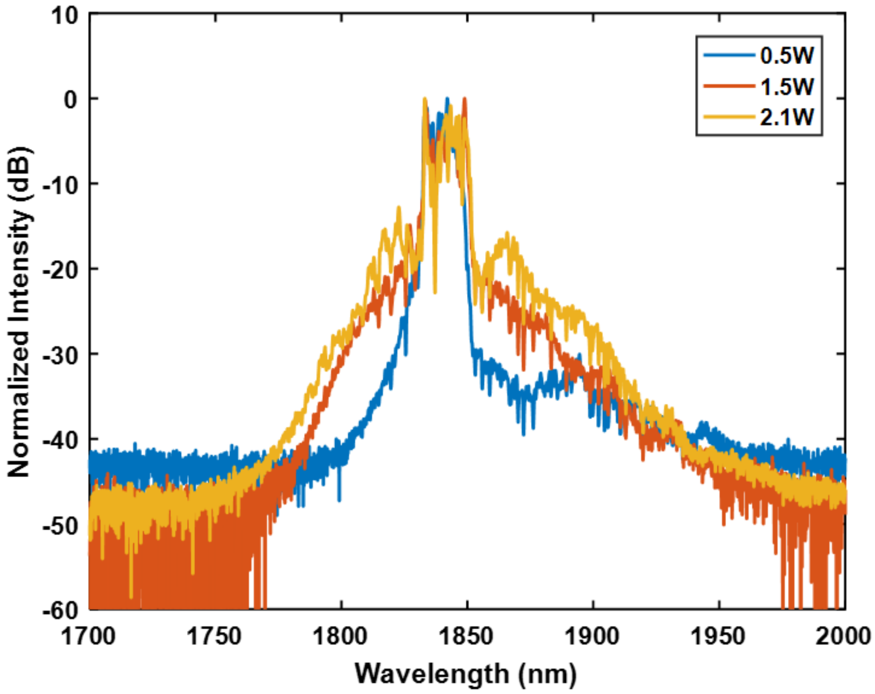

Figure 4.17: Spectral measurement of the second fibre amplifier with the 9-$\mu$m core diameter TDF.

The pulses then passed through a free-space isolator, as shown in Figure 4.15. The loss of the isolator is measured to be 1.67 dB.

After passing through a free-space isolator, the output beam was collimated and delivered into a pulse compressor, which consisted of a pair of fused silica transmission gratings with groove density of 560 lines/mm and a roof mirror (shown in Figure 4.15). The combined loss of the isolator and pulse compressor was measured to be around 3 dB. The auto-correlation measurement of the compressed pulses at the maximum power is shown in Figure 4.18. The Gaussian fitted pulse width is calculated to be 705 fs, however, a large pedestal of the auto-correlation trace indicates the strong nonlinear effects result in the pulse distortion and degrade the pulse quality.

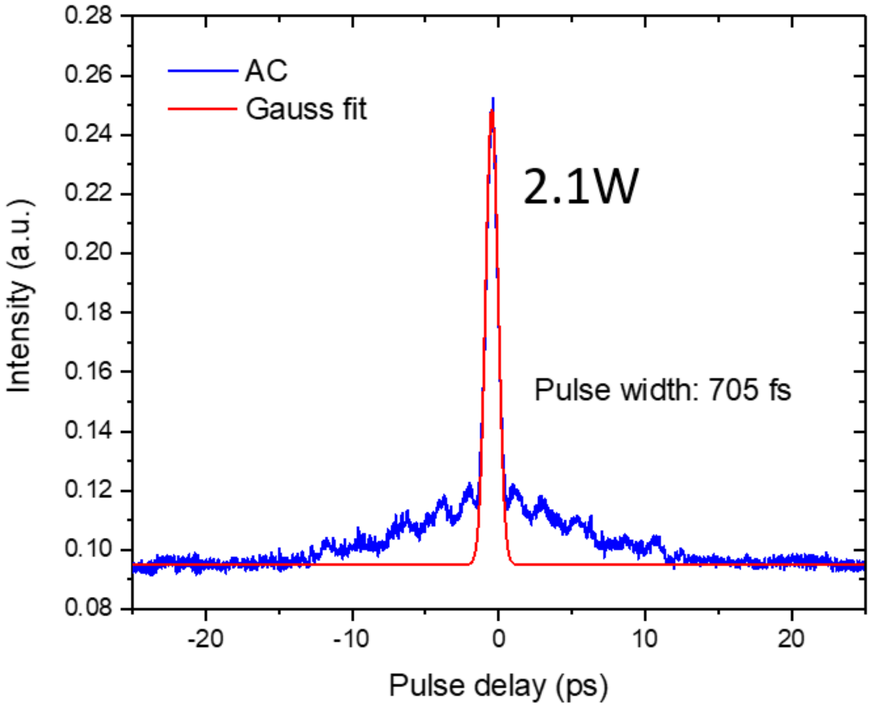

Figure 4.18: Auto-correlation measurement of the second fibre amplifier with the 9-$\mu$m core diameter TDF.

In order to eliminate the nonlinear distortion, an in-house designed and fabricated single-mode TDF, which had a larger core size of 10 $\mu$m and a higher absorption of 37 dB/m at the pump wavelength, was employed to allow a shorter length of TDF in the fibre power amplifier [22] to reduce even eliminate the nonlinear distortion. By characterizing the amplifier power performance with different lengths of TDF (0.5 m, 0.7 m and 1 m), as shown in Figure 4.19, an optimum length of 0.7 m was chosen for the fibre amplifier.

The output power increased with the pump power at a slope efficiency of 44% and reached a maximum of 2.5 W at a pump power of 6 W, corresponding to a maximum pulse energy of 150 nJ. In comparison to the previous results, the slope efficiency and maximum output power are better, the output spectrum in Figure 4.20 did not exhibit obvious nonlinear distortion at such power levels.

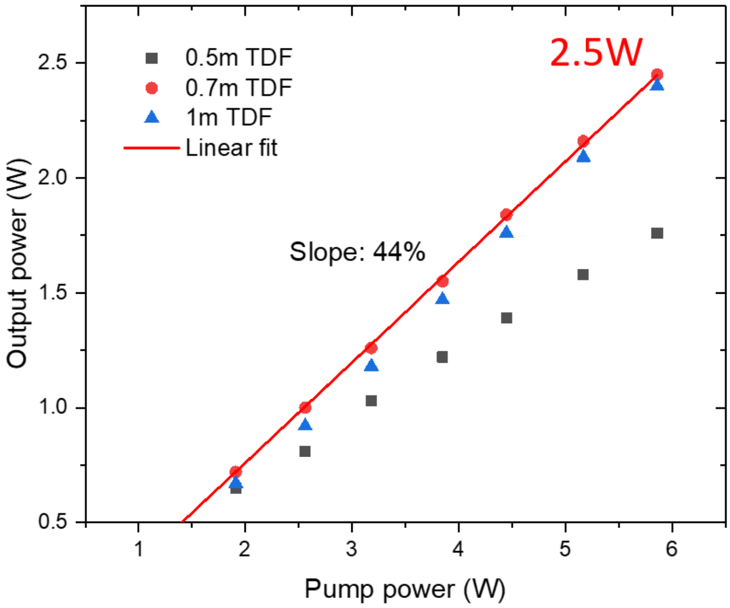

Figure 4.19: Output power measurement of the second fibre amplifier with the 10-$\mu$m core diameter TDF.

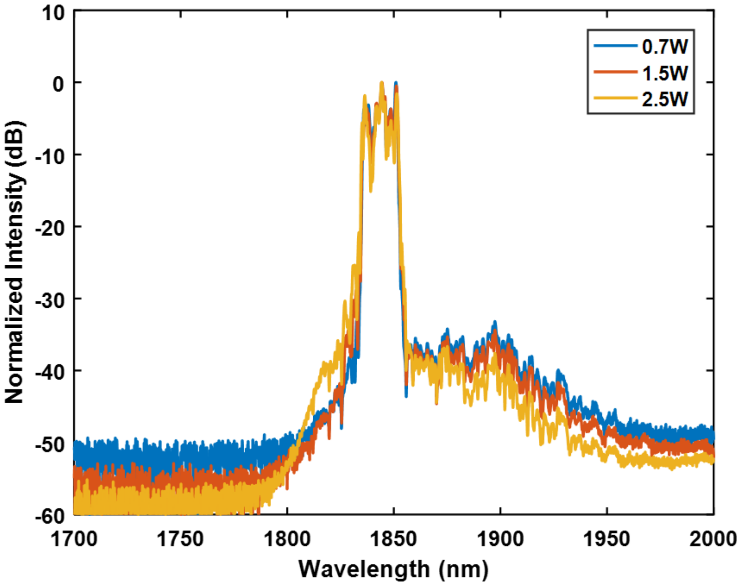

Figure 4.20: Spectral measurement of the second fibre amplifier with the 10-$\mu$m core diameter TDF.

The output beam was collimated and delivered through a free-space isolator into a pulse compressor. The auto-correlation measurement of the compressed pulses is shown in Figure 4.21, which exhibited a pulse width of 416 fs by a Lorentzian fit or 582 fs by a Gaussian fit. Due to the non-PM fibres used in the fibre amplifiers, the polarization of the output beam from the power amplifier was not linear which resulted in a loss by passing through the free-space isolator.

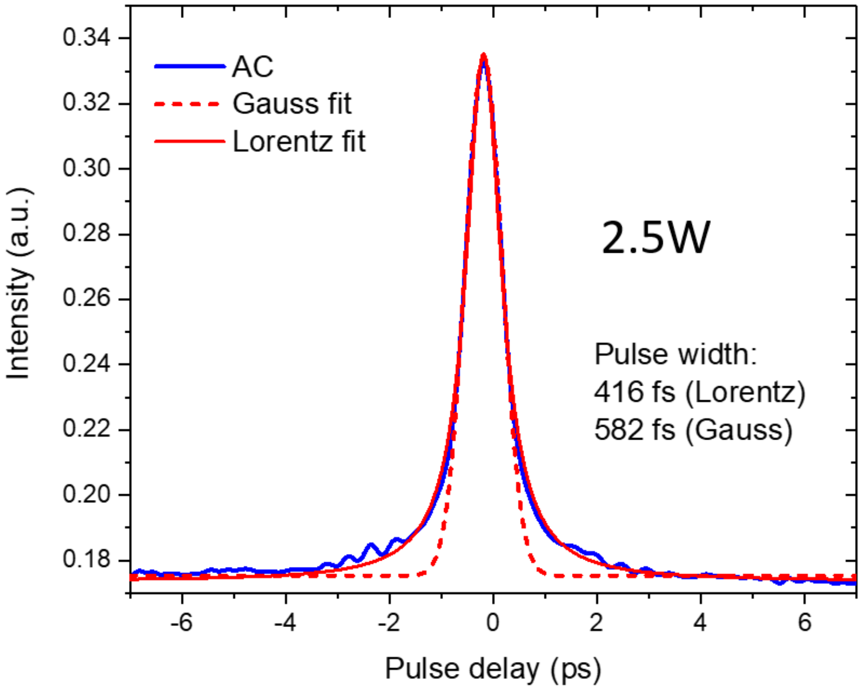

Figure 4.21: Auto-correlation measurement of the second fibre amplifier with the 10-$\mu$m core diameter TDF.

The assembled laser system has a size of 60cm in length, 30cm in width and 35cm in height, as shown in Figure 4.22 and Figure 4.23. Layout of all the components in the two layers is showed in Figure 4.24. The laser system was moved to IfLS building and integrated into the multi-photon imaging microscopy in the IfLS bio-imaging lab.

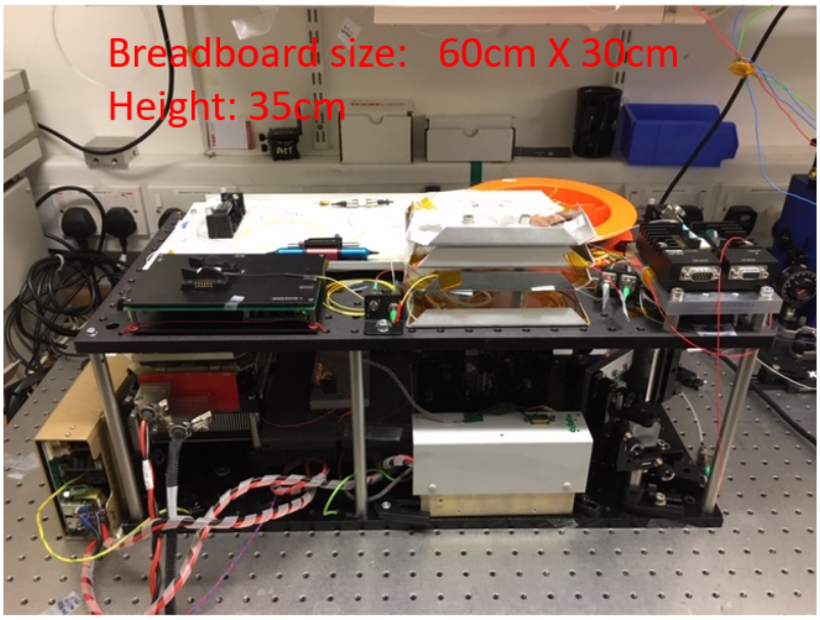

Figure 4.22: Photo of the system.

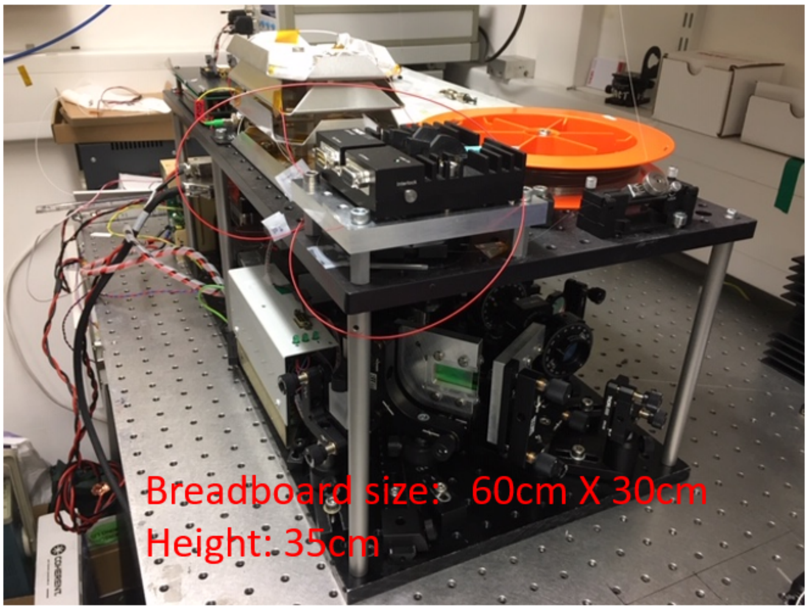

Figure 4.23: Photo of the system.

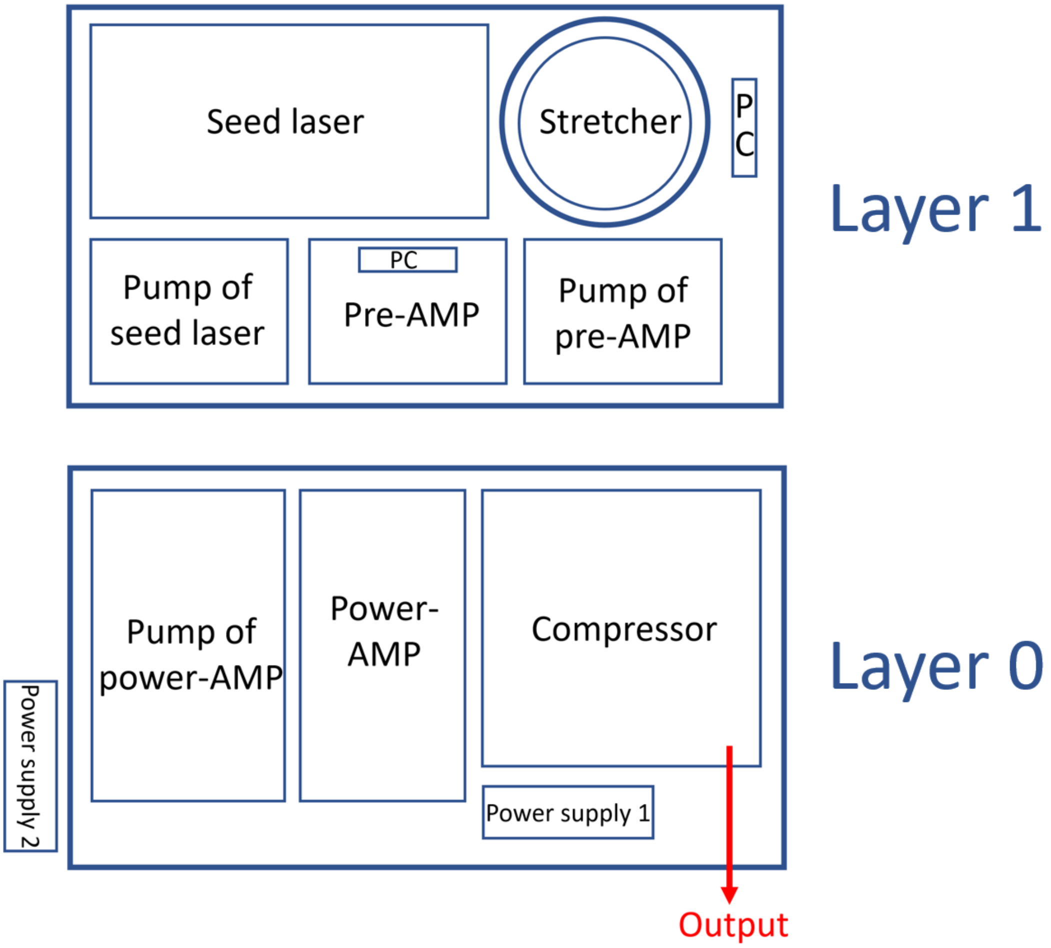

Figure 4.24: Layout of the system in two layers.

## 4.4 Third-harmonic generation microscopy

The imaging was performed with a custom-built inverted microscope based on a Nikon Ti Eclipse frame, which was equipped with a pair of galvanometer mirrors for laser scanning. The output beam of the thulium fibre laser was coupled into the scanner, and after passing through a pair of lenses (scan lens and tube lens) the beam was reflected by a short-pass dichroic (excitation dichroic) beam splitter and focused on the samples through an infinity corrected objective. The THG signal was collected in the back-scattering (epi-detection) geometry from the same objective and delivered through optics comprising of the excitation dichroic, mirrors, lenses, and short-pass filters, as well as a narrow band-pass filter to a photomultiplier tube (PMT) detector. The scanner and the detector were interfaced with a DAQ-PCI6110 to a desktop computer. The laser scanning and the acquisition were controlled with Scanimage 6.1 (Vidrio Technologies). All the image acquisitions were performed with a 20× objective lens with a numerical aperture (NA) of 0.75. The pixel resolution of each image was 512 × 512 which, for the objective and the scanning settings that we have used, corresponded to a field of view of 250 $\mu$m × 250 $\mu$m, while the pixel dwell time was 16 $\mu$s. For one of the samples shown in figure 9, SHG images were concurrently acquired with the THG images to demonstrate complementary information about the tissues. Multimodal multiphoton microscopy to acquire both SHG and THG by using the thulium fibre laser was not undertaken, due to the lack of suitable PMTs displaying good response at the SHG wavelength of the thulium fibre laser, but in principle could work. In this case, a 1031-nm 2-ps 80-MHz laser, whose output had been made colinear with the thulium fibre laser output, was used for the excitation of the SHG. The THG and SHG signals were spectrally separated with a long pass dichroic beam – splitter in the detection branch, with the SHG signal being reflected and passed through another band-pass filter centered at 520 nm, with a full width at half maximum (FWHM) of 40 nm, towards a second PMT. Firstly, the THG imaging capabilities of the apparatus were tested by imaging agglomerates of $BaTiO_3$ nanocrystals (Figure 4.25 and 4.26), known for their high third order susceptibility [8]. Nanocrystals with diameters between 50 to 100 nm, in a powder form, were dispersed on a microscope slide and covered with a glass coverslip (0.17 mm thickness). As described above, a band-pass filter with a central wavelength of 620 nm and a FWHM of 20 nm was placed in front of the detector. Verified by using different filters to exclude the spectrum ranging between 610 to 629 nm, no signal was observed, which strongly suggested that the detected signals when using the above–mentioned band-pass filter were indeed from the THG of the excitation. The same tests were applied during the image acquisition for all the other samples presented in this work. In addition, a sample consisting of 40-$\mu$m-diameter polystyrene beads was chosen to test the THG imaging system functionality. Clear imaging showing strong signals at the boundaries of the polystyrene spheres and negligible signal from the bulk was achieved, as presented in Figure 4.26 (b), which is known due to the surface enhancement of THG [187, 13].

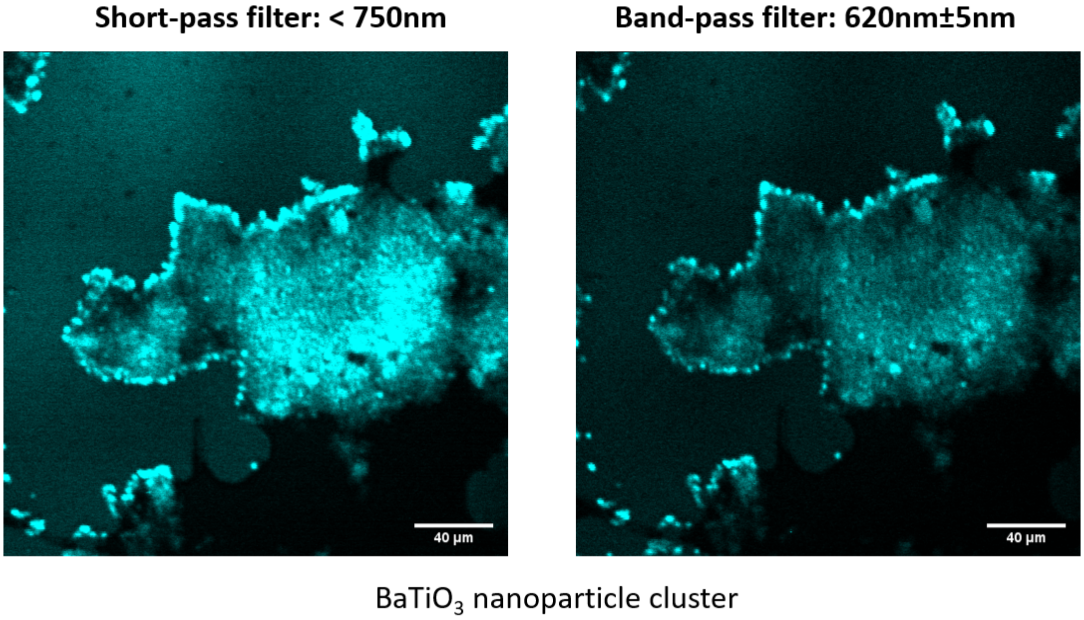

Figure 4.25: THG imaging of $BaTiO_3$ nanoparticle cluster with different filters.

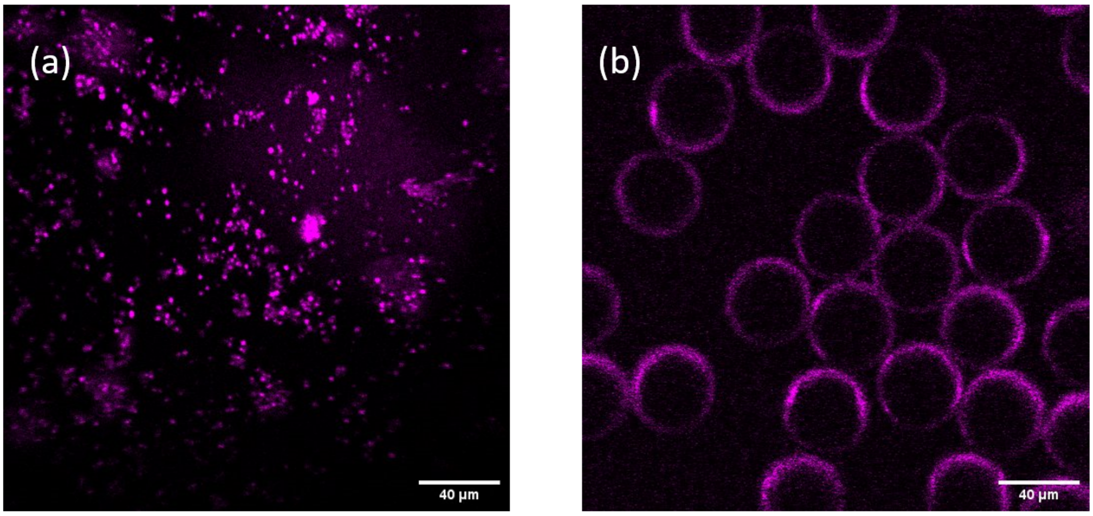

Figure 4.26: THG imaging of (a) BaTiO3 nanocrystals and (b) polystyrene beads.

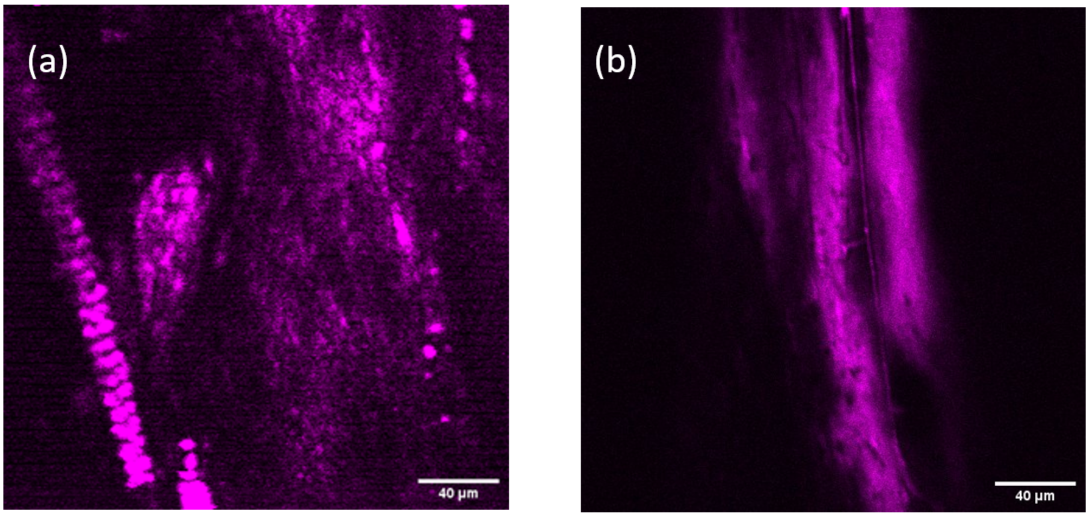

Figure 4.27: THG imaging of (a) section of rat tail tendon and (b) section of rat tail with skin removed.

In order to demonstrate the biomedical imaging application of the Thulium fibre laser, a number of fixed soft and hard tissue samples were prepared and tested. Images were acquired by using the optical lay-out and imaging settings described above. Regarding the preparation of the animal samples, all procedures were carried out in accordance with the Animals (Scientific Procedures) Act 1986 set out by the UK Home Office. The human samples were purchased from a commercial company (Amsbio, USA). No additional ethics approval relevant to the use of biological samples in the project work is needed.

Figure 4.27 (a) shows an image of a rat tail tendon using THG microscopy illustrating an array of dotted and fibrillar areas that likely represent collagen bundles at the interface with the proteoglycan matrix, which has strong THG signals. A part of a rat-tail from which the skin has been removed and includes muscle tissue and blood vessels is shown in Figure 4.27 (b). Vascular canals and the surrounded collagen matrix can be clearly observed from this image.

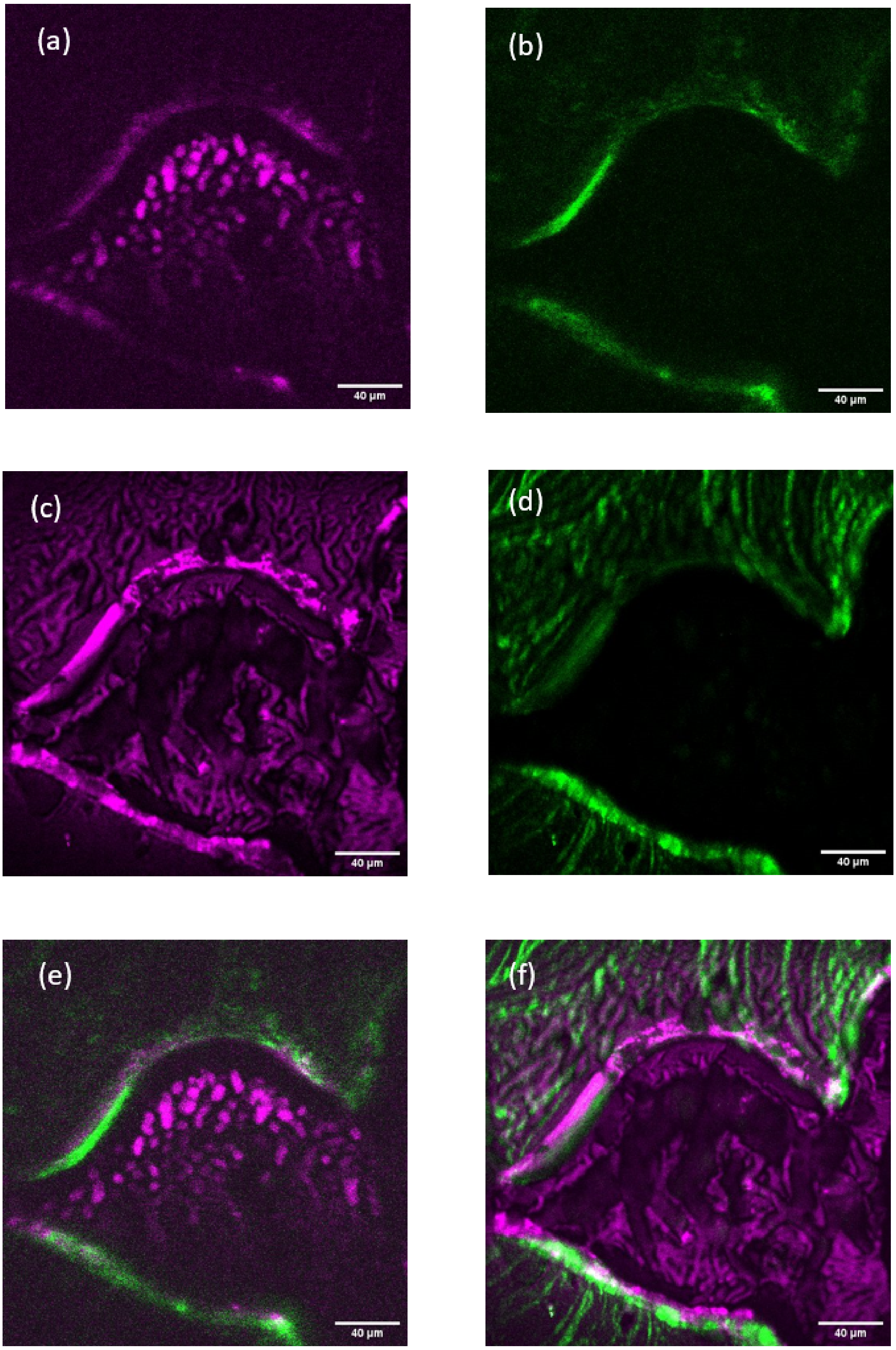

Figure 4.28: THG (a) and SHG (b) images of the superficial human rib bone layer, THG highlighting vascular cnaals and erythrocytes (c) and SHG demonstrating bone matrix compartment (d) of the deep bone layer (21 $\mu$m depth). Composite images THG (magenta) and SHG (green) image of surface (e) and deep (f) layers of (a), (b) and (c), (d) respectively.

THG and SHG images of a section of fetal human rib-cage bone sample, which were acquired concurrently using the two independent lasers, are shown in Figure 4.28. The respective THG and SHG images of the human rib bone sample at the surface layer are depicted in Figure 4.28 (a) and Figure 4.28 (b). As expected, the THG image shows a granular structure in the bone marrow compartment and a part of the surrounding inorganic matrix deposit with high contrast, while the SHG image delineates different components of the bone. SHG demonstrated the collagen matrix with excellent contrast and an absence of signal in the bone marrow compartment. In Figure 4.28 (c), THG imaging of bone layer at a depth of 21 $\mu$m in the same section highlights the soft tissue compartment, with vascular canals and blood vessels clearly visible. Erythrocytes, (large dots) within the blood vessels can also be observed. On the periphery of the bone marrow compartment, the bone mineral matrix can be clearly delineated using this approach. The corresponding SHG image in Figure 4.28 (d) demonstrates, solely, the surrounding collagen matrix. The composite image of the bone sample at the surface layer is shown in Figure 4.28 (e), where the THG is depicted in magenta and SHG is depicted in green. Similarly, the composite image of Figure 4.28 (c) and Figure 4.28 (d) is shown in Figure 4.28 (f) using the same colours for the THG and SHG.

Preliminary studies of multiphoton microscopy based on THG by using the all-fiberized thulium fibre laser demonstrate excellent potential in biological imaging of soft and hard tissues. Further experiment of systematic characterization of the multiphoton microscopic imaging and exploration of deep penetration by using different objectives and filters is underway.

## 4.5 Summary

In summary, an all-fiberized 1840-nm thulium fibre laser source comprising of a dissipative-soliton mode-locked seed laser and a chirped-pulse-amplification system has been developed and been applied for label-free biological imaging through multiphoton microscopy. The mode-locked thulium fibre laser generated pre-chirped pulses with duration of 7 ps and pulse energy of 1 nJ. A chirped-pulse fibre amplification system was built, where commercially available low-absorption and in-house fabricated high-absorption single-mode thulium fibres were employed and compared, which delivered pulses with energies up to 105 nJ. The pulses were compressed to 416 fs by passing through a grating pair. The third-harmonic generation microscopy imaging capability of the laser system was demonstrated on $BaTiO_3$ nanocrystals and soft and hard biological tissues.

# Chapter 5

# All-PM mode-locked fibre laser development

## 5.1 Introduction

In Chapter 4, a 1840-nm femtosecond thulium fibre laser system has been developed and applied in label-free third-harmonic generation microscopy for bioimaging experiments. However, due to the non-PM fibres and components being used, the operation of the mode-locked thulium fibre laser was sensitive to environmental pertubations and temperature variations, which would be problematic for future clinical usage in terms of long term and reliable operation.

In this Chapter, I present the studies of all-PM mode-locked thulium fibre laser cavities targeting stable and robust mode locking operation. I demonstrate, to the best of my knowledge, the first experimental realization of an all-PM thulium-doped 1.9 $\mu$m dissipative soliton mode-locked fibre laser based on the nonlinear optical loop mirror (NOLM) SA mechanism. This work is part of EPSRC funded project 'Lighting the Way to a Healthy Nation - Optical 'X-rays' for Walk Through Diagnosis & Therapy'. The entire work was undertaken and completed by me independently, under the guidance of my colleagues at ORC. The numerical simulation work was carried out by myself.

I first discuss the general design concerns for developing an all-PM mode-locked fibre laser compared to a non-PM mode-locked fibre laser. Next, a series of experiments and simulations are presented in Section 5.2. These experiments include building all-PM mode-locked thulium-doped fibre laser cavities by using SESAM and NOLM mechanisms as saturable absorbers. Mode-locked caivties with different net dispersion designs to operate in conventional-soliton, stretched-pulse-soliton and dissipative-soliton regions have been proposed and demonstrated. This section also includes experiments and characterizations of the spectral response of the NOLM and polarization maintaining properties of the PM DCF that were employed in the mode-locked fibre lasers. A high pulse energy and stable dissipative-soliton all-PM mode-locked laser cavity at 1900 nm is successfully demonstrated, and a numerizal simulation of the laser performance is also given. To the best of my knowledge, this is the first time that a dissipative soliton all-PM mode-locked thulium-doped fibre laser cavity has been achieved (Huang et al. got all-PM dissipative soliton result at 2-micron [82] but they used silicate based fiber).

### 5.1.1 Cavity design consideration

At this point, it would be useful to briefly discuss why we need an All-PM design dissipative soliton thulium-doped fibre laser cavity. Previously I have discussed the advantages of dissipative soliton mode locking compared to other mode locking states in Chapter 2. As its name suggests, PM fibres and components will significantly improve the stability and reliability of the mode-locked laser. For instance, a non-PM fibre laser cavity requires careful insulation and protection from external perturbation and environmental temperature vibration due to the thermal and mechanical sensitivity of the birefringence of non-PM fibres. Furthermore, polarization controllers are required as essential components to initialize mode locking in non-PM fibre cavities, the mechanical drift or degradation of the polarization controller can cause instability into the mode locking. On the contrary, PM fibres naturely have high birefringence and are insensitive to environmental temperature variations and can even tolerant tight fibre bending. Mode-locked fibre laser cavities with all-PM fibres would considerably improve the long-term operational stability of the laser systems we need for medical imaging.

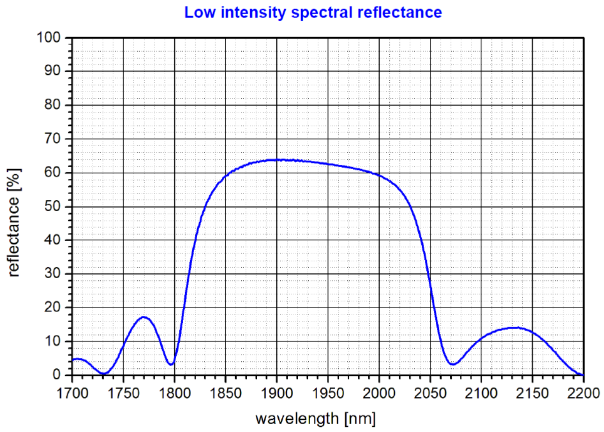

Figure 5.1: Reflective spectrum of commercial SESAM (Batop, SAM-1920-36-10ps). [15]

Saturable absorbers (SAs) are essential for mode locking in the fibre laser cavity. In the previous non-PM fibre cavity design in Chapter 4, commercial reflective SESAMs were used for the mode locking. Although a SESAM based mode-locked cavity provides good performance, the SA material has a low damage threshold and could exhibit degradation of its optical properties during laser operation over a long time. In comparison to SESAMs, a NOLM SA can handle much higher power levels without damage due to its all-fibre nature. Moreover, a SESAM has a strong wavelength dependant response, as shown in Figure 5.1, which can limit its application for laser cavity development where more wavelength flexibility is required. On the contrary, a NOLM has a much wider operation wavelength range compared to a SESAM so it can reduce wavelength-dependant loss and allow for a shorter wavelength tuning for example to below 1800 nm to optimize laser performance for deep-penetration bio-imaging applications.

So using an all-PM-fibre cavity and a NOLM as a SA, I have targetted realization of a fully fiberized, self-starting and environmentally stable ultrafast laser. The NOLM SA mechanism has been introduced in Chapter 2. It can be briefly described as: in the fibre loop, the optical Kerr effect causes a phase shift difference for counter-propagating pulses. An asymmetric splitting ratio of the fibre coupler and a long passive fibre in the loop leads to an intensity dependent loop mirror reflectivity, which can act as a fast modulator of losses in a laser cavity. Compared to the material-based SA, such an “artificial” SA has the latent advantages of a high damage threshold and long working lifetime.

At the very early stage of this project, there had been little research on the development of all-PM dissipative soliton mode locked thulium-doped fibre lasers. I studied the laser cavity design and experiments by employing SESAM and NOLM as SAs to demonstrate and characterize all-PM thulium fibre mode-locked fibre lasers operating in conventional-soliton, stretched-pulse-soliton and dissipative-soliton pulses regimes.

### 5.1.2 Review of prior art

In recent years, some works on passively mode-locked TDFLs with an all-PM fibre configuration were reported. By using a SESAM as an SA, Liu et al. achieved mode-locked pulses with a pulse duration of ∼ 10 ps [113]. However a PM fiber Bragg grating (FBG) was required. Based on graphene SAs, soliton and stretched pulses were obtained, respectively, by Sobon and co-authors [172, 173]. But graphene can not handle high pulse energy due to its low damage threshold. Other than the material-based SAs, “artificial” SAs such as a NALM and NOLM also can be used for mode locking operation in an all-PM fibre configuration, which has been widely studied in the ∼ 1.1 µm and 1.5 µm spectral regime [17, 4, 219]. However, there are only few reports on 2 µm all-fibre mode-locked lasers based on NOLM/NALMs. Michalska and Swiderski reported a soliton mode-locked TDFL with an all-PM fibre configuration based on a NOLM [129].

A NALM based all-PM thulium fibre cavity generating noise-like (NL) pulses was also reported [130]. Dispersion managed mode locking by a NOLM was reported by [128] but the dissipative soliton result from this paper was not all-PM (they replaced the PM DCF (PM2000D) by non-PM DCF (UHNA4) and applied two polarization controllers).

## 5.2 Experiments and simulations

This section shows the systematical experiments I conducted on all-PM mode-locked thulium-doped fibre lasers and the associated numerical simulation results. A SESAM based cavity is studied and demonstrated first to provide conventional solitons. Following that, NOLM based cavities with different dispersions are designed and developed. An all-PM oscillator that can deliver dissipative solitons is successfully demonstrated from the NOLM based cavity with a net normal dispersion and with a maximum output of 4 nJ pulse energy and 350 fs pulse width after external compression.

### 5.2.1 SESAM based all-PM fibre cavity

In this section, I present my work on investigating a SESAM based saturable absorber all-PM mode-locked fibre laser ring cavity generating conventional solitons. At the first stage, I was seeking a solution for an all-PM cavity with the SESAM mechanism. I successfully got conventional soliton mode locking from the following design.

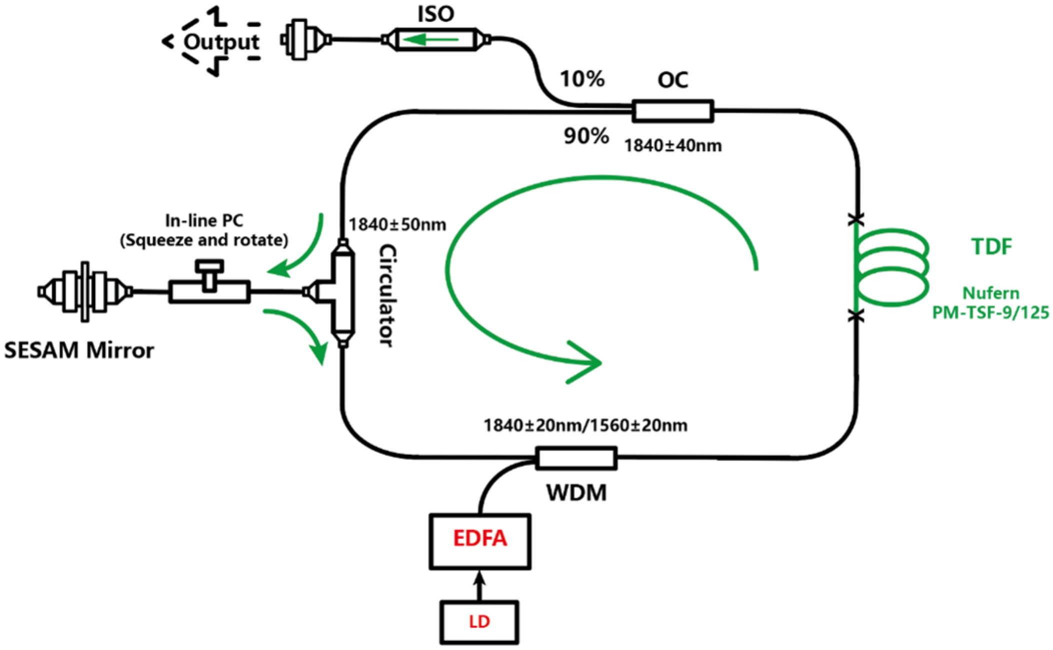

Figure 5.2: Schematic of SESAM based mode locking cavity

A schematic of the mode-locked cavity is shown in Figure 5.2. All the fibre pigtails of components in the cavity are PM single mode fibres (Nufern, PM1550) and its dispersion at $\sim$ 1850 nm wavelength is -0.068 $ps^2/m$ [87]. A 1 m length of PM TDF (Nufern, PM-TSF-9/125) was selected as the gain fibre for laser operation at the short wavelength end of the thulium emission bandwidth. The dispersion of the gain fibre was -0.076 $ps^2/m$ [87]. The total cavity length was 4.6 m and the net dispersion of the cavity was calculated to be -0.32 $ps^2$. The laser was pumped by a 1560 nm homemade fibre laser source (LD seeded EDFA) through a PM 1560 nm/1840 nm wavelength-division multiplexer (WDM). 1560-nm pump source is very cost-effective that can offer high power high brightness and shorter fibre option for Tm-doped fibre system to achieve high efficiency and shorter wavelength operation, mentioned in Chapter 2. A SESAM with a non-saturable reflection of 60% and a modulation depth of 20% (Batop, SAM-1920-36-10ps) was attached to the fibre end (sandwiched between two fibre APC patch cord) of a polarization-dependent (PD) circulator which ensured unidirectional oscillation in the cavity. A 10% PM output coupler (OC) was used to extract the laser output. A PM isolator and a PM WDM are placed after the output of the OC to prevent any back reflection and to filter out the residual pump. All fibre splices were undertaken by using a PM fusion splicer (Fujikura FSM-100P) with careful fast/slow axis alignment.

Q-switched mode locking pulses from the cavity were observed on an oscilloscope when the pump power was increased to around 250 mW. Frequent damage of the facet of the fibre patch cord that attached to the SESAM occurred during the experiments, which is likely due to the high intensity of the Q-switched pulses being over the damage threshold of the SESAM component. No observation of conventional-soliton mode locking was found in those experimental trials. As there was not much control and adjustment of the all-PM cavity apart from varying the pump power, I applied an in-line polarization controller (PC) on the fibre between the SESAM and the circulator to test whether the PC would help to change the intra-cavity loss and favour the mode locking. The circulator had a fast-axis block function, so that the polarization inside the fibre after passing through the PC could be adjusted and consequently the loss from the cirulator could be varied, from which we hoped to reduce the Q-switched mode locking pulses and avoid damaging the fibre and SESAM. Also the PC can change the polarization of the light on the SESAM surface. Interestingly, stable and single-pulse conventional-soliton mode locking was obtained at a pump power of 325 mW by properly adjusting the PC. With a fixed PC setting, the mode locking could be self started by turning the pump power over this threshold level. The output power was measured to be 3 mW, and the output spectrum had a central wavelength at 1850 nm with a 3-dB spectral bandwidth of 6 nm. The spectrum exhibited a typical soliton-like shape with characteristic Kelly's sidebands, which generally results from the all-anomalous dispersion cavity, as shown in Figure 5.3. The recorded oscilloscope traces of the pulse train is captured in Figure 5.5. The pulses are equally spaced by 22.8 ns, which corresponds to a 43.9 MHz pulse repetition rate that matches well with the 4.6-meter-long cavity. From the auto-correlation measurement shown in Figure 5.4, the auto-correlation width at FWHM is 1.06 ps which indicates a real pulse width of 690 fs by Sech$^2$ function fitting (typical for conventional solitons). The pulse width obtained from the experiment is close to the value (631 fs) achieved from my simulation (shown later in the text). The calculated time-bandwidth product (TBP) of the output pulse is 0.36 which is close to the transform-limited value of 0.315. The equipments used for the above measurements are optical spectrum analyzer (Yokogawa AQ6375), 60 MHz digital oscilloscope (Tektronix TDS210), and auto-correlator (APE pulsecheck). The mode-locked status remains stable and unaffected, irrespective of physical interaction with the PM1550 fiber or Thulium-doped fiber (TDF).

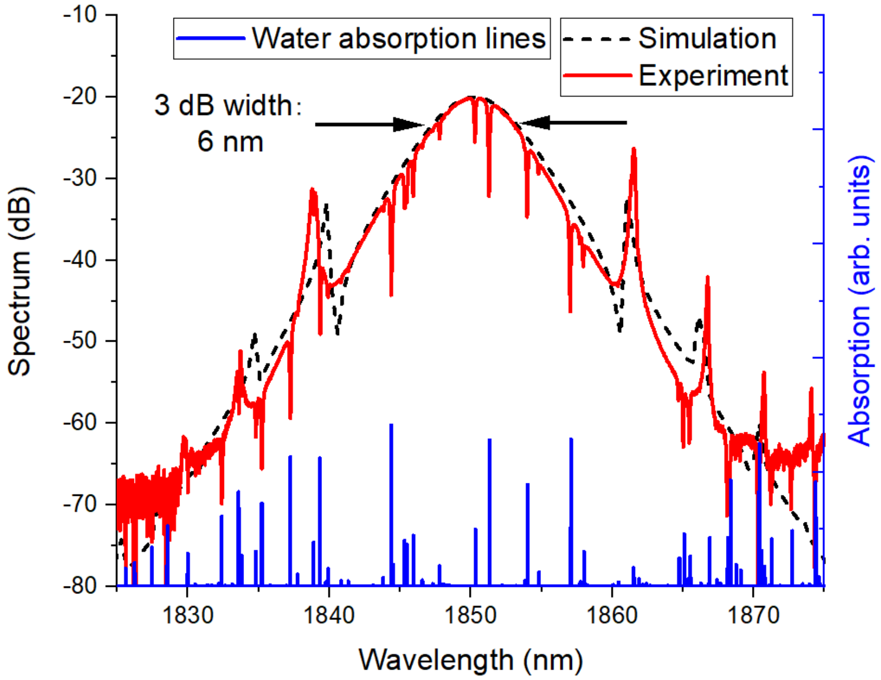

Figure 5.3: Spectrum of conventional soliton mode locking output: experimental result (solid red line) and numerical simulation result (dashed black line). Water absorption lines (solid blue line)

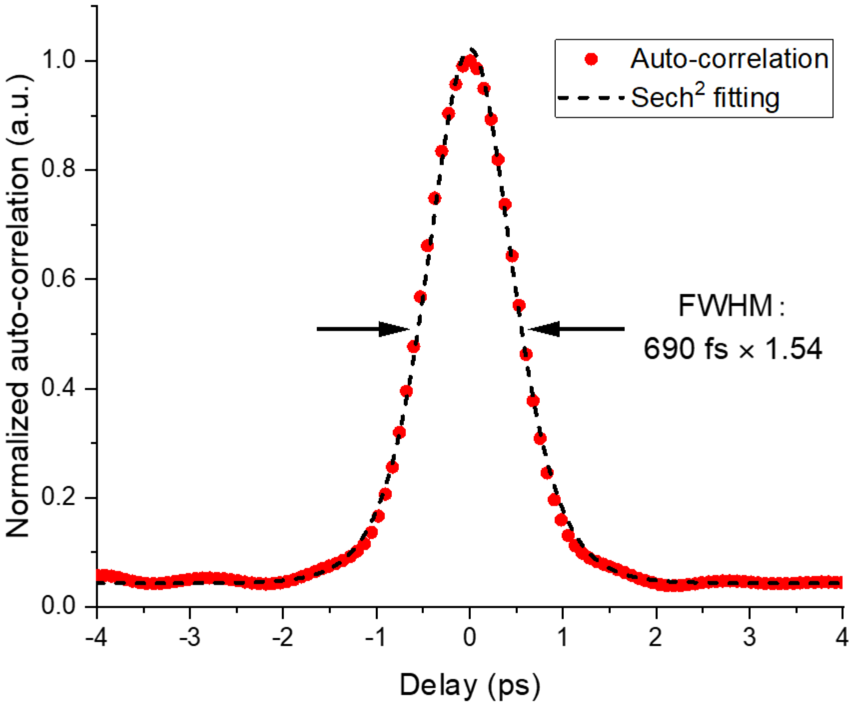

Figure 5.4: Auto-correlation of the pulse: red points: experimental auto-correlation traces; dashed black line: Sech$^2$ fitting of the auto-correlation.

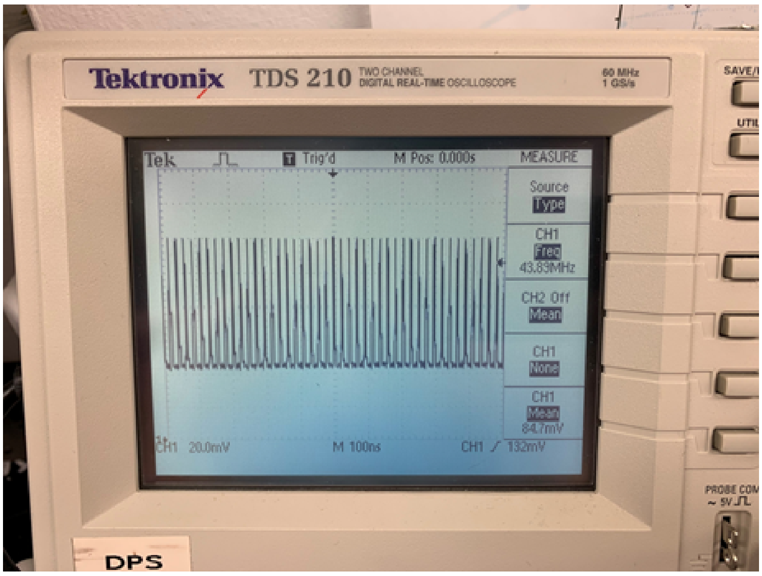

Figure 5.5: Pulse train measured by the oscilloscope and photodetector.

We can calculate the net group delay dispersion (GDD) of the laser resonator, according to the following formula 5.1

$$|D_2| = \pi \cdot n \frac{\tau_p^2}{\left(\ln\left(1+\sqrt{2}\right)\right)^2} \cdot \frac{1}{1+\left(\frac{2\pi c \cdot \tau_p \cdot \Delta\lambda}{\lambda_c^2}\right)^2} \tag{5.1}$$

where $D_2$ denotes the second-order dispersion, n is the sideband order, $\tau_p$ is the pulse duration, $\Delta\lambda$ denotes the sideband separation, and $\lambda_c$ is the central wavelength. By using the values (690 fs pulse duration, 1852 nm central wavelength and 22 nm sideband separation at n = 1) from measurement for the formula, we obtained a $|D_2|$ of 0.32 ps$^2$, which matches well with the net cavity dispersion calculated from the reference fibre dispersion data.

The output spectrum exhibited some modulation at several wavelengths with sharp dip lines could likely originate from the strong water absorptions within the 1.8 - 1.9 $\mu$m wavelength region in atmospheric air in the optical spectrum analyzer (OSA). I have compared the laser spectrum and the absorption spectrum of light over a 1 m path in the air with 1% water content using the high-resolution transmission molecular absorption (HITRAN) database [164] and plotted them in Figure 5.3 (with a blue line). The location and amplitude of the dips in the spectrum match wells with the water absorption lines.

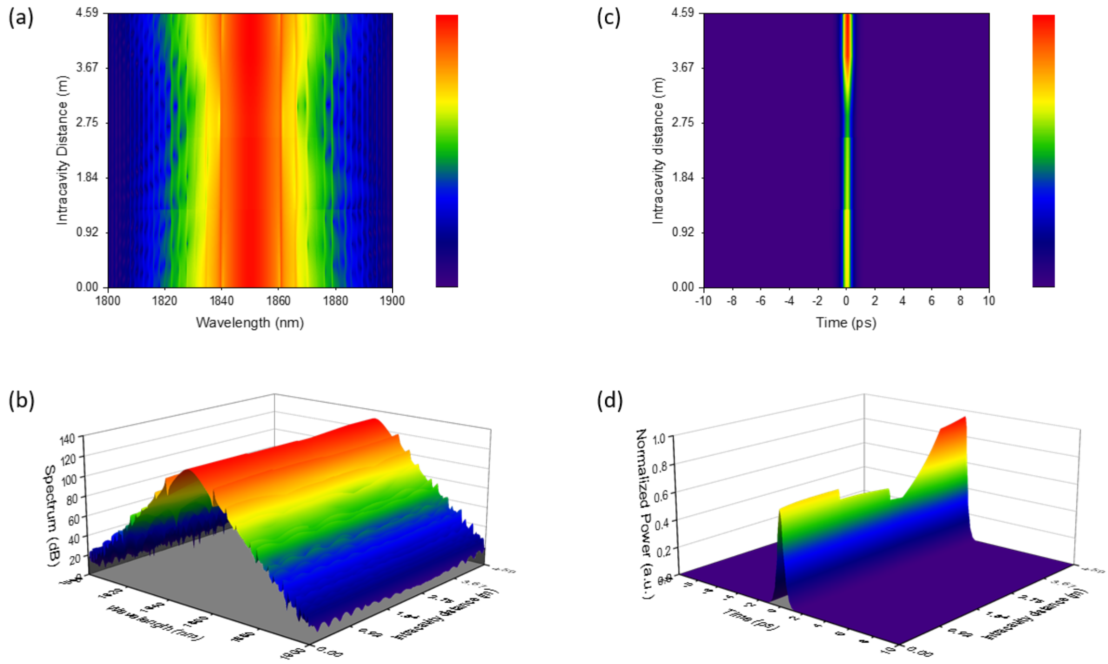

Figure 5.6: Simulation of intracavity laser performance characterization: (a) (b) Spectrum heat map and 3D plot of range 1800 nm - 1900 nm in a single round cavity, (c) (d) time domain heat map and 3D plot of range -10 ps - +10 ps in a single round cavity

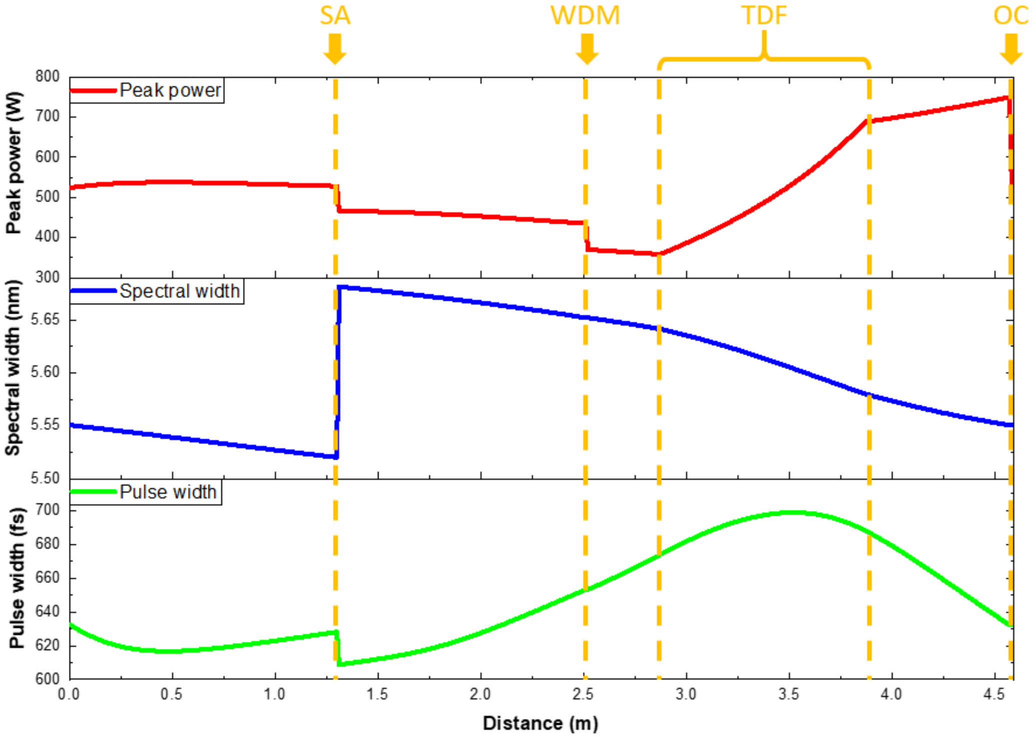

Figure 5.7: Intracavity laser performance characterization of peak power, spectral width and pulse width based on numerical simulations.

To complement the experimental results, numerical simulations of the cavity were executed using Fiberdesk, a commercial software. This software operates based on the generalized Schrödinger equation, which is solved using a split-step Fourier method. To minimize computational effort, an arbitrary seed pulse was initially used, and simulations were repeated until a stable state was attained. The parameters of the fibers, as previously described, were factored into the simulations. Table 5.1 provides a summary of all the fiber parameters used in the simulation. A saturable absorber model was employed to calculate the SESAM. The established model was then used to investigate intracavity pulse dynamics in a traditional soliton fiber laser. The intracavity spectrum and time domain evolution are presented in Figure 5.6, while Figure 5.7 illustrates the position of key components within the cavity and the evolution of temporal, spectral, and power aspects. The starting point of the simulations was the output coupler (OC). In the passive fiber sections, due to the interplay of negative chirp and self-phase modulation, the pulse stretches temporally and the spectral bandwidth narrows. After traversing the gain fiber, the mode-locked pulse exhibits a substantial increase in pulse energy and peak power.

| Fibre | $\beta_2$ (Group velocity dispersion parameter) | D (Dispersion parameter) |
|---|---|---|
| PMF (PM1550) | -0.068 $ps^2/m$ | 37.4 ps/nm/km |
| TDF (PMTSF 9/125) | -0.076 $ps^2/m$ | 41.8 ps/nm/km |

Table 5.1: Fibre parameters in the simulation.

The stable operation of the mode-locked thulium fibre laser by using all-PM fibres has been achieved, however, the possibility of SESAM damaged and the employment of the PC do not offer a reliable solution for long-term running of the laser system.

### 5.2.2 NOLM based all-PM cavity

This section introduces the design and development of all-PM mode-locked thulium fibre lasers based on NOLM SA mechanism. The principle of the NOLM has been discussed in the previous theory part which can act as a fast modulator of losses in a laser cavity also known as a saturable absorber. The experiments to be presented in the following sections includes conventional-soliton mode locking, stretched-pulse mode locking and dissipative-soliton mode locking from all-PM NOLM-based fibre laser cavities, and corresponding simulation results. Characterization of the loop mirror and numerical simulations of those mode-locked laser cavities are also shown.

#### 5.2.2.1 Conventional-soliton mode locking

The oscillator was structured in a 'figure of eight' layout, where the main (left) loop functioned as a ring laser and the right served as a nonlinear loop mirror, acting as a saturable absorber. The cavity was constructed using all-polarization-maintaining (PM) fibres, specifically Panda-type fibres. All fibre components were fused together using a Fujikura FSM-100P filament fusion splicer. A 90-cm length of single-mode PM thulium-doped fibre (from Nufern, PMTSF-9/125) was core pumped through a PM 1560/1840 WDM (from AFR) using a custom-built LD-seeded EDFA source, which provided a continuous-wave (CW) output power of up to 5 W at 1564 nm. A PM fibre optic isolator (from AFR) was integrated into the main loop to guarantee unidirectional laser operation. A 2 × 2 PM tunable coupler (Phoenix Photonics FTDC-P-155-NO) divided the power from the main loop into two waves propagating in opposite directions in the nonlinear optical loop mirror (NOLM). To lower the peak power required for saturation and reach the mode-locking threshold, and to provide sufficient phase shift difference for the counter-propagating beams, 20 m of PM1550 (from Nufern) was spliced into the nonlinear loop. Pulses were coupled out of the resonator through a 10% PM output coupler (from AFR). The total length of the resonator was approximately 27.4 m, including a 90 cm long PM thulium-doped fibre (TDF), 22 m-long PM1550 fibre in the NOLM, and 3.5 m long PM1550 pigtail fibre on the couplers and optical isolator. The dispersion of the PM1550 and PM TDF fibres was -0.068 $ps^2/m$ and -0.076 $ps^2/m$, respectively, and the estimated net group delay dispersion (GDD) was -1.87 $ps^2$.

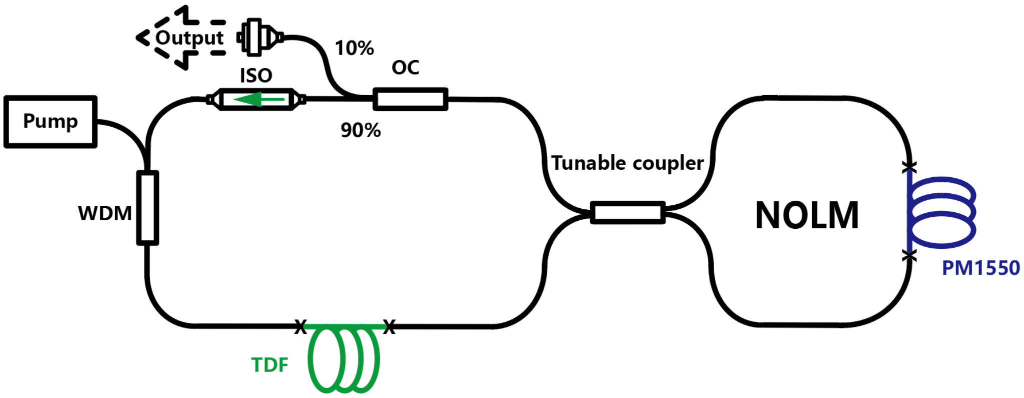

Figure 5.8: Schematic of the all-PM NOLM-based stretched pulse cavity (no SESAM included)

The tunable coupler (shown in Figure 5.9) used in the cavity allows control of the splitting ratio for the NOLM, which can be adjusted to vary the modulation depth of the effective SA and help to initiate the starting of mode locking. There are 0 - 45 scale settings on the rotary knob.

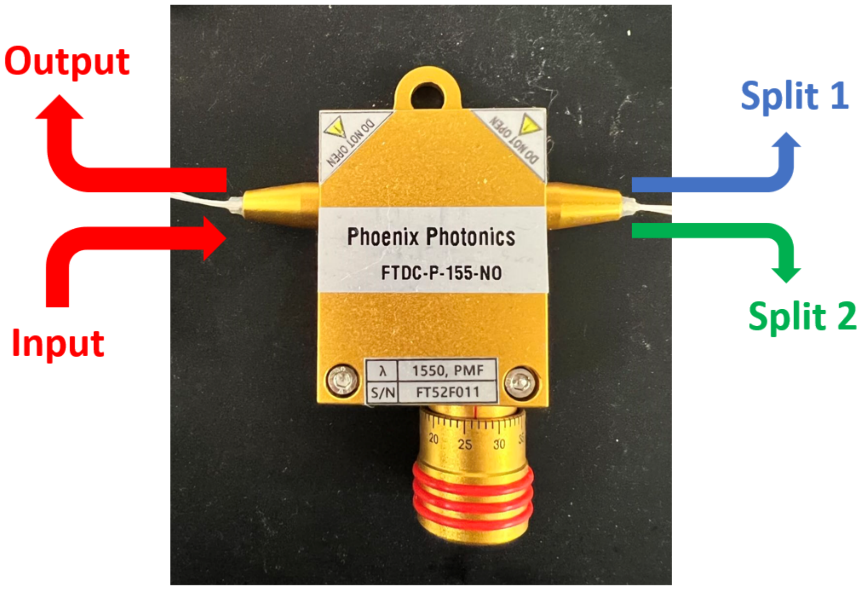

Figure 5.9: Tunable coupler

Although the tunable coupler was originally designed for 1550 nm wavelength, I tested the function at 1875 nm by using a narrow-linewidth CW diode laser and the results are shown in Figure 5.10. The power coupling ratio of the coupler can be tuned seamlessly from 0 to 100% The insertion loss was around 0.9 dB.

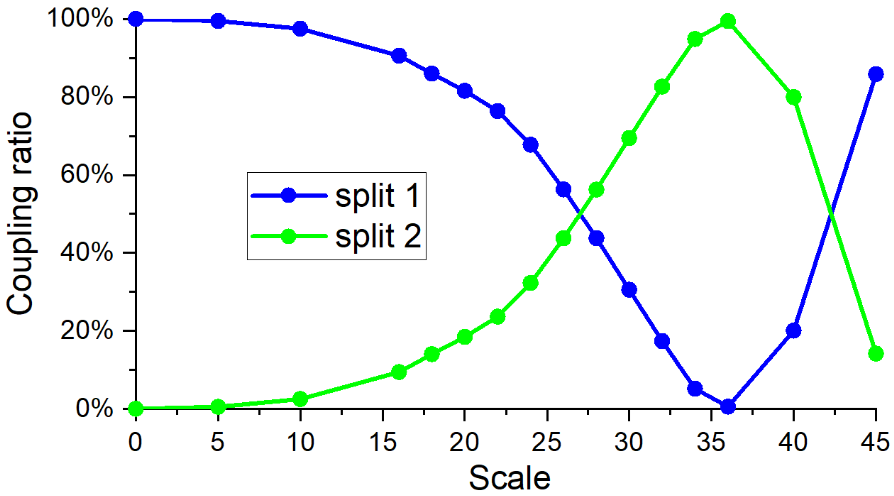

Figure 5.10: Tunable coupler coupling ratio

In order to check the wavelength dependant coupling ratio of the tunable coupler, I characterized it by using a PM fibre based wideband ASE source that covered wavelengths from 1700 nm to 1950 nm. The ratio calculated by the power of split 1/split 2 is plotted and shown in Figure 5.11. From the results, at three different scales of the tunable coupler, the 1 to 1 ratio or 50% point has three different corresponding wavelengths. The power ratio with respect to the wavelength has a close-to-linear function, which indicates there will be some bandpass filtering effects from the tunable coupler.

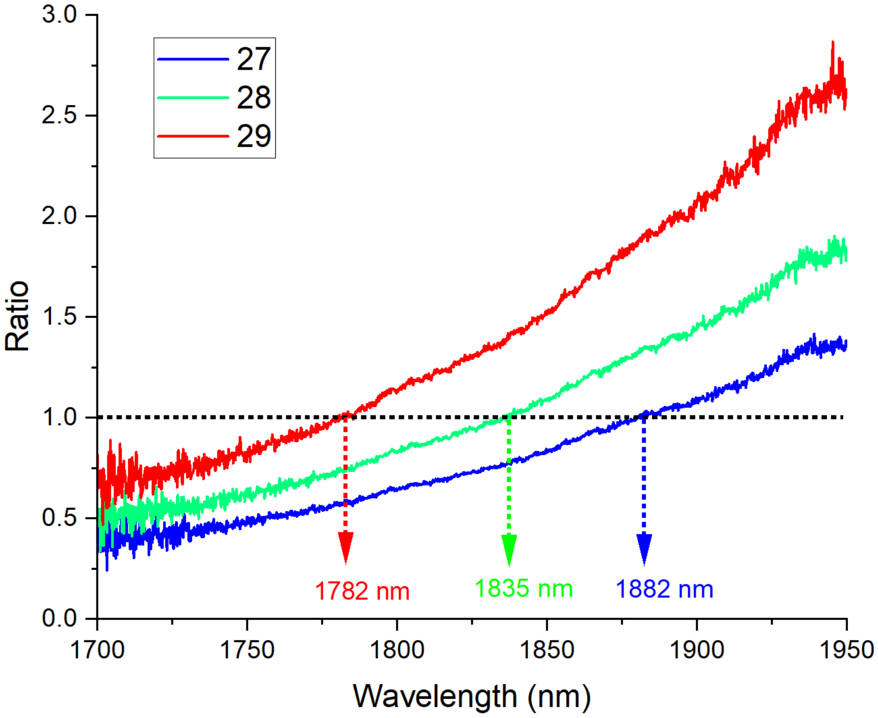

Figure 5.11: Tunable coupler wavelength dependence (Scale setting on the rotary knob 27 :blue, 28: green, 29 red.)

Mode locking was observed when the pump power was increased above 1.8 W when the coupler ratio was set at around 70/30 (at wavelength of 1875 nm). At lower pump powers, the oscillator lases at 1875 nm. Upon increasing the pump power to 1.8 W, we observed a broadening of the spectral linewidth due to self-phase modulation and the generation of multiple pulses, as depicted in Figure 5.15. The inclusion of the tunable coupler in the NOLM led to radiation leakage through the loop mirror. This leakage could supply the requisite noise to initiate the pulse formation process, potentially leading to multi-pulse operation just beyond threshold. When we reduced the pump power to 0.3 W, the oscillator consistently produced single-pulse CW-mode-locked pulses (as shown in Figure 5.14). These pulses had a fundamental repetition rate of 7.44 MHz, aligning closely with the length of the cavity. The output average power was measured to be 0.6 mW, corresponding to a pulse energy of 80 pJ.

The mode-locked spectrum had a central wavelength of 1875 nm and a 3-dB bandwidth of 5.2 nm, as shown in Figure 5.12. Kelly sidebands, which are evenly spaced around the primary peak, can be seen. These sidebands result from the interaction between the solitons and the coincident dispersive waves. An intensity auto-correlation measurement is demonstrated in Figure 5.13, and the experimental data was aligned with a sech$^2$-pulse profile. The full width at half maximum (FWHM) of the auto-correlation trace measures 1.125 ps. Therefore, the estimated real pulse duration is 730 fs, and the calculated time-bandwidth product is 0.324 matching the simulated 680 fs pulse width very well. The mode-locked status remains stable and unaffected, irrespective of physical interaction with the PM1550 fiber or Thulium-doped fiber (TDF).

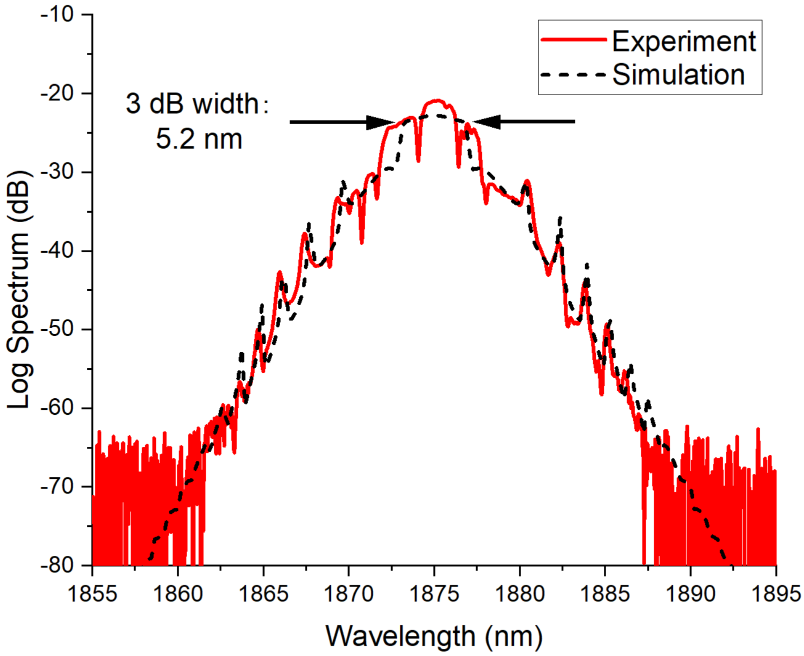

Figure 5.12: Spectrum of conventional soliton mode locking output: experimental result (solid red line) and numerical simulation result (dashed black line).

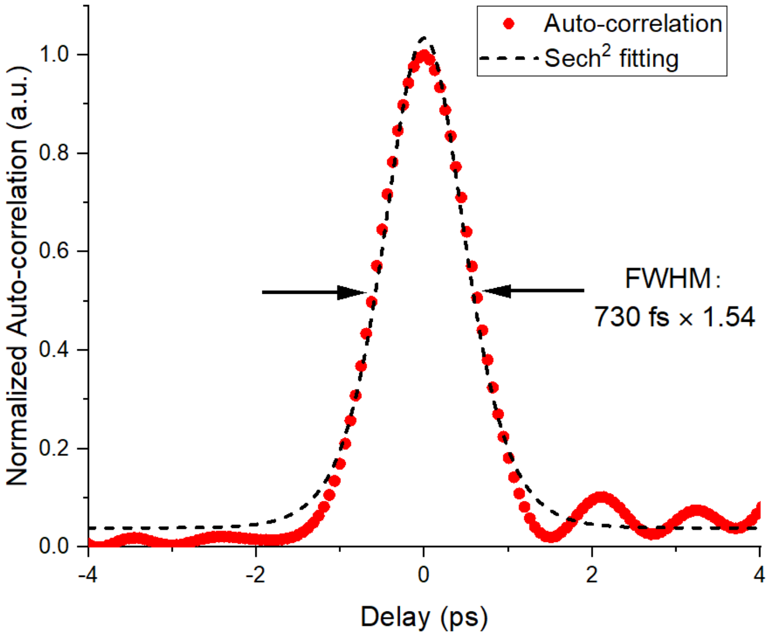

Figure 5.13: Auto-correlation of the pulse: red points: experimental auto-correlation traces; dashed black line: Sech$^2$ fitting of the auto-correlation.

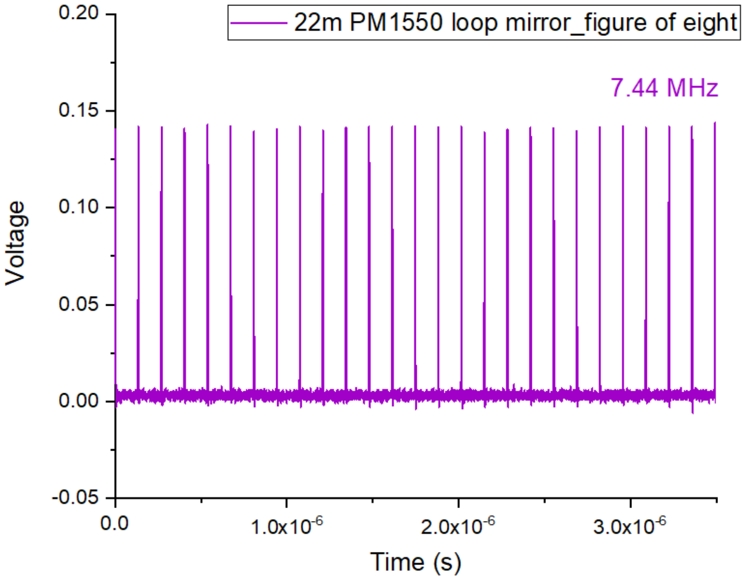

Figure 5.14: Mode-locked oscilloscope traces (single-pulse)

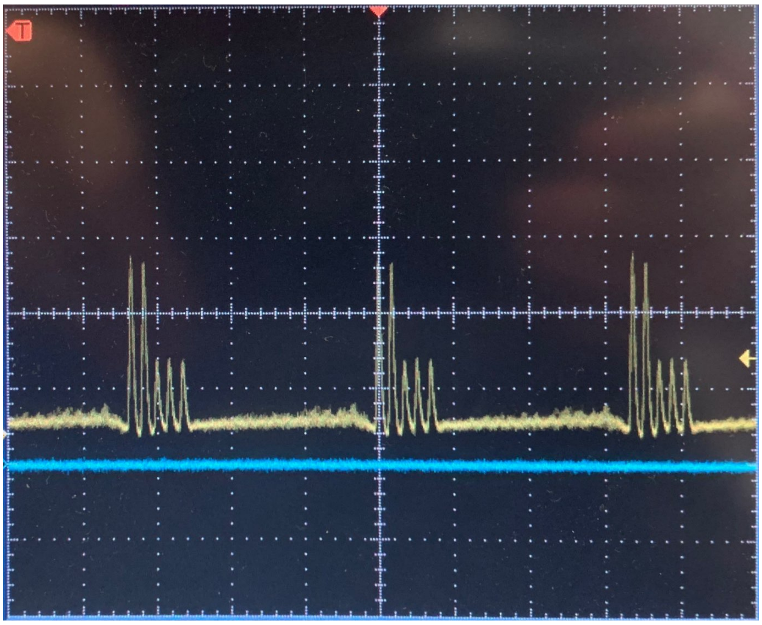

Figure 5.15: Mode-locked oscilloscope traces (multi-pulse)

Numerical simulations for the NOLM cavity were carried out with the fibre parameters shown in Table 5.2. The modelling also included the 22-m-long PM1550 fibre-based NOLM with a coupling ratio of 30/70. The intracavity pulse evolution of the conventional soliton in the time and spectral domains is shown in Figure 5.16. Figure 5.17 presents the changes of pulse width, spectral width and peak power inside the cavity, in which positions of key components have been shown to help understand the influence of the fibres and components on the mode-locked solitons. The output coupler (OC) is the starting point of the simulations. In the passive fibre sections, the pulse strongly stretches in time. The spectral bandwidth narrows due to the co-action of the negative chirp and self-phase modulation. From Figure 5.17, the pulse energy and the peak power increase significantly after the mode-locked pulse passes through the gain fibre. The NOLM section is also modelled in the simulation, in which counter propagation of the pulses experience different nonlinear phase shift due to the non-symmetrical split ratio of the coupler hence resulting in a SA effect in the cavity. To simplify the plot in Figure 5.17, the NOLM is represented as a single-point element.

| Fibre | $\beta_2$ (Group velocity dispersion parameter) | D (Dispersion parameter) |
|---|---|---|
| PMF (PM1550) | -0.068 $ps^2/m$ | 37.4 ps/nm/km |
| TDF (PMTSF 9/125) | -0.076 $ps^2/m$ | 41.8 ps/nm/km |

Table 5.2: Fibre parameters in the simulation.

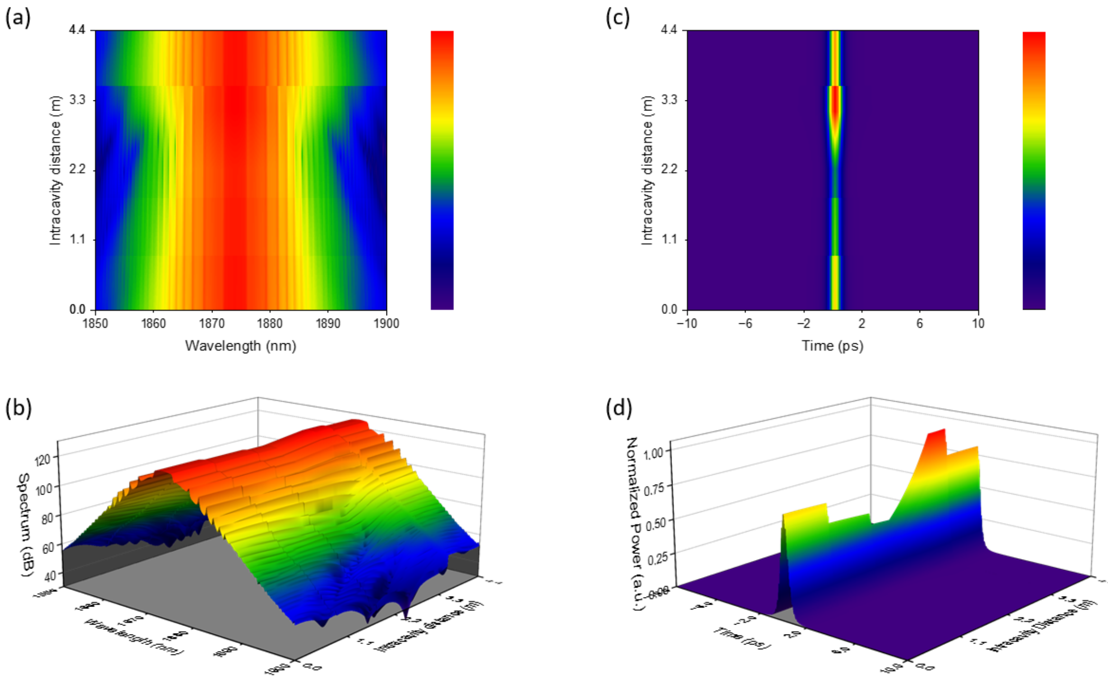

Figure 5.16: Intracavity laser performance characterization: (a) (b) Spectrum heat map and 3D plot of range 1850 nm - 1900 nm in a single round cavity, (c) (d) time domain heat map and 3D plot of range -10 ps - +10 ps in a single round cavity

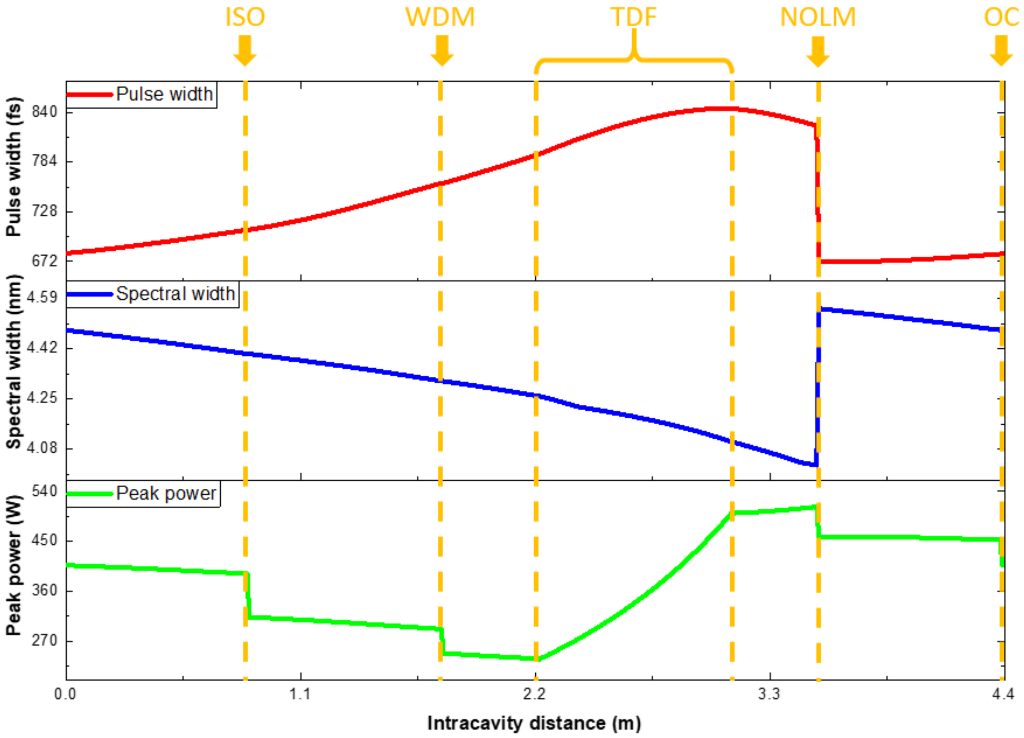

Figure 5.17: Intracavity laser performance characterization of peak power, spectral width and pulse width based on numerical simulations.

Conventional-soliton mode locking was achieved experimentally from this NOLM-based all-PM cavity and the numerical simulations were implemented to provide pulse evolution inside the cavity.

#### 5.2.2.2 Stretched-pulse mode locking

As discussed in Chapter 2, dispersion managed cavities can provide stretched-pulse mode locking with net-anomalous-dispersion which allows higher output pulse energies compared to conventional-soliton mode locking. This subsection presents the experimental testing of a dispersion managed cavity achieved by adding a piece of normal dispersion PM fibre for enabling stretched-pulse mode locking operation.

The PM1550 fibre section of the NOLM in Figure 8 was shortened to a length of 10 m and a piece of DCF (Nufern PM2000D) was added as shown in Figure 5.18. The dispersion of the DCF was estimated to be + 0.085 $ps^2/m$ according to measurements reported in the literature [42], and a 4 m length was chosen to provide a net dispersion of + 0.82 ps$^2$ for the cavity. The length of the DCF were informed by simulations and one of the best results chosen from several experiments.

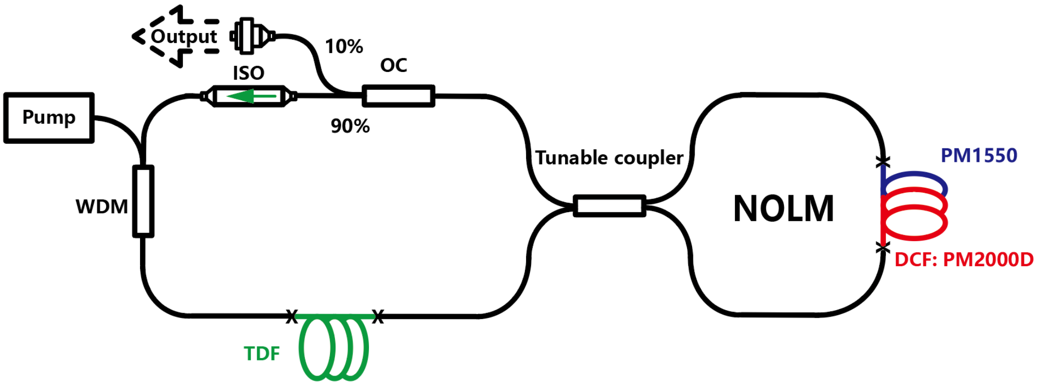

Figure 5.18: Schematic of the all-PM NOLM-based dissipative soliton cavity.

Strong spectral broadening was observed from the cavity output when the pump power was increased to over 1 W and the onset of multi-pulse mode locking was observed on an oscilloscope at a pump power of 1.9 W. By decreasing the pump power, the multi-pulse mode locking gradually evolved to single-pulse mode locking and the associated pump power was found to be 0.38 W. The output pulses had a repetition rate of 10.5 MHz and an average power of 3 mW. The corresponding pulse energy was calculated to be 0.28 nJ which is three times higher than that of the conventional-soliton pulse. The output spectrum of the stretched pulse is shown in Figure 5.19.

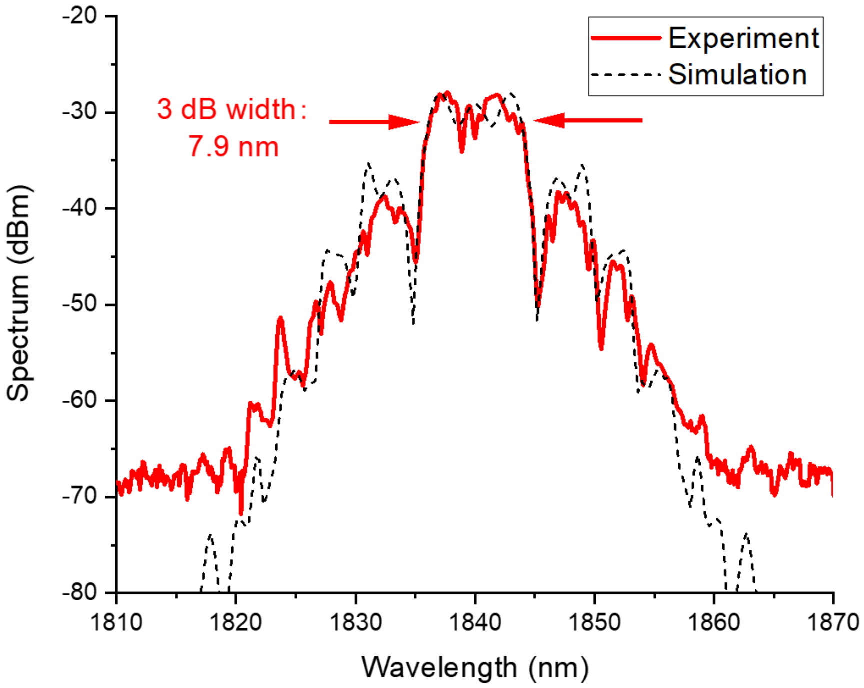

Figure 5.19: Spectrum of the stretched pulse mode locking output: experimental result (solid red line) and numerical simulation result (dashed black line).

It was worth noting that the stretch-pulse mode locking was found to be unstable when the DCF was moved or slightly bent. Since the all-PM conventional-soliton mode locking operation was very stable and insensitive to the external perturbation of the PM1550 fibres, I decided to check the PM properties and performance of the PM2000D fibre. A simple experiment was set up, as shown in Figure 5.20. A 1987-nm laser diode having a PM1950 fibre patch cord pigtail was used as a linearly polarized light source. A 1 m length of PM1550 fibre patch cord was connected to the PM1950 fibre end, and the output of the PM1550 fibre was collimated and passed through a half-wave plate (HWP) and a polarization beam splitter (PBS) before a power meter. The HWP was adjusted to align the beam polarization with the PBS to measure the maximum power. As shown in Figure 5.20, the power was very stable during measurement over a 10-minute period and slight bending of the PM1550 fibre did not change the power or by means the polarization. In comparison, a 1 m length of PM2000D was spliced to the end of the PM1550 fibre patch cord and the output power from the PM2000D was measured. Although the splice point of the PM2000D to the PM1550 was protected and secured, the power fluctuated significantly when touching or slightly bending the PM2000D fibre and power changes were observed even the fibre was not touched. It seems that the PM behaviour of the PM2000D was not as good as expected. I have contacted supplier to report fibre not working properly and there was no alternative PM DCFs available to test the cavity performance.

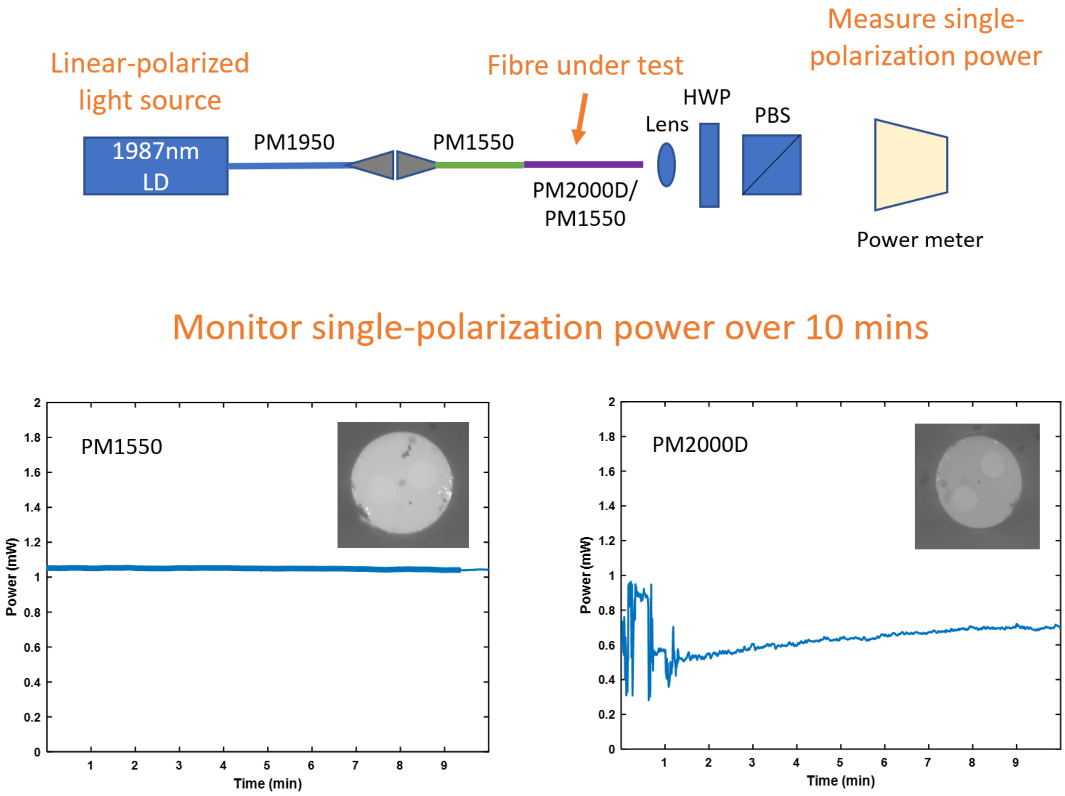

Figure 5.20: PM2000D problem measurement compared with PM1550

Nevertheless, simulation of the stretched-pulse mode locking operation from the cavity was performed while the non-ideal PM property of the DCF was ignored. The simulated spectrum matches well with the experimental spectrum shown in Figure 5.19. Figure 5.21 shows the spectrum and pulse changes in the cavity during one round trip. Note that in the time domain the pulse changes shape a lot during the round trip and it is not a single peak pulse shape so it will not benefit bio-imaging due to the split peaks.

| Fibre | $\beta_2$ (Group velocity dispersion parameter) | D (Dispersion parameter) |
|---|---|---|
| PMF (PM1550) | -0.068 $ps^2/m$ | 37.4 ps/nm/km |
| TDF (PMTSF 9/125) | -0.076 $ps^2/m$ | 41.8 ps/nm/km |
| DCF (PM2000D) | 0.085 $ps^2/m$ | -46.8 ps/nm/km |

Table 5.3: Fibre parameters in the simulation.

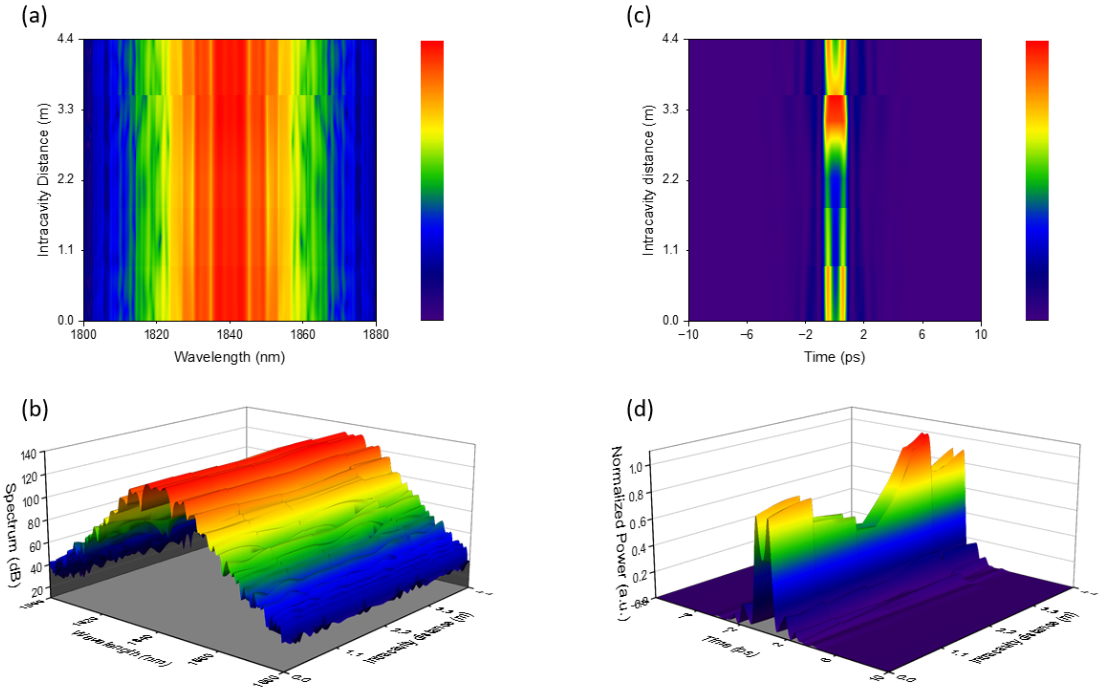

Figure 5.21: Intracavity laser performance characterization: (a) (b) Spectrum heat map and 3D plot of range 1800 nm - 1880 nm in a single round cavity, (c) (d) time domain heat map and 3D plot of range -10 ps - +10 ps in a single round cavity

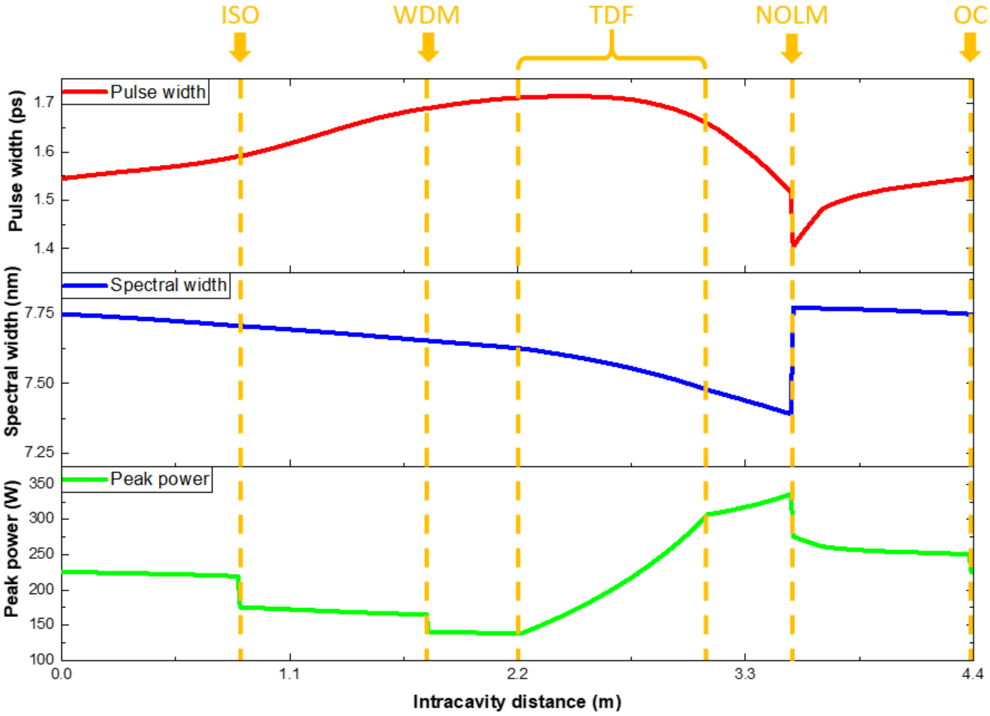

Figure 5.22: Intracavity laser performance characterization of peak power, spectral width and pulse width based on numerical simulations.

#### 5.2.2.3 Dissipative soliton mode locking

In order to reduce the effect of the non-ideal PM performance of the PM2000D, the NOLM cavity was modified to shorten the PM2000D fibre length and to provide net normal dispersion. With the PM1550 fibre being removed and only a 5 m long length of PM2000D in the NOLM, the cavity net dispersion was estimated to be 0.047 ps$^2$. However, no spectral broadening was observed from the cavity output even at a high pump power, which was probably due to the short length of fibre forming the NOLM resulting in a high saturation threshold. To increase the signal gain, I changed the TDF from PM-TSF-9/125 to PM-TSF-5/125 which has a higher absorption and also shortened the PM2000D DCF from 5 m to 4 m. The cavity net dispersion was estimated to be 0.03 ps$^2$. Also, the 10% output coupler was replaced with a 30% OC to provide more output power and pulse energy. In this cavity configuration, I removed the PM1550 fibre in the loop mirror and applied two in-line polarization controllers on the PM2000D fibre. They are used to stabilize the polarization of the DCF in the loop mirror and to contribute to the band pass effect of the loop mirror.

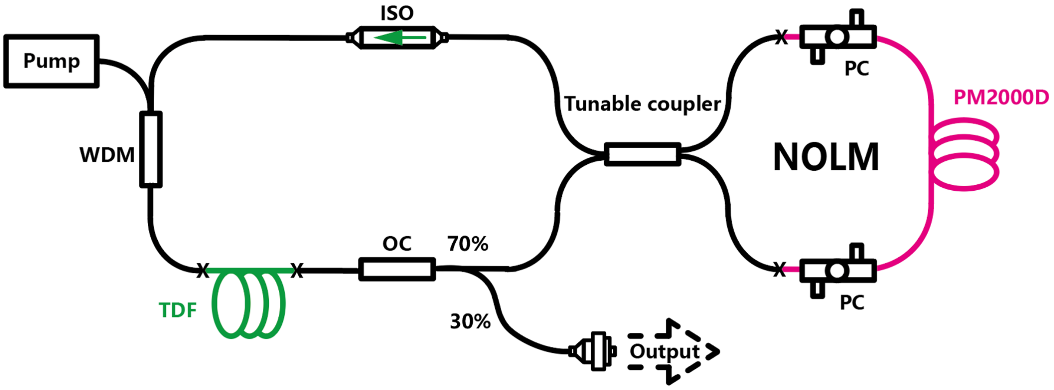

Figure 5.23: Schematic

Mode-locked pulses were observed but they were extremely unstable even with the PM2000D fibre was left untouched. In order to try to control the pulse polarization inside the PM2000D fibre, both end sections of the fibre were mounted in in-line polarization controllers (PCs).

By properly adjusting the PCs, a tunable coupler ratio and pump power, stable single pulse dissipative-soliton mode locking could be achieved with a threshold pump power level of 1.6 W and a tunable coupler coupling ratio of $\sim 0.3$. The output pulses had a repetition rate of 25 MHz which agreed with the total cavity length of 8.65 m (3.65 m in the main loop, 5 m in the NOLM loop). The pulse train displayed on an oscilloscope is shown in Figure 5.26. As can be seen from Figure 5.24, the output spectrum has steep edges at both sides, which strongly indicates the dissipative-soliton mode-locked operation. The spectrum has a central wavelength of 1905 nm and a 3-dB bandwidth of 7.7 nm (10-dB bandwidth of 29 nm). The output pulse width was measured with an auto-correlator and is shown in Figure 5.25. By using a Gaussian function fitting, the output pulse width is found to be 4.9 ps. To check the compressibility, the output pulses were coupled into and passed through a piece of single mode fibre (SMF28) before making an auto-correlation measurement. With a 6.5 m long SMF28 fibre, the pulse was compressed to 350 fs assuming a Gaussian fit (Figure 5.27). The power scaling of the dissipative-soliton mode-locked laser has been characterized and the result is shown in Figure 5.28. Due to concerns about damage to the WDM, the pump power was only increased to 1.83 W and a maximum of 90 mW output power was obtained which corresponded to a pulse energy of 4 nJ. This result is significantly higher than those from the other two mode-locked laser cavities.

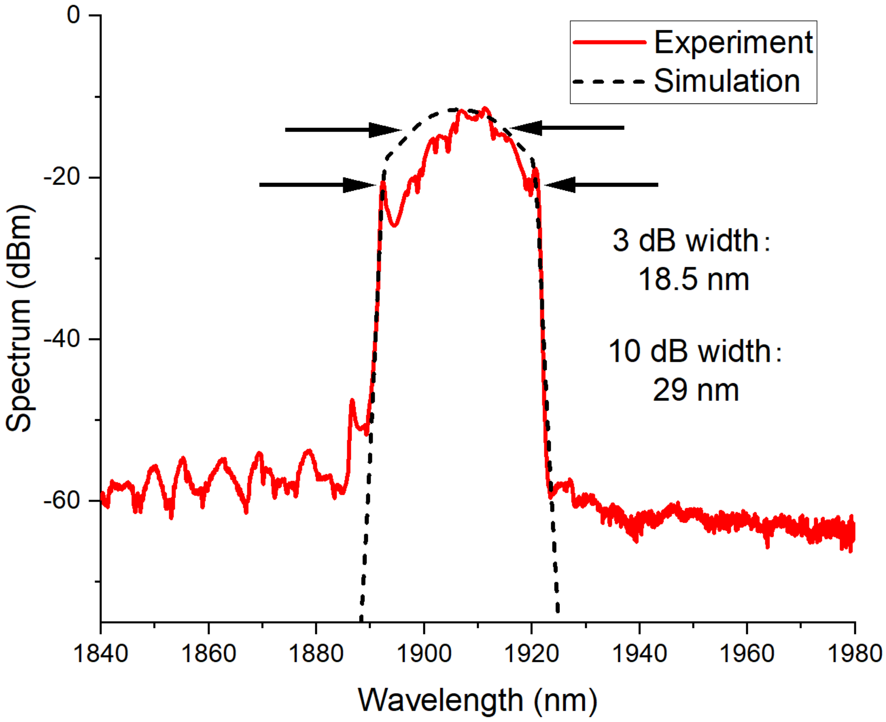

Figure 5.24: Spectrum of dissipative soliton mode locking output: experimental result (solid red line) and numerical simulation result (dashed black line).

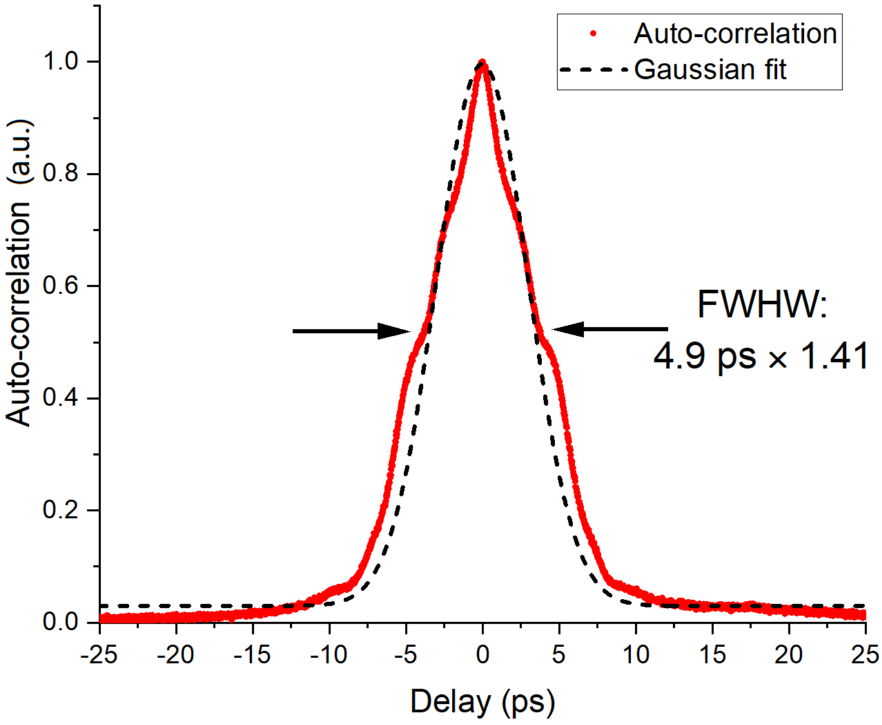

Figure 5.25: Auto-correlation of direct output pulse

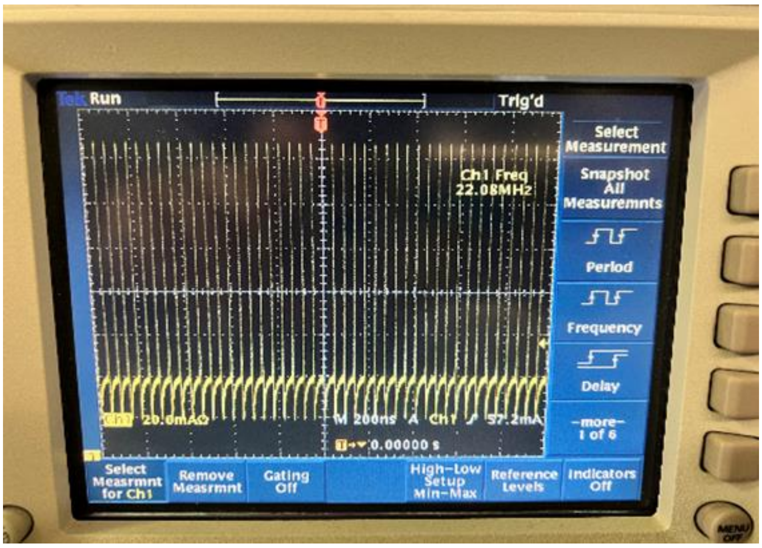

Figure 5.26: Mode-locked oscilloscope traces (screenshot)

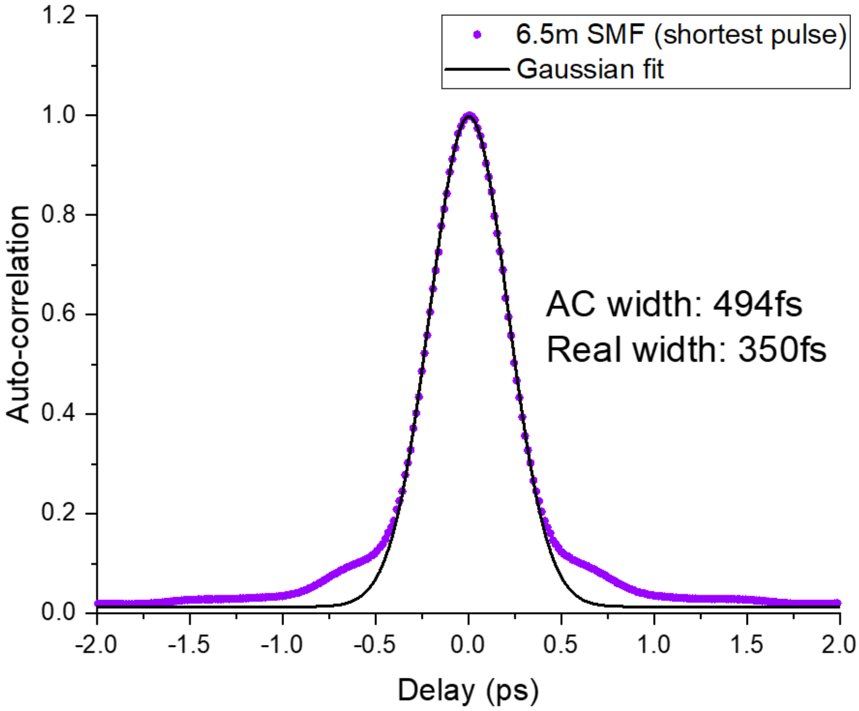

Figure 5.27: Auto-correlation of compressed pulse by 6.5 m long SMF.

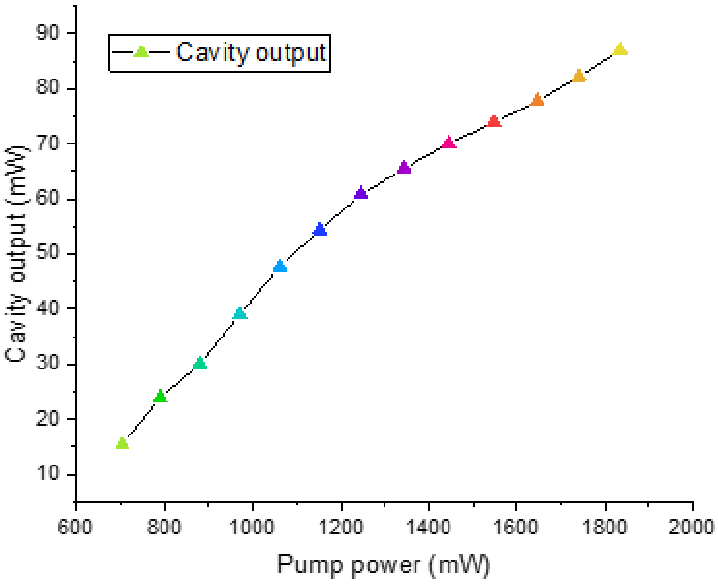

Figure 5.28: Cavity output power curve (Decrease the pump power).

The mode locking performance of this laser was found to be quite good. I have tested and monitored the output of the dissipative-soliton mode-locked over a period of 100 minutes. Figure 5.29 shows the output power was relatively stable exhibiting only slow and small variations (± 10 %) that could be due to the temperature changes/cycles from the air conditioner in the lab and the movement of the PCs. Infinite persistence mode of pulse measurement during the 100 minutes displayed on the oscilloscope is shown in the inset of Figure 5.29. The output spectrum was recorded every 20 minutes, as shown in Figure 5.30, showing no obvious changes, and further proving the good mode locking stability. The mode-locked status remains stable and unaffected, irrespective of physical interaction with the PM1550 fiber or Thulium-doped fiber (TDF).

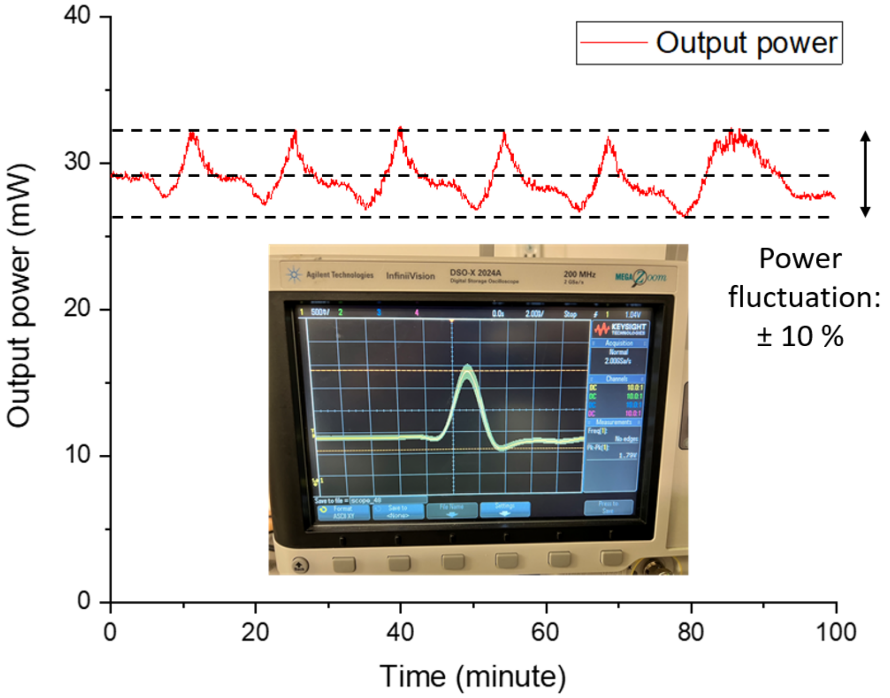

Figure 5.29: Cavity output power stability test over 100mins. Inset: Pulse stability in the oscilloscope over 100 mins.

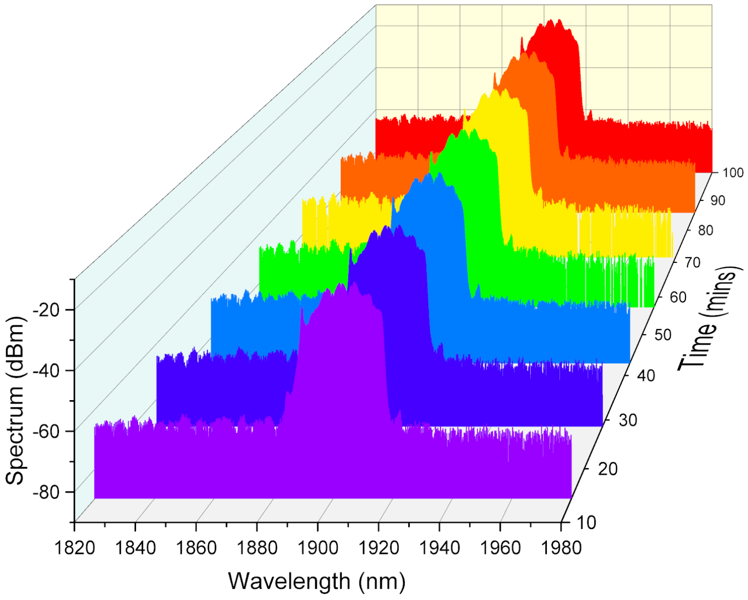

Figure 5.30: Spectral stability over 100mins

A numerical simulation of the dissipative-soliton mode locking was also performed. Good agreement of the output spectrum between the simulation and experiment has been achieved and is shown in Figure 5.24. Figure 5.31 presents the intracavity spectrum and time domain map/evolution. Figure 5.32 presents the cavity position of key components and the temporal, spectral, and power evolution inside the cavity. The output coupler (OC) is the starting and end point of the simulations. In the passive fibre sections, the pulse strongly stretches in time. The spectral bandwidth narrows due to the co-action of the negative chirp and self-phase modulation. From Figure 5.32, the pulse energy and the peak power increase significantly after the mode-locked pulse passes through the gain fibre. The NOLM with 1 m PM1550 and 4 m PM2000D fibre stretched the pulse width significantly.

| Fibre | $\beta_2$ (Group velocity dispersion parameter) | D (Dispersion parameter) |
|---|---|---|
| PMF (PM1550) | -0.068 $ps^2/m$ | 37.4 ps/nm/km |
| TDF (PMTSF 5/125) | -0.020 $ps^2/m$ | 11 ps/nm/km |
| DCF (PM2000D) | 0.085 $ps^2/m$ | -46.8 ps/nm/km |

Table 5.4: Fibre parameters in the simulation.

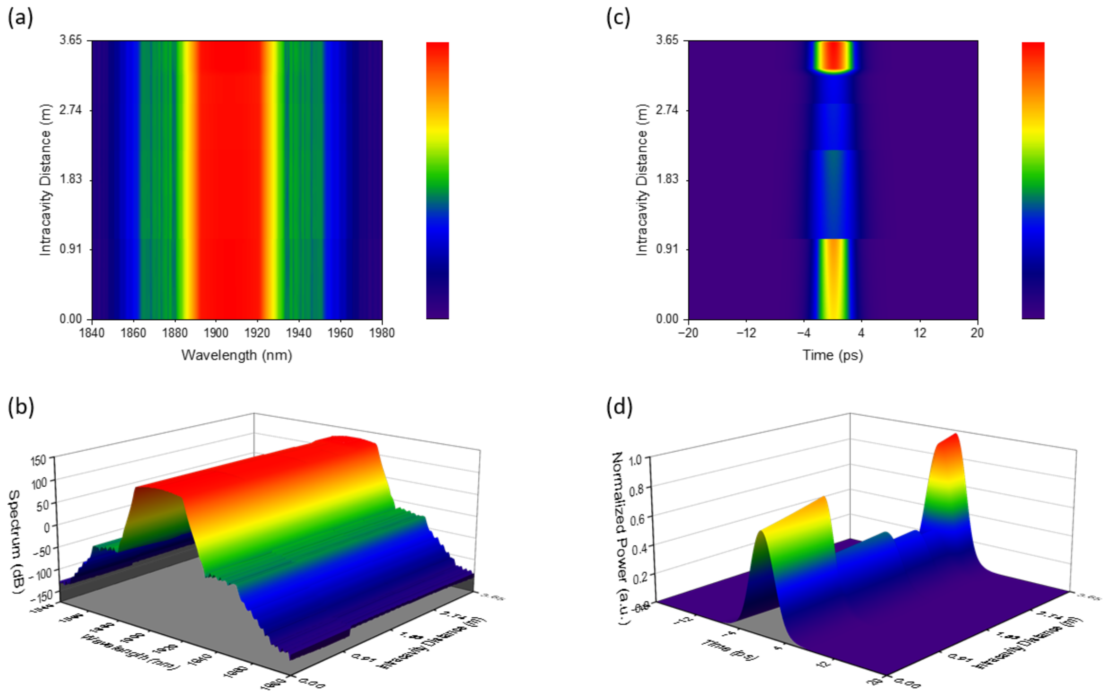

Figure 5.31: Intracavity laser performance characterization: (a) (b) Spectrum heat map and 3D plot of range 1840 nm - 1980 nm in a single round cavity, (c) (d) time domain heat map and 3D plot of range -20 ps - +20 ps in a single round cavity.

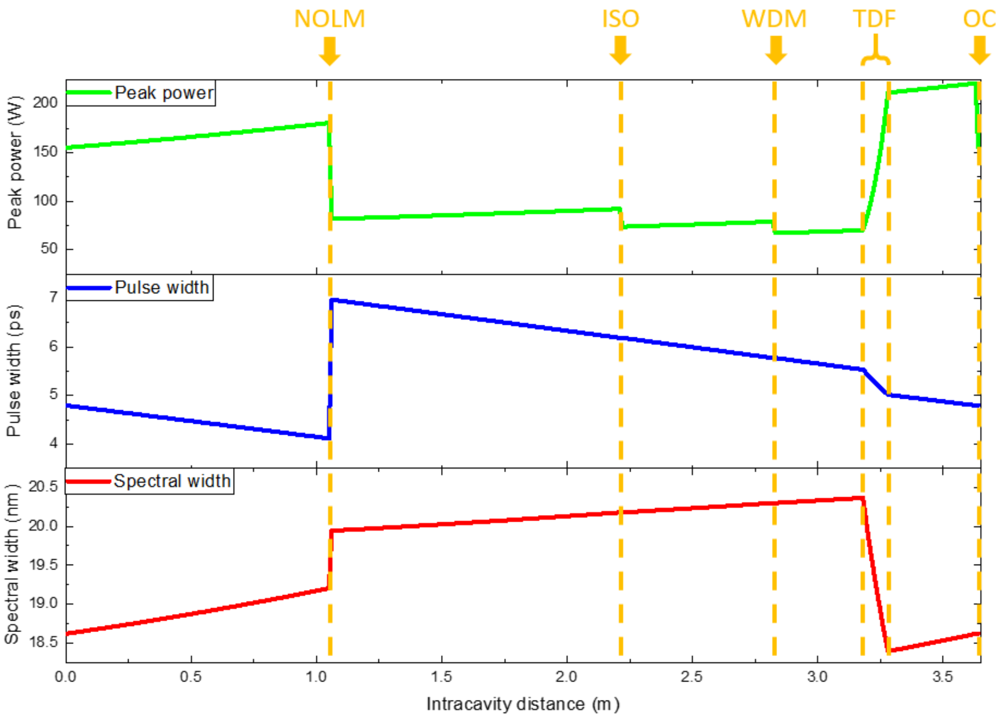

Figure 5.32: Intracavity laser performance characterization of peak power, spectral width and pulse width based on numerical simulations.

## 5.3 Summary

In summary, I have shown the world-first demonstration of a compact and reliable, stable all-PM thulium-doped dissipative soliton mode-locked fibre laser by NOLM (Huang et al. got all-PM dissipative soliton result at 2-micron [82] but they used silicate based fiber). This laser is shown to have a 4nJ pulse energy and 350 fs pulse width (after compression) with an 18.5 nm spectral width and 22 MHz rep. rate at around 1900 nm. The mode locking was achieved by exploring the NOLM mechanism and the dispersion was managed to net positive by inserting a piece of DCF in the loop mirror. I demonstrated that it can be used either on its own as a light source or in association with the following CPA system for bio-microscopy. I also presented the progress of demonstrating this laser including NOLM-based conventional soliton pulse and stretched pulse and SESAM-based cavity with conventional soliton pulse output. Table 5.5 gives a summary of every mode-locked laser cavities and figure 5.33 gives a summary of the NOLM based mode-locked laser results based on different DCF length/GDD.

Table 5.5: Summary of mode-locked laser cavities

| Mode locking mechanism | Cavity output | Net dispersion ($ps^2$) | Pulse energy |
|---|---|---|---|
| SESAM | Conventional soliton | -0.32 | 80 pJ |
| NOLM | Conventional soliton | -1.87 | 80 pJ |
| NOLM | Stretched pulse | -0.82 | 0.28 nJ |
| NOLM | Dissipative soliton | +0.03 | 4 nJ |

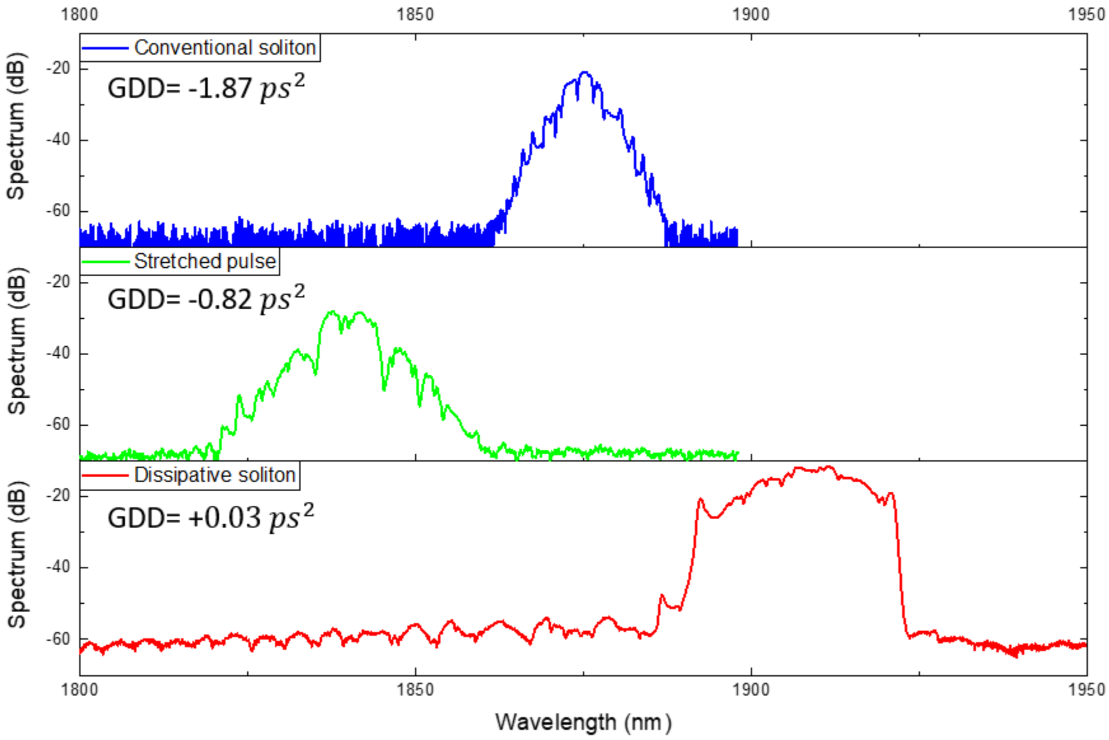

Figure 5.33: Evolution of the output spectrum by varying the intracavity dispersion

A SESAM based conventional soliton mode-locked all-PM fibre laser at 1850 nm was developed. Due to the Q-switched mode locking, damage to the SESAM and fiber end and limitation of shorter wavelength there is no further dispersion managed mode locking by this SESAM based all-PM cavity. To obtain a much higher damage threshold and a potential shorter wavelength operation rang, a NOLM saturable absorber based all-PM 1875 nm conventional soliton mode-locked fibre laser is demonstrated. The pulse energy of this configuration is too low to become a ideal seed laser of a MOPA/CAS system for bio-imaging. To increase the pulse energy, a piece of DCF was inserted into the loop mirror (net dispersion still negative). Stretched pulse mode locking at 1840 nm was achieved by 10 m PM1550 and 4 m PM2000D in the cavity. The pulse energy of the stretched pulse was still relatively low and the PM2000D fibre did not maintain the polarization well so the results were unstable and not useful.

By applying the NOLM technique in an all-PM fibre mode-locked cavity, our work gave a more stable and compact option for THG imaging compared to SESAM-based cavities or non-PM cavities.

The entire work was undertaken and completed by me independently, under the guidance of my colleagues at ORC especially my supervisor Lin Xu.

We are in contact with Nufern to solve the problem with the PM2000D DCF. Next step we should be able to use a true PM DCF in the cavity and apply a band pass filter at 1800 nm (less water absorption compared with 1900 nm) in the cavity such that the pulse energy can also be increased by precise dispersion management and cavity design without considering the damage to the SESAM or other low damage threshold materials like graphene. In-line polarization controllers will not be needed in such a cavity.

# Chapter 6

# Conclusions and future directions

## 6.1 Summary of the thesis

In summary, I have shown the demonstration of a compact and reliable, tunable, CW seeded synchronization-free PPLN OPA pumped by a picosecond, 1 μm commercial pump laser and shown its performance when used as a simple yet powerful source for label-free CARS and concurrent SHG and TPEF microscopy in an epi-detection geometry. This laser and OPA combination is shown to be well suited for label-free CARS and concurrent SHG and two-photon fluorescence microscopy in an epi detection geometry. Rapid and accurate tuning between Raman resonances was achieved by changing the channels and temperatures of OPA and SHG crystals concurrently with tuning the CW OPA seed wavelength. The average power level of above 175 mW, spectral resolution of 8 $cm^{-1}$, and 2 ps pulse duration are well optimized for CARS microscopy in bioscience and bio-medical imaging systems. The final output tuning range is 775 nm - 805 nm. The corresponding pump-Stokes frequency detuning range was from 2700 to 3200 $cm^{-1}$, thus fully covering the C-H stretching band that is typically used for the imaging of lipids. I also presented a similar OPA but seeded by a CW laser diode source which costs much less than a tunable laser source seed. This OPA was a versatile light source module that can be tailored to the tunability and affordability requirements of the specific application. I demonstrated that it could be used either on its own as a light source or in association with an OPO for multimodal CRS microscopy corresponding Pump-Stokes frequency detuning range from 340 to 2400 $cm^{-1}$ which covers the fingerprint region. By combining elements of multiphoton techniques in an inexpensive and compact configuration, our work paves the way for the simple implementation of multimodal CARS with concurrent SHG/TPEF imaging capability. Power level, spectral resolution and dwell times are all comparable with previous reports [175], while utilizing a much simpler setup. This stepping stone points to a lower cost future route to the translation of nonlinear laser microscopy imaging for biomedical research and imaging based diagnostics in the clinic. The next steps in the translation of the nonlinear source to clinics and hospitals will involve progressing the system into a robust prototype that can operate in a non-specialised environment.

An all-fiberized 1840-nm thulium fibre laser source comprising a dissipative-soliton mode-locked seed laser and a chirped-pulse-amplification system has been developed and applied for label-free biological imaging through multiphoton microscopy. The mode-locked thulium fibre laser generated pre-chirped pulses with duration of 7 ps and pulse energy of 1 nJ. A chirped-pulse fibre amplification system was built, where commercially available low-absorption and in-house fabricated high-absorption single-mode thulium fibres were employed and compared, which delivered pulses with energies up to 105 nJ. The pulses were compressed to 416 fs by passing through a grating pair. The third-harmonic generation microscopy imaging capability of the laser system was demonstrated on $BaTiO_3$ nanocrystals and soft and hard biological tissues.

I have shown the world-first demonstration of a compact, stable and reliable all-PM thulium-doped dissipative soliton mode-locked fibre laser by NOLM (Huang et al. got all-PM dissipative soliton result at 2-micron [82] but they used silicate based fiber). This laser was shown to have a 4 nJ pulse energy and 350 fs pulse width (after compression) with an 18.5 nm spectral width and 22 MHz repetition rate at around 1900 nm. The mode locking was achieved by the NOLM mechanism and the dispersion was managed to net positive by inserting a piece of DCF in the loop mirror. I demonstrated that it could be used either on its own as a light source or in association with the following CPA system for bio-microscopy. I also presented the progress in demonstrating this laser including NOLM-based conventional soliton pulse and stretched pulse and SESAM-based cavity with conventional soliton pulse output. By applying the NOLM technique in an all-PM fibre mode-locked cavity, our work gave a more stable and compact option for THG imaging compared to SESAM-based cavities or non-PM cavities.

## 6.2 Future work

### 6.2.1 Wider range OPA imaging system

In order to manage CARS imaging of multiple different biological samples, a wider wavelength/frequency coverage OPA system will be developed based on a new designed 1.95 $\mu$m fibre laser combined with the existing OPO system. IfLS has ordered several new laser diodes as seeds of the OPA to extend the wavelength tuning range. In addition, IfLS might take over this OPA system and apply it to stimulated Raman scattering (SRS) microscopy.

Additionally we will need to progress with clinical feasibility studies with such a microscope system based on the developed laser to demonstrate reproducible performance and visualisation ability for improved diagnosis.

### 6.2.2 Higher power non-PM laser system for deeper THG imaging

In the future, adaptive pulse control will be applied in the 1840-nm femtosecond thulium fibre laser system for label-free third-harmonic generation microscopy. In order to increase the pulse energy we can reduce the repetition rate by using an Acousto-optic modulator (AOM) or Electro-optic modulator (EOM) in the control loop shown in Figure 6.1.

The idea of reducing the repetition rate of the non-PM system is aiming to achieve higher peak powers and better imaging results (deeper). For this purpose, nonlinear effects in the amplifiers need to be considered and addressed. For example, to increase the stretched pulse width, use larger mode area gain fibres and etc.

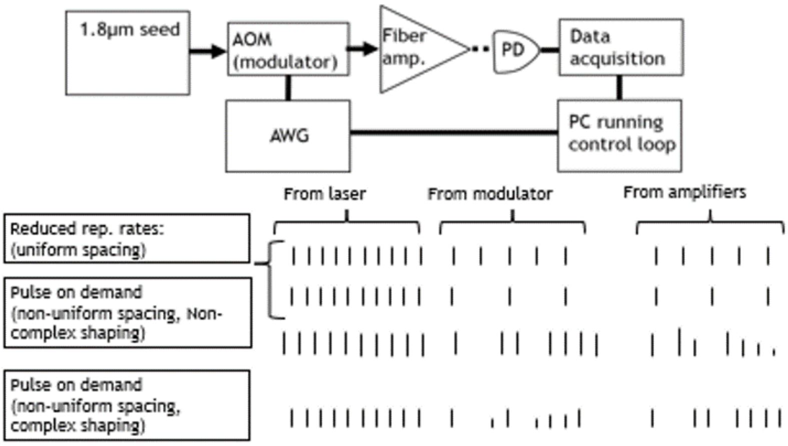

Figure 6.1: Schematic of adaptive pulse control

We have developed a preliminary adaptive pulse control laser system by applying an AOM in the control loop. It can deliver 400 fs pulses with 20 MHz repetition rate and 60 kW peak power, 10 MHz repetition rate and 118 kW peak power, 5 MHz repetition rate and 235 kW peak power, 2 MHz repetition rate and 625 kW peak power. Some THG imaging experiments have been tested as well. From THG images of the spongy bone in Figure 6.2, obviously 2 MHz repetition rate operation had the best contrast comparing to 20 MHz, 10 MHz, 5 MHz repetition rate operation. In addition, 2 MHz repetition rate operation could go deeper up to 110 $\mu$m compared to 60 $\mu$m in 20 MHz repetition rate operation.

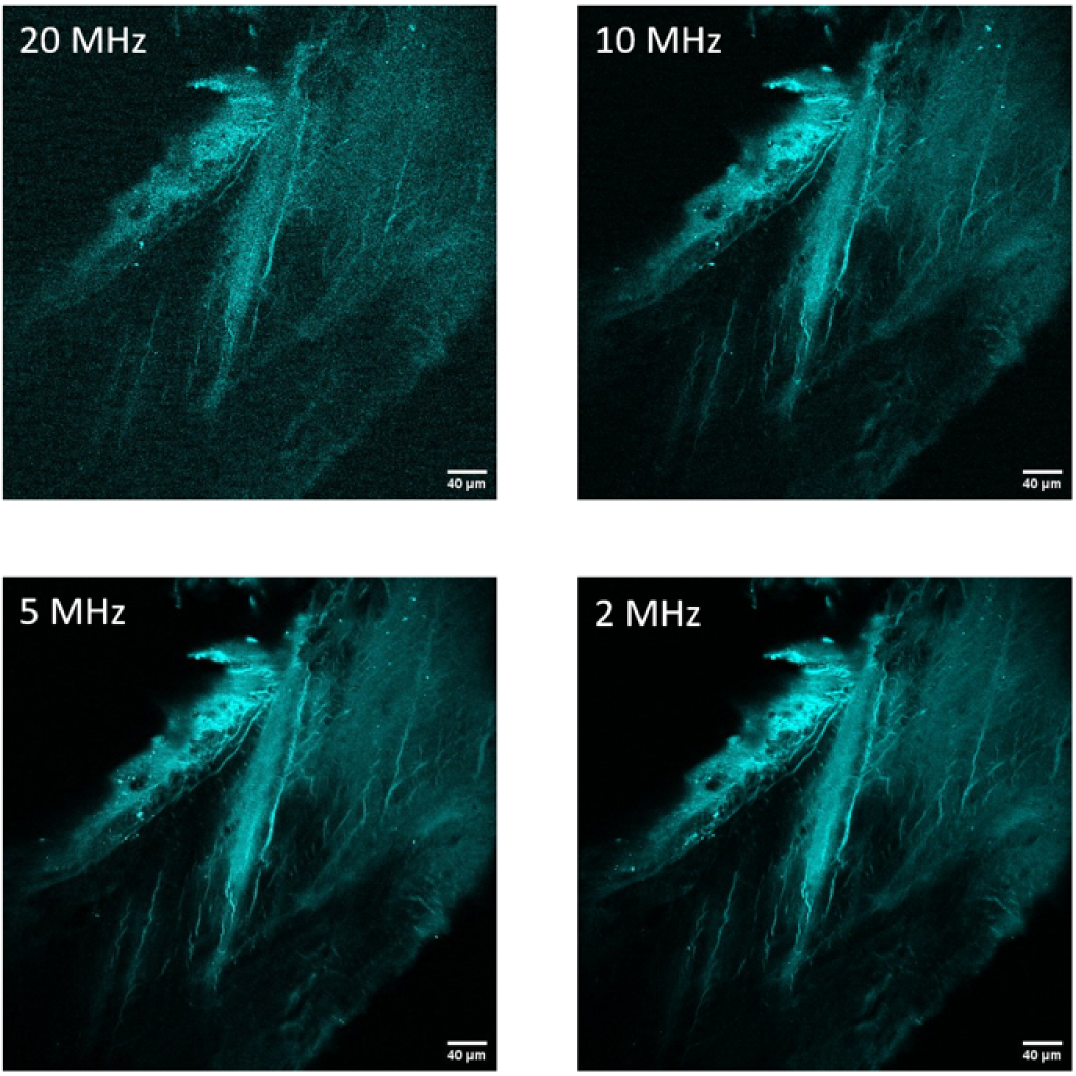

Figure 6.2: THG images of the spongy bone (part of human femoral head) from 20 MHz, 10 MHz, 5 MHz and 2 MHz repetition rate operation.

Additionally, we have several carbon nanotube (CNT) samples from Cambridge so they can be applied in the seed cavity to replace the SESAM. SESAMs generally have a limited bandwidth which results from their resonant design and require complex semiconductor fabrication processes, packaging and integration. CNTs possess ultrafast recovery time, large modulation depth and wide operation bandwidth [216], [192]. It means it will have a wider spectral tuning range, a shorter pulse width and is easier to get mode locking compared with SESAMs.

### 6.2.3 Apply bandpass filter in all-PM laser system

We are in contact with Nufern to solve the problem with the PM2000D DCF. Next step we should be able to use a true PM DCF in the cavity and apply a band pass filter at 1800 nm (less water absorption compared with 1900 nm) in the cavity such that the pulse energy can also be increased by precise dispersion management and cavity design without considering the damage to the SESAM or other low damage threshold materials like graphene. In-line polarization controllers will not be needed in such a cavity.

A 1800 nm fiberized bandpass filter has been ordered. The design of the cavity is shown in Figure 6.3. Ideally we will get dissipative soliton mode locking at 1800 nm with more than 5 nJ pulse energy. It can act as a direct laser source on its own or following a CPA as a whole system for THG/3PM microscopy.

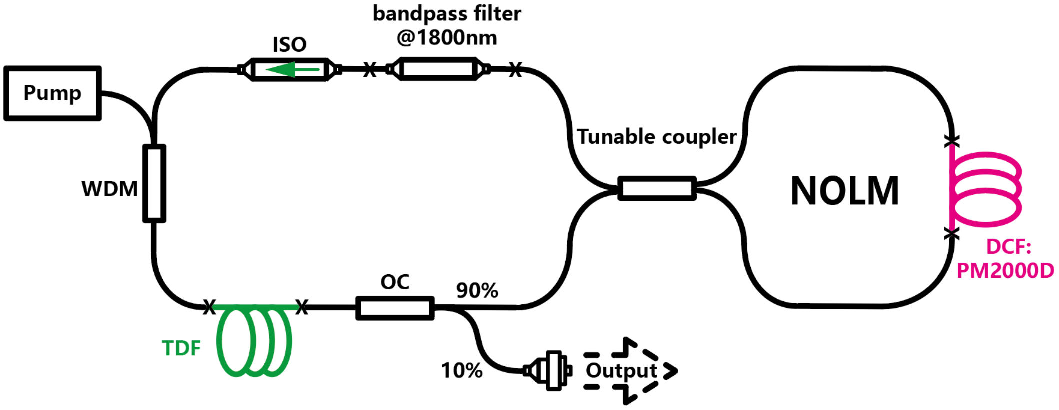

Figure 6.3: Schematic of the cavity with a bandpass filter.

## 6.3 List of publications

- Duanyang Xu, Sijing Liang, Lin Xu, Konstantinos N. Bourdakos, Peter Johnson, James Read, Jonathan H. V. Price, Sumeet Mahajan, and David J. Richardson, “Widely-tunable synchronisation-free picosecond laser source for multimodal CARS, SHG, and two-photon microscopy,” Biomed. Opt. Express 12, 1010-1019 (2021).

- Konstantinos N. Bourdakos, Duanyang Xu, Peter B. Johnson, Anna Crisford, Lin Xu, Sijing Liang, Jonathan H. V. Price, David J. Richardson, Sumeet Mahajan, “A versatile, low cost light source module for multiphoton imaging,” Proc. SPIE 11879, Frontiers in Biophotonics and Imaging, 1187903 (6 October 2021).

- K. N. Bourdakos, D. Xu, P. B. Johnson, A. Crisford, L. Xu, S. Liang, J. H. V. Price, D. J. Richardson, and S. Mahajan, “A synchronisation free, versatile Optical Parametric Amplifier as a low cost light source for multiphoton imaging.,” in OSA Nonlinear Optics 2021, R. Boyd, C. Conti, D. Christodoulides, and P. Rakich, eds., OSA Technical Digest (Optica Publishing Group, 2021), paper NF1B.1.

- D. Lin, D. Xu, J. He, Y. Feng, Z. Ren and D. J. Richardson, “Generation of 625nJ Pulses from a Mamyshev Oscillator with a few-mode LMA Yb-doped Fiber,” 2021 Conference on Lasers and Electro-Optics Europe & European Quantum Electronics Conference (CLEO/Europe-EQEC), Munich, Germany, 2021, pp. 1-1.

- Di Lin, Duanyang Xu, Jing He, Yutong Feng, Zhengqi Ren , Raghuraman Sidharthan, Yongmin Jung, Seongwoo Yoo, and David J. Richardson, “The Generation of 1.2 $\mu$J Pulses From a Mamyshev Oscillator Based on a High Concentration, Large-Mode-Area Yb-Doped Fiber,” in Journal of Lightwave Technology, vol. 40, no. 21, pp. 7175-7179, 1 Nov.1, 2022.

- Lin Xu, Duanyang Xu, Konstantinos N. Bourdakos, Peter B. Johnson, Anna Crisford, Ibrahim Abughazaleh, Panuwat Srisamran, Qiang Fu, Sumeet Mahajan, and David J. Richardson, “1840-nm femtosecond thulium fiber laser system for label-free third-harmonic generation microscopy,” in Conference on Lasers and Electro-Optics, Technical Digest Series (Optica Publishing Group, 2022).

- Panuwat Srisamran, Duanyang Xu, Ibrahim Abughazaleh, Matthew Gerard, Sijing Liang, David Richardson and Lin Xu, “1875-nm high-energy mode-locked thulium fiber laser,” in EPJ Web Conf., 267 (2022) 02013.

- Konstantinos N. Bourdakos, Lin Xu, Anna Crisford, Duanyang Xu, Ibrahim Abughazaleh, Peter B. Johnson, Hiroki Cook, Panuwat Srisamran, Richard O. C. Oreffo, David J. Richardson, Sumeet Mahajan, “Deep tissue imaging with multiphoton microscopy in the short-wavelength infrared windows,” Proc. SPIE 12333, Frontiers in Biophotonics and Imaging II, 123330E (11 January 2023).

# References

[1] Z. A. Vibrational mircoscopy using coherent anti-Stokes Raman scattering. *Phys. Rev. Lett.*, 82:4014–, 1999.

[2] O. Acuto. T cell-dendritic cell interaction in vivo: random encounters favor development of long-lasting ties. *Science's STKE : signal transduction knowledge environment*, 2003(192), jul 2003.

[3] G. Agrawal. *Nonlinear Fiber Optics.* Elsevier Inc., fifth edition, 2012.

[4] C. Aguergaray, N. G. R. Broderick, M. Erkintalo, J. S. Y. Chen, and V. Kruglov. Mode-locked femtosecond all-normal all-PM Yb-doped fiber laser using a nonlinear amplifying loop mirror. *Optics Express*, 20(10):10545, may 2012.

[5] S. A. Akhmanov, A. I. Kovrigin, A. S. Piskarskas, V. V. Fadeev, and R. V. Khokhlov. Observation of parametric amplification in the optical range. *Soy. Phys. JETP*, 2:191–193, 1965.

[6] V. Andresen, S. Alexander, W. M. Heupel, M. Hirschberg, R. M. Hoffman, and P. Friedl. Infrared multiphoton microscopy: subcellular-resolved deep tissue imaging. *Current Opinion in Biotechnology*, 20:54–62, 2 2009.

[7] F. Aptel, N. Olivier, A. Deniset-Besseau, J. M. Legeais, K. Plamann, M. C. Schanne-Klein, and E. Beaurepaire. Multimodal nonlinear imaging of the human cornea. *Investigative Ophthalmology and Visual Science*, 51(5):2459–2465, may 2010.

[8] M. Baba, R. A. Ganeev, M. Suzuki, M. Ichihara, and H. Kuroda. Low- and high-order nonlinear optical properties of $BaTiO_3$ and $SrTiO_3$ nanoparticles. *JOSA B, Vol. 25, Issue 3, pp. 325-333*, 25:325–333, 3 2008.

[9] B. J. Bacskai, S. T. Kajdasz, R. H. Christie, C. Carter, D. Games, P. Seubert, D. Schenk, and B. T. Hyman. Imaging of amyloid-$\beta$ deposits in brains of living mice permits direct observation of clearance of plaques with immunotherapy. *Nature Medicine*, 7(3):369–372, 2001.

[10] B. J. Bacskai, S. T. Kajdasz, M. E. McLellan, D. Games, P. Seubert, D. Schenk, and B. T. Hyman. Non-Fc-mediated mechanisms are involved in clearance of

amyloid-$\beta$ in vivo by immunotherapy. *Journal of Neuroscience*, 22(18):7873–7878, sep 2002.

[11] Y. Barad, H. Eisenberg, M. Horowitz, and Y. Silberberg. Nonlinear scanning laser microscopy by third harmonic generation. *Applied Physics Letters*, 70(8):922–924, aug 1997.

[12] Y. Barad, H. Eisenberg, M. Horowitz, and Y. Silberberg. Nonlinear scanning laser microscopy by third harmonic generation. *Applied Physics Letters*, 70(8):922–924, aug 1997.

[13] Y. Barad, H. Eisenberg, M. Horowitz, and Y. Silberberg. Nonlinear scanning laser microscopy by third harmonic generation. *Applied Physics Letters*, 70:922–924, 2 1997.

[14] W. L. Barnes and J. E. Townsend. Highly tunable and efficient diode pumped operation of $Tm^{3+}$ doped fibre lasers. *Electronics Letters*, 26(11):746–747, 1990.

[15] BATOP-GmbH. https://www.batop.de/, 2022.

[16] BATOP-GmbH. https://www.batop.de/information/sam_infos.html, 2022.

[17] A. A. Borodkin, D. V. Khudyakov, and S. K. Vartapetov. Subnanosecond and picosecond generation regimes of all-pm yb-doped fiber lasermode-locked by nolm. volume 747. Institute of Physics Publishing, 9 2016.

[18] K. Bourdakos, D. Xu, P. Johnson, A. Crisford, L. Xu, A. Konstantinos, N. Bourdakos, P. B. Johnson, S. Liang, J. H. V. Price, D. J. Richardson, K. N. Bourdakos, and S. Mahajan. A versatile, low cost light source module for multiphoton imaging. *Frontiers in Biophotonics and Imaging*, 11879:9–14, 10 2021.

[19] A. Brenier, C. Pedrini, B. Moine, J. L. Adam, and C. Pledel. Fluorescence mechanisms in Tm3+ singly doped and $Tm^{3+}$, $Ho^{3+}$ doubly doped indium-based fluoride glasses. *Physical Review B*, 41(8):5364–5371, 1990.

[20] E. B. Brown, R. B. Campbell, Y. Tsuzuki, L. Xu, P. Carmeliet, D. Fukumura, and R. K. Jain. In vivo measurement of gene expression, angiogenesis and physiological function in tumors using multiphoton laser scanning microscopy. *Nature Medicine*, 7(7):864–868, 2001.

[21] J. M. Bueno, F. J. Ávila, and P. Artal. Second Harmonic Generation Microscopy: A Tool for Quantitative Analysis of Tissues. In *Microscopy and Analysis*. IntechOpen, sep 2016.

[22] M. D. Burns, P. C. Shardlow, P. Barua, T. L. Jefferson-Brain, J. K. Sahu, and W. A. Clarkson. 47 w continuous-wave 1726 nm thulium fiber laser core-pumped by an erbium fiber laser. *Optics Letters*, 44:5230, 11 2019.

[23] M. D. Cahalan, I. Parker, S. H. Wei, and M. J. Miller. Two-photon tissue imaging: Seeing the immune system in a fresh light. *Nature Reviews Immunology*, 2(11):872–880, nov 2002.

[24] C. H. Camp and M. T. Cicerone. Chemically sensitive bioimaging with coherent Raman scattering. *Nature Photonics 2015 9:5*, 9(5):295–305, apr 2015.

[25] P. J. Campagnola, H. A. Clark, W. A. Mohler, A. Lewis, and L. M. Loew. Second-harmonic imaging microscopy of living cells. *Journal of Biomedical Optics*, 6(3):277, jul 2001.

[26] P. J. Campagnola, A. C. Millard, M. Terasaki, P. E. Hoppe, C. J. Malone, and W. A. Mohler. Three-dimensional high-resolution second-harmonic generation imaging of endogenous structural proteins in biological tissues. *Biophysical Journal*, 82(1):493–508, jan 2002.

[27] P. J. Campagnola, A. C. Millard, M. Terasaki, P. E. Hoppe, C. J. Malone, and W. A. Mohler. Three-dimensional high-resolution second-harmonic generation imaging of endogenous structural proteins in biological tissues. *Biophysical Journal*, 82(1):493–508, 2002.

[28] P. J. Campagnola, M. D. Wei, A. Lewis, and L. M. Loew. High-resolution nonlinear optical imaging of live cells by second harmonic generation. *Biophysical Journal*, 77:3341–3349, 1999.

[29] G. A. Cervantes. *Technical fundamentals of radiology and CT*. IOP Publishing Ltd, jan 2016.

[30] W. Chang, A. Ankiewicz, J. M. Soto-Crespo, and N. Akhmediev. Dissipative soliton resonances. *Physical Review A - Atomic, Molecular, and Optical Physics*, 78(2), 2008.

[31] B. Chen, T. Jiang, W. Zong, L. Chen, Z. Zhang, and A. Wang. 910nm femtosecond Nd-doped fiber laser for in vivo two-photon microscopic imaging. *Optics Express*, 24:16544, 7 2016.

[32] H. Chen, H. Wang, M. N. Slipchenko, Y. Jung, Y. Shi, J. Zhu, K. K. Buhman, and J.-X. Cheng. A multimodal platform for nonlinear optical microscopy and microspectroscopy. *Optics Express*, 17:1282, 2 2009.

[33] J.-X. Chen, X.-Y. Li, T.-J. Li, Z.-Y. Zhan, M. Liu, C. Li, A.-P. Luo, P. Zhou, K. K.-Y. Wong, W.-C. Xu, and Z.-C. Luo. 1.7-$\mu$m dissipative soliton Tm-doped fiber laser. *Photonics Research*, 9:873, 5 2021.

[34] S. Chen, Y. Chen, K. Liu, R. Sidharthan, H. Li, C. J. Chang, Q. J. Wang, D. Tang, and S. Yoo. W-type normal dispersion thulium-doped fiber-based high-energy all-fiber femtosecond laser at 1.7 µm. *Optics Letters*, 46:3637, 8 2021.

[35] S.-Y. Chen, C.-Y. S. Hsu, and C.-K. Sun. Epi-third and second harmonic generation microscopic imaging of abnormal enamel. *Optics Express*, 16(15):11670, jul 2008.

[36] X. Chen and P. J. Campagnola. SHG Microscopy and Its Comparison with THG, CARS, and Multiphoton Excited Fluorescence Imaging. In *Second Harmonic Generation Imaging*, pages 81–100. CRC Press, jan 2016.

[37] J.-X. Cheng, A. Volkmer, and X. S. Xie. Theoretical and experimental characterization of coherent anti-Stokes Raman scattering microscopy. *Journal of the Optical Society of America B*, 19(6):1363, jun 2002.

[38] J. X. Cheng and X. S. Xie. Coherent anti-stokes raman scattering microscopy: Instrumentation, theory, and applications. *Journal of Physical Chemistry B*, 108:827–840, 2004.

[39] J. X. Cheng and X. S. Xie. Coherent anti-Stokes Raman scattering microscopy: Instrumentation, theory, and applications. *Journal of Physical Chemistry B*, 108(3):827–840, 2004.

[40] J. X. Cheng and X. S. Xie. Vibrational spectroscopic imaging of living systems: An emerging platform for biology and medicine. *Science*, 350(6264), nov 2015.

[41] R. H. Christie, B. J. Bacskai, W. R. Zipfel, R. M. Williams, S. T. Kajdasz, W. W. Webb, and B. T. Hyman. Growth arrest of individual senile plaques in a model of Alzheimer's disease observed by in vivo multiphoton microscopy. *Journal of Neuroscience*, 21(3):858–864, 2001.

[42] P. Ciąćka, A. Rampur, A. Heidt, T. Feurer, and M. Klimczak. Dispersion measurement of ultra-high numerical aperture fibers covering thulium, holmium, and erbium emission wavelengths. *Journal of the Optical Society of America B*, 35(6):1301, 2018.

[43] Covesion-Ltd. https://covesion.com/en/resource/wavelength-engineering-white-paper/, 2022.

[44] C. L. Cox, W. Denk, D. W. Tank, and K. Svoboda. Action potentials reliably invade axonal arbors of rat neocortical neurons. *Proceedings of the National Academy of Sciences of the United States of America*, 97(17):9724–9728, aug 2000.

[45] J. D. D'Amore, S. T. Kajdasz, M. E. McLellan, B. J. Bacskai, E. A. Stern, and B. T. Hyman. In vivo multiphoton imaging of a transgenic mouse model of Alzheimer disease reveals marked thioflavine-S-associated alterations in neurite trajectories. *Journal of Neuropathology and Experimental Neurology*, 62(2):137–145, feb 2003.

[46] J. M. O. Daniel, N. Simakov, M. Tokurakawa, M. Ibsen, and W. A. Clarkson. Ultra-short wavelength operation of a thulium fibre laser in the 1660–1750 nm wavelength band. *Optics Express*, 23:18269, 7 2015.

[47] D. Débarre, W. Supatto, A. M. Pena, A. Fabre, T. Tordjmann, L. Combettes, M. C. Schanne-Klein, and E. Beaurepaire. Imaging lipid bodies in cells and tissues using third-harmonic generation microscopy. *Nature Methods*, 3(1):47–53, dec 2006.

[48] W. Denk, J. H. Strickler, and W. W. Webb. Two-photon laser scanning fluorescence microscopy. *Science*, 248(4951):73–76, 1990.

[49] W. Denk, J. H. Strickler, and W. W. Webb. Two-photon laser scanning fluorescence microscopy. *Science*, 248:73–76, 4 1990.

[50] M. J. F. Digonnet. *Rare-Earth-Doped Fiber Lasers and Amplifiers, Revised and Expanded*. CRC Press, may 2001.

[51] D. A. Dombeck, K. A. Kasischke, H. D. Vishwasrao, M. Ingelsson, B. T. Hyman, and W. W. Webb. Uniform polarity microtubule assemblies imaged in native brain tissue by second-harmonic generation microscopy. *Proceedings of the National Academy of Sciences of the United States of America*, 100(12):7081–7086, jun 2003.

[52] N. J. Doran and D. Wood. Nonlinear-optical loop mirror. *Optics Letters*, 13(1):56, jan 1988.

[53] W. Du, H. Li, J. Li, P. Wang, S. Zhang, and Y. Liu. Mechanism of dissipative-soliton-resonance generation in fiber laser mode-locked by real saturable absorber. *Optics Express*, 26(16):21314, aug 2018.

[54] I. N. Duling, C. J. Chen, P. K. Wai, and C. R. Menyuk. Operation of a Nonlinear Loop Mirror in a Laser Cavity. *IEEE Journal of Quantum Electronics*, 30(1):194–199, 1994.

[55] M. D. Duncan, J. Reintjes, and T. J. Manuccia. Scanning coherent anti-Stokes Raman microscope. *Optics Letters*, 7(8):350, aug 1982.

[56] C. L. Evans and X. S. Xie. Coherent anti-stokes raman scattering microscopy: Chemical imaging for biology and medicine. *Annual Review of Analytical Chemistry*, 1:883–909, 7 2008.

[57] C. L. Evans and X. S. Xie. Coherent anti-Stokes Raman scattering microscopy: Chemical imaging for biology and medicine. *Annual Review of Analytical Chemistry*, 1(1):883–909, 2008.

[58] M. E. Fermann, A. Galvanauskas, G. Sucha, and D. Harter. Fiber-lasers for ultrafast optics. *Applied Physics B: Lasers and Optics*, 65(2):259–275, 1997.

[59] P. A. Franken, A. E. Hill, C. W. Peters, and G. Weinreich. Generation of optical harmonics. *Physical Review Letters*, 7(4):118–119, aug 1961.

[60] C. W. Freudiger, W. Yang, G. R. Holtom, N. Peyghambarian, X. S. Xie, and K. Q. Kieu. Stimulated raman scattering microscopy with a robust fibre laser source. *Nature Photonics*, 8:153–159, 2 2014.

[61] I. Freund and M. Deutsch. Second-harmonic microscopy of biological tissue. *Optics Letters*, 11(2):94, feb 1986.

[62] A. Frick, J. Magee, H. J. Koester, M. Migliore, and D. Johnston. Normalization of Ca2+ signals by small oblique dendrites of CA1 pyramidal neurons. *Journal of Neuroscience*, 23(8):3243–3250, apr 2003.

[63] Y. Furukawa, K. Kitamura, A. Alexandrovski, R. K. Route, M. M. Fejer, and G. Foulon. Green-induced infrared absorption in MgO doped LiNbO3. *Applied Physics Letters*, 78(14):1970–1972, 2001.

[64] A. Galvanauskas, M. E. Fermann, D. Harter, K. Sugden, and I. Bennion. All-fiber femtosecond pulse amplification circuit using chirped Bragg gratings. *Applied Physics Letters*, 66(9):1053–1055, jun 1995.

[65] H. W. Gandy, R. J. Ginther, and J. F. Weller. Stimulated emission of $\mathrm{Tm}^{3+}$ radiation in silicate glass. *Journal of Applied Physics*, 38(7):3030–3031, 1967.

[66] F. Ganikhanov, S. Carrasco, X. S. Xie, M. Katz, W. Seitz, and D. Kopf. Broadly tunable dual-wavelength light source for coherent anti-stokes raman scattering microscopy. *Optics Letters*, 31:1292, 2006.

[67] S. Golovynskyi, I. Golovynska, L. I. Stepanova, O. I. Datsenko, L. Liu, J. Qu, and T. Y. Ohulchanskyy. Optical windows for head tissues in near-infrared and short-wave infrared regions: Approaching transcranial light applications. *Journal of Biophotonics*, 11, 12 2018.

[68] L. A. Gomes, L. Orsila, T. Jouhti, and O. G. Okhotnikov. Picosecond SESAM-based ytterbium mode-locked fiber lasers. *IEEE Journal on Selected Topics in Quantum Electronics*, 10(1):129–136, jan 2004.

[69] P. Grelu and N. Akhmediev. Dissipative solitons for mode-locked lasers. *Nature Photonics*, 6:84–92, 2012.

[70] I. Gryczynski, H. Szmacinski, and J. R. Lakowicz. Rapid Communication: On the Possibility of Calcium Imaging Using Indo-1 with Three-Photon Excitation. *Photochemistry and Photobiology*, 62(4):804–808, 1995.

[71] R. Gumenyuk, I. Vartiainen, H. Tuovinen, and O. G. Okhotnikov. Dissipative dispersion-managed soliton 2 $\mu$m thulium/holmium fiber laser. *Optics Letters*, 36(5):609, mar 2011.

[72] D. C. Hanna, R. M. Percival, R. G. Smart, and A. C. Tropper. Efficient and tunable operation of a Tm-doped fibre laser. *Optics Communications*, 75(3-4):283–286, mar 1990.

[73] J. Hansryd, P. A. Andrekson, M. Westlund, J. Li, and P. O. Hedekvist. Fiber-based optical parametric amplifiers and their applications. *IEEE Journal on Selected Topics in Quantum Electronics*, 8:506–520, 5 2002.

[74] A. Hasegawa and F. Tappert. Transmission of stationary nonlinear optical pulses in dispersive dielectric fibers. I. Anomalous dispersion. *Applied Physics Letters*, 23(3):142–144, oct 1973.

[75] H. A. Haus, K. Tamura, L. E. Nelson, and E. P. Ippen. Stretched-Pulse Additive Pulse Mode-Locking in Fiber Ring Lasers: Theory and Experiment. *IEEE Journal of Quantum Electronics*, 31(3):591–598, 1995.

[76] F. Haxsen, A. Ruehl, M. Engelbrecht, D. Wandt, U. Morgner, and D. Kracht. Stretched-pulse operation of a thulium-doped fiber laser. *Optics Express*, 16(25):20471, dec 2008.

[77] T. Hellerer, A. M. Enejder, and A. Zumbusch. Spectral focusing: High spectral resolution spectroscopy with broad-bandwidth laser pulses. *Applied Physics Letters*, 85:25–27, 7 2004.

[78] F. Helmchen, K. Svoboda, W. Denk, and D. W. Tank. In vivo dendritic calcium dynamics in deep-layer cortical pyramidal neurons. *Nature Neuroscience*, 2(11):989–996, nov 1999.

[79] K. P. Herdzik, K. N. Bourdakos, P. B. Johnson, A. P. Lister, A. P. Pitera, C. yu Guo, P. Horak, D. J. Richardson, J. H. Price, and S. Mahajan. Multimodal spectral focusing cars and sfg microscopy with a tailored coherent continuum from a microstructured fiber. *Applied Physics B: Lasers and Optics*, 126:84, 2020.

[80] M. Horowitz, Y. Barad, and Y. Silberberg. Noiselike pulses with a broadband spectrum generated from an erbium-doped fiber laser. *Optics Letters*, 22(11):799, jun 1997.

[81] N. G. Horton, K. Wang, D. Kobat, C. G. Clark, F. W. Wise, C. B. Schaffer, and C. Xu. In vivo three-photon microscopy of subcortical structures within an intact mouse brain. *Nature Photonics*, 7:205–209, 3 2013.

[82] C. Huang, Q. Wang, J. Geng, T. Luo, R. Liang, and S. Jiang. All-PM dissipative soliton fiber laser at 2-micron. In *Optics InfoBase Conference Papers*, page JTu2A.22. Optica Publishing Group, oct 2017.

[83] S. Huang, A. A. Heikal, and W. W. Webb. Two-photon fluorescence spectroscopy and microscopy of nad(p)h and flavoprotein. *Biophysical Journal*, 82:2811–2825, 2002.

[84] Ibsen-photonics. https://ibsen.com/wp-content/uploads/white-paper-pulse-stretching-and-compressing-using-grating-pairs_v1.pdf, 2022.

[85] B. Ihnatsenka and A. P. Boezaart. Ultrasound: Basic understanding and learning the language. *International Journal of Shoulder Surgery*, 4(3):55–62, Jul 2010.

[86] S. D. Jackson. Cross relaxation and energy transfer upconversion processes relevant to the functioning of 2 $\mu$m $Tm^{3+}$-doped silica fibre lasers. *Optics Communications*, 230(1-3):197–203, jan 2004.

[87] S. D. Jackson. The spectroscopic and energy transfer characteristics of the rare earth ions used for silicate glass fibre lasers operating in the shortwave infrared. *Laser and Photonics Reviews*, 3(5):466–482, 2009.

[88] S. D. Jackson and T. A. King. Theoretical modeling of Tm-doped silica fiber lasers. *Journal of Lightwave Technology*, 17(5):948–956, May 1999.

[89] S. D. Jackson and S. Mossman. Efficiency dependence on the $Tm^{3+}$ and $Al^{3+}$ concentrations for $Tm^{3+}$-doped silica double-clad fiber lasers. *Applied Optics*, 42(15):2702, may 2003.

[90] S. D. Jackson, A. Sabella, and D. G. Lancaster. Application and development of high-power and highly efficient silica-based fiber lasers operating at 2 $\mu$m. *IEEE Journal on Selected Topics in Quantum Electronics*, 13(3):567–572, may 2007.

[91] Y. Jeong, P. Dupriez, J. K. Sahu, J. Nilsson, D. Shen, W. A. Clarkson, and S. D. Jackson. Thulium-ytterbium co-doped fiber laser with 75 W of output power at 2 $\mu$m. In *Solid State Laser Technologies and Femtosecond Phenomena*, volume 5620, page 28. SPIE, dec 2004.

[92] M. Ji, S. Lewis, S. Camelo-Piragua, S. H. Ramkissoon, M. Snuderl, S. Venneti, A. Fisher-Hubbard, M. Garrard, D. Fu, A. C. Wang, J. A. Heth, C. O. Maher, N. Sanai, T. D. Johnson, C. W. Freudiger, O. Sagher, X. S. Xie, and D. A. Orringer. Detection of human brain tumor infiltration with quantitative stimulated Raman scattering microscopy. *Science Translational Medicine*, 7(309):309ra163, oct 2015.

[93] M. Ji, D. A. Orringer, C. W. Freudiger, S. Ramkissoon, X. Liu, D. Lau, A. J. Golby, I. Norton, M. Hayashi, N. Y. Agar, G. S. Young, C. Spino, S. Santagata, S. Camelo-Piragua, K. L. Ligon, O. Sagher, and X. Sunney Xie. Rapid, label-free detection of brain tumors with stimulated raman scattering microscopy. *Science Translational Medicine*, 5(201):201ra119, sep 2013.

[94] T. Kagawa, S. Yoshida, T. Shiraishi, M. Hashimoto, D. Inadomi, M. Sato, T. Tsuzuki, K. Miwa, and K. Yuasa. Basic principles of magnetic resonance imaging for beginner oral and maxillofacial radiologists. 33(2):92–100, may 2017.

[95] I. Kaminer, J. Nemirovsky, and M. Segev. Optimizing 3D multiphoton fluorescence microscopy. *Optics Letters*, 38(19):3945, oct 2013.

[96] U. Keller. Recent developments in compact ultrafast lasers. *Nature*, 424(6950):831–838, 2003.

[97] U. Keller. Ultrafast solid-state laser oscillators: A success story for the last 20 years with no end in sight. *Applied Physics B: Lasers and Optics*, 100(1):15–28, may 2010.

[98] T. Khan, E. S. Muise, P. Iyengar, Z. V. Wang, M. Chandalia, N. Abate, B. B. Zhang, P. Bonaldo, S. Chua, and P. E. Scherer. Metabolic dysregulation and adipose tissue fibrosis: Role of collagen vi. *Molecular and Cellular Biology*, 29:1575–1591, 3 2009.

[99] D. Kobat, N. G. Horton, and C. Xu. In vivo two-photon microscopy to 1.6-mm depth in mouse cortex. *Journal of Biomedical Optics*, 16(10):1, oct 2011.

[100] H. L. Kuo and W. P. Lin. Generation of double-Brillouin-frequency spaced multi wave length and millimeter wave carrier in one loop structure. In *2014 IEEE International Conference on Communication Problem-Solving, ICCP 2014*, pages 230–232, 2014.

[101] R. LaComb, O. Nadiarnykh, S. S. Townsend, and P. J. Campagnola. Phase matching considerations in second harmonic generation from tissues: Effects on emission directionality, conversion efficiency and observed morphology. *Optics Communications*, 281(7):1823–1832, apr 2008.

[102] T. Ladewig, P. Kloppenburg, P. M. Lalley, W. R. Zipfel, W. W. Webb, and B. U. Keller. Spatial profiles of store-dependent calcium release in motoneurones of the nucleus hypoglossus from newborn mouse. 547(3):775–787, mar 2003.

[103] J. R. Lakowicz, I. Gryczynski, H. Malak, M. Schrader, P. Engelhardt, H. Kano, and S. W. Hell. Time-resolved fluorescence spectroscopy and imaging of DNA labeled with DAPI and Hoechst 33342 using three-photon excitation. *Biophysical Journal*, 72(2 I):567–578, 1997.

[104] W. Langbein, I. Rocha-Mendoza, and P. Borri. Coherent anti-stokes raman microspectroscopy using spectral focusing: Theory and experiment. *Journal of Raman Spectroscopy*, 40:800–808, 2009.

[105] B. Lendvai, T. Zelles, B. Rozsa, and E. S. Vizi. A vinca alkaloid enhances morphological dynamics of dendritic spines of neocortical layer 2/3 pyramidal cells. *Brain Research Bulletin*, 59(4):257–260, jan 2003.

[106] H. Li, M. Yan, J. Yu, Q. Xu, X. Xia, J. Liao, and W. Zheng. In vivo identification of arteries and veins using two-photon excitation elastin autofluorescence. *Journal of Anatomy*, 236:171–179, 2020.

[107] J. Li, Z. Sun, H. Luo, Z. Yan, K. Zhou, Y. Liu, and L. Zhang. Wide wavelength selectable all-fiber thulium doped fiber laser between 1925 nm and 2200 nm. *Optics Express*, 22(5):5387, mar 2014.

[108] R. Li, X. Wang, Y. Zhou, H. Zong, M. Chen, and M. Sun. Advances in nonlinear optical microscopy for biophotonics. *Journal of Nanophotonics*, 12(03):1, aug 2018.

[109] S. Li, Y. Li, R. Yi, L. Liu, and J. Qu. Coherent Anti-Stokes Raman Scattering Microscopy and Its Applications. 8:515, dec 2020.

[110] Z. Li, A. M. Heidt, N. Simakov, Y. Jung, J. M. O. Daniel, S. U. Alam, and D. J. Richardson. Diode-pumped wideband thulium-doped fiber amplifiers for optical communications in the 1800 – 2050 nm window. *Optics Express*, 21:26450, 11 2013.

[111] R. S. Lim, A. Kratzer, N. P. Barry, S. Miyazaki-Anzai, M. Miyazaki, W. W. Mantulin, M. Levi, E. O. Potma, and B. J. Tromberg. Multimodal cars microscopy determination of the impact of diet on macrophage infiltration and lipid accumulation on plaque formation in apoe-deficient mice. *Journal of Lipid Research*, 51:1729–1737, 7 2010.

[112] J. Lin, S. Teh, W. Zheng, Z. Wang, and Z. Huang. Multimodal nonlinear optical microscopic imaging provides new insights into acetowhitening mechanisms in live mammalian cells without labeling. *Biomedical Optics Express*, 5:3116, 9 2014.

[113] J. Liu, C. Liu, H. Shi, and P. Wang. High-power linearly-polarized picosecond thulium-doped all-fiber master-oscillator power-amplifier. *Optics Express*, 24:15005, 6 2016.

[114] F. K. Lu, S. Basu, V. Igras, M. P. Hoang, M. Ji, D. Fu, G. R. Holtom, V. A. Neel, C. W. Freudiger, D. E. Fisher, and X. S. Xie. Label-free dna imaging in vivo with stimulated raman scattering microscopy. *Proceedings of the National Academy of Sciences of the United States of America*, 112:11624–11629, 9 2015.

[115] F. K. Lu, S. Basu, V. Igras, M. P. Hoang, M. Ji, D. Fu, G. R. Holtom, V. A. Neel, C. W. Freudiger, D. E. Fisher, and X. S. Xie. Label-free DNA imaging in vivo with stimulated Raman scattering microscopy. *Proceedings of the National Academy of Sciences of the United States of America*, 112(37):11624–11629, sep 2015.

[116] Z. F. Mainen, R. Malinow, and K. Svoboda. Synaptic calcium transients in single spines indicate that NMDA receptors are not saturated. *Nature*, 399(6732):151–155, may 1999.

[117] S. Maiti, J. B. Shear, R. M. Williams, W. R. Zipfel, and W. W. Webb. Measuring serotonin distribution in live cells with three-photon excitation. *Science*, 275(5299):530–532, jan 1997.

[118] A. Majewska, A. Tashiro, and R. Yuste. Regulation of spine calcium dynamics by rapid spine motility. *Journal of Neuroscience*, 20(22):8262–8268, nov 2000.

[119] C. Manzoni, G. Cirmi, D. Brida, S. D. Silvestri, and G. Cerullo. Optical-parametric-generation process driven by femtosecond pulses: Timing and carrier-envelope phase properties. *Physical Review A - Atomic, Molecular, and Optical Physics*, 79, 2009.

[120] M. E. Marhic. *Fiber optical parametric amplifiers, oscillators and related devices.* Cambridge University Press, 2008.

[121] V. J. Matsas, T. P. Newson, D. J. Richardson, and D. N. Payne. Selfstarting passively mode-locked fibre ring soliton laser exploiting nonlinear polarisation rotation. *Electronics Letters*, 28(15):1391–1393, jul 1992.

[122] V. J. Matsas, T. P. Newson, and M. N. Zervas. Self-starting passively mode-locked fibre ring laser exploiting nonlinear polarisation switching. *Optics Communications*, 92(1-3):61–66, aug 1992.

[123] N. Mazumder, N. K. Balla, G. Y. Zhuo, Y. V. Kistenev, R. Kumar, F. J. Kao, S. Brasselet, V. V. Nikolaev, and N. A. Krivova. Label-free non-linear multimodal optical microscopy—basics, development, and applications. *Frontiers in Physics*, 7:461294, 10 2019.

[124] mbfbioscience. https://www.mbfbioscience.com/, 2023.

[125] D. M. McDonald and P. L. Choyke. Imaging of angiogenesis: From microscope to clinic. *Nature Medicine*, 9(6):713–725, jun 2003.

[126] J. Mertz and L. Moreaux. Second-harmonic generation by focused excitation of inhomogeneously distributed scatterers. *Optics Communications*, 196(1-6):325–330, sep 2001.

[127] T. Meyer, H. Bae, S. Hasse, J. Winter, T. von Woedtke, M. Schmitt, K. D. Weltmann, and J. Popp. Multimodal nonlinear microscopy for therapy monitoring of cold atmospheric plasma treatment. *Micromachines*, 10(9), sep 2019.

[128] M. Michalska. Dispersion managed thulium-doped fiber laser mode-locked by the nonlinear loop mirror. *Optics & Laser Technology*, 138:106923, 6 2021.

[129] M. Michalska and J. Swiderski. All-fiber thulium-doped mode-locked fiber laser and amplifier based on nonlinear fiber loop mirror. *Optics and Laser Technology*, 118:121–125, 2019.

[130] M. Michalska and J. Swiderski. Noise-like pulse generation using polarization maintaining mode-locked thulium-doped fiber laser with nonlinear amplifying loop mirror. *IEEE Photonics Journal*, 11, 12 2019.

[131] D. R. Miller, A. M. Hassan, J. W. Jarrett, F. A. Medina, E. P. Perillo, K. Hagan, S. M. S. Kazmi, T. A. Clark, C. T. Sullender, T. A. Jones, B. V. Zemelman, and A. K. Dunn. In vivo multiphoton imaging of a diverse array of fluorophores to investigate deep neurovascular structure. *Biomedical Optics Express*, 8:3470, 7 2017.

[132] M. J. Miller, S. H. Wei, M. D. Cahalan, and I. Parker. Autonomous T cell trafficking examined in vivo with intravital two-photon microscopy. *Proceedings of the National Academy of Sciences of the United States of America*, 100(5):2604–2609, mar 2003.

[133] M. J. Miller, S. H. Wei, I. Parker, and M. D. Cahalan. Two-photon imaging of lymphocyte motility and antigen response in intact lymph node. *Science*, 296(5574):1869–1873, jun 2002.

[134] W. Min, C. W. Freudiger, S. Lu, and X. S. Xie. Coherent Nonlinear Optical Imaging: Beyond Fluorescence Microscopy. *Annual review of physical chemistry*, 62:507, may 2011.

[135] W. Miniscalco. *Optical and Electronic Properties of Rare Earth Ions in Glasses.* 05 2001.

[136] L. P. Mollenauer and R. H. Stolen. The Soliton Laser. In *Optics InfoBase Conference Papers*, volume 9, pages 13–15. Optica Publishing Group, jan 1984.

[137] L. Moreaux, O. Sandre, S. Charpak, M. Blanchard-Desce, and J. Mertz. Coherent scattering in multi-harmonic light microscopy. *Biophysical Journal*, 80(3):1568–1574, mar 2001.

[138] C. C. Moura, K. N. Bourdakos, R. S. Tare, R. O. Oreffo, and S. Mahajan. Live-imaging of bioengineered cartilage tissue using multimodal non-linear molecular imaging. *Scientific Reports*, 9:1–9, 2019.

[139] C. C. Moura, S. A. Lanham, T. Monfort, K. N. Bourdakos, R. S. Tare, R. O. Oreffo, and S. Mahajan. Quantitative temporal interrogation in 3d of bioengineered human cartilage using multimodal label-free imaging. *Integrative Biology (United Kingdom)*, 10:635–645, 2018.

[140] M. Müller, J. Squier, C. A. De Lange, and G. J. Brakenhoff. CARS microscopy with folded BoxCARS phasematching. *Journal of Microscopy*, 197(2):150–158, 2000.

[141] M. Müller, J. Squier, K. R. Wilson, and G. J. Brakenhoff. 3D microscopy of transparent objects using third-harmonic generation. *Journal of Microscopy*, 191(3):266–274, sep 1998.

[142] L. E. Nelson, D. J. Jones, K. Tamura, H. A. Haus, and E. P. Ippen. Ultrashort-pulse fiber ring lasers. *Applied Physics B: Lasers and Optics*, 65(2):277–294, 1997.

[143] Y. Nomura, H. Murakoshi, and T. Fuji. Short-wavelength, ultrafast thulium-doped fiber laser system for three-photon microscopy. *OSA Continuum*, 3:1428, 6 2020.

[144] V. Nucciotti, C. Stringari, L. Sacconi, F. Vanzi, L. Fusi, M. Linari, G. Piazzesi, V. Lombardi, and F. S. Pavone. Probing myosin structural conformation in vivo by second-harmonic generation microscopy. *Proceedings of the National Academy of Sciences of the United States of America*, 107(17):7763–7768, apr 2010.

[145] T. G. Oertner. Functional imaging of single synapses in brain slices. *Experimental Physiology*, 87(6):733–736, 2002.

[146] M. Onesto. https://blog.biodock.ai/one-vs-two-photon-microscopy/.

[147] D. Oron, D. Yelin, E. Tal, S. Raz, R. Fachima, and Y. Silberberg. Depth-resolved structural imaging by third-harmonic generation microscopy. *Journal of Structural Biology*, 147(1):3–11, jul 2004.

[148] D. G. Ouzounov, T. Wang, M. Wang, D. D. Feng, N. G. Horton, J. C. Cruz-Hernández, Y. T. Cheng, J. Reimer, A. S. Tolias, N. Nishimura, and C. Xu. In vivo three-photon imaging of activity of gcamp6-labeled neurons deep in intact mouse brain. *Nature Methods*, 14:388–390, 2017.

[149] A. F. Pegoraro, A. Ridsdale, D. J. Moffatt, Y. Jia, J. P. Pezacki, and A. Stolow. Optimally chirped multimodal cars microscopy based on a single ti:sapphire oscillator. *Optics Express*, 17:2984, 2 2009.

[150] A. F. Pegoraro, A. D. Slepkov, A. Ridsdale, D. J. Moffatt, and A. Stolow. Hyperspectral multimodal CARS microscopy in the fingerprint region. *Journal of Biophotonics*, 7(1-2):49–58, jan 2014.

[151] E. P. Perillo, J. E. McCracken, D. C. Fernée, J. R. Goldak, F. A. Medina, D. R. Miller, H.-C. Yeh, and A. K. Dunn. Deep in vivo two-photon microscopy with a low cost custom built mode-locked 1060 nm fiber laser. *Biomedical Optics Express*, 7:324, 2 2016.

[152] J. P. Pezacki, J. A. Blake, D. C. Danielson, D. C. Kennedy, R. K. Lyn, and R. Singaravelu. Chemical contrast for imaging living systems: molecular vibrations drive CARS microscopy. *Nature Chemical Biology*, 7(3):137, 2011.

[153] C. V. Raman and K. S. Krishnan. A new type of secondary radiation. 121(3048):501–502, 1928.

[154] M. Rehberg, F. Krombach, U. Pohl, and S. Dietzel. Label-free 3D visualization of cellular and tissue structures in intact muscle with second and third harmonic generation microscopy. *PLoS ONE*, 6(11):e28237, nov 2011.

[155] Z. Ren. *Compact femtosecond chirped pulse amplification system based on thulium doped fibre*. PhD thesis, University of Southampton, April 2021.

[156] Z. Ren, F. ben Slimen, J. Lousteau, N. White, Y. Jung, J. H. V. Price, D. J. Richardson, and F. Poletti. Compact chirped-pulse amplification systems based on highly $Tm^{3+}$ -doped germanate fiber. *Optics Letters*, 46(13):3013, jul 2021.

[157] Z. Ren, Q. Fu, L. Xu, J. H. V. Price, S.-u. Alam, and D. J. Richardson. Compact, high repetition rate, 42 MW peak power, 1925 nm, thulium-doped fiber chirped-pulse amplification system with dissipative soliton seed laser. *Optics Express*, 27(25):36741, dec 2019.

[158] Z. Ren, Q. Fu, L. Xu, J. H. V. Price, S. ul Alam, and D. J. Richardson. Compact, high repetition rate, 42 mw peak power, 1925 nm, thulium-doped fiber chirped-pulse amplification system with dissipative soliton seed laser. *Optics Express*, 27:36741, 12 2019.

[159] W. H. Renninger, A. Chong, and F. W. Wise. Dissipative solitons in normal-dispersion fiber lasers. *Physical Review A - Atomic, Molecular, and Optical Physics*, 77(2), 2008.

[160] D. J. Richardson, J. Nilsson, and W. A. Clarkson. High power fiber lasers: current status and future perspectives [Invited]. *Journal of the Optical Society of America B*, 27(11):B63, nov 2010.

[161] H. Rigneault and P. Berto. Tutorial: Coherent Raman light matter interaction processes. *APL Photonics*, 3(9):091101, jul 2018.

[162] D. Roesel, M. Eremchev, T. Schönfeldová, S. Lee, and S. Roke. Water as a contrast agent to quantify surface chemistry and physics using second harmonic scattering and imaging: A perspective. *Applied Physics Letters*, 120(16):160501, apr 2022.

[163] C. Rose, Y. Kovalchuk, J. Eilers, and A. Konnerth. Two-photon Na+ imaging in spines and fine dendrites of central neurons. *Pflügers Archiv - European Journal of Physiology*, 439(1):201–207, dec 1999.

[164] L. S. Rothman, I. E. Gordon, A. Barbe, D. C. Benner, P. F. Bernath, M. Birk, V. Boudon, L. R. Brown, A. Campargue, J. P. Champion, K. Chance, L. H. Coudert, V. Dana, V. M. Devi, S. Fally, J. M. Flaud, R. R. Gamache, A. Goldman, D. Jacquemart, I. Kleiner, N. Lacome, W. J. Lafferty, J. Y. Mandin, S. T. Massie, S. N. Mikhailenko, C. E. Miller, N. Moazzen-Ahmadi, O. V. Naumenko, A. V. Nikitin, J. Orphal, V. I. Perevalov, A. Perrin, A. Predoi-Cross, C. P. Rinsland, M. Rotger, M. Šimečková, M. A. Smith, K. Sung, S. A. Tashkun, J. Tennyson, R. A. Toth, A. C. Vandaele, and J. Vander Auwera. The HITRAN 2008 molecular spectroscopic database. *Journal of Quantitative Spectroscopy and Radiative Transfer*, 110(9-10):533–572, 2009.

[165] rp photonics. https://www.rp-photonics.com, 2023.

[166] B. L. Sabatini and K. Svoboda. Analysis of calcium channels in single spines using optical fluctuation analysis. *Nature*, 408(6812):589–593, nov 2000.

[167] N. M. Sharif, N. M. Yusoff, F. Ahmad, S. W. Harun, and H. Ahmad. Investigation of nitrogen doped graphene as saturable absorber in Thulium-Doped Fiber Laser. In *2015 International Conference on Telematics and Future Generation Networks, TAFGEN 2015*, pages 103–106. Institute of Electrical and Electronics Engineers Inc., oct 2015.

[168] D. Y. Shen, J. K. Sahu, and W. A. Clarkson. High-power widely tunable Tm:fibre lasers pumped by an Er,Yb co-doped fibre laser at 1.6 $\mu$m. *Optics Express*, 14(13):6084, jun 2006.

[169] C. J. R. Sheppard and R. Kompfner. Resonant scanning optical microscope. *Applied Optics*, 17(18):2879, sep 1978.

[170] D. A. Simpson and G. Baxter. Spectroscopy of Thulium Doped Silica Glass. *School of Electrical Engineering*, page 181, 2007.

[171] N. J. Smith, K. J. Blow, and I. Andonovic. Sideband generation through perturbations to the average soliton model. *Journal of Lightwave Technology*, 10(10):1329–1333, oct 1992.

[172] G. Sobon, J. Sotor, I. Pasternak, A. Krajewska, W. Strupinski, and K. M. Abramski. All-polarization maintaining, graphene-based femtosecond Tm-doped all-fiber laser. *Optics Express*, 23:9339, 4 2015.

[173] J. Sotor, J. Bogusławski, T. Martynkien, P. Mergo, A. Krajewska, A. Przewłoka, W. StrupiŃski, and G. SoboŃ. All-polarization-maintaining, stretched-pulse Tm-doped fiber laser, mode-locked by a graphene saturable absorber. *Optics Letters*, 42:1592, 4 2017.

[174] J. M. Squirrell, D. L. Wokosin, J. G. White, and B. D. Bavister. Long-term two-photon fluorescence imaging of mammalian embryos without compromising viability. *Nature Biotechnology*, 17(8):763–767, aug 1999.

[175] T. Steinle, V. Kumar, M. Floess, A. Steinmann, M. Marangoni, C. Koch, C. Wege, G. Cerullo, and H. Giessen. Synchronization-free all-solid-state laser system for stimulated raman scattering microscopy. *Light: Science and Applications*, 5:1–6, 2016.

[176] J. C. Stockert and A. Blazquez-Castro. *Fluorescence Microscopy in Life Sciences.* Bentham Science Publishers, 2017.

[177] R. H. Stolen. Phase-matched-stimulated four-photon mixing in silica-fiber waveguides. *IEEE Journal of Quantum Electronics*, 11:100–103, 1975.

[178] C. Stosiek, O. Garaschuk, K. Holthoff, and A. Konnerth. In vivo two-photon calcium imaging of neuronal networks. *Proceedings of the National Academy of Sciences of the United States of America*, 100(12):7319–7324, jun 2003.

[179] D. Strickland and G. Mourou. Compression of amplified chirped optical pulses. *Optics Communications*, 56(3):219–221, dec 1985.

[180] C. K. Sun, S. W. Chu, S. Y. Chen, T. H. Tsai, T. M. Liu, C. Y. Lin, and H. J. Tsai. Higher harmonic generation microscopy for developmental biology. *Journal of Structural Biology*, 147(1):19–30, jul 2004.

[181] K. Svoboda, W. Denk, D. Kleinfeld, and D. W. Tank. In vivo dendritic calcium dynamics in neocortical pyramidal neurons. *Nature*, 385(6612):161–165, jan 1997.

[182] K. Svoboda, D. W. Tank, and W. Denk. Direct measurement of coupling between dendritic spines and shafts. *Science*, 272(5262):716–719, may 1996.

[183] K. Tamura, E. P. Ippen, H. A. Haus, and L. E. Nelson. 77-fs pulse generation from a stretched-pulse mode-locked all-fiber ring laser. *Optics Letters*, 18(13):1080, jul 1993.

[184] Y. P. Tan and I. Llano. Modulation by K+ channels of action potential-evoked intracellular Ca2+ concentration rises in rat cerebellar basket cell axons. *Journal of Physiology*, 520(1):65–78, oct 1999.

[185] W. M. Tolles, J. W. Nibler, J. R. McDonald, and A. B. Harvey. A review of the theory and application of coherent anti-stokes raman spectroscopy (cars). *Appl. Spectrosc.*, 31:253–271, 7 1977.

[186] E. B. Treacy. Optical Pulse Compression with Diffraction Gratings. *IEEE Journal of Quantum Electronics*, 5(9):454–458, 1969.

[187] T. Y. Tsang. Optical third-harmonic generation at interfaces. *Physical Review A*, 52:4116–4125, 1995.

[188] G. J. Tserevelakis, E. V. Megalou, G. Filippidis, B. Petanidou, C. Fotakis, and N. Tavernarakis. Label-free imaging of lipid depositions in C. elegans using third-harmonic generation microscopy. *PLoS ONE*, 9(1):e84431, jan 2014.

[189] B. M. Walsh and N. P. Barnes. Comparison of Tm: ZBLAN and Tm: Silica fiber lasers; Spectroscopy and tunable pulsed laser operation around 1.9 $\mu$m. *Applied Physics B: Lasers and Optics*, 78(3-4):325–333, feb 2004.

[190] H. W. Wang, T. T. Le, and J. X. Cheng. Label-free imaging of arterial cells and extracellular matrix using a multimodal cars microscope. *Optics Communications*, 281:1813–1822, 2008.

[191] J. Wang, S. Liang, Q. Kang, Y. Jung, S. ul Alam, and D. J. Richardson. Broadband silica-based thulium doped fiber amplifier employing multi-wavelength pumping. *Optics Express*, 24:23001, 10 2016.

[192] J. Wang, X. Liang, G. Hu, Z. Zheng, S. Lin, D. Ouyang, X. Wu, P. Yan, S. Ruan, Z. Sun, and T. Hasan. 152 fs nanotube-mode-locked thulium-doped all-fiber laser. *Scientific Reports*, 6(1):1–7, jul 2016.

[193] K. Wang, Y. Pan, S. Tong, H. Liang, and P. Qiu. Deep-skin multiphoton microscopy of lymphatic vessels excited at the 1700-nm window in vivo. *Biomedical Optics Express*, 12:6474, 10 2021.

[194] W. Wang, J. B. Wyckoff, V. C. Frohlich, Y. Oleynikov, S. Hüttelmaier, J. Zavadil, L. Cermak, E. P. Bottinger, R. H. Singer, J. G. White, J. E. Segall, and J. S. Condeelis. Single cell behavior in metastatic primary mammary tumors correlated with gene expression patterns revealed by molecular profiling. *Cancer Research*, 62(21):6278–6288, 2002.

[195] T. Watanabe, A. Thayil, A. Jesacher, K. Grieve, D. Debarre, T. Wilson, M. Booth, and S. Srinivas. Characterisation of the dynamic behaviour of lipid droplets in the early mouse embryo using adaptive harmonic generation microscopy. *BMC Cell Biology*, 11(1):1–11, jun 2010.

[196] S. H. Wei, M. J. Miller, M. D. Cahalan, and I. Parker. Two-photon imaging in intact lymphoid tissue. *Advances in Experimental Medicine and Biology*, 512:203–208, 2002.

[197] B. Weigelin, G.-J. Bakker, and P. Friedl. Intravital third harmonic generation microscopy of collective melanoma cell invasion. *IntraVital*, 1(1):32–43, jul 2012.

[198] A. M. Weiner. *Ultrafast Optics*, chapter 2, pages 32–84. John Wiley & Sons, Ltd, 2009.

[199] Wikipedia. https://en.wikipedia.org/wiki/second-harmonic_imaging_microscopy#advantages.

[200] Wikipedia. https://en.wikipedia.org/wiki/Two-photon_excitation_microscopy.

[201] R. M. Williams, J. B. Shear, W. R. Zipfel, S. Maiti, and W. W. Webb. Mucosal mast cell secretion processes imaged using three-photon microscopy of 5-hydroxytryptamine autofluorescence. *Biophysical Journal*, 76(4):1835–1846, 1999.

[202] R. H. Wilson, K. P. Nadeau, F. B. Jaworski, B. J. Tromberg, and A. J. Durkin. Review of short-wave infrared spectroscopy and imaging methods for biological tissue characterization. *Journal of Biomedical Optics*, 20(3):030901, mar 2015.

[203] F. W. Wise, A. Chong, and W. H. Renninger. High-energy femtosecond fiber lasers based on pulse propagation at normal dispersion. *Laser and Photonics Reviews*, 2(1-2):58–73, apr 2008.

[204] K. Wolf, I. Mazo, H. Leung, K. Engelke, U. H. Von Andrian, E. I. Deryugina, A. Y. Strongin, E. B. Bröcker, and P. Friedl. Compensation mechanism in tumor cell migration: Mesenchymal-amoeboid transition after blocking of pericellular proteolysis. *Journal of Cell Biology*, 160(2):267–277, jan 2003.

[205] K. K. Wong, B. P. Kuo, M. E. Marhic, G. Kalogerakis, and L. G. Kazovsky. Recent advances in the practical fiber optical parametric amplifiers. *2007 Asia Optical Fiber Communication and Optoelectronic Exposition and Conference, AOE*, pages 203–205, 2007.

[206] C. Xu, W. Zipfel, J. B. Shear, R. M. Williams, and W. W. Webb. Multiphoton fluorescence excitation: New spectral windows for biological nonlinear microscopy. *Proceedings of the National Academy of Sciences of the United States of America*, 93(20):10763–10768, oct 1996.

[207] D. Xu, S. Liang, L. Xu, K. N. Bourdakos, P. Johnson, J. Read, J. H. V. Price, S. Mahajan, and D. J. Richardson. Widely-tunable synchronisation-free picosecond laser source for multimodal CARS, SHG, and two-photon microscopy. *Biomedical Optics Express*, 12(2):1010, feb 2021.

[208] M. Yarbakht, P. Pradhan, N. Köse-Vogel, H. Bae, S. Stengel, T. Meyer, M. Schmitt, A. Stallmach, J. Popp, T. W. Bocklitz, and T. Bruns. Nonlinear Multimodal Imaging Characteristics of Early Septic Liver Injury in a Mouse Model of Peritonitis. *Analytical Chemistry*, 91(17):11116–11121, sep 2019.

[209] C. H. Yeh, C. C. Lee, and S. Chi. 120-nm bandwidth erbium-doped fiber amplifier in parallel configuration. *IEEE Photonics Technology Letters*, 16(7):1637–1639, jul 2004.

[210] D. Yelin, D. Oron, E. Korkotian, M. Segal, and Y. Silberberg. Third-harmonic microscopy with a titanium-sapphire laser. *Applied Physics B: Lasers and Optics*, 74:97–101, jun 2002.

[211] Y. Yu, P. V. Ramachandran, and M. C. Wang. Shedding new light on lipid functions with CARS and SRS microscopy. *Biochimica et biophysica acta*, 1841(8):1120, 2014.

[212] S. Yue, M. N. Slipchenko, and J. X. Cheng. Multimodal nonlinear optical microscopy. *Laser and Photonics Reviews*, 5:496–512, 2011.

[213] R. Yuste and W. Denk. Dendritic spines as basic functional units of neuronal integration. *Nature*, 375(6533):682–684, 1995.

[214] N. J. Zabusky and M. D. Kruskal. Interaction of “solitons” in a collisionless plasma and the recurrence of initial states. *Physical Review Letters*, 15(6):240–243, aug 1965.

[215] C. Zhang and J. X. Cheng. Perspective: Coherent Raman scattering microscopy, the future is bright. *APL Photonics*, 3(9):090901, jul 2018.

[216] Z. Zhang, M. Zhang, L. Chen, Y. Jiao, Z. Tu, L. Ren, Y. Cai, and C. Zhou. Advances in SESAM and carbon nanotube saturable absorber mode locked fiber lasers. In *Optics InfoBase Conference Papers*, page TuF4_2. Optica Publishing Group, aug 2009.

[217] Z. Y. Zhang, A. E. Oehler, B. Resan, S. Kurmulis, K. J. Zhou, Q. Wang, M. Mangold, T. Süedmeyer, U. Keller, K. J. Weingarten, and R. A. Hogg. 1.55 $\mu$m InAs/-GaAs quantum dots and high repetition rate quantum dot SESAM mode-locked laser. *Scientific Reports*, 2(1):1–5, jun 2012.

[218] A. M. Zheltikov. Coherent anti-stokes raman scattering: from proof-of-the-principle experiments to femtosecond cars and higher order wave-mixing generalizations. *Journal of Raman Spectroscopy*, 31:653–667, 2000.

[219] Y. Zhou, K. Xu, and Y. Zeng. All polarization-maintaining, figure-of-9 dispersion-managed er: fiber laser. page 61. SPIE-Intl Soc Optical Eng, 11 2018.

[220] W. R. Zipfel, R. M. Williams, R. Christiet, A. Y. Nikitin, B. T. Hyman, and W. W. Webb. Live tissue intrinsic emission microscopy using multiphoton-excited native fluorescence and second harmonic generation. *Proceedings of the National Academy of Sciences of the United States of America*, 100:7075–7080, 2003.

[221] W. R. Zipfel, R. M. Williams, and W. W. Webb. Nonlinear magic: Multiphoton microscopy in the biosciences. *Nature Biotechnology*, 21:1369–1377, 2003.

[222] A. Zoumi, A. Yeh, and B. J. Tromberg. Imaging cells and extracellular matrix in vivo by using second-harmonic generation and two-photon excited fluorescence. *Proceedings of the National Academy of Sciences of the United States of America*, 99(17):11014–11019, aug 2002.

[223] A. Zumbusch, W. Langbein, and P. Borri. Nonlinear vibrational microscopy applied to lipid biology. *Progress in Lipid Research*, 52:615–632, 10 2013.